



UNIVERSITÉ DE LIÈGE  
FACULTÉ DES SCIENCES APPLIQUÉES  
COLLÈGE DE DOCTORAT EN ELECTRICITÉ,  
ELECTRONIQUE ET INFORMATIQUE

# **Correction of Electromagnetic Measurements and Active Shaping of Electromagnetic Fields in Complex and Reverberating Environments**

— Numerical and Experimental Applications —

DOCTORAL DISSERTATION PRESENTED BY  
**MAXIME SPIRLET**

IN FULLFILMENT OF THE REQUIREMENTS FOR THE DEGREE OF  
*Docteur en Sciences de l'Ingénieur*

– March 2018–



## Thesis committee:

---

Dr. Philippe Besnier (Directeur de recherche CNRS, INSA Rennes, France)  
Prof. Pierre Bonnet (Université Clermont Auvergne, France)  
Prof. Christophe Craeye (Université catholique de Louvain)  
Ir. Véronique Beauvois (Université de Liège)  
Prof. Jean-Jacques Embrechts (Université de Liège), Président  
Prof. Christophe Geuzaine (Université de Liège), Promoteur

## Version history:

---

December 2017: version submitted to the committee,  
March 2018: final version.





---

## Abstract

WITH the growing number of wireless devices and connected objects, the level of electromagnetic noise could reach unprecedented levels, potentially leading to malfunctions. In order to limit this effect, it is important on the one hand to develop systems with enhanced immunity to radiated electromagnetic fields and, on the other hand, to further rationalize the electromagnetic radiation of wireless devices by improving their design.

In this dissertation, two axes of research are addressed. The first aims to help prototyping antennas by accelerating and simplifying the measurement of antenna radiation patterns by performing this measurement in non-dedicated environments, i.e. outside fully anechoic chambers. To achieve this, a method of correction is applied to measured electromagnetic fields *a posteriori* to remove from the radiation pattern the spurious contributions introduced by reflections occurring in the reverberating test environment. The method described in the first part of the manuscript is based on the angular deconvolution of the impulse response of the environment from the echoic pattern. At the end, the results of experimental validations, obtained through several test cases, are presented.

The second axis focuses on the electromagnetic field shaping in reverberating and complex environments, as it would be particularly useful for radiated immunity electromagnetic compatibility tests, allowing them to be performed in arbitrarily reverberating environments without requiring the systematic use of anechoic chambers. Field shaping techniques aim on the one hand to suppress any electromagnetic field introduced by one or more sources of undesired noise in a determined part of an arbitrary environment, and on the other hand to superimpose any arbitrary electromagnetic field map such as plane waves used for radiated immunity tests. To achieve this, a method of field shaping, based on the optimal control theory of Maxwell's equations, is presented. The potential of this method can be appreciated thanks to several numerical simulations presented for various environments. Then, by means of two experimental test cases of more modest complexity, the experimental validity of the method is established.





---

## Résumé

AVEC le nombre grandissant de dispositifs sans fil et d'objets connectés, le niveau de bruit électromagnétique pourrait atteindre des valeurs sans précédents, pouvant potentiellement devenir la cause de dysfonctionnements. Afin de limiter cet effet, il est important d'une part, de développer des systèmes ayant une meilleure immunité face aux champs électromagnétiques rayonnés, et d'autre part, de rationaliser davantage le rayonnement électromagnétique des dispositifs sans-fil.

Dans cette dissertation, deux axes de recherches sont abordés. Le premier vise à simplifier le prototypage d'antennes en accélérant et en simplifiant la mesure de diagrammes de rayonnement d'antennes en effectuant cette mesure dans un environnement non dédié, i.e. autre qu'une chambre complètement anéchoïque. Il s'agit principalement d'appliquer une méthode de correction à des mesures de champs électromagnétiques *a posteriori*, dont le rôle est de retirer du digramme de rayonnement les contributions non-désirées, introduites par des réflexions se produisant dans l'environnement de test réverbérant. La méthode présentée dans la première partie du manuscrit est basée sur la déconvolution angulaire de la réponse impulsionnelle de l'environnement. A la fin de la première partie, les résultats de validations expérimentales, obtenus au travers de nombreux cas tests, sont présentés.

Le second axe s'attache à la mise en forme de champs électromagnétiques en environnement réverbérant, trouvant ainsi notamment son utilité dans les tests de compatibilité électromagnétique en immunité rayonnée qui pourraient dès lors s'effectuer dans un environnement arbitrairement réverbérant, ne nécessitant dès lors plus le recours systématique à une chambre semi-anéchoïque. Cette mise en forme de champ vise, d'une part, à supprimer un quelconque champ électromagnétique introduit par une ou plusieurs sources de bruit indésirable dans une partie définie d'un environnement arbitraire, et d'autre part, d'y superposer un profil de champ électromagnétique arbitraire tel qu'une onde plane pour de l'immunité rayonnée. Pour ce faire une méthode de mise en forme de champs, basée sur la théorie du contrôle optimal des équations de Maxwell, est présentée. Le potentiel de cette méthode pourra être apprécié grâce aux nombreuses simulations numériques présentées pour des environnements variés. Ensuite, au moyen de deux cas-tests expérimentaux de complexité plus modeste, la viabilité expérimentale de la méthode est établie.





---

## Acknowledgements

AU terme de ces quatre années de thèse bien remplies, il est déjà temps de formuler les remerciements d'usage. Tout d'abord, je remercie mon promoteur, Christophe Geuzaine, de m'avoir fait confiance, et plus encore de m'avoir donné confiance en ma capacité à entreprendre une thèse. Ton optimisme à toute épreuve aura finalement eu raison de mon pessimisme chronique.

Je remercie également les membres de mon jury, Philippe Besnier, Pierre Bonnet, Christophe Craeye, Véronique Beauvois et Jean-Jacques Embrechts d'avoir accepté de lire et de critiquer les travaux repris dans cette thèse.

Je souhaite remercier Pierre Bonnet et Sébastien Lalléchère de m'avoir invité et accueilli à l'Institut Pascal de Clermont-Ferrand. Nos différents échanges ont été pour moi d'une aide précieuse dans mes recherches. Je remercie Christophe Craye et Pascal Simon de l'Université Catholique de Louvain de m'avoir donné la possibilité d'utiliser la chambre "full-anéchoïque" de la plate-forme WELCOME, cela a largement contribué à la qualité des résultats expérimentaux présentés dans ce manuscrit.

Si ces quatre années de thèse à l'université de Liège ont passé aussi rapidement, c'est sans nul doute grâce au bon esprit qui a régné au sein du groupe ACE depuis le départ. Je remercie tous les collègues que j'ai eu l'occasion d'y rencontrer, en particulier Anthony, Alexandre H., Alexandre V., Amaury, Axel, Christophe, David, Erin, Fabrice, François, Frédéric O., Frédéric P., Innocent, Isabel, Jean, Jean de Dieu, Jonathan, Kevin, Maryse, Maxime G., Nicolas, Patrick, Pierre, Ruth, Simon, Sophie, Steven, Valera, Vanessa, Véronique, Vincent et Yannick.

Entreprendre une thèse essentiellement expérimentale ne s'improvise pas et nécessite bon nombre de moyens techniques et d'instruments de mesures fragiles et onéreux. Le laboratoire de compatibilité électromagnétique de l'université de Liège étant fort bien équipé, j'ai eu l'immense privilège de pouvoir y mener à bien mes recherches expérimentales dans les meilleures conditions. Bien entendu, même les meilleurs instruments de mesures racontent n'importe quoi si on les utilise mal. Je souhaite donc adresser un remerciement tout particulier à mes collègues "CEM" : Jean, Pierre, Valera et Véronique, jamais avarés de conseils, qui m'ont toujours suivis dans mes tribulations expérimentales, et avec lesquels j'ai appris énormément (et ce n'est pas terminé).

Rien pour moi n'aurait été plus improbable que d'arriver au bout d'une thèse de doctorat. Sans nul doute, c'est à certaines personnes, croisées au fil des années, que je le dois. Ces personnes, qui se reconnaîtront, ont d'une manière ou d'une autre irremédiablement influencé (positivement bien-sûr) le cours de mon existence, je les en remercie.

Je remercie également mes parents et ma soeur de m'avoir encouragé de manière indéfectible depuis toujours, quel qu'ait été mon choix. Je remercie tous mes proches, en particulier ma belle famille: Ariane, Jean-Marc, Alexandre, Aurélie, Nadège et François, pour tous ces bons moments passés ensemble.

Enfin, je remercie ma tendre épouse, Laure-Anne, qui m'a accompagnée dans mon délire d'entreprendre une thèse à trente ans et qui m'a supporté jour après jour. Merci de t'être occupée de nos quatre enfants au quotidien. Merci d'avoir veillé sur nos enfants lorsque je partais en congrès et bien plus encore, Merci d'être toi. Quant à mes enfants Rafaël, Olivier, Romain et Martin, merci d'être là.

Maxime Spirlet



---

# Contents

<b>Abstract</b>	<b>iii</b>
<b>Résumé</b>	<b>v</b>
<b>Acknowledgements</b>	<b>vii</b>
<b>Contents</b>	<b>ix</b>
<b>List of symbols and notations</b>	<b>xiii</b>
<b>Acronyms</b>	<b>xv</b>
<b>Introduction</b>	<b>1</b>
Context and motivations . . . . .	1
Aims and scope of this work . . . . .	2
Outline . . . . .	3
Contributions . . . . .	4
<b>I A posteriori correction of electromagnetic field measurements</b>	<b>5</b>
<b>1 Introduction: overview of electromagnetic correction methods</b>	<b>7</b>
1.1 Introduction . . . . .	7
1.2 Fourier Transform (FT) . . . . .	9
1.3 Matrix Pencil (MP), Total Least Squares (TLS) and other variants . . . . .	10
1.4 Maximum A Priori (MAP) . . . . .	12
1.5 Comparison between FT, MP, TLS and MAP methods through a numerical example . . . . .	14
1.6 Conclusions . . . . .	20
<b>2 Angular Deconvolution Method</b>	<b>21</b>
2.1 Introduction . . . . .	21
2.2 Angular response deconvolution . . . . .	22

2.3	Conclusions . . . . .	28
<b>3</b>	<b>Experimental angular deconvolution method</b>	<b>31</b>
3.1	Introduction . . . . .	31
3.2	Experimental validation and uncertainty . . . . .	31
3.3	Experimental test cases in semi-anechoic environment . . . . .	36
3.4	Experimental parametric test cases . . . . .	41
3.5	Environment response invariance analysis . . . . .	45
3.6	Experimental test cases in realistic environment . . . . .	47
3.7	Conclusions . . . . .	48
<b>II</b>	<b>Active shaping of electromagnetic fields</b>	<b>57</b>
<b>4</b>	<b>Introduction: active shaping of electromagnetic fields</b>	<b>59</b>
4.1	Introduction . . . . .	59
4.2	Hilbert Uniqueness Method . . . . .	60
4.2.1	General principle . . . . .	60
4.2.2	Numerical examples . . . . .	63
4.3	Time Reversal . . . . .	74
4.3.1	Time Reversal in free-space for harmonic sources . . . . .	75
4.3.2	Time Reversal Mirror . . . . .	78
4.3.3	Time Reversal in reverberating cavities for pulsed sources . . . . .	84
4.4	Conclusions . . . . .	94
<b>5</b>	<b>Optimal control of time-harmonic electromagnetic fields</b>	<b>95</b>
5.1	Introduction . . . . .	95
5.2	Numerical examples . . . . .	98
5.3	Noise reconstruction . . . . .	104
5.4	Numerical examples with noise reconstruction . . . . .	106
5.5	Conclusions . . . . .	108
<b>6</b>	<b>Experimental control of time-harmonic electromagnetic fields</b>	<b>113</b>
6.1	Introduction . . . . .	113
6.2	Voltage control within a transmission line . . . . .	114
6.3	Electric field control within a waveguide . . . . .	117
6.4	Conclusions . . . . .	121
	<b>Conclusions</b>	<b>125</b>
6.5	Main achievements and conclusions . . . . .	125
6.6	Prospects for future work . . . . .	126
<b>Appendix A</b>	<b>Measurement chain from chapter 3</b>	<b>129</b>
<b>Appendix B</b>	<b>Measurement chain from chapter 6</b>	<b>133</b>
<b>Appendix C</b>	<b>Hardware and software development</b>	<b>137</b>

C.1	EMCLab . . . . .	137
C.1.1	Instrument Library . . . . .	137
C.1.2	Instrument Manager . . . . .	138
C.1.3	Measurement Chain Editor . . . . .	139
C.1.4	Execution Engine . . . . .	139
C.2	Mobile turntable . . . . .	140
C.3	RF probe meter . . . . .	141
C.4	Phase coherent dual source generator . . . . .	141
<b>List of Figures</b>		<b>145</b>
<b>List of Tables</b>		<b>148</b>
<b>Bibliography</b>		<b>151</b>



# List of symbols and notations

## Notations

$\mathbf{M}$  Matrix  $M$

$\mathbf{v}$  Vector  $v$  (one-dimensional matrix)

$\hat{\mathbf{x}}$  Dual quantity of  $\mathbf{x}$  involved in a Fourier transform

$f$  Scalar quantity

$\vec{A}$  Vector quantity

$\vec{G}$  Tensor quantity

$\vec{\nabla}V$  Gradient of a scalar quantity

$\vec{\nabla} \times \vec{A}$  Curl of a vector quantity

$\vec{\nabla} \cdot \vec{B}$  Divergence of a vector quantity

$A \star B$  Convolution product

$\mathcal{F}_\theta$  Fourier transform with respect to  $\theta$

$\mathcal{F}_\theta^{-1}$  Inverse Fourier transform with respect to  $\theta$

$\tilde{P}$  Estimator of  $P$

$j$  Imaginary unit

$\|\vec{A}\|$   $L_2$  norm of a vector quantity

$\frac{\partial f}{\partial t}$  Partial first derivative of  $f$  with respect to time  $t$

$\frac{\partial^2 f}{\partial t^2}$  Partial second derivative of  $f$  with respect to time  $t$

$\Re$  Real part of a complex quantity

$\Im$  Imaginary part of a complex quantity

## Symbols

---

- $\vec{E}$  Electric field [ $\text{Vm}^{-1}$ ]  
 $\vec{B}$  Magnetic induction [T]  
 $\vec{H}$  Magnetic field [ $\text{Am}^{-1}$ ]  
 $\vec{J}$  Current density [ $\text{Am}^{-2}$ ]  
 $\vec{D}$  Electric displacement [ $\text{Cm}^{-2}$ ]  
 $\vec{n}$  Outgoing unit normal

## Constants

---

- $\epsilon$  Absolute permittivity ( $\epsilon = \epsilon_r \epsilon_0$ ) [ $\text{Fm}^{-1}$ ]  
 $\epsilon_0$  Vacuum permittivity ( $8.854\,187 \times 10^{-12} \text{Fm}^{-1}$ )  
 $\epsilon_r$  Relative permittivity []  
 $\mu$  Absolute permeability ( $\mu = \mu_r \mu_0$ ) [ $\text{Hm}^{-1}$ ]  
 $\mu_0$  Vacuum permeability ( $1.256\,637 \times 10^{-6} \text{Hm}^{-1}$ )  
 $\mu_r$  Relative permeability []  
 $c$  Speed of light [ $\text{ms}^{-1}$ ]  
 $c_0$  Speed of light in vacuum ( $2.997\,924 \times 10^8 \text{ms}^{-1}$ )  
 $Z$  Characteristic impedance [ $\Omega$ ]  
 $Z_0$  Characteristic impedance of vacuum ( $377 \Omega$ )



---

# Acronyms

<b>ADM</b>	Angular Deconvolution Method.....	21
<b>AF</b>	Antenna Factor .....	8
<b>AUT</b>	Antenna Under Test .....	21
<b>AC</b>	Anechoic Chamber .....	9
<b>DFT</b>	Discrete Fourier Transform .....	9
<b>DUT</b>	Device Under Test .....	52
<b>EMC</b>	Electromagnetic Compatibility .....	1
<b>ESN</b>	Equivalent Surface Network .....	86
<b>EUT</b>	Equipment Under Test .....	2
<b>FAC</b>	Full-Anechoic Chamber .....	2
<b>FEM</b>	Finite Element Method .....	23
<b>FFT</b>	Fast Fourier Transform .....	23
<b>FIR</b>	Finite Impulse Response .....	11
<b>FSP</b>	Free-SPace .....	9
<b>FSPL</b>	Free-Space Path Loss .....	8
<b>FT</b>	Fourier Transform .....	ix
<b>GCC</b>	Geometrical Control Condition .....	62
<b>HUM</b>	Hilbert Uniqueness Method .....	60
<b>IBC</b>	Impedance Boundary Condition .....	103
<b>IoT</b>	Internet of Things .....	2
<b>LCCF</b>	Linear Combination of Configuration Fields .....	86
<b>LOS</b>	Line Of Sight .....	9
<b>MAP</b>	Maximum A Priori .....	ix
<b>MIMO</b>	Multiple-Input Multiple-Output .....	7

<b>MP</b>	Matrix Pencil .....	ix
<b>MSRC</b>	Mode Stirred Reverberation Chamber .....	7
<b>NUDFT</b>	Non Uniform Discrete Fourier Transform .....	24
<b>NUFFT</b>	Non Uniform Fast Fourier Transform .....	24
<b>OATS</b>	Open Area Test Site .....	2
<b>PDE</b>	Partial Differential Equation .....	3
<b>PEC</b>	Perfect Electric Conductor .....	23
<b>PMC</b>	Perfect Magnetic Conductor .....	81
<b>PML</b>	Perfectly Matched Layer .....	23
<b>SAC</b>	Semi-Anechoic Chamber .....	1
<b>SCPI</b>	Standard Commands for Programmable Instruments .....	137
<b>SVD</b>	Singular Values Decomposition .....	11
<b>TLS</b>	Total Least Squares .....	ix
<b>TR</b>	Time Reversal .....	74
<b>TREC</b>	Time Reversal Electromagnetic Chamber .....	86
<b>TRM</b>	Time Reversal Mirror .....	78
<b>TZF</b>	Test Zone Field .....	21
<b>UHF</b>	Ultra High Frequency .....	74
<b>USFFT</b>	Unequally Spaced Fast Fourier Transform .....	24
<b>UWB</b>	Ultra Wideband .....	7
<b>VISA</b>	Virtual Instrument Software Architecture .....	137
<b>VNA</b>	Vector Network Analyzer .....	32



---

# Introduction

---

## Context and motivations

SINCE the early 1950's, Electromagnetic Compatibility (EMC) has become more and more important due to the continuous increase of electric and electronic device use. According to the European directive 2014/30/EU [34], this rather general concept describes the ability of an electric/electronic device not to induce or react to electromagnetic interferences from other electric/electronic devices:

*Equipment shall be so designed and manufactured, having regard to the state of the art, as to ensure that:*

- (a) the electromagnetic disturbance generated does not exceed the level above which radio and telecommunications equipment or other equipment cannot operate as intended;*
- (b) it has a level of immunity to the electromagnetic disturbance to be expected in its intended use which allows it to operate without unacceptable degradation of its intended use.*

This directive only makes sense if the prescribed immunity level remains beyond the emission level for any device. For radiated immunity and emission, most of the applicable standards require to perform the tests in a controlled environment. To comply with national and international laws prohibiting interference to radio communications, a shielded enclosure is generally used to avoid any disturbance to propagate outside the enclosure. Additionally, the shielded enclosure also limits the influence of the outside perturbations on the measurements. Furthermore, reflections must also be restrained to comply with the standards limits, and thus enforcing free-space radiation conditions. These conditions are generally fulfilled (approximately) inside Semi-Anechoic Chambers (SACs) by the use of ferrites and electromagnetic absorbers placed on the enclosure walls, except on the floor, which acts as a normalized ground plane.

---

[34] Council of European Union *Directive 2014/30/EU of the european parliament and of the council.*

Using such facilities to perform EMC compliance tests is thus almost unavoidable nowadays. But due to the cost and the large dimensions of such facilities, those are generally devoted to accredited EMC laboratories or very large companies. However, with the increase of embedded and connected electronic devices, companies increasingly need to perform EMC tests and measurements. For example, a good practice for complex projects is to perform pre-compliance tests during the whole process of the electric/electronic design which is rather expensive when performed by an (accredited) EMC laboratory. Alternative pre-compliance test methods without using any SAC, ideally carried out inside the company itself, would certainly save time and money.

Other problems arise with too large or too heavy Equipments Under Test (EUTs), since very large facilities are costly and not common. The only solution is to perform *in-situ* tests, which are generally of poor quality due to the uncontrolled reverberating electromagnetic environment. Any solution to improve measurement accuracy, by better controlling the environment, would be desirable. This motivation is directly linked with the previous one concerning the achievement of pre-compliance tests in undedicated environments.

In addition to the motivations described above, the need for accurate electromagnetic measurements in uncontrolled environment also arises in case of *intended* radiations, e.g. for rapid antenna prototyping. Indeed, efficient, compact and cheap antennas are required to meet the needs of the new arising world of the Internet of Things (IoT) and the wireless connected objects. Although nowadays, antenna prototyping and optimization is mainly driven by electromagnetic simulation software, model validation using physical prototypes remains mandatory. Obtaining antenna radiation patterns is a long and tedious task requiring dedicated facilities, namely Full-Anechoic Chambers (FACs), since any reflection should be avoided during the antenna characterization to prevent spurious patterns. Obtaining accurate antenna radiation patterns outside any FAC would therefore be useful to companies which cannot afford extensive prototyping through dedicated facilities.

Outside of actual measurements performed in large Open Area Test Site (OATS), turnkey systems other than FACs or SACs (i.e. based on electromagnetic absorbers), allowing to confidently simulate free-space conditions are currently not available. The control of electromagnetic fields and waves is therefore a relevant open topic to be addressed. In fact, many control methods have already been demonstrated to be very efficient, theoretically and numerically. But, those methods have very rarely been analyzed experimentally.

## Aims and scope of this work

---

The European directive 2014/30/EU imposes to fulfill both emission and immunity requirements at the same time, but since they are intrinsically different, two different topics should actually be addressed.

On the one hand, radiated emissions, whether intended or not, are basically assessed by collecting and analyzing/processing electromagnetic field measurements. In this

case, the test environment is weakly coupled to the measurement and does not actually impact the way the measured samples are gathered, but only impact the data, for which it is possible to apply postprocessing algorithms to correct the final results. The first part of this manuscript is devoted to the accurate measurement of intended radiated emissions in complex and reverberating environments using *a posteriori* correction methods.

On the other hand, radiated immunity is environment dependent and causes the radiated electromagnetic fields to be strongly coupled to the propagated electromagnetic fields. The second part of this manuscript is therefore dedicated to shaping methods allowing to generate and impose a given electromagnetic field in a given time and place, and particularly in complex and reverberating environments.

While the concepts and methods addressed in this work are generally valid for the whole electromagnetic spectrum, due to the targeted EMC applications, the UHF range (300 MHz to 3000 MHz) is mainly considered.

## Outline

---

The manuscript is divided into two parts.

The first part, containing three chapters, addresses correction methods being applied by postprocessing data samples obtained using classical measurement methods for antennas.

The first chapter proposes an overview of classical correction methods, turning echoic measurements into free-space results. Each correction method is theoretically presented and illustrated using a numerical example. A comparison of the efficiency of the methods is also drawn. Chapter 2 introduces the Angular Deconvolution Method, which is based on exploiting the angular emission spectrum in order to process the radiation pattern as a whole and not azimuth by azimuth like all classical frequency sweep techniques reviewed in chapter 1. After a detailed theoretical description, the method is illustrated by several numerical examples. The third chapter addresses the Angular Deconvolution Method from an experimental point of view. The experimental viability of the method is established through extensive experimental test cases. An analysis of the uncertainty on the results is provided.

In the second part of the manuscript, several methods allowing to actively shape electromagnetic fields are presented.

At the beginning of the fourth chapter contains some elements of the theoretical foundations used in the most general “active shaping” techniques for electromagnetic fields using the optimal control of Partial Differential Equations (PDEs). Such techniques allow in theory to generate arbitrary electromagnetic fields in any given environment. The complexity of performing such active shaping is illustrated through numerical examples. At the end of chapter 4, a simpler alternative based on Time Reversal is presented. Although the Time Reversal technique allows to focus energy in space and time, we present several extensions that allow to perform more elaborate active shaping. The

fifth chapter considers active shaping in the harmonic regime, which is very relevant for EMC purposes. The optimal control of PDEs is thus revisited in the harmonic domain. After some theoretical considerations, several numerical examples are provided to assess the potential of the method. The last chapter deals with the experimental application of the optimal control technique which leads to a much simpler shaping technique in the harmonic regime. The effectiveness of the method is demonstrated on two different experimental control test cases.

## Contributions

---

The original contributions are mainly experimental, since in this thesis, two different methods have been transposed from the numerical world to the experimental world.

The first contribution concerns the *a posteriori* angular deconvolution correction method allowing, using reference measurements, to fit antenna patterns from a given environment to another. The original method, proposed in [93] has been extended to retrieve free-space patterns from arbitrary environments and has for the first time been comprehensively studied experimentally.

The second contribution is achieved through the active shaping method in the frequency domain using optimal control techniques. The method has been tested and validated experimentally, and it has also been demonstrated that the need of physically sampling the electromagnetic field to be compensated can be circumvented using an accurate numerical model.

The work summarized in this thesis has been published in the following journal articles and conference proceedings:

- M. Spirlet, V. Broun, P. Camus, C. Geuzaine, V. Beauvois, and I. Molenberg. “Modelling time reversal applications in a reverberation chamber using the current image method”. In: *Electromagnetic Compatibility (EMC EUROPE), 2013 International Symposium on*. 2013, pp. 359–364,
- M. Spirlet, C. Geuzaine, and V. Beauvois. “Estimation of semi-anechoic chamber radiation patterns from in-situ measurements using the angular responses of the environment”. In: *18th International Symposium on ElectroMagnetic Compatibility (CEM 2016 Rennes)*. July 11, 2016,
- M. Spirlet, C. Geuzaine, and V. Beauvois. “Experimental Correction of Radiation Patterns Between Electromagnetic Environments”. In: *IEEE Transactions on Antennas and Propagation* 65.3 (Mar. 2017), pp. 1330–1338,
- M. Spirlet. “Experimental Control of One-Dimensional Electromagnetic Environments in the UHF Range”. In: *PIERS 2017*. St-Petersburg, May 24, 2017,
- M. Spirlet, C. Geuzaine, and V. Beauvois. “Optimal Control of Time Harmonic Electromagnetic Waves in the UHF Range”. In: *IEEE Transactions on Microwave Theory and Techniques* (2018). Submitted.

PART

I

---

A POSTERIORI CORRECTION OF  
ELECTROMAGNETIC FIELD  
MEASUREMENTS



---

# Introduction: overview of electromagnetic correction methods

---

## 1.1 Introduction

---

VERY few techniques of antenna characterization are available for non-anechoic environments. One notable exception is the measurement of antenna efficiency and diversity gain in Mode Stirred Reverberation Chambers (MSRCs), which has been an active research topic in the past twenty years [74],[131],[92],[94],[84], [126], [130], [99], [81], [96], [6], [101], [102]. This topic became popular with the advent of Ultra Wideband (UWB) antennas [11],[85],[135] combined with multipath Multiple-Input Multiple-

---

[74] Hallbjörner, P. “Reflective antenna efficiency measurements in reverberation chambers”.

[131] Rosengren, K. et al. “Characterization of antennas for mobile and wireless terminals in reverberation chambers: Improved accuracy by platform stirring”.

[92] Kildal, P.-S. et al. “Measurement of free-space impedances of small antennas in reverberation chambers”.

[94] Kunisch, J. et al. “UWB radio channel modeling considerations”.

[84] Huang, Y. et al. “Electromagnetic coupling effects on the cavity measurement of antenna efficiency”.

[126] Piette, M. “Antenna radiation efficiency measurements in a reverberation chamber”.

[130] Rosengren, K. et al. “Radiation efficiency, correlation, diversity gain and capacity of a six-monopole antenna array for a MIMO system: theory, simulation and measurement in reverberation chamber”.

[99] Lee, C. et al. “Antenna Efficiency Measurements in a Reverberation Chamber Without the Need for a Reference Antenna”.

[81] Holloway, C. et al. “Reverberation Chamber Techniques for Determining the Radiation and Total Efficiency of Antennas”.

[96] Le Fur, G. “Contribution aux méthodes de mesure de rendement d’antenne. Caractérisation par “ULB Wheeler Cap” et via le retournement temporel en chambre réverbérante”.

[6] Andries, M. I. “Recherche de méthodes expérimentales de simulation de canaux de propagation en chambre réverbérante à brassage de modes”.

[101] Lemoine, C. et al. “On the K-factor estimation for rician channel simulated in reverberation chamber”.

[102] Lemoine, C. et al. “Statistical estimation of antenna gain from measurements carried out in a mode-stirred reverberation chamber”.

[11] Bégaud, X. *Les antennes Ultra Large Bande*.

[85] Huynh, M. *Wideband Compact Antennas for Wireless Communication Applications*.

[135] Schantz, H. *The Art And Science Of Ultrawideband Antennas*.

Output (MIMO) communication systems [8], [151], [63]. Before the emergence of these techniques, reverberation chambers had been seldom used for antenna characterization [153]. While the stochastic description of the behavior of the electromagnetic fields in MSRCs introduced by Hill, D. A. in 1998 [80], [79] has probably contributed a lot to the development of several alternative methods proposed in the last twenty years, using a MSRC remains controversial, considering the expected statistical behavior of the electromagnetic fields developed inside it and the their real behavior [100]. MSRCs exhibit more interesting behaviors in the time domain (pulsed regime), which also replaces advantageously frequency domain methods when a very large frequency range has to be covered. Unfortunately, one of the most relevant characteristics of an antenna, its radiation pattern, cannot be extracted in MSRCs and is only reserved to free-space. We will thus concentrate on frequency domain approaches in what follows.

Free-space conditions have indeed very appealing and convenient implications for practical generation and measurement of electromagnetic fields. Free-space conditions allow for example to derive straightforward relationships to quantify the transmission attenuation between two antennas at a given frequency  $f$  corresponding to an electromagnetic wavelength  $\lambda$ ), i.e. the Friis formula [9]

$$\frac{P_r}{P_t} = G_r G_t \left( \frac{\lambda}{4\pi R} \right)^2 = \frac{G_r G_t}{\text{FSPL}}, \quad (1.1)$$

where  $G_r$  and  $G_t$  are respectively the *free-space* antenna gains for the receiving ( $r$ ) and transmitting ( $t$ ) antennas,  $R$  is the distance between the antennas and Free-Space Path Loss (FSPL) is defined as

$$\text{FSPL} = \left( \frac{4\pi R}{\lambda} \right)^2, \quad (1.2)$$

which is thus both proportional to the square of the frequency and the distance. Converted into decibels,

$$P_r[\text{dB}] = P_t[\text{dB}] + G_r[\text{dB}] + G_t[\text{dB}] - \text{FSPL}[\text{dB}], \quad (1.3)$$

this relationship is one of the cornerstones of EMC testing and is implicitly used in every standard. Another example of free-space condition is the Antenna Factor (AF), binding the induced voltage  $V$  across the  $50\ \Omega$  loaded terminal of an antenna to the ambient electric field strength  $E$  can be established as

$$\text{AF} = \frac{E}{V} \underset{50\ \Omega}{\approx} \frac{9.73}{\lambda\sqrt{G_r}}. \quad (1.4)$$

---

[8] Babour, L. "Etude et Conception d'Antennes Ultra Large Bande Miniaturisées en Impulsionnel".

[151] Tounou, C. "Contribution à l'étude de systèmes à diversité d'antennes sur terminaux compacts".

[63] Fortino, N. "Conception et caractérisation d'antennes imprimées pour systèmes Ultra-Large-Bande impulsionnels".

[153] Wheeler, H. "The Radiansphere around a Small Antenna".

[80] Hill, D. A. "Plane wave integral representation for fields in reverberation chambers".

[79] Hill, D. A. *Electromagnetic theory of reverberation chambers*.

[100] Lemoine, C. "Contribution à l'analyse statistique des mesures en chambre réverbérante à brassage de modes. Applications à la détermination de l'efficacité de brassage et de l'incertitude de mesure dans un contexte CEM et radiofréquences".

[9] Balanis, C. A. *Antenna Theory: Analysis and Design*.

Due to their ease of use, such relationships are also used when using FACs and SACs for EMC and antenna measurements. Since the exact Free-SPace (FSP) conditions are not exactly met in such Anechoic Chambers (ACs), several methods have been proposed over the last decades to correct the measurements *a posteriori* e.g. to remove the influence of antenna masts or access ramps. We describe the main classical frequency domain correction techniques in the following sections, in order to motivate the development in chapter 2 of a more powerful correction technique that will be able to restore free-space conditions from more severe reverberating environments.

## 1.2 Fourier Transform (FT)

---

One of the first correction techniques designed to remove echoes exploits the time delays introduced by the various reflections and is based on a Fourier Transform (FT) on samples obtained by a frequency sweep [112],[62]. In this approach, the Line Of Sight (LOS) path is assumed to have the shortest time delay and the frequency sweep is required to identify the direct path modes. The LOS components are then transformed back in the time domain, leading to a fully anechoic pattern.

Let  $\mathbf{x}$  a vector matrix populated by the frequency samples  $x_n$ ,  $n = 0, 1, \dots, N - 1$  to be processed for echo removal. Let  $t_{\text{LOS}}$  the time corresponding to the propagation through the LOS path, and  $\tau$  the shortest time delay introduced by the first reflection in the environment from the LOS propagation time. Assuming that the sampling and the bandwidth of the frequency samples of  $\mathbf{x}$  allow to discriminate two modes separated by  $\tau$  in the time domain, the Discrete Fourier Transform (DFT) of  $\mathbf{x}$ ,  $\hat{\mathbf{x}}$  provides the time domain profile of the encountered reflections along the propagation path. Using the magnitude of the complex components of  $\hat{\mathbf{x}}$ , i.e.  $|\hat{x}_n|$ , the first peak, corresponding to the LOS path has to be isolated by truncating  $\hat{\mathbf{x}}$ , such that

$$\begin{aligned} \hat{\mathbf{x}}_{\text{LOS}} [t] &= \hat{\mathbf{x}} [t], & \text{if } t \leq t_{\text{LOS}} + \epsilon, \\ &= 0, & \text{if } t > t_{\text{LOS}} + \epsilon, \end{aligned} \quad (1.5)$$

with  $\epsilon$  chosen such that  $0 < \epsilon < \tau$ . Transforming back the truncated signal  $\hat{\mathbf{x}}_{\text{LOS}} [t]$  from the time domain to the frequency domain leads to corrected echo free samples  $\mathbf{x}_{\text{LOS}}$ .

This method usually requires an important bandwidth to be able to discriminate the LOS path from the first echo, but this can not always be met in practice with narrow-band antennas. An alternative, but similar, method based on the z-transform [44] also exists.

---

[112] Loredó, S. et al. "Echo identification and cancellation techniques for antenna measurement in non-anechoic test sites".

[62] Fiumara, V. et al. "Free-Space Antenna Field / Pattern Retrieval in Reverberation Environments".

[44] Dadić, M. et al. "A technique for elimination of reflected rays from antenna measurements performed in echoic environment".

### 1.3 Matrix Pencil (MP), Total Least Squares (TLS) and other variants

As an alternative to purely Fourier based techniques, frequency datasets can be decomposed into a more general sum of complex exponentials. Those methods encompass the Matrix Pencil (MP) method [82],[103], the Total Least Squares (TLS) method [83] and other variants [65], [67], [66], [51].

Let the samples  $x_n$ ,  $n = 0, 1, \dots, N-1$  to be modeled by a sum of  $K$  damped complex exponentials:

$$x_n = \sum_{k=1}^K a_k e^{-d_k n \Delta t + j(2\pi f_k n \Delta t + \phi_k)} + e_n, \quad (1.6)$$

where  $a_k$  is the amplitude,  $d_k$  the attenuation factor,  $f_k$  the frequency and  $\phi_k$  the phase delay for the  $k^{th}$  exponential;  $\Delta t$  is the sampling period and  $e_n$  is some Gaussian white noise. Defining

$$c_k = a_k e^{j\psi_k}, \quad z_k = e^{(-d_k + j2\pi f_k)\Delta t}, \quad (1.7)$$

such that

$$x_n = \sum_{k=1}^K c_k z_k^n + e_n, \quad (1.8)$$

one has to find the  $K$  values of  $c_k$  and  $z_k$  providing the best fit of the  $N$  samples  $x_n$ . The fitting is achieved as follows.

The Hankel matrix  $\mathbf{X}$  is built in the following way:

$$\mathbf{X} = \begin{bmatrix} x_0 & x_1 & x_2 & \dots & x_{M-1} \\ x_1 & x_2 & \cdot & \dots & \cdot \\ x_2 & \cdot & \cdot & \dots & \dots \\ \vdots & \vdots & \vdots & \vdots & \vdots \\ x_{L-1} & \dots & \dots & \dots & x_N \end{bmatrix}, \quad (1.9)$$

with  $L > K$ ,  $M > K$ ,  $N = L + M - 1$ . For noiseless data, i.e. with  $e_n = 0$ , it can be shown that  $\mathbf{X}$  has a Vandermonde decomposition [82] such that

$$\begin{bmatrix} 1 & \dots & 1 \\ z_1^1 & \dots & z_K^1 \\ \vdots & \vdots & \vdots \\ z_1^{L-1} & \dots & z_K^{L-1} \end{bmatrix} \begin{bmatrix} c_1 & & \\ & c_2 & \\ & & \ddots \\ & & & c_K \end{bmatrix} \begin{bmatrix} 1 & z_1^1 & \dots & z_1^{M-1} \\ \vdots & \vdots & \vdots & \vdots \\ 1 & z_K^1 & \dots & z_K^{M-1} \end{bmatrix} = \mathbf{SCT}^T, \quad (1.10)$$

[82] Hua, Y. et al. "Matrix pencil method for estimating parameters of exponentially damped/undamped sinusoids in noise".

[103] Leon Fernandez, G. et al. "Radiation pattern retrieval in non-anechoic chambers using the matrix pencil algorithm".

[83] Hua, Y. et al. "On SVD for estimating generalized eigenvalues of singular matrix pencil in noise".

[65] Fourestie, B. et al. "Anechoic chamber evaluation using the matrix pencil method".

[67] Fourestie, B. et al. "Correlate measurements at different test sites".

[66] Fourestie, B. et al. "Efficient detection of resonances in anechoic chambers using the matrix pencil method".

[51] Du, Z. et al. "Generation of Free Space Radiation Patterns From Non-Anechoic Measurements Using Chebyshev Polynomials".

where  $\cdot^T$  denotes the transposition.  $\mathbf{S}$  and  $\mathbf{T}$  have the rotational invariance property:  $\mathbf{S}^\dagger = \mathbf{S}^\perp \mathbf{Z}$ ,  $\mathbf{T}^\dagger = \mathbf{T}^\perp \mathbf{Z}$ , using the notation  $\cdot^\perp$  ( $\cdot^\dagger$ ) meaning the matrix where the first (last) row is removed, and  $\mathbf{Z} = \text{diag}(z_1, z_2, \dots, z_K)$ .

The matrix  $\mathbf{X}$  can also be shown to be expressed exactly by the truncated Singular Values Decomposition (SVD) [82]:

$$\mathbf{X} = \mathbf{U}_K \Sigma_K \mathbf{V}_K^H, \quad (1.11)$$

where  $\cdot^H$  denotes the conjugated transposition.

Then, since

$$\mathbf{SCT}^T = \mathbf{X} = \mathbf{U}_K \Sigma_K \mathbf{V}_K^H, \quad (1.12)$$

it follows that  $\mathbf{U}_K$  and  $\mathbf{V}_K$  also have the rotational invariance property  $\mathbf{U}_K^\dagger = \mathbf{U}_K^\perp \mathbf{Z}$ ,  $\mathbf{V}_K^\dagger = \mathbf{V}_K^\perp \mathbf{Z}^H$ .

In the original MP method, the eigenvalues  $z_k$  of  $\mathbf{Z}$  are found using the state space method:

$$z_k = \text{eig}(\mathbf{Y}_2^{-1} \mathbf{Y}_1), \quad \text{with, } \mathbf{Y}_1 = \mathbf{U}_K \Sigma_K \mathbf{V}_K^\perp, \quad \mathbf{Y}_2 = \mathbf{U}_K \Sigma_K \mathbf{V}_K^\dagger \quad (1.13)$$

whereas in the TLS method, the eigenvalues  $z_k$  are found by computing the joint SVD of

$$[\mathbf{U}_K^\dagger \mathbf{U}_K^\perp], \quad \text{or} \quad [\mathbf{V}_K^\dagger \mathbf{V}_K^\perp], \quad (1.14)$$

and finally computing

$$z_k = \text{eig}\left(-\mathbf{V}_K^\perp^{-1} \mathbf{V}_K^\dagger\right), \quad (1.15)$$

with  $\mathbf{V}_K^\perp$  ( $\mathbf{V}_K^\dagger$ ) the lower (upper) part of the  $\mathbf{V}$  matrix of the SVD.

Once the  $z_k$  found, the values of  $c_k$  can be found using the least squares fitting. Since

$$x_n = \sum_{k=1}^K c_k z_k^n, \quad n = 0, 1, \dots, N-1, \quad (1.16)$$

we get

$$c_k = (\mathbf{c}_K)_k = \left( (\mathbf{Z}_{NK} \mathbf{Z}_{NK}^T)^{-1} \mathbf{Z}_{NK}^T \mathbf{x}_N \right)_k, \quad (1.17)$$

with  $(\mathbf{x}_N)_n = x_n$ ,  $(\mathbf{Z}_{NK})_n = z_k^n$  and  $(\mathbf{c}_K)_k = c_k$ .

Without noise, the number of complex exponentials does not need to be known in advance, since when computing the SVD, the number significant values of  $\text{diag}(\Sigma)$  matches exactly the number of involved exponentials. Unfortunately, dealing with noisy data, the values of  $\text{diag}(\Sigma)$  tend to decrease uniformly, which can lead to bad estimations of  $K$ . To overcome this problem, variants such as FIR-HTLS [33], where Finite Impulse Response (FIR) pre-filtering using a Toeplitz matrix is applied, allows to reduce noise before applying the SVD. A variant also exists where the TLS method is used twice, once to isolate the *non-LOS* components of the frequency signal, which is then subtracted from the original data to be processed a second time with cleaner input data, leading to a better identifications of the number of exponentials and their parameters.

---

[33] Chen, H. et al. "Frequency-selective techniques based on singular value decomposition (SVD), total least squares (TLS), and bandpass filtering".

## 1.4 Maximum A Priori (MAP)

---

The MP method and its variants have intrinsic limitations when using noisy datasets. The Maximum A Priori (MAP) [7], [133], [134] method on the other hand directly exploits the fact that noise is inherent to real processed data to improve the accuracy of the original FT method.

It is known that using zero fill-in allows to increase the resolution of a DFT, but with the undesirable effect to enhance the dual domain lobes induced by the windowing effect, potentially leading to a wrong identification or discrimination of the relevant peaks. In the MAP method, this effect is circumvented by using a statistical Cauchy-Gauss model to approximate the frequency response, allowing to iteratively regularize the processed sequence while the DFT algorithm is applied.

Identifying the time response of a system can be reduced to the estimation of  $M$  time samples  $\mathbf{h} = [h[0], h[1], \dots, h[M-1]]^T$  of a sequence of  $N$  frequency samples  $\hat{\mathbf{h}} = [\hat{h}(\omega_0), \hat{h}(\omega_1), \dots, \hat{h}(\omega_{M-1})]^T$  with  $\omega = 2\pi f$ . This problem can be solved using Bayesian inference: the optimal estimation of the samples of  $\mathbf{h}$  is given by the argument maximizing the conditional probability density  $p(\mathbf{h}|\hat{\mathbf{h}})$ , i.e. the most probable value of  $\mathbf{h}$ , knowing that  $\hat{\mathbf{h}}$  has been observed.

According Bayes theorem, we have

$$p(\mathbf{h}|\hat{\mathbf{h}}) = \frac{p(\hat{\mathbf{h}}|\mathbf{h}) p(\mathbf{h})}{p(\hat{\mathbf{h}})} \quad (1.18)$$

where  $p(\mathbf{h})$  is the probability density to estimate,  $p(\hat{\mathbf{h}})$  is a scale factor, and  $p(\hat{\mathbf{h}}|\mathbf{h})$  is the maximum likelihood function of the observations.

Moreover,  $\mathbf{h}$  and  $\hat{\mathbf{h}}$  are related by

$$\hat{\mathbf{h}} = \mathbf{F}\mathbf{h} + \mathbf{n} \quad (1.19)$$

where  $\mathbf{n}$  is a noise vector and  $\mathbf{F}$  a matrix of size  $N \times M$  containing the elements

$$f_n^k = e^{-\frac{j2\pi nk}{N}}, \quad (1.20)$$

which is nothing else than the DFT operator matrix.

Finding

$$\operatorname{argmax} \{p(\mathbf{h}|\hat{\mathbf{h}})\} \quad (1.21)$$

is equivalent to find

$$\operatorname{argmax} \{\ln(p(\mathbf{h}|\hat{\mathbf{h}}))\} \quad (1.22)$$

---

[7] Ayestaran, R. et al. "Sparse deconvolution based on regularisation for echo correction in antenna measurement".

[133] Sacchi, M. et al. "Interpolation and extrapolation using a high-resolution discrete Fourier transform".

[134] Santamaría-Caballero, I. et al. "Sparse deconvolution using adaptive mixed-Gaussian models".

which is also equivalent to find

$$\operatorname{argmax} \{ \ln(p(\hat{\mathbf{h}}|\mathbf{h})) + \ln(p(\mathbf{h})) \}. \quad (1.23)$$

Taking into account that the observed noise is assumed to be some Gaussian white noise of zero mean and standard deviation  $\sigma$  (variance  $\sigma^2$ ), and that  $\hat{\mathbf{h}}$  is the sum of a constant vector  $\mathbf{F}\mathbf{h}$  and of a vector  $\mathbf{n}$  containing  $N$  Gaussian random variables of zero mean, one conclude that  $\hat{\mathbf{h}}$  is a Gaussian random vector of size  $N$  and of mean  $\mathbf{F}\mathbf{h}$ . As a result

$$p(\hat{\mathbf{h}}|\mathbf{h}) = \left( \frac{1}{\sqrt{2\pi}\sigma} \right)^N e^{-\frac{1}{2\sigma^2} \|\hat{\mathbf{h}} - \mathbf{F}\mathbf{h}\|_2^2}, \quad (1.24)$$

which leads to a minimization of the cost function  $J(\mathbf{h})$

$$J(\mathbf{h}) = \sigma^{-2} \|\hat{\mathbf{h}} - \mathbf{F}\mathbf{h}\|_2^2 + P(\mathbf{h}), \quad (1.25)$$

with  $\sigma^2$  the variance of the intrinsic noise of the measurements samples.

The term  $P(\mathbf{h})$  is thus used for regularization in the optimization problem, and models the log-derivative of the distribution of  $\mathbf{h}$  *a priori*. This arbitrary regularization term is chosen to match a Cauchy model [133]

$$P(\mathbf{h}) = \sum_{k=0}^{M-1} \ln \left( 1 + \frac{|\mathbf{h}[k]|^2}{\sigma_h^2} \right), \quad (1.26)$$

where  $\sigma_h^2$  is a control parameter acting on the sparsity of the solution.

The maximization of (1.18) yields

$$\mathbf{h} = (\lambda \mathbf{Q}^{-1} + \mathbf{F}^H \mathbf{F})^{-1} \mathbf{F}^H \hat{\mathbf{h}} \quad (1.27)$$

where  $\lambda = \frac{\sigma^2}{\sigma_h^2}$  and  $\mathbf{Q}$  is a diagonal matrix whose elements are given by

$$(\mathbf{Q})_{ii} = 1 + \frac{|\mathbf{h}[i]|^2}{2\sigma_h^2}, \quad i = 0, \dots, M-1. \quad (1.28)$$

The matrix  $\mathbf{Q}$  depends on  $h$ , and an iterative scheme has thus to be used to converge toward  $\mathbf{h}$ :

$$\mathbf{b}^{j-1} = (\lambda \mathbf{I}_N + \mathbf{F}\mathbf{Q}^{j-1}\mathbf{F}^H)^{-1} \hat{\mathbf{h}} \quad (1.29)$$

$$\mathbf{h}^j = \mathbf{Q}^{j-1} \mathbf{F}^H \mathbf{b}^{j-1}. \quad (1.30)$$

At the beginning,  $\mathbf{h}^0$  is initialized by the inverse DFT of the samples of  $\hat{\mathbf{h}}$ , then  $\mathbf{Q}^0$  is computed. The convergence criterion to reach is:

$$2 \frac{|J^j - J^{j-1}|}{|J^j| + |J^{j-1}|} < \epsilon \quad (1.31)$$

---

[133] Sacchi, M. et al. "Interpolation and extrapolation using a high-resolution discrete Fourier transform".

where  $\epsilon$  is arbitrary.

The parameter  $\sigma_h$  is chosen in the confidence interval of the  $\chi^2$  test of the assumed noise variance  $\sigma$ , knowing that  $\sigma$  is empirically or experimentally determined from the samples of  $\hat{\mathbf{h}}$ .

Other similar methods, using *a priori* data were also developed, by considering that the frequency response is either approximated using Chebyshev polynomials [51] or Gabor schemes [64].

## 1.5 Comparison between FT, MP, TLS and MAP methods through a numerical example

---

All the methods presented above have been implemented with MATLAB, and tested using a benchmark numerical example which allows to control the amount of noise and assess its impact on the correction. We consider the measurement of the transmission coefficient between two antennas,  $S_{21}$ . We assume that the exact coefficient  $S_{21}$  is given by

$$\begin{aligned} S_{21} = & (0.1 + j0.0002) e^{(0.03 - j0.85)1 \times 10^{-8} f} \\ & + (0.1 - j0.0015) e^{(-0.05 - j0.025)1 \times 10^{-8} f} \\ & + (0.1 + j0.002) e^{(-0.06 - j0.25)1 \times 10^{-8} f}. \end{aligned} \quad (1.32)$$

A realistic frequency sweep for  $f$  of 128 values linearly spaced between 1 GHz to 3 GHz has provided the dataset  $S_{21}$  exploited in this benchmark.

In Fig. 1.1, the original clean signal  $S_{21}$  — and its LOS component - - -, characterized by the shortest time delay, are represented. The different methods have been tested against this example for different noise kinds and levels, introduced as follows in the samples:

$$S_{21}^{\text{noisy}}(f) = S_{21}(f) + \mathcal{N}(\mu = 0, \sigma = \sigma_w) + \sigma_r \cos(2\pi f t_i), \quad (1.33)$$

by tuning the values of  $\sigma_w$  and  $\sigma_r$ . The second term simulates Gaussian white noise of zero mean and  $\sigma_w$  standard deviation (i.e. wideband noise in the time domain), whereas the last term containing  $\sigma_r$  simulates a superimposed frequency contribution of higher frequency (i.e. pulse noise in the time domain at time  $t_i = 8$  ns).

As a first test, no noise is added ( $\sigma_w = \sigma_r = 0$ ), such that  $S_{21}^{\text{noisy}} = S_{21}$ . The resulting curves after applying the different corrections methods are displayed in Fig. 1.2, as well as the corresponding time spectra. Except for the FT method, the other correction methods are accurately identifying the shortest time delay and reconstructing the right LOS. A higher resolution in the time spectrum of the simple FT method would certainly improve the correction. But this is only possible by increasing the sampling frequency bandwidth which is not always possible with narrow-band antennas as already explained. It should be emphasized that for the MP and FIR-HTLS methods, the number of exponentials has not been predetermined and uses an “automatic” criterion to truncate the SVD matrices accordingly.

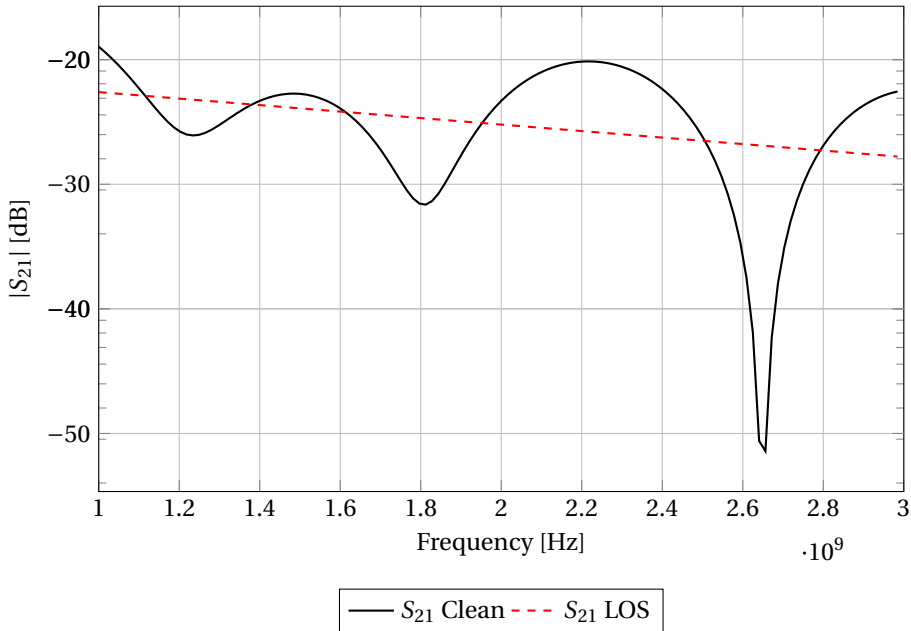


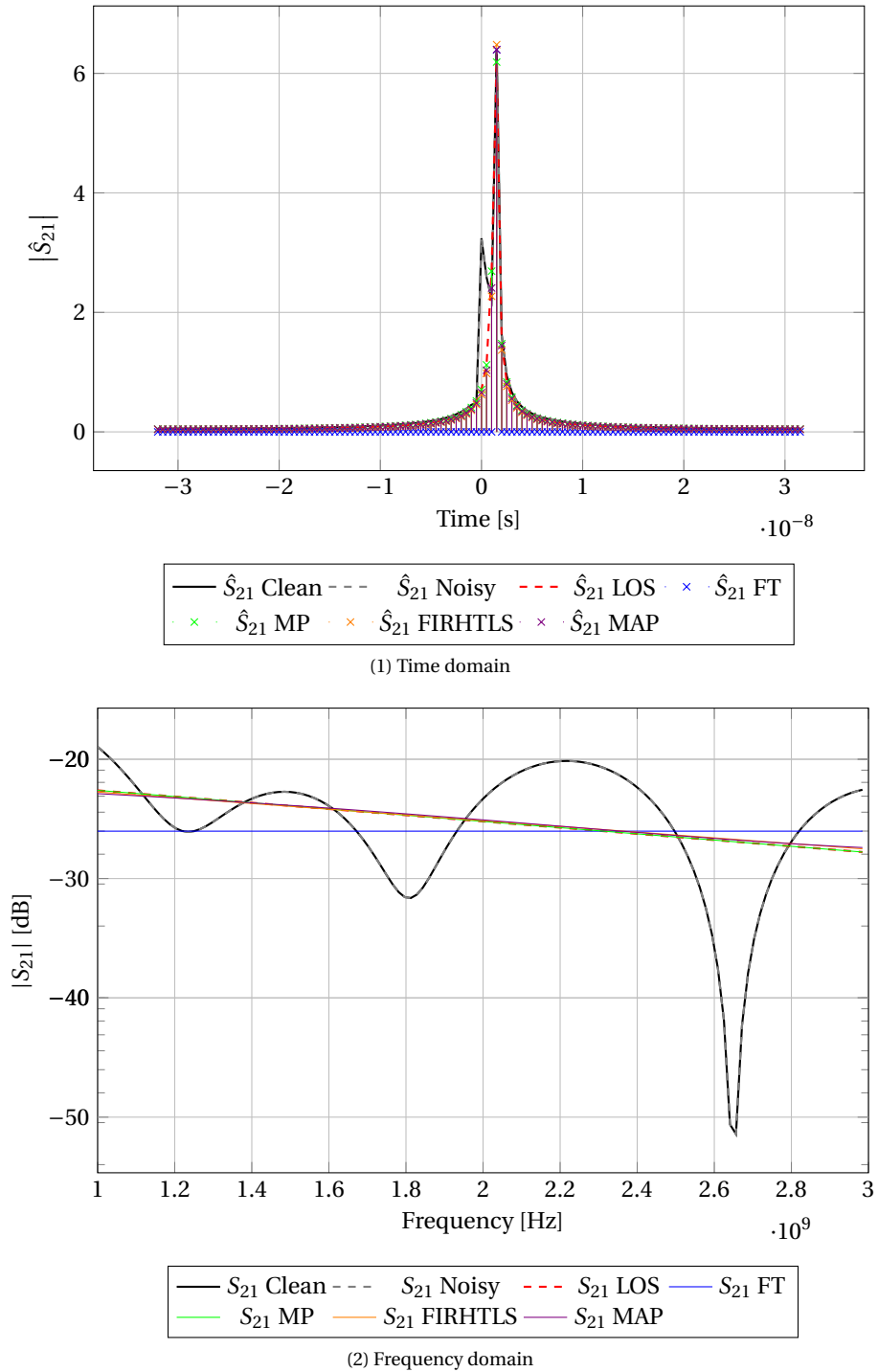
Figure 1.1: Experimental data sweep used for benchmarking the different correction methods.

For a second test, white noise is introduced by setting  $\sigma_w = 0.01$ , causing a rather disturbed noisy signal  $S_{21}^{\text{noisy}}$ , which does not actually impact the time signal too much, as seen in Fig. 1.3. The behavior of the correction methods is globally the same, with a slight degradation of the correction showed by a very small decrease in the slope of the resulting LOS contribution.

The third test uses a value of  $\sigma_r = 0.03$ , leading to a signal  $S_{21}^{\text{noisy}}$  containing a superimposed sinusoid on the original signal  $S_{21}$ . As depicted in Fig. 1.4, two new peaks are populating the time-spectrum. This causes the MP method to identify a wrong LOS contribution. On the contrary, the FIR-HTLS and MAP methods are still providing the right LOS contribution, thanks to the filtering applied in both methods.

Finally, the last test, shown in Fig. 1.5 mixes both noise types by setting  $\sigma_w = 0.01$  and  $\sigma_r = 0.01$ . Almost all methods fail to retrieve the right LOS contribution except the MAP method which still discriminates the right component thanks to the high resolution FT.

Considering the 4 tests, the MAP method clearly outperforms the other ones. It also worth noting that the FT method, in each situation has provided a constant, but not accurate, LOS contribution, even in the presence of high noise levels. The MP and FIR-HTLS methods are the most sensitive to noise due to the eigenvalues spreading in the SVD. Actually, the DFT based methods (FT and MAP) have performed well due to the applied windowing in the time-spectrum. But the windowing is only efficient if the window is centered at the right time position. As an improvement, something

Figure 1.2: Correction methods without noise ( $\sigma_w = 0, \sigma_r = 0$ ).

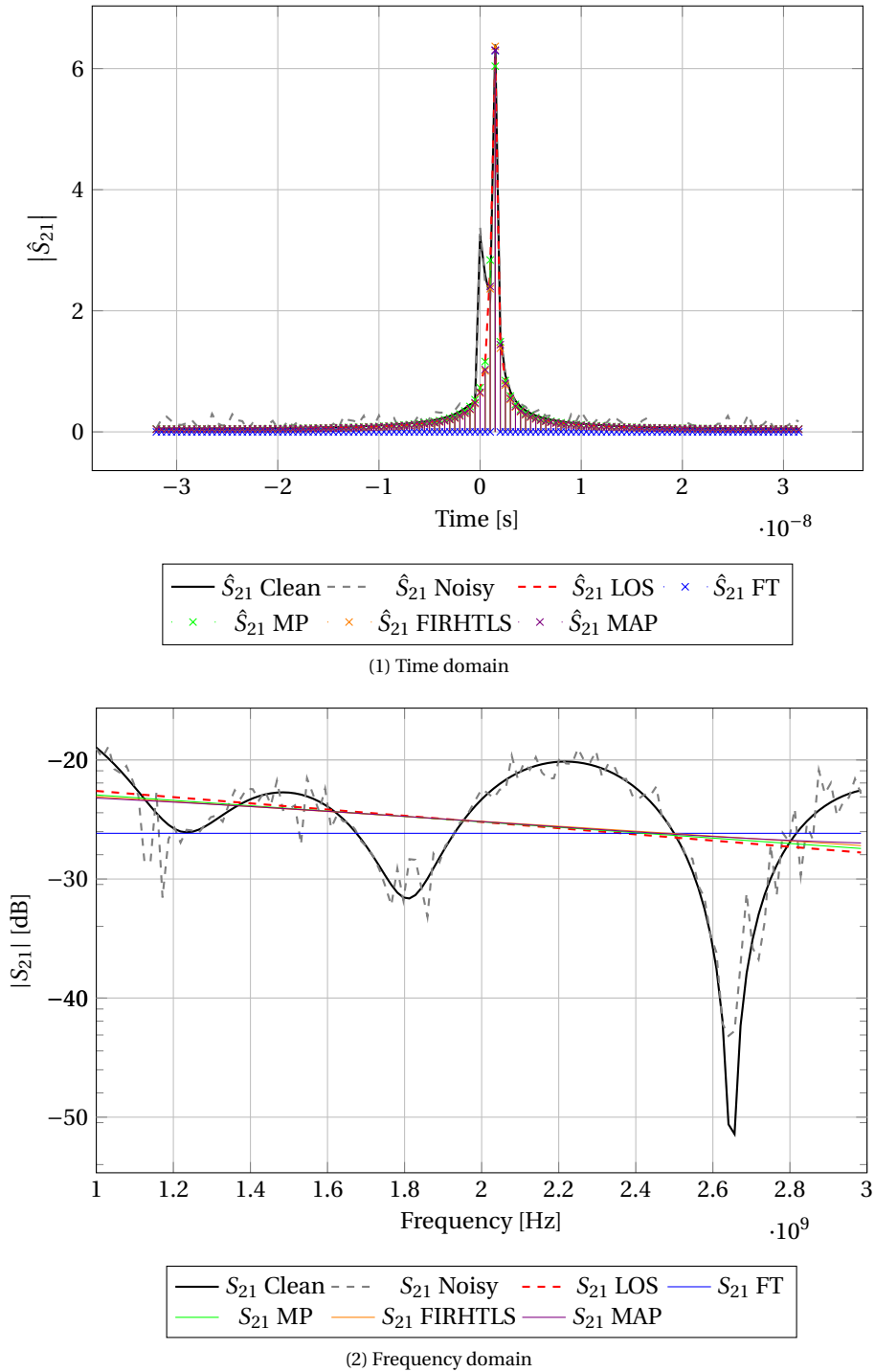
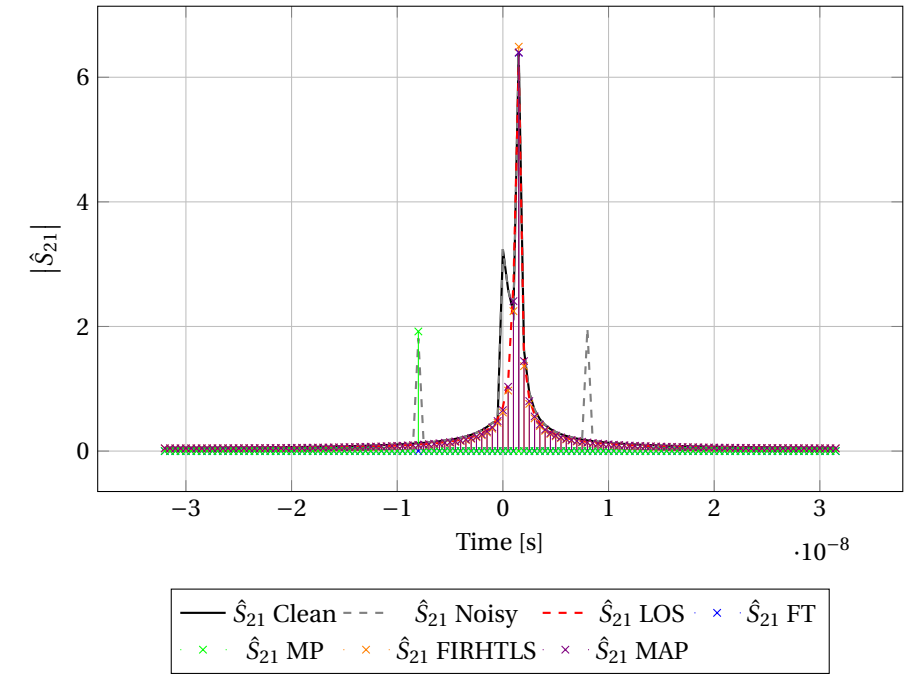
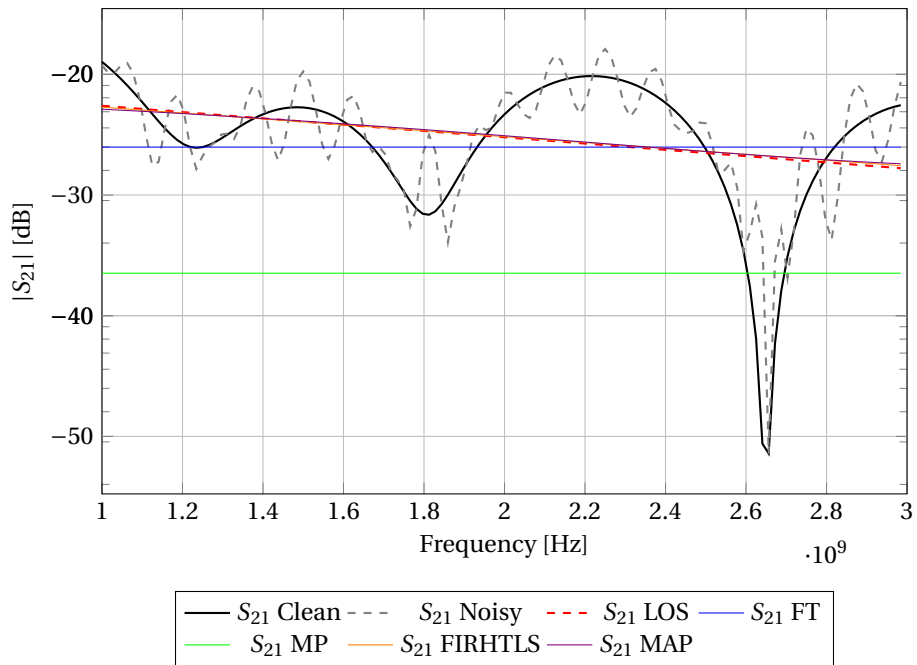


Figure 1.3: Correction methods with noise ( $\sigma_w = 0.01, \sigma_r = 0$ ).



(1) Time domain



(2) Frequency domain

Figure 1.4: Correction methods with noise ( $\sigma_w = 0, \sigma_r = 0.03$ ).

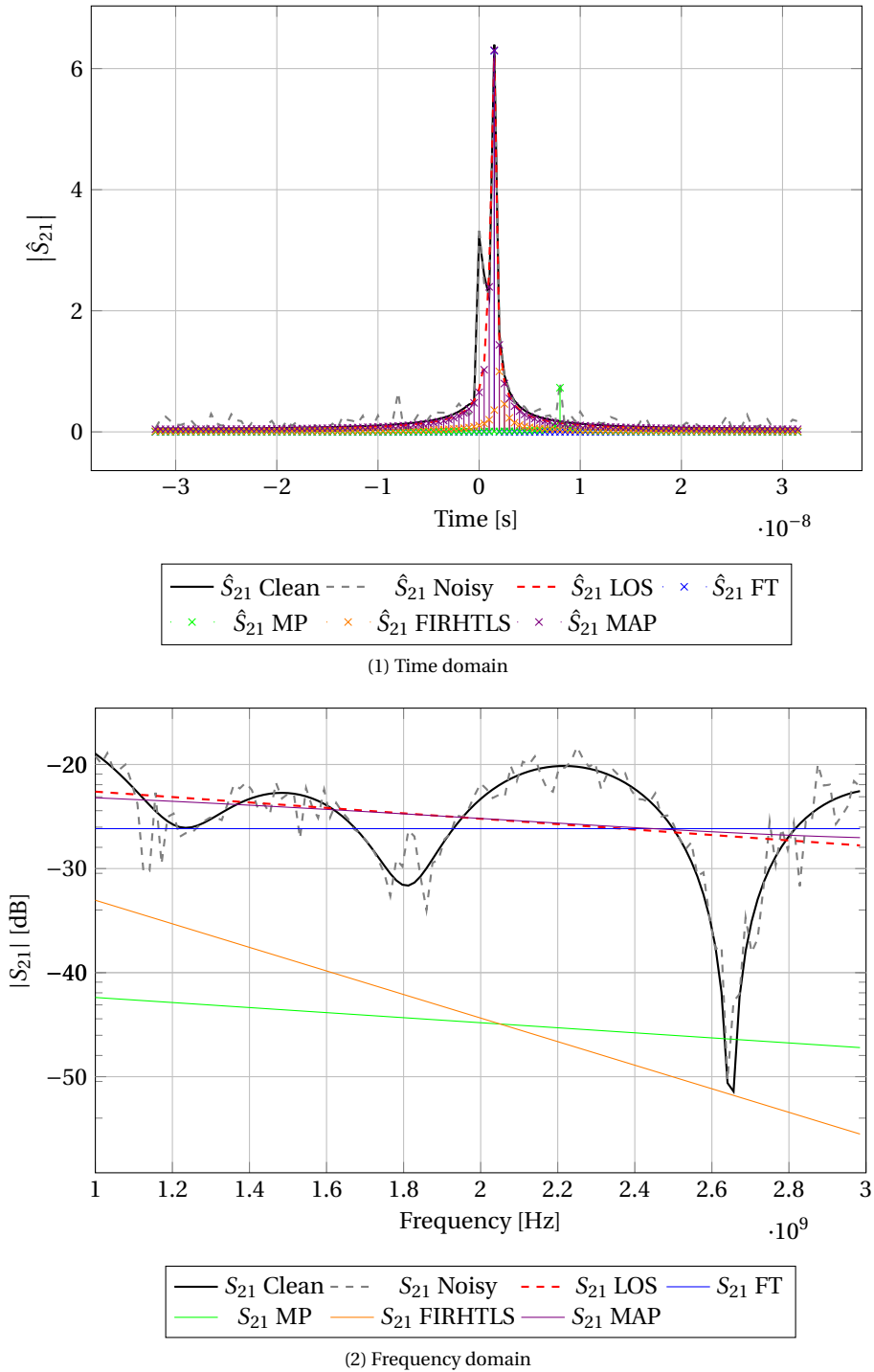


Figure 1.5: Correction methods with noise ( $\sigma_w = 0.01, \sigma_r = 0.01$ ).

similar could be applied with MP and FIR-HTLS methods. However, in the context of measuring antenna patterns, all of these methods intrinsically process a single azimuth dataset at a time, and the windowing parameters need to be adapted for each new azimuth, since they lead to different reflection conditions.

## 1.6 Conclusions

---

This chapter has presented an overview of classical methods to correct echoic data in the frequency domain and remove the contribution of the reverberating environment. These correction methods have the advantage to be cheap as they only require simple digital signal processing. However, as shown on a simple example, the main issue of such frequency sweep correction methods is the fact that they perform well only if relevant *a priori* information is given, such as the estimated time delay of the LOS path, or the number of reflections to consider. Providing bad estimations of those parameters can dramatically deteriorate the right LOS component estimation. Furthermore, having correct estimated parameters is certainly not trivial in experimental situations, especially in complex environments. It is even more difficult when considering antenna radiation pattern corrections, since those parameters are very likely to be different at each considered antenna azimuth (or tilt). In the following chapter, a correction method able to process the radiation pattern as a whole and not azimuth by azimuth is therefore proposed as an alternative to the classical frequency sweep methods.

---

# Angular Deconvolution Method

---

## 2.1 Introduction

---

As alternatives to the classical correction methods based on the FT of frequency samples to identify the minimum time delay path, several techniques have been proposed for antenna characterization in the literature [19], [97], [150], [76] which exploit instead the FT on *angular* samples. Amongst those methods the most mature is the Test Zone Field (TZF) compensation [19], which allows to increase pattern measurement accuracy by compensating the superimposed fields induced by reflections using an angular iterative modal expansion. However, the TZF method requires a tedious characterization of the neighborhood of the Antenna Under Test (AUT) using a Test Zone Field probe, and is mainly devoted for reflections occurring in FACs, introduced for example by antenna masts and fastenings.

In this chapter, we propose another method based on the FT of angular samples which is much more straightforward to use. The technique, dubbed the Angular Deconvolution Method (ADM), is based on the reconstruction method originally proposed in [93] which we extend to reconstruct patterns from a given arbitrary test environment to a reference environment. One of the originalities of the ADM is that it allows to reconstruct not only the true pattern but also a non-ideal pattern such as the one obtained in a FAC with its small imperfections. The theoretical description of the ADM presented hereafter has been published in [143].

---

[19] Black D.N., J. et al. "Test zone field compensation".

[97] Leatherwood, D. A. et al. "Plane wave, pattern subtraction, range compensation".

[150] Toivanen, J. T. et al. "Modified Test Zone Field Compensation for Small-Antenna Measurements".

[76] Hansen, T. B. "Spherical Near-Field Scanning With Higher-Order Probes".

[93] Koh, J. et al. "Free Space Radiation Pattern Reconstruction from Non-Anechoic Measurements Using an Impulse Response of the Environment".

[143] Spirelet, M. et al. "Experimental Correction of Radiation Patterns Between Electromagnetic Environments".

## 2.2 Angular response deconvolution

Let us first consider an Antenna Under Test (AUT) radiating in Free-Space (FSP) at a fixed frequency  $f_0$ . Any complex (with amplitude and phase) quantity  $X_{AUT}^{FSP}(\theta)$ , measured when varying the angle  $\theta$  around a rotation axis of the antenna, matches the exact pattern  $X_{AUT}(\theta)$ , since by definition, the free-space pattern is convolved with an azimuth impulse,  $H^{FSP}(\theta) = \delta(\theta)$ :

$$X_{AUT}^{FSP}(\theta) = X_{AUT}(\theta) \star H^{FSP}(\theta) = X_{AUT}(\theta). \quad (2.1)$$

While in what follows we only consider the angle  $\theta$  to be the azimuth or tilt angle of the antenna, all the following developments could be adapted to 3D pattern reconstruction. The measured values  $X$  are usually the  $S_{21}$  values but could as well be any measurement containing both amplitude and phase information, such as the electric field  $E$ .

In a test echoic environment (TEST), however, the measured complex pattern  $X_{AUT}^{TEST}$  differs from the free-space pattern  $X_{AUT}$ , since it is now convolved by a function depending on the echoic environment  $H^{TEST}(\theta)$ :

$$X_{AUT}^{TEST}(\theta) = X_{AUT}(\theta) \star H^{TEST}(\theta). \quad (2.2)$$

Assuming that for a given reference antenna both echoic and anechoic patterns have been measured, a response of the test environment can be constructed from (2.1) by applying a DFT on the azimuth ( $\theta$ ) dataset:

$$H^{TEST}(\theta) = \mathcal{F}_\theta^{-1} \left( \frac{\mathcal{F}_\theta(X_{REF}^{TEST})}{\mathcal{F}_\theta(X_{REF})} \right), \quad (2.3)$$

where  $\mathcal{F}_\theta(\cdot)$  and  $\mathcal{F}_\theta^{-1}(\cdot)$  denote the discrete and the inverse discrete Fourier transform in the angular domain.

Using this environment response  $H^{TEST}(\theta)$ , and considering that the environment remains constant, any free-space pattern  $X_{AUT}(\theta)$  from any AUT can be reconstructed from a dataset obtained in the test environment by using:

$$X_{AUT}(\theta) = \mathcal{F}_\theta^{-1} \left( \frac{\mathcal{F}_\theta(X_{AUT}^{TEST})}{\mathcal{F}_\theta(H^{TEST})} \right) \quad (2.4)$$

$$= \mathcal{F}_\theta^{-1} \left( \frac{\mathcal{F}_\theta(X_{AUT}^{TEST}) \mathcal{F}_\theta(X_{REF})}{\mathcal{F}_\theta(X_{REF}^{TEST})} \right). \quad (2.5)$$

Of course,  $\mathcal{F}_\theta(X_{REF}^{TEST})$  should not have any zero mode to avoid singularities in (2.5), which is enforced by using a regularized Fourier transform in which any component of  $\mathcal{F}_\theta(X_{REF}^{TEST})$  such that  $|\mathcal{F}_\theta(X_{REF}^{TEST})[\vartheta]| < \epsilon$  is replaced by  $\epsilon$  (typically  $\epsilon = 1 \times 10^{-12}$ ).

Mathematically, there is no reason to limit the reconstruction from an echoic test environment to the free-space reference environment. Indeed, the reference environment

could be chosen as any other echoic environment. Any pattern  $X_{AUT}^{REF}$  can be reconstructed in a non free-space reference environment by convolving each side of (2.4) by the response of this reference environment  $H^{REF}$ :

$$X_{AUT} \star H^{REF} = \mathcal{F}_\theta^{-1} \left( \frac{\mathcal{F}_\theta(X_{AUT}^{TEST})}{\mathcal{F}_\theta(H^{TEST})} \right) \star H^{REF}, \quad (2.6)$$

yielding:

$$X_{AUT}^{REF}(\theta) = \mathcal{F}_\theta^{-1} \left( \mathcal{F}_\theta(X_{AUT}^{TEST}) \frac{\mathcal{F}_\theta(H^{REF})}{\mathcal{F}_\theta(H^{TEST})} \right) \quad (2.7)$$

$$= \mathcal{F}_\theta^{-1} \left( \mathcal{F}_\theta(X_{AUT}^{TEST}) \frac{\mathcal{F}_\theta(H^{REF} X_{REF})}{\mathcal{F}_\theta(H^{TEST} X_{REF})} \right) \quad (2.8)$$

$$= \mathcal{F}_\theta^{-1} \left( \frac{\mathcal{F}_\theta(X_{AUT}^{TEST}) \mathcal{F}_\theta(X_{REF}^{REF})}{\mathcal{F}_\theta(X_{REF}^{TEST})} \right). \quad (2.9)$$

As a result, the same expression allows to reconstruct either free-space (2.5) or arbitrary environment (2.9) patterns by simply changing the reference environment.

To illustrate the deconvolution method, let us consider a relevant numerical example of converting the pattern measured in a SAC into the pattern that would be obtained in a FAC. Indeed, SAC are generally preferred in EMC testing but they can lead to spurious pattern estimation due to the presence of a metallic ground plane, which is avoided using a FAC. Using the ADM, the ground plane effects can be removed (or at least attenuated), reconstructing thus a FAC pattern.

Idealized versions of the FAC and the SAC are considered in the numerical simulation, where the electromagnetic absorbers have been replaced by Perfectly Matched Layers (PMLs) and the ground plane has been replaced by a Perfect Electric Conductor (PEC) (as detailed in Fig. 2.1). The chosen reference environment is thus the FAC, while the test environment is chosen to be the SAC. Using the Finite Element Method (FEM) [89] solver GetDP, the necessary angular datasets to be processed for echo removal were obtained. As stated in (2.9), three different datasets are needed to achieve the correction: the first with the reference antenna in the reference environment ( $X_{REF}^{REF}$ ), the second with the same reference antenna in the test environment ( $X_{REF}^{TEST}$ ) and the third with a different AUT in the test environment ( $X_{AUT}^{TEST}$ ) (plus the true dataset  $X_{AUT}^{REF}$ , to have some comparison). In this example, for  $X$ , we have chosen to apply the correction on the electric field  $E$ , which is thus the quantity that will be corrected by the ADM.

Numerically, the electric field is collected at the probe location while rotating the antenna ( $REF$  or  $AUT$ ) in the environment ( $REF$  or  $TEST$ ). (In this two-dimensional simulation, the angle  $\theta$  actually corresponds to the tilt of the antenna.) The rotating step has been fixed to  $\Delta\theta = 1^\circ$  such that  $\theta = n\Delta\theta$ ,  $n = \{0, 1, \dots, N-1\}$ . The applied DFT is achieved using the Fast Fourier Transform (FFT) algorithm [87],[69] after having

[89] Jin, J. *The Finite Element Method in Electromagnetics*.

[87] James W. Cooley, J. W. T. "An Algorithm for the Machine Calculation of Complex Fourier Series".

[69] Frigo, M. et al. "FFTW: an adaptive software architecture for the FFT".

regularized the datasets to avoid zero modes, as explained previously. It is mandatory to respect a constant angular step between samples to apply a DFT algorithm, otherwise an interpolation should be performed on the non uniformly spaced samples. As an alternative, it is also possible to use a Non Uniform Discrete Fourier Transform (NUDFT) on the non uniformly spaced samples, such as the Non Uniform Fast Fourier Transform (NUFFT) [58] or the Unequally Spaced Fast Fourier Transform (USFFT) [23], [53] algorithms.

The collected data  $E_\alpha^\beta$  used for the correction are shown in Fig. 2.2, as well as the corrected pattern  $\tilde{E}_{AUT}^{REF}$  and the exact  $E_{AUT}^{REF}$ . The correction is effective for large amplitudes, mostly when the antenna is facing the probe, while the correction is poorer for lower amplitudes. This behavior is easily understandable, since the numerical errors/uncertainties are relatively higher for lower signal amplitudes. However, another element has to be taken into account: the environment response invariance. Since the reference antenna and the AUT have different shapes, the reflections occurring between the ground plane and the considered antenna do not remain constant, breaking the environment response invariance. Globally, however, the corrected pattern is satisfactory compared to the original one, as they differ by about 1 dB to 2 dB in the main emission beam.

Interestingly, the environment response  $H(\theta)$  and its DFT have an almost chaotic behavior, as depicted in Fig. 2.3. This would make their *a priori* estimation very difficult, in contrast with the theoretical impulse response of the ideal half-space over a ground plane. To illustrate this point, we consider an even simpler model of the SAC, using the current image theory [148], as in [56] and [125], i.e. considering the SAC as a half-space over a PEC.

As illustrated in Fig. 2.4, when a ground plane is present, the radiated contribution  $\vec{E}_1$  due to the current flowing through the antenna has to be added to the radiated contribution  $\rho_{TM}\vec{E}_2$  of the image current brought by the ground plane, with  $\rho_{TM}$  the transverse magnetic reflection coefficient of the ground (of permittivity  $\epsilon = \epsilon_r\epsilon_0$ , and conductivity  $\sigma$ ), defined by

$$\rho_{TM} = \frac{\sqrt{n^2 - \sin^2 \theta} - n^2 \cos \theta}{\sqrt{n^2 - \sin^2 \theta} + n^2 \cos \theta}, \quad (2.10)$$

with

$$n^2 = \epsilon_r - j \frac{Z_0}{2\pi} \sigma \lambda, \quad (2.11)$$

where  $\lambda$  is the wavelength and  $Z_0$  the characteristic impedance of vacuum (air) and  $\theta$  the considered tilt angle.

---

[58] Fessler, J. A. et al. "Nonuniform fast Fourier transforms using min-max interpolation".

[23] Boyd, J. P. "A fast algorithm for Chebyshev, Fourier, and sinc interpolation onto an irregular grid".

[53] Dutt, A. et al. "Fast Fourier Transforms for Nonequispaced Data".

[148] Stratton, J. A. *Electromagnetic Theory*.

[56] Farahbakhsh, A. et al. "Analytic Method to Retrieve Antenna Free-Space Radiation Pattern Above Ground Plane".

[125] Orfanidis, S. J. *Electromagnetic Waves and Antennas*.

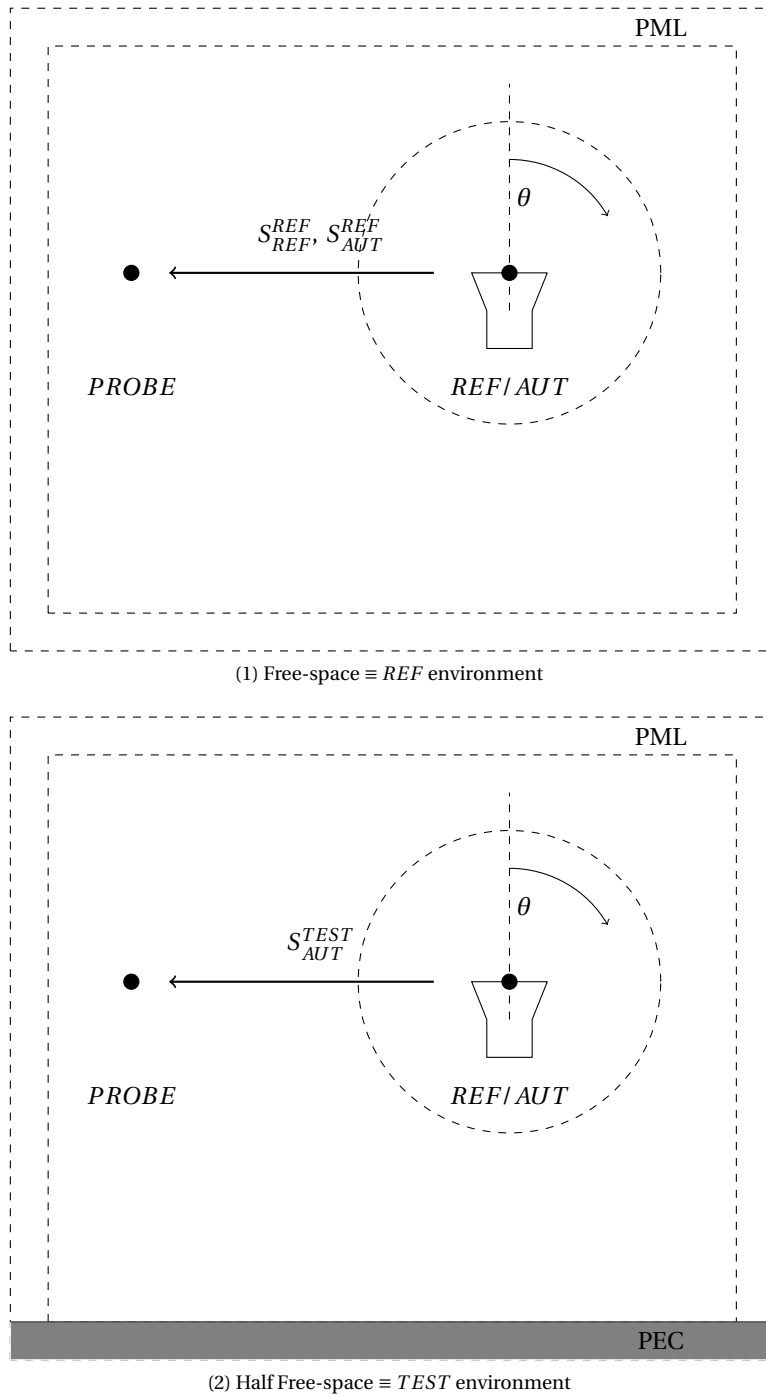


Figure 2.1: Illustration example setup: the deconvolution method requires 2 measurement steps in the test (*TEST*) environment plus one step in the reference (*REF*) environment.

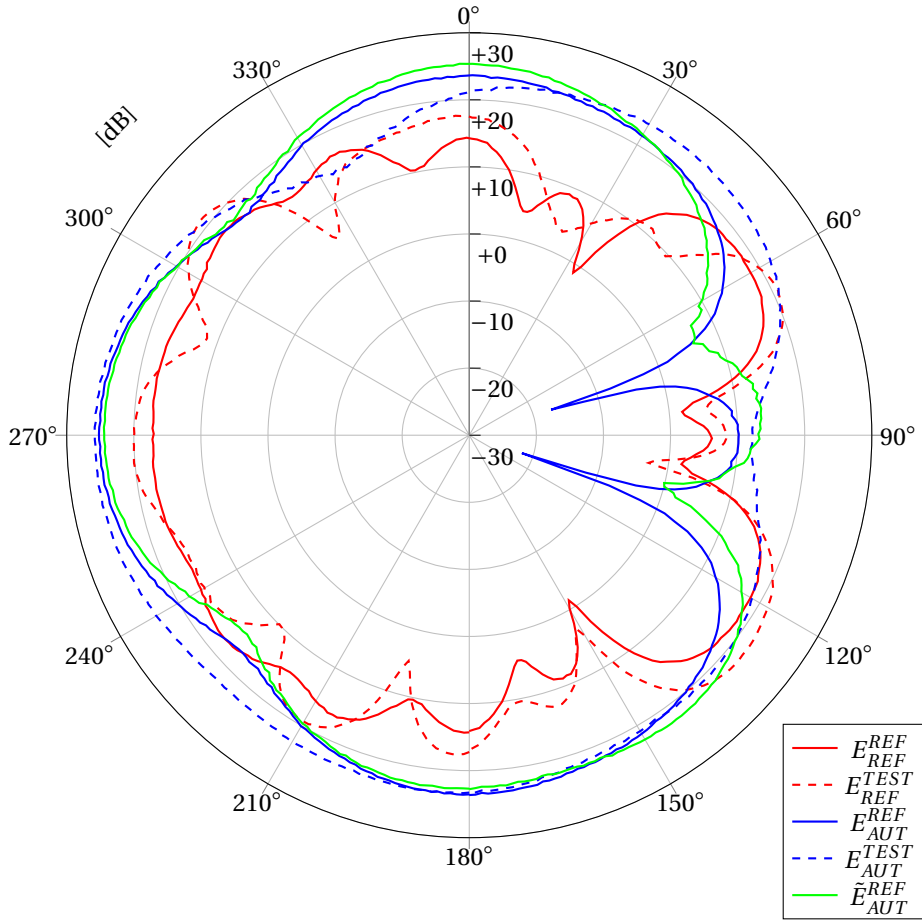


Figure 2.2: Correction using the angular deconvolution method of the echoic pattern  $E_{AUT}^{TEST}$ . The corrected pattern is  $\tilde{E}_{AUT}^{REF}$  and should match the true pattern  $E_{AUT}^{REF}$  whereas the environment transfer function has been estimated using  $E_{REF}^{REF}$  and  $E_{REF}^{TEST}$ .

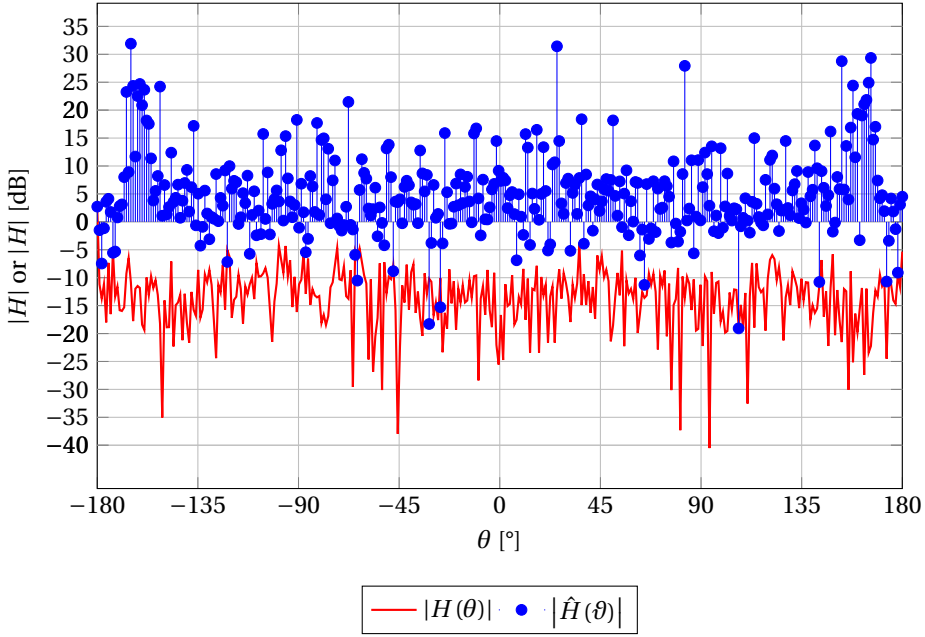


Figure 2.3: Environment response estimation and its Fourier Transform.

Respecting the reflection sign convention, the total radiated field at an observation point  $(r, \theta)$  is:

$$\vec{E}(r, \theta) = \vec{E}_1 - \rho_{TM} \vec{E}_2. \quad (2.12)$$

Each contribution can be decomposed in two factors: a propagation factor and a radiating/shape factor.

Since the image antenna is the same as the true antenna, and making the classical approximation that the vectors arriving at the observation point are parallel ( $\vec{r}_1 \parallel \vec{r} \parallel \vec{r}_2$ ), the total radiated field (phasor) can be written as

$$\vec{E}(r, \theta) = \vec{E}_1 - \rho_{TM} \vec{E}_2 \quad (2.13)$$

$$= \frac{\vec{I}}{I} J k Z_0 \frac{e^{-Jkr_1}}{4\pi r_1} F_z(\theta) \sin \theta - \frac{\vec{I}}{I} J k Z_0 \frac{e^{-Jkr_2}}{4\pi r_2} \rho_{TM} F_z(\theta) \sin \theta \quad (2.14)$$

$$= \frac{\vec{I}}{I} J k Z_0 \frac{e^{-Jkr}}{4\pi r} F_z(\theta) \sin \theta \left( e^{Jkh \cos \theta} - \rho_{TM} e^{-Jkh \cos \theta} \right). \quad (2.15)$$

Typically, for perfect conducting ground planes,  $\rho_{TM} = -1$  and (2.15) can be reexpressed as:

$$\vec{E}_{PEC}(r, \theta) = \frac{\vec{I}}{I} J k Z_0 \frac{e^{-Jkr}}{4\pi r} F_z(\theta) \sin \theta \left( e^{Jkh \cos \theta} + e^{-Jkh \cos \theta} \right) \quad (2.16)$$

$$= \frac{\vec{I}}{I} J k Z_0 \frac{e^{-Jkr}}{2\pi r} F_z(\theta) \sin \theta \cos(kh \cos \theta). \quad (2.17)$$

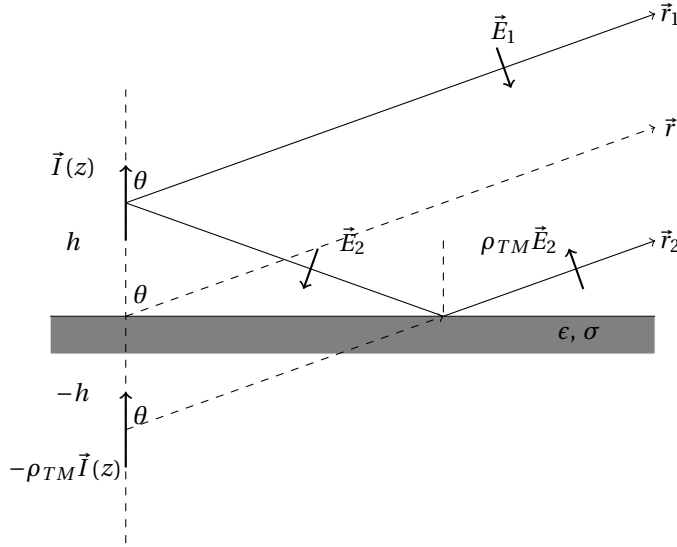


Figure 2.4: Illustration of the reflection caused by a ground plane.

Since, in free-space,  $\rho_{TM} = 0$ , the radiated field [128],[9] is:

$$\vec{E}_{FSP}(r, \theta) = \frac{\vec{I}}{I} J k Z_0 \frac{e^{-jk(r+h \cos \theta)}}{4\pi r} F_z(\theta) \sin \theta, \quad (2.18)$$

the PEC ground plane roughly introduces a  $2 \cos(kh \cos \theta)$  factor (between (2.17) and (2.18)), which introduces grating lobes for  $h > \lambda/4$  on the free-space antenna pattern.

This theoretical behavior is confirmed by the actual antenna radiating patterns (obtained by measuring around the antenna), shown in Fig. 2.5, computed with GetDP on the same configuration as Fig. 2.1. The patterns  $P_{REF}^{REF}$  and  $P_{AUT}^{REF}$  were obtained using two different antennas in free-space, whereas the patterns  $P_{REF}^{TEST}$  and  $P_{AUT}^{TEST}$  were obtained with the same corresponding antennas in a half free-space with a PEC ground plane ( $h = 2.5$  m). As expected by (2.17), the half free-space patterns contain a large amount of grating lobes, since their number increases with the distance  $h$  to the ground plane.

## 2.3 Conclusions

In this chapter, we have addressed a different approach to correct echoic patterns to fit any reference environment by using the ADM. Using this technique it is possible to deconvolve the response introduced by an environment and replace it by the response

[128] Ramo, S. et al. *Fields and Waves in communication electronics*.

[9] Balanis, C. A. *Antenna Theory: Analysis and Design*.

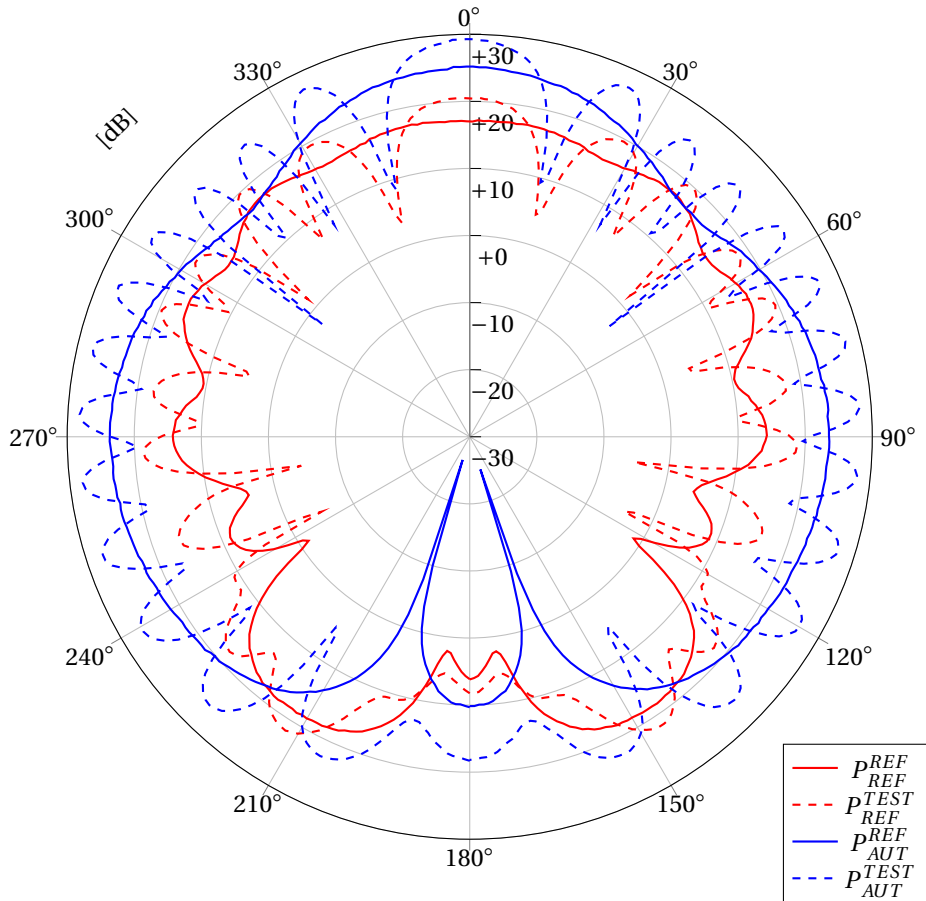


Figure 2.5: Radiating patterns of two different antennas (*TEST* and *AUT*) in free-space (*REF*) or in the presence of a PEC ground plane (*TEST*), with the effect of introducing grating lobes in the antenna patterns  $P_{REF}^{TEST}$  and  $P_{REF}^{AUT}$ .

of another environment, whether free-space or not. This method has the advantage that it is not limited by the AUT bandwidth since it does not require to perform a frequency sweep. Furthermore, since the method uses a reference antenna, it is possible to achieve the major part of the measurement only once for all and thus only effectively measure the AUT in the test environment. However, the method has some limitations, particularly when dealing with the silent zone of the measured antenna where the uncertainty tends to increase, causing the quality reconstruction of the antenna pattern to decrease.

---

# Experimental angular deconvolution method

---

## 3.1 Introduction

IN this chapter, we test the ADM introduced in chapter 2 experimentally and analyze its performance and robustness in a controlled but realistic testing environment.

First, the experimental uncertainty introduced by the ADM is assessed using an appropriate experimental test case. Next, some experimental test cases are used to highlight the key experimental parameters providing accurate reconstructed patterns. Finally, the performance and the robustness of the ADM are evaluated on experimental datasets obtained in increasingly complex and reverberating environments.

The experimental results presented in this chapter expand on those published in [143].

---

## 3.2 Experimental validation and uncertainty

Since the method relies on the environment transfer function invariance  $H^{TEST}$ , the simplest ideal and non trivial validation case can be achieved by using the same antenna as reference (REF) antenna and as test antenna (AUT) to prevent any unintended geometrical change. Moreover, the uncertainty introduced by the correction method can be investigated through repetitive experimental tests, whose goal is to estimate the variability in the quality of reconstructed patterns.

The tests were performed in the SAC of ULiège, following the setup detailed in Fig. 3.1. An ultra-log antenna was used for emission while a single double ridged horn antenna has been used both for the reference antenna and for the AUT, placed at  $d = 300$  cm from the fixed emitting antenna. The integrated turntable of the SAC was used, with a rotation angle step fixed to  $\Delta\theta = 2^\circ$ . To guarantee the environment impulse invariance, the door of the chamber was open only once during the whole test to remove the metal plate used to introduce echoes in the environment. This metal plate was placed

---

[143] Spirlet, M. et al. "Experimental Correction of Radiation Patterns Between Electromagnetic Environments".

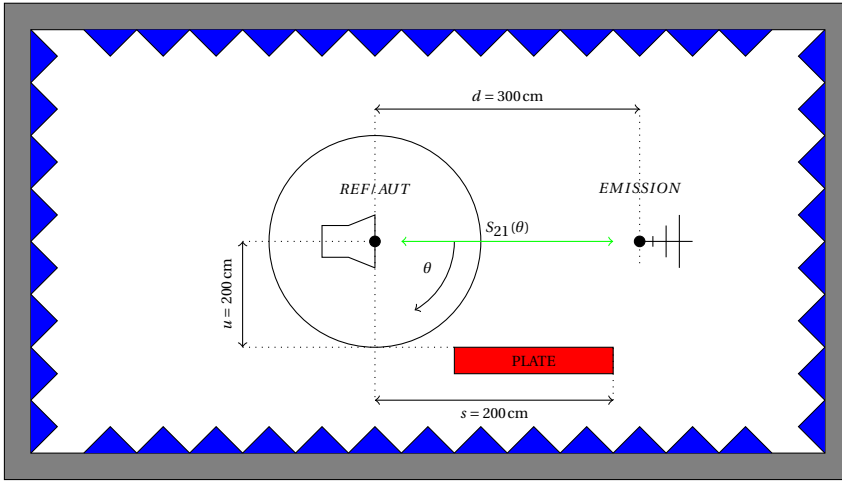


Figure 3.1: Setup of the uncertainty tests.

at  $s = 200\text{ cm}$  and had a vertical surface of  $1.0\text{ m}^2$ . The transmission coefficient  $S_{21}$  was collected in function of the rotation angle  $\theta$  using a calibrated Vector Network Analyzer (VNA) [78]. Both the turntable and the VNA were driven by a computer using the software detailed in Appendix C.1.

Obviously, performing such a test only makes sense within an experimental context, as theoretically a perfect reconstruction should be obtained using the same antenna for the reference and the test antennas ( $X_{REF}^{REF} = X_{AUT}^{REF}$  and  $X_{REF}^{TEST} = X_{AUT}^{TEST}$  in (2.9)). Experimentally, by performing the measurement 4 times with the metal plate and 4 times without the metal plate, a total of  $4^3 = 64$  different reconstructed patterns are expected. The resulting patterns have then been analyzed statistically to estimate some error bounds on the pattern reconstruction. Moreover, a frequency sweep from 200 MHz to 1000 MHz with a step of 100 MHz was also applied through the VNA to characterize the pattern reconstruction in function of the frequency. The minimum and maximum bounds shown in Fig. 3.2 were fixed to statistically encompass 99% of the samples for each considered angle. Fig. 3.2 also shows the mean value of the reconstructed pattern (mean  $\bar{S}_{AUT}^{REF}$ ), as well as the mean values of the measured pattern in the reference environment (mean  $S_{AUT}^{REF}$ ) and in the test environment (mean  $S_{AUT}^{TEST}$ ).

At first glance, Fig. 3.2 exhibits a good behavior of the reconstruction method, as the mean reconstructed pattern mean  $\bar{S}_{AUT}^{REF}$  fits the mean of the original patterns mean  $S_{AUT}^{REF}$ . However, the quality of the reconstructed patterns does not remain constant, with a dependency in function of the frequency and of the level of  $S_{21}(\theta)$ . A deeper analysis is thus needed to evaluate the quality of the reconstructed patterns. To

[78] Hiebel, M. *Fundamentals of Vector Network Analysis*.

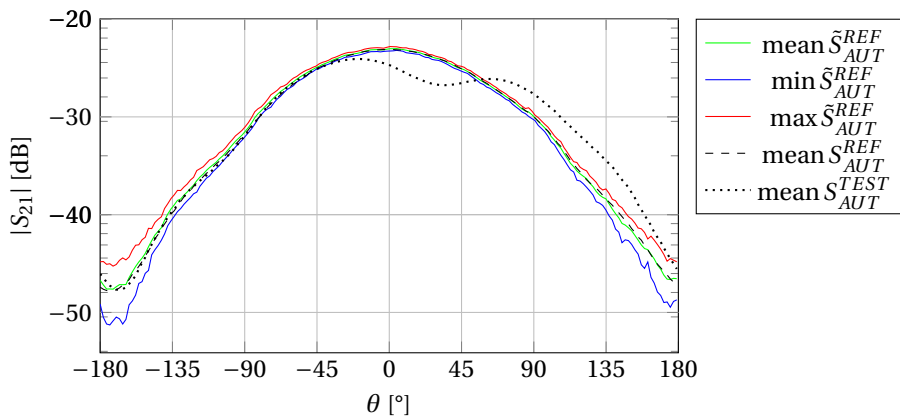
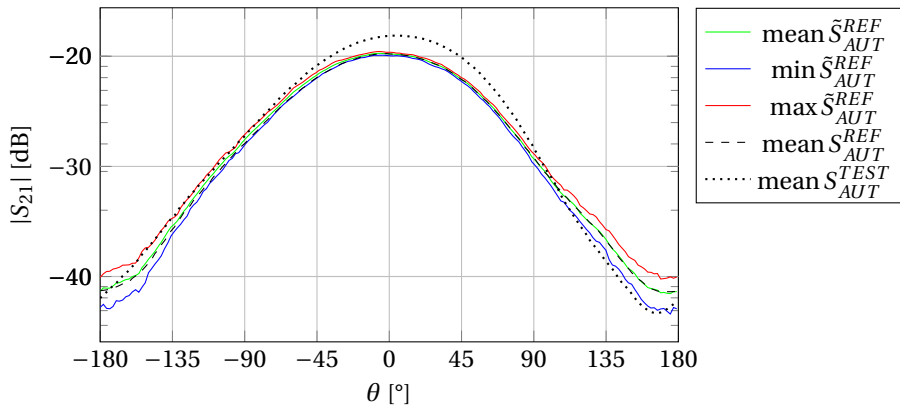
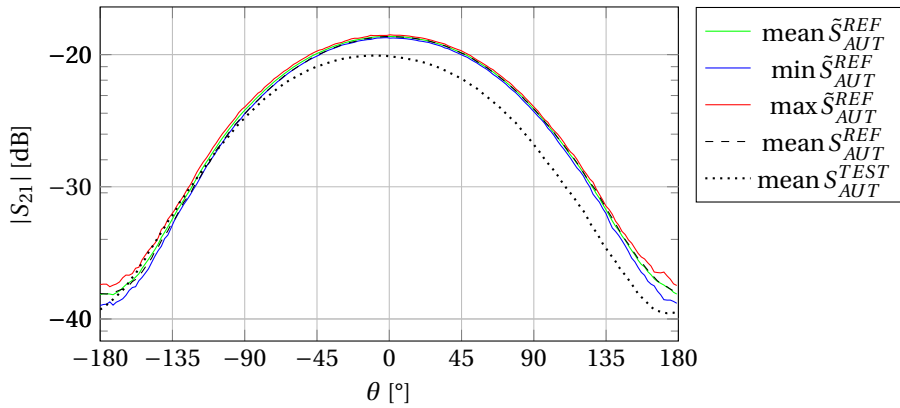


Figure 3.2: Experimental deconvolution with uncertainty bounds (1/3).

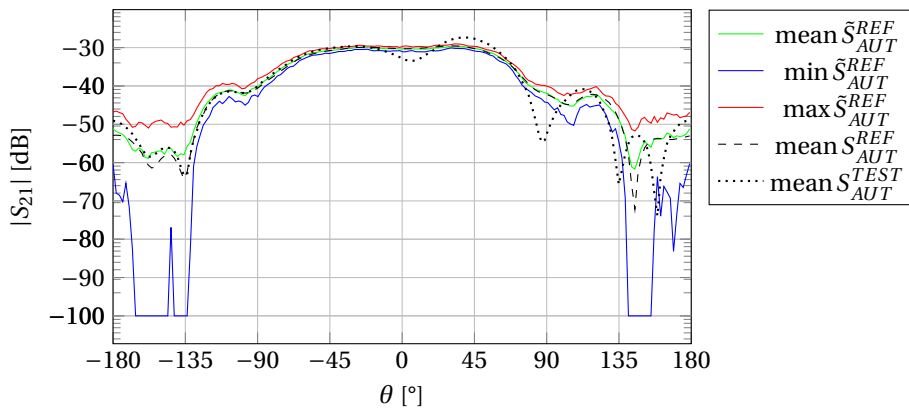
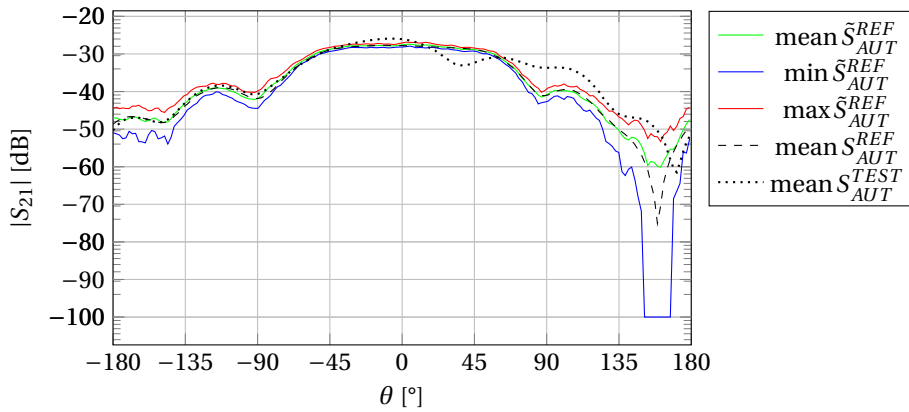
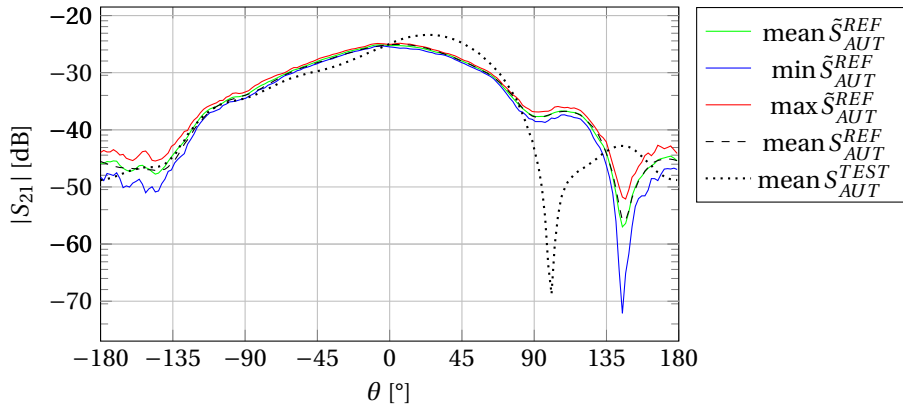


Figure 3.2: Experimental deconvolution with uncertainty bounds (2/3).

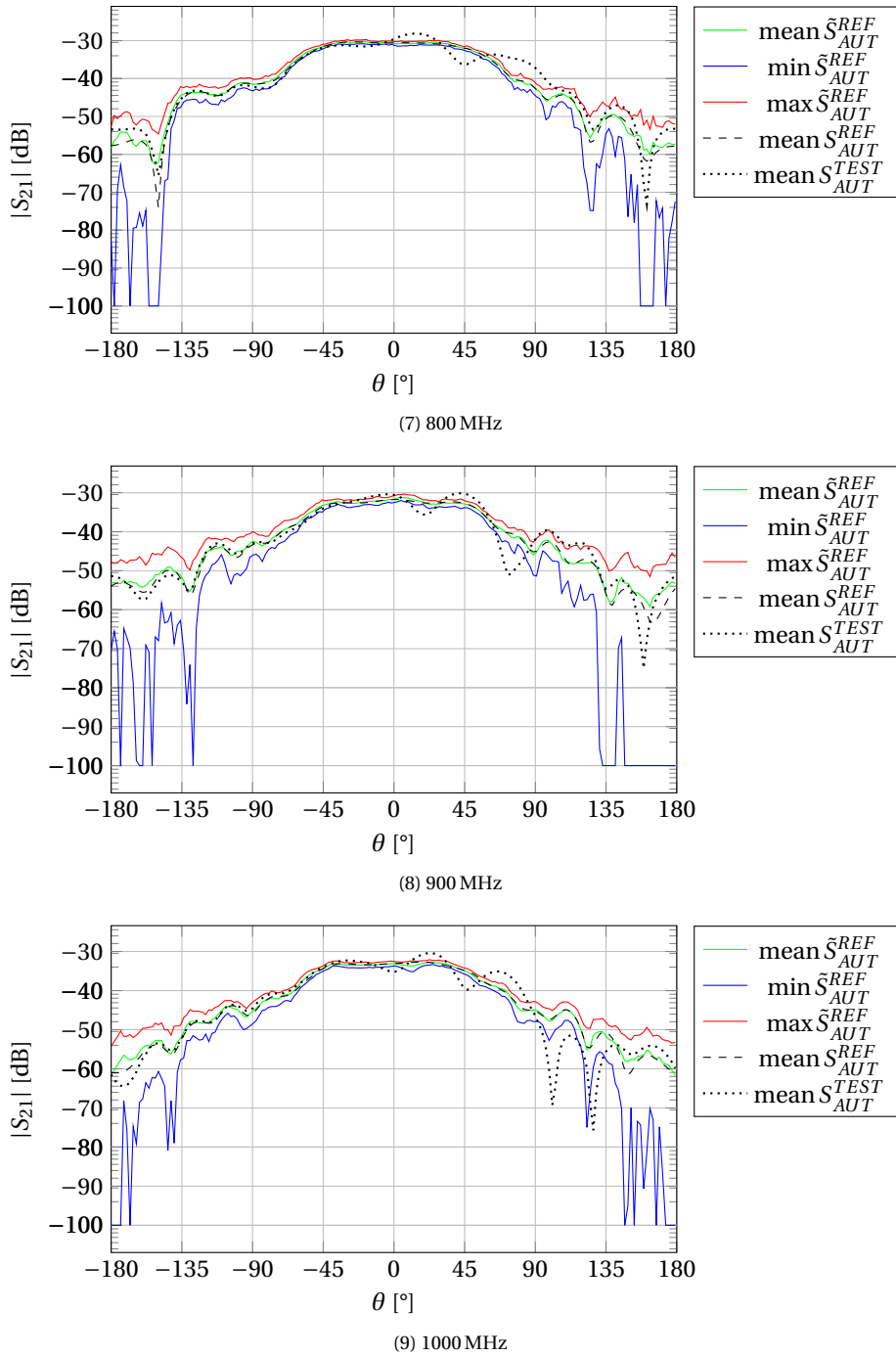


Figure 3.2: Experimental deconvolution with uncertainty bounds (3/3).

do so, a composite quality index  $Q$  is introduced:

$$Q(\theta) = 1 - \frac{\text{std } \tilde{S}(\theta) + |\text{mean } S(\theta) - \text{mean } \tilde{S}(\theta)|}{2 \text{mean } \tilde{S}(\theta)}, \quad (3.1)$$

with  $\text{std}(\cdot)$  the standard deviation,  $S$  the exact measured pattern  $S_{AUT}^{REF}$ , and  $\tilde{S}$  the reconstructed pattern  $\tilde{S}_{AUT}^{REF}$ . A value of  $Q = 1.00$  yields the best quality of reconstruction (trueness [146],[68],[127]), whereas getting  $Q \rightarrow 0.00$  indicates a poor reconstruction. The best indices are obtained if the standard deviation is low (good precision) and the difference between the mean value of the measured pattern and the reconstructed pattern is low (good accuracy).

The  $Q$  values are summarized in Table 3.1 with respect to frequency and with respect to the azimuth angle  $\theta$ . Of course, a threshold has to be determined to distinguish bad and good  $Q$  values, meaning a bound under which the reconstruction is considered as bad. Arbitrarily, a limit value of  $Q = 0.95$  is chosen, which represents a global mismatch of  $\approx 1$  dB. The bad  $Q$  values appear in red whereas the good  $Q$  values are colored in green in the table.

Analyzing Table 3.1, the overall tendency is that the quality of the reconstructed patterns remains good as long as the the amplitude of  $S_{21}(\theta)$  is high. From  $S_{21}(\theta)$  amplitudes lower than about  $-40$  dB, the quality of the reconstructed patterns can dramatically decrease locally. Physically, it is an expected experimental behavior since the measured noise level by the VNA increases the uncertainty of low measured amplitudes of  $S_{21}$ , which has no real impact when considering the main beam of the pattern.

After establishing the experimental validity of the ADM, the following of this chapter is devoted to the analysis of experimental test cases exploring the behavior of the method in increasingly more complex configurations. The various considered test cases are summarized in Table 3.2.

### 3.3 Experimental test cases in semi-anechoic environment

To gradually increase the level of reflections in the environment, the test case 1 and the test case 2 are set up by using a SAC as reference environment, whereas a simple echoic test environment is simulated by introducing a metal plate ( $1 \text{ m} \times 1 \text{ m}$ ) in the SAC, as described in Figs. 3.3 and 3.4. The procedure to collect data remains always the same for each test case:

1. Measure  $S_{REF}^{REF}(f = f_0, \theta = n\Delta\theta)$ : the reference pattern in the reference environment,
2. Measure  $S_{REF}^{TEST}(f = f_0, \theta = n\Delta\theta)$ : the reference pattern in the test environment,

[146] Standardization, I. O. for ISO 5725 : Accuracy (trueness and precision) of measurement methods and results.

[68] Fridman, A. E. *The Quality of Measurements: A Metrological Reference*.

[127] Rabinovich, S. G. *Measurement Errors and Uncertainties: Theory and Practice*.

Table 3.1: Experimental deconvolution uncertainty results ( $Q_x$  where  $x$  is the frequency in MHz)

$\theta$	$Q_{200}$	$Q_{300}$	$Q_{400}$	$Q_{500}$	$Q_{600}$	$Q_{700}$	$Q_{800}$	$Q_{900}$	$Q_{1000}$
-180.0°	0.98	0.97	0.91	0.94	0.85	0.78	0.78	0.79	0.74
-170.0°	0.98	0.95	0.92	0.91	0.92	0.77	0.70	0.83	0.68
-159.9°	0.98	0.96	0.93	0.94	0.86	0.63	0.80	0.70	0.78
-149.9°	0.97	0.95	0.93	0.93	0.92	0.60	0.36	0.80	0.83
-139.9°	0.97	0.96	0.95	0.93	0.90	0.63	0.87	0.83	0.76
-129.9°	0.98	0.97	0.97	0.92	0.92	0.76	0.96	0.77	0.86
-119.8°	0.97	0.97	0.96	0.95	0.96	0.89	0.96	0.87	0.94
-109.8°	0.98	0.97	0.97	0.97	0.95	0.95	0.94	0.96	0.92
-99.8°	0.98	0.97	0.97	0.98	0.92	0.93	0.96	0.82	0.93
-89.7°	0.98	0.97	0.97	0.99	0.95	0.92	0.95	0.89	0.90
-79.7°	0.98	0.97	0.97	0.96	0.89	0.94	0.95	0.96	0.95
-69.7°	0.98	0.98	0.97	0.98	0.94	0.96	0.94	0.93	0.96
-59.7°	0.99	0.97	0.98	0.98	0.97	0.97	0.96	0.95	0.93
-49.6°	0.99	0.98	0.98	0.99	0.97	0.98	0.97	0.94	0.96
-39.6°	0.99	0.98	0.99	0.98	0.98	0.98	0.98	0.97	0.97
-29.6°	0.99	0.99	0.99	0.98	0.98	0.99	0.98	0.97	0.97
-19.6°	0.99	0.99	0.99	0.98	0.99	0.98	0.98	0.98	0.98
-9.5°	1.00	0.99	0.99	0.98	0.98	0.98	0.99	0.97	0.98
+0.5°	0.99	1.00	0.99	0.99	0.97	0.98	0.98	0.97	0.99
+10.5°	1.00	1.00	0.99	0.98	0.97	0.98	0.98	0.95	0.92
+20.6°	1.00	1.00	0.99	0.98	0.97	0.97	0.99	0.98	0.98
+30.6°	1.00	0.99	1.00	0.99	0.98	0.99	0.97	0.97	0.97
+40.6°	1.00	1.00	0.99	0.99	0.98	0.98	0.99	0.96	0.98
+50.6°	1.00	1.00	0.99	0.99	0.98	0.98	0.98	0.98	0.95
+60.7°	1.00	0.99	0.99	0.99	0.98	0.97	0.97	0.96	0.97
+70.7°	1.00	0.99	0.99	0.98	0.97	0.97	0.98	0.94	0.94
+80.7°	1.00	0.99	0.99	0.97	0.97	0.96	0.95	0.93	0.89
+90.8°	0.99	0.99	0.99	0.98	0.94	0.94	0.96	0.88	0.93
+100.8°	1.00	0.98	0.98	0.98	0.94	0.94	0.92	0.90	0.90
+110.8°	0.99	0.98	0.97	0.98	0.91	0.94	0.93	0.89	0.95
+120.8°	0.99	0.98	0.98	0.98	0.92	0.94	0.85	0.80	0.89
+130.9°	0.99	0.97	0.96	0.94	0.90	0.85	0.80	0.80	0.88
+140.9°	0.98	0.97	0.94	0.87	0.84	0.67	0.85	0.68	0.87
+150.9°	0.98	0.96	0.96	0.89	0.69	0.71	0.79	0.74	0.69
+160.9°	0.98	0.96	0.97	0.92	0.42	0.82	0.57	0.56	0.75
+171.0°	0.98	0.97	0.92	0.95	0.84	0.78	0.83	0.56	0.79

Table 3.2: Summary of the considered test cases.

Section	Test case	Antenna	Reference Setup	Results
Section 3.3	1	log-periodic	Fig. 3.3 (Fig. 3.5)	Fig. 3.6
	2	yagi-uda	Fig. 3.4	Fig. 3.7
Section 3.4	Parametric $d$	log-periodic	Fig. 3.3	Fig. 3.8
	Parametric $d$	yagi-uda	Fig. 3.3	Fig. 3.9
	Parametric $s$	log-periodic	Fig. 3.3	Fig. 3.10
	Parametric $s$	yagi-uda	Fig. 3.3	Fig. 3.11
	3	log-periodic	Fig. 3.4	Fig. 3.17
	4	yagi-uda	Fig. 3.4 (Fig. 3.16)	Fig. 3.18
Section 3.6	5	yagi-uda	Fig. 3.4	Fig. 3.21
	6	yagi-uda	Fig. 3.4 (Fig. 3.22)	Fig. 3.23

3. Measure  $S_{AUT}^{TEST}(f=f_0, \theta=n\Delta\theta)$ : the test pattern in the test environment (to be corrected),
4. Measure  $S_{AUT}^{REF}(f=f_0, \theta=n\Delta\theta)$ : the test pattern in the reference environment (only for comparison).

To analyze the behavior of the ADM when considering different incidences of reflections, the metal plate is placed at two different locations: in test case 1, the distance  $s$  between the rotating antenna and the metal plate is 2.0 m (Fig. 3.3) whereas in test case 2, the plate is located at  $t = 1.6$  m behind the rotating antenna (Fig. 3.4).

The setup is identical for test cases 1 and 2, except for the metal plate positioning. The distance between the rotating antenna and the static antenna is fixed to  $d = 120$  cm. The emission antenna is a log-periodic antenna in test case 1, and is a yagi-uda antenna in test case 2. The rotating antennas (*REF* and *AUT*) are two different double-ridged horn antennas (Rohde & Schwarz HL907 and Schwarzbeck BBHA-9120-AS). A sinusoidal signal at the frequency of 1.0 GHz is injected in the emission antenna with the VNA (Rohde & Schwarz ZVA24). The turntable from the SAC is used to incrementally rotate the antennas by  $\Delta\theta = 2^\circ$ . The whole process is controlled with a computer running the software detailed in Appendix C.1. Fig. 3.5 depicts the real experimental setup in the echoic configuration, with the metal plate simulating a simple echoic environment.

In Figs. 3.6 and 3.7,  $S_{REF}^{REF}$ ,  $S_{REF}^{TEST}$  (—),  $S_{AUT}^{TEST}$  (- - -), the corrected pattern  $\tilde{S}_{AUT}^{REF}$  (—) and the true pattern  $S_{AUT}^{REF}$  (—) of the AUT are displayed. Comparing the reconstructed pattern  $\tilde{S}_{AUT}^{REF}$  to  $S_{AUT}^{REF}$  on Fig. 3.6, it appears that the matching is excellent. A small degradation of the pattern reconstruction quality is noticeable in Fig. 3.7 for test case 2, probably due to the increase of uncertainty brought by a predominant number of lower amplitudes in the transmission coefficient  $S_{21}$ .

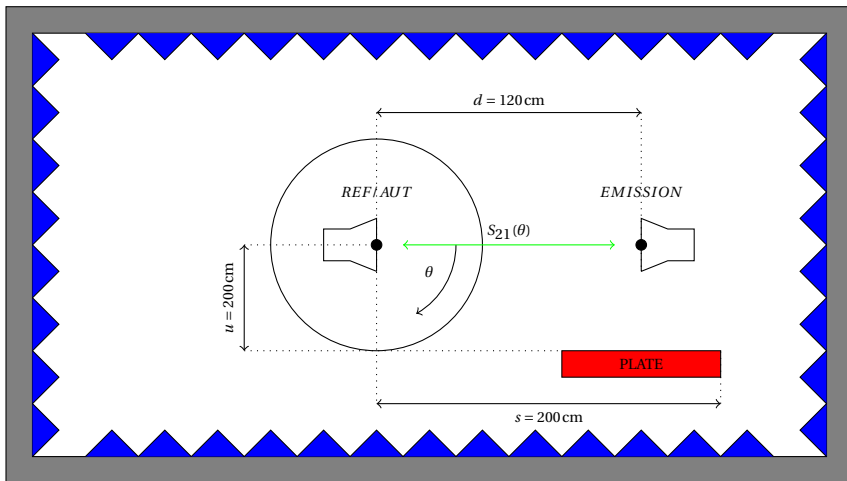


Figure 3.3: Setup of the test case 1.

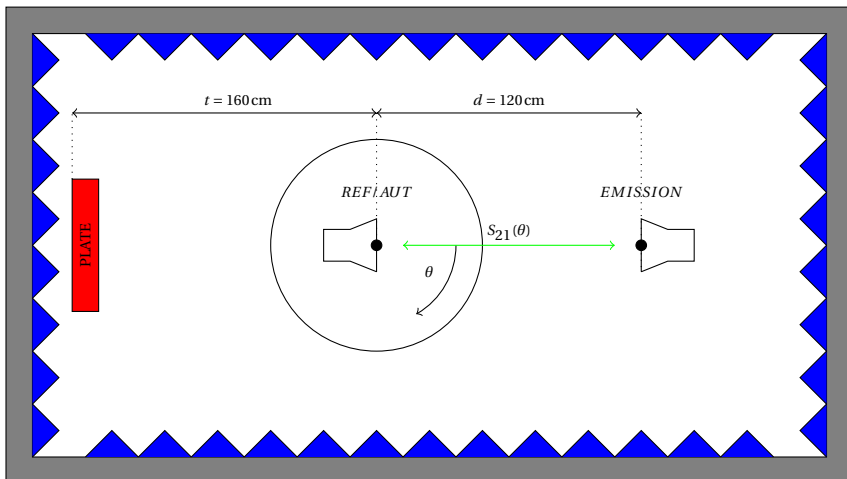


Figure 3.4: Setup of the test case 2.



Figure 3.5: Experimental deconvolution setup for test case 1.

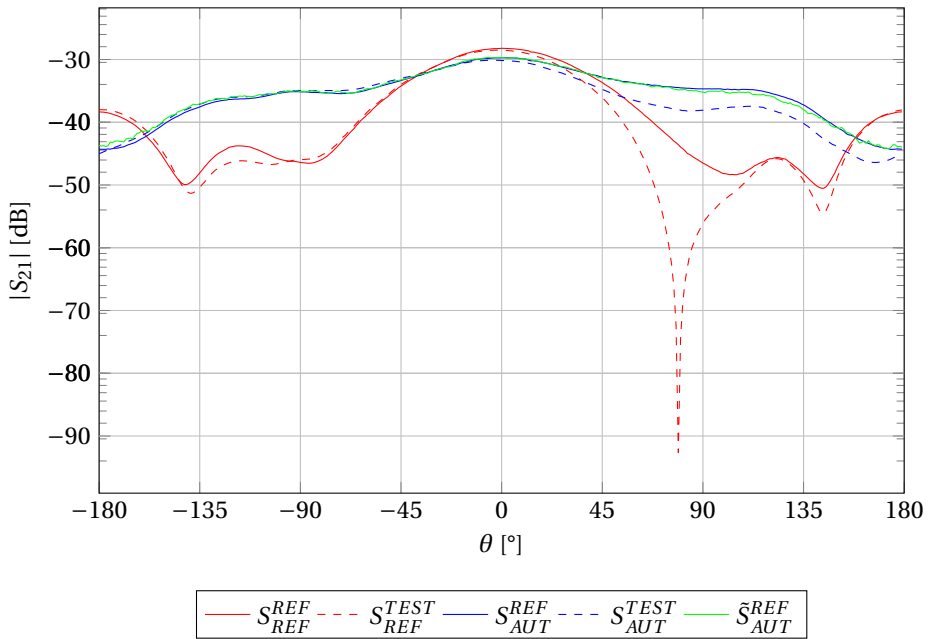


Figure 3.6: Experimental deconvolution results for test case 1.

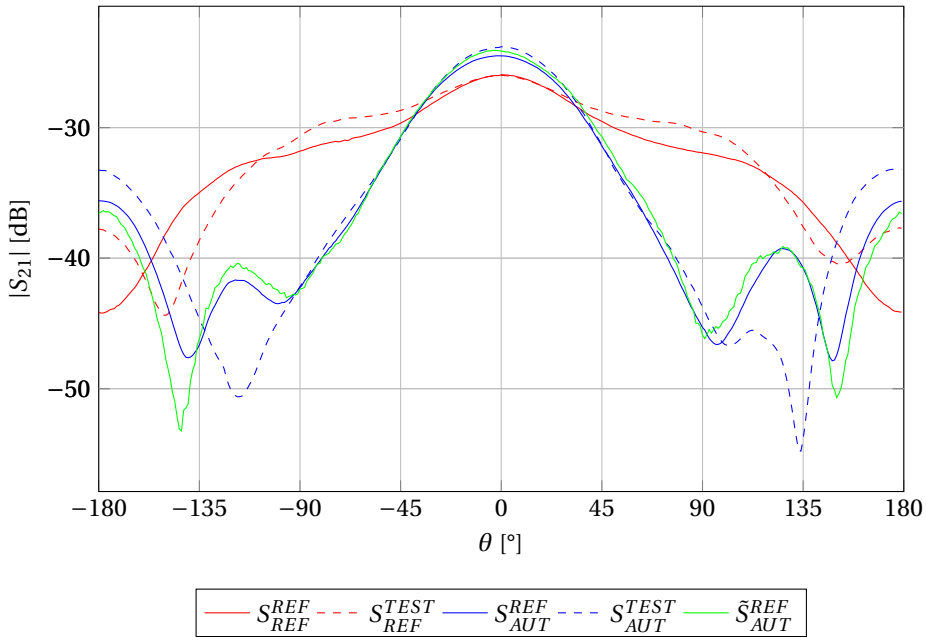


Figure 3.7: Experimental deconvolution results for test case 2.

### 3.4 Experimental parametric test cases

Based on the results from the previous section, the behavior of the method according to the position of the reflective elements and the antennas is not obvious. In order to establish some rules to obtain accurate reconstructed patterns, we have completed parametric test cases, varying the distance  $d$  between the fixed antenna and the rotating antenna on one hand (see Fig. 3.3), and on the other hand, varying the distance  $s$  between the rotating antenna and the metal plate (see Fig. 3.3). The tests have been achieved using either a low directive antenna (log-periodic) or a high directive antenna (yagi-uda) as fixed antenna, to compare the efficiency of the method regarding the emission antenna type.

The synthesis of all the results has been obtained by considering the error between the real pattern and the reconstructed pattern according to:

$$E_S = \sqrt{\frac{\sum_{i=0}^{N-1} (|S_{AUT}^{REF}(\theta_i)| - |\tilde{S}_{AUT}^{REF}(\theta_i)|)^2}{\sum_{i=0}^{N-1} |S_{AUT}^{REF}(\theta_i)|^2}}. \quad (3.2)$$

Once again, a threshold value should be determined to decide whether the error on the reconstructed pattern is satisfactory or not. This bound  $\bar{E}_S$  has been determined by averaging the errors obtained by (3.2) on the 64 results from the validation and

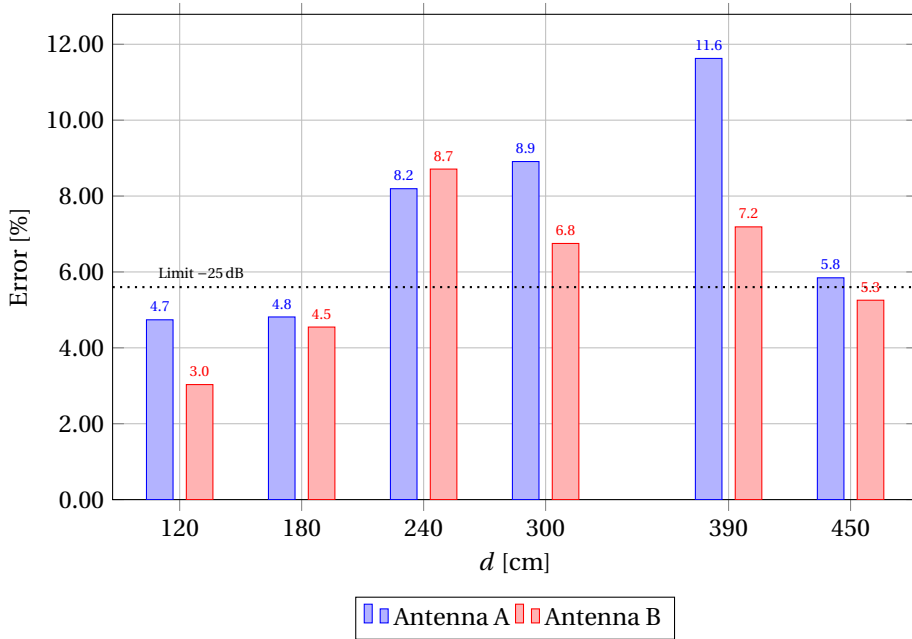


Figure 3.8: Parametric results depending on  $d$  for the experimental deconvolution at 1000 MHz, using a log-periodic fixed antenna.

uncertainty tests from section 3.2 at the frequency of 300.0 MHz which corresponds to the global worse satisfactory quality pattern encountered. Considering a confidence interval of 99 %,  $\bar{E}_S$  has been set to 5.6 %, or equivalently  $-25$  dB.

For each test, the patterns in the reference environment and in the test environment have been measured for each antenna (*REF* and *AUT*). As a result, each antenna can actually be used as reference antenna or *AUT*. This is interesting, since for the same effort of measurement, the number of reconstructed patterns is doubled. In the following results, “Antenna A” denotes the error on the reconstruction of the pattern for the first antenna with the second antenna as reference, whereas “Antenna B” denotes the error on the reconstruction of the pattern for the second antenna, using the first antenna as reference.

**Varying the distance  $d$  between the two antennas** For these tests, the same configuration setup as for the test case 1 (Fig. 3.3) is used. Only the distance  $d$  between the antennas is changed between 120 cm and 450 cm. The error with the log-periodic emission antenna is reported in Fig. 3.8, whereas the error with the yagi-uda is summarized in Fig. 3.9.

As shown in Fig. 3.8, the reconstructing error using a log-periodic antenna is globally high for the distances between the fixed and the rotating antenna from 240 cm to 390 cm.

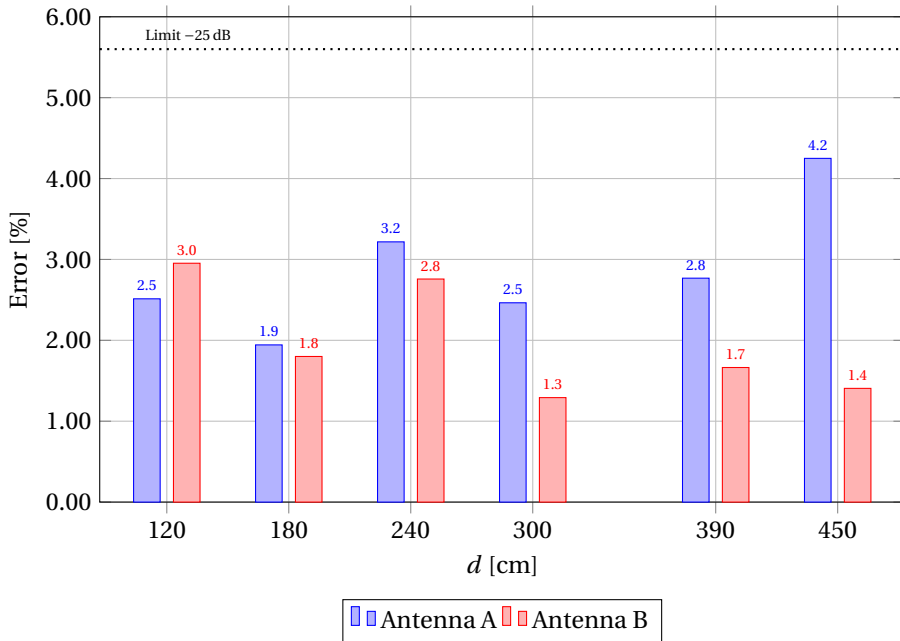


Figure 3.9: Parametric results depending on  $d$  for the experimental deconvolution at 1000 MHz, using a yagi-uda fixed antenna.

Two elements can justify this behavior: the first is that, in this configuration, since the metal plate is positioned half way from the two antennas, the reflections are highly impinging on the rotating antenna which does not preserve the impulse environment response invariance; the second is that due to the increase of the distance, the amplitude level of  $S_{21}$  decreases, which induces an increase of the uncertainty on the measurement due to noise. Considering a yagi-uda antenna as emission fixed antenna, which is a more directive antenna, the reconstruction errors, given in Fig. 3.9 are fairly low. An accurate pattern reconstruction is achieved in all the test cases, according to the fixed criterion. It means that the method provides a good suppression of the reflection caused by the metal plate. Using a directive fixed antenna would then guarantee the response invariance, by lowering the second order reflections, thus improving the reconstruction accuracy.

**Varying the distance  $s$  between the rotating antenna and the metal plate** The configuration setup from the test case 1 (Fig. 3.3) is once again used, but this time, the distance  $s$  between the rotating antenna and the metal plate is changed from 0 cm to 300 cm while keeping the distance  $d$  constant. The reconstruction errors are reported in Figs. 3.10 and 3.11 using respectively the log-periodic emission antenna and the yagi-uda antenna. The reconstruction errors appear to depend strongly on the metal plate location, for both emission antennas. A deeper analysis shows that the average recon-

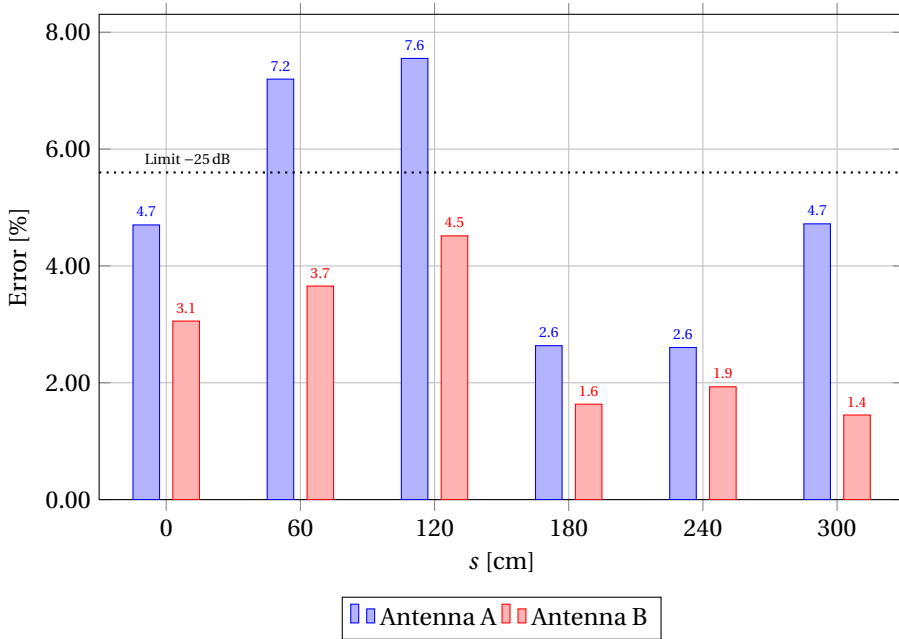


Figure 3.10: Parametric results depending on  $s$  for the experimental deconvolution at 1000 MHz, using a log-periodic fixed antenna.

struction errors are more or less equivalent between the two emission antennas (3.80 % for the log-periodic and 3.56 % for the yagi-uda), but the directive antenna provides a lower standard deviation compared to less directive one (1.62 % and 2.04 %). Using a more directive antenna is thus once again more suitable to improve the accuracy of the reconstruction.

After analyzing the results of these two parametric test cases, an overall conclusion can already be drawn: using a directive antenna for the emission improves the reconstruction trueness (in precision and in accuracy). However, our error criterion (3.2) is rather pessimistic since no further data processing is applied to the corrected patterns. The worse results (i.e. those having the highest error) from the parametric test cases are shown in Figs. 3.12 to 3.15. A deeper analysis of those figures actually reveals a rather accurate reconstruction in the main beam of the antenna, with a degradation in the silence zones, as expected. Furthermore, the corrected patterns also contain a superimposed high frequency component (in the dual angular domain) brought by the numerical processing. Since these components have been introduced by the numerical processing, an appropriate filtering could also be applied to remove them. The origin of the high frequency components is however no very clear, as it does not occur on each corrected pattern.

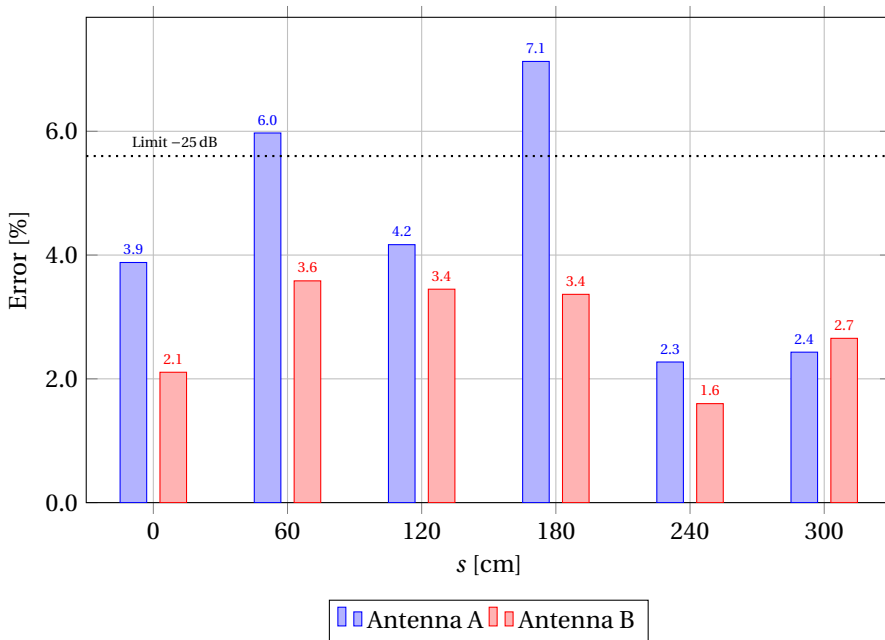


Figure 3.11: Parametric results depending on  $s$  for the experimental deconvolution at 1000 MHz, using a yagi-uda fixed antenna.

### 3.5 Environment response invariance analysis

The behavior of the correction method is thus globally satisfactory for a simple echoic environment correction. But, even in such a simple test environment, the reflections occurring between the environment and the rotating antenna seem to have a significant impact on the quality of the reconstructed patterns. To evaluate the contribution of the environment response invariance in the reconstruction error, two other test cases are proposed. The following test cases 3 and 4 rely on a setup similar to test case 2 (see Fig. 3.4), but the echoic environment has been complexified by introducing two additional metal plates. An illustration of the physical setup of test case 4 is depicted in Fig. 3.16.

The impact of the emission antenna is still evaluated using two antennas having different directivities. The results of test case 3 using the log-periodic antenna are displayed in Fig. 3.17 whereas those for the test case 4, using the more directive antenna, yagi-uda, are presented in Fig. 3.18.

Both test cases exhibit a poor reconstruction quality, according to our quality limit of 5.6% (errors according to (3.2): 14.4% for the log-periodic and 9.3% for the yagi-uda). The correction has almost no effect in the case of the directive antenna, and few effects for the less directive antenna. To validate the importance of the invariance of the environment transfer function to build accurate reconstructed patterns, we compare the

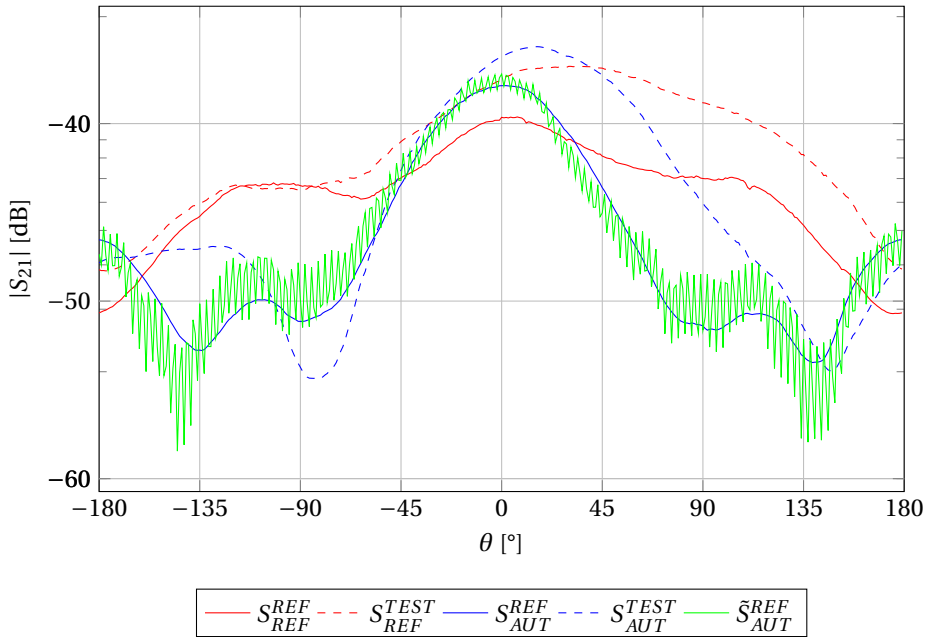


Figure 3.12: Visualization of the worse reconstruction result from Fig. 3.8 obtained using Antenna “A” with  $d = 390$  cm.

environment responses for the best reconstructed pattern of the parametric test cases (from Fig. 3.9 with  $d = 300$ ), and for the worse reconstructed pattern (from Fig. 3.18). The environment responses collected using the *REF* antenna and the *TEST* antenna for the two different test cases are plotted in Fig. 3.19. As can be seen, the estimated environment responses are very different, even for the configuration where the invariance response was assumed, which is also confirmed by the cross correlation function  $\Gamma$  [118], plotted in Fig. 3.20.

Consequently, due to the “chaotic” nature of the environment response, the impact of the reflections on the environment impulse response is difficult to predict. The invariance of the impulse response of the environment does have a critical impact but it is more likely to be a sufficient condition rather than a necessary condition. Less restrictive conditions bringing quality reconstructed patterns remain to be investigated. However, it should also be emphasized that the method does not produce a worse pattern than the non-corrected echoic pattern, even if the correction method fails.

[118] Montgomery, D. C. et al. *Applied Statistics and Probability for Engineers*.

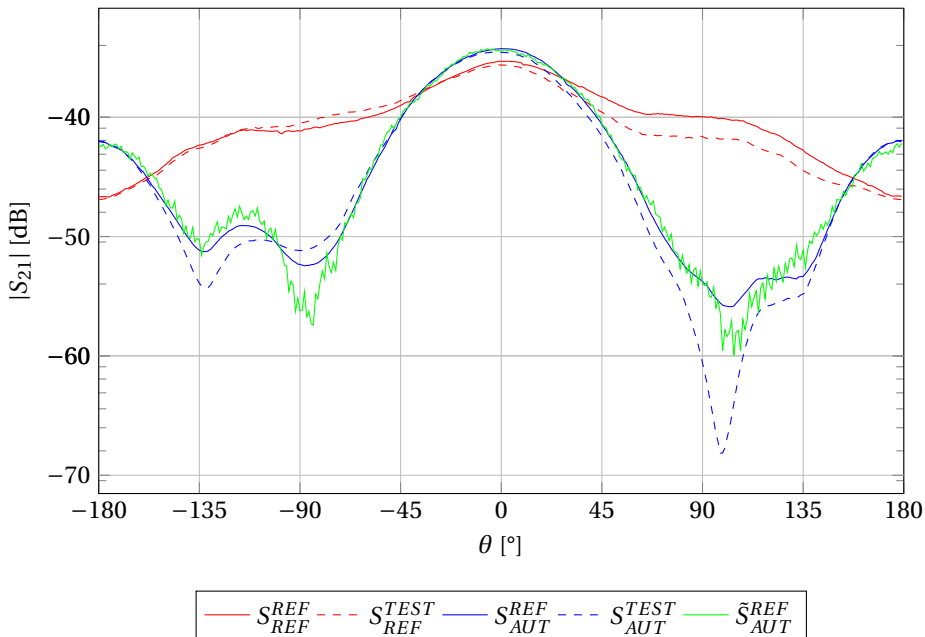


Figure 3.13: Visualization of the worse reconstruction result from Fig. 3.9 obtained using Antenna “A” with  $d = 450$  cm.

### 3.6 Experimental test cases in realistic environment

After having introduced slight reflections in a SAC as test environment, the next environment to be considered is more realistic and more complex, since it consists in an electrical machines laboratory. A mobile turntable, detailed in Appendix C.2, has thus been built to allow measurements outside the SAC. In the test case 5, a metal plate is used inside the room to act as test environment while the room itself is used as the reference environment to reach a configuration very similar to the one of the test case 2 (Fig. 3.4). The yagi-uda antenna is used, as the previous test results have shown that using a directive emission antenna improves the quality of the reconstructed patterns.

The reconstructed pattern and the other collected data are summarized in Fig. 3.21. As expected with this weak reverberating albeit complex environment, the reconstructed pattern  $\tilde{S}_{AUT}^{REF}$  matches accurately the measured pattern  $S_{AUT}^{REF}$ . Although the aim of this test case 5 is to evaluate the behavior of the method in a more complex environment, only a few changes between the reference and the test environment were made. On the contrary, the test case 6 extends the test case 5 in realistic environments by using a totally different reference environment, since the reference measurements were obtained in the FAC from the “Welcome Technological Platform” at the University of Louvain-La-Neuve while keeping the test environment in the electrical machines test benches laboratory, as depicted in Fig. 3.22. The configuration from one site has been reproduced

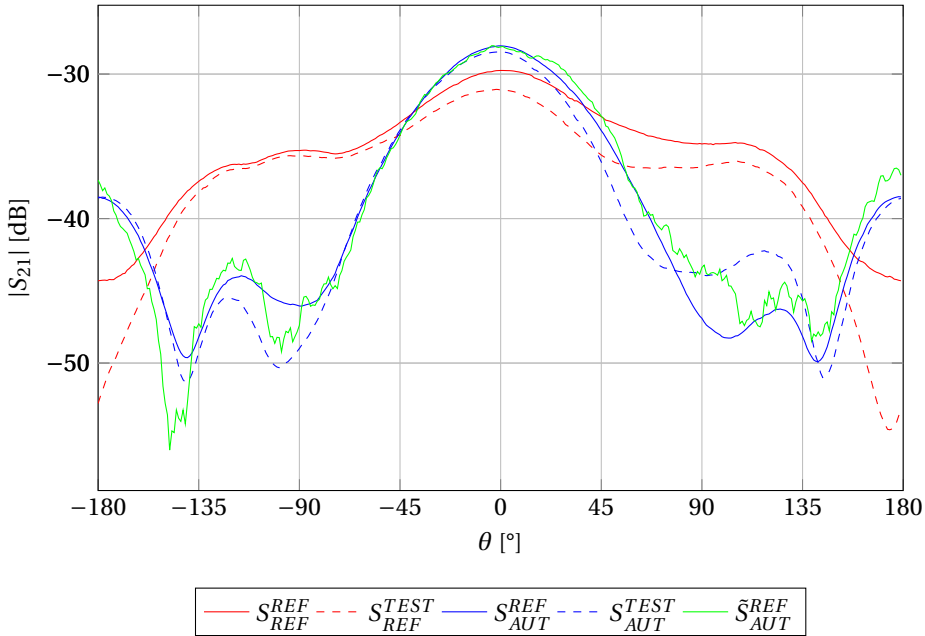


Figure 3.14: Visualization of the worse reconstruction result from Fig. 3.10 obtained using Antenna “A” with  $s = 120$  cm.

in the other site with greatest care, e.g. by ensuring the feeding cables were placed in the same locations and that the relative position of all the equipments were identical.

The results of this final test case, shown in Fig. 3.23, exhibit a very good confidence between the true measured pattern of the AUT in the FAC and the reconstructed pattern. A slight degradation of the reconstruction pattern quality is noticeable, compared to test case 5, but it is somehow expected since the whole setup has been moved from one site to another causing inevitably some mismatch.

This last test case, performed between a realistic environment and a different test environment demonstrates the ability of the ADM to be used in practice to retrieve radiation patterns using in-situ measurements.

### 3.7 Conclusions

This chapter has demonstrated the viability of the ADM as an alternative method to estimate antenna radiation patterns from measurements obtained in echoic environments, with the best results obtained by using a directive emission antenna. The method has nevertheless some limitations due to the fact that it requires the inferred environment response to remain constant. This is not guaranteed, particularly when the AUT is geometrically different from the reference antenna. In order to have a better understanding

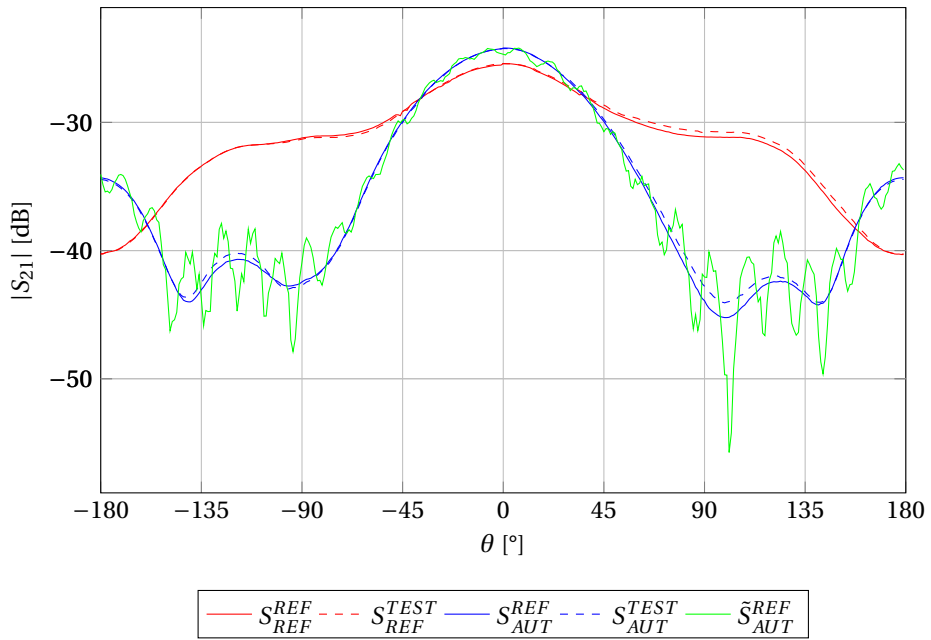


Figure 3.15: Visualization of the worse reconstruction result from Fig. 3.11 obtained using Antenna “A” with  $s = 180$  cm.



Figure 3.16: Experimental deconvolution setup for test case 4.

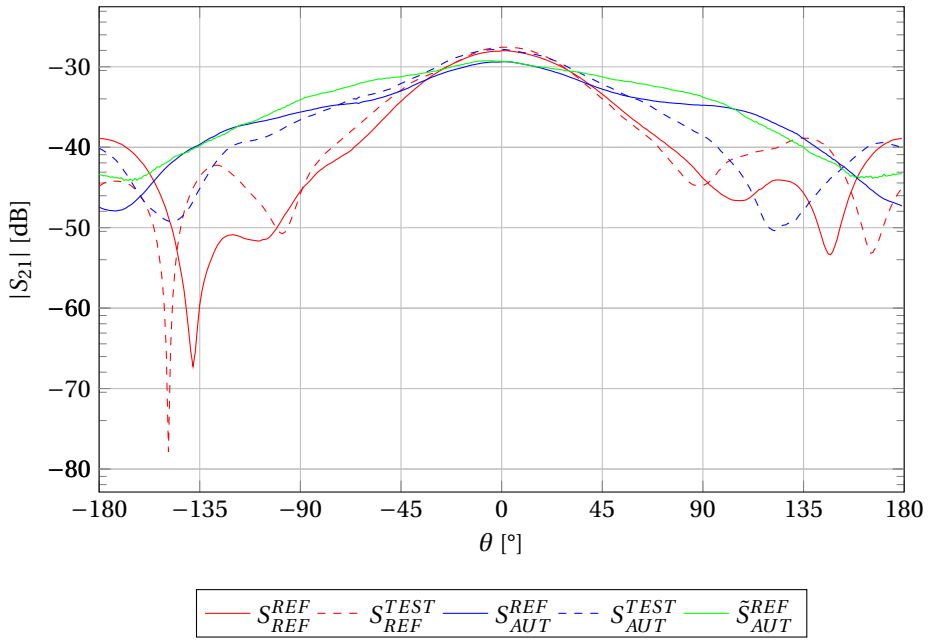


Figure 3.17: Experimental deconvolution results for test case 3.

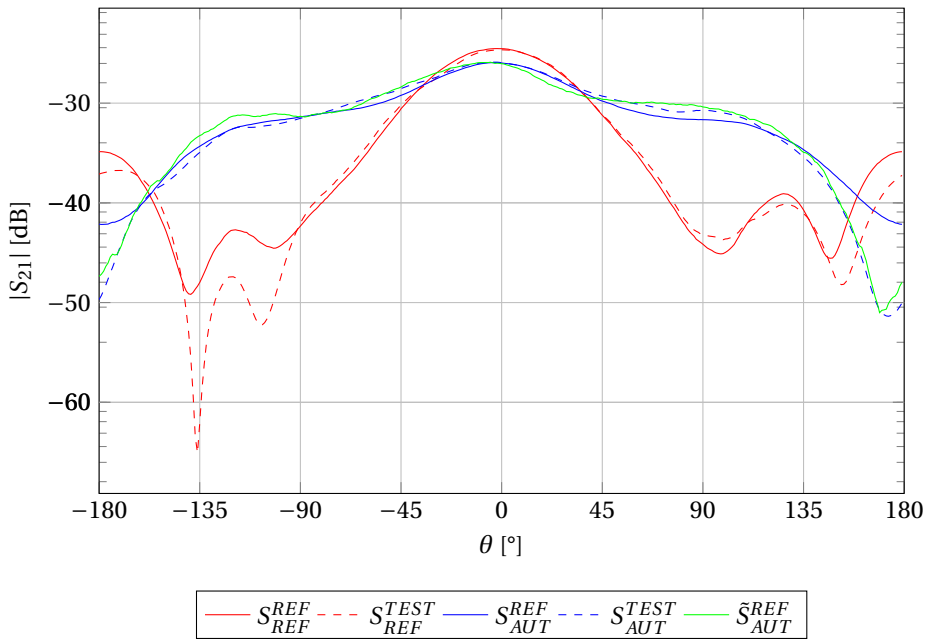
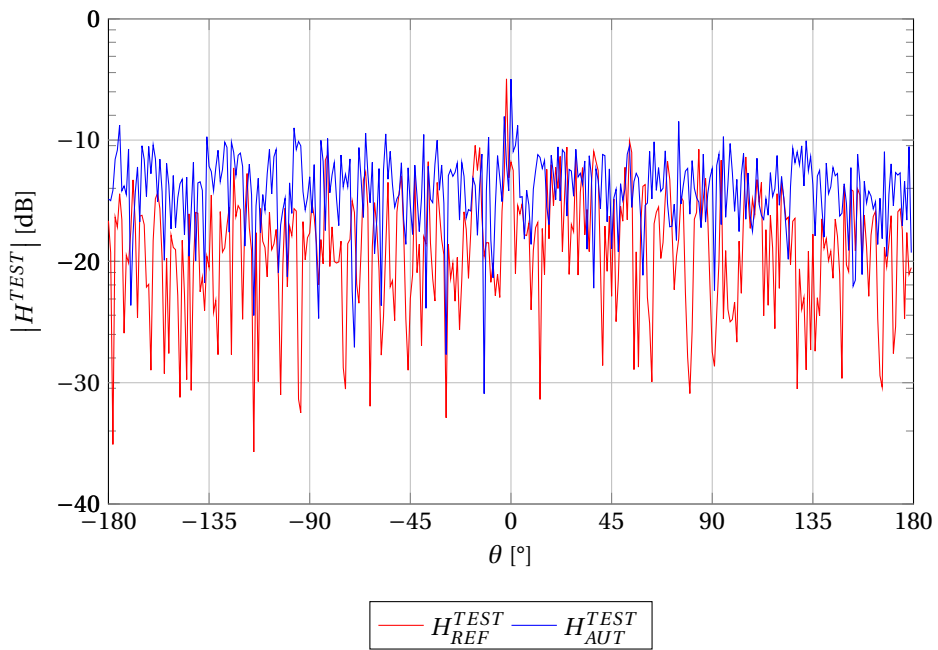
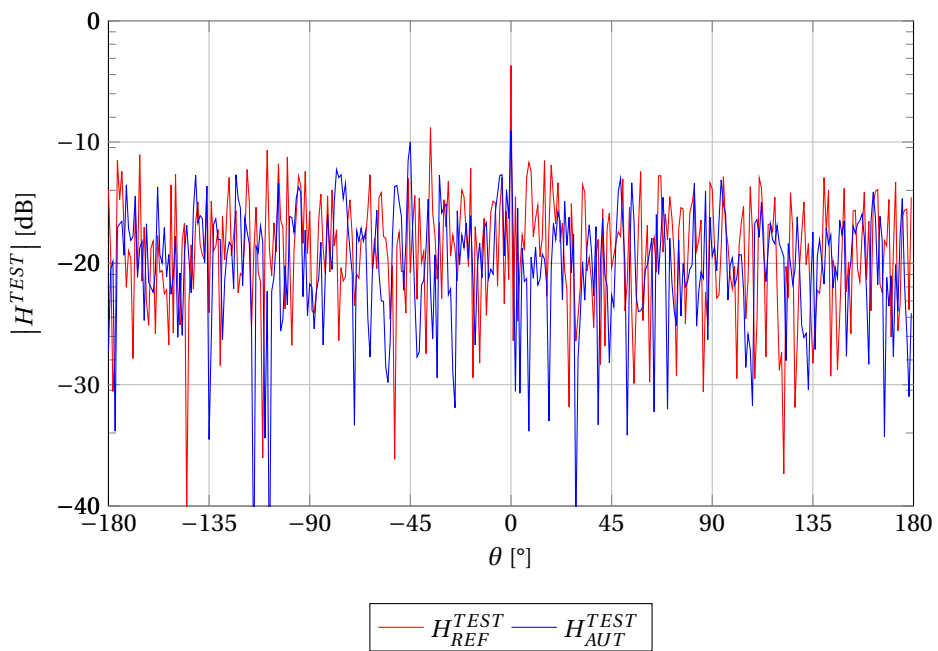


Figure 3.18: Experimental deconvolution results for test case 4.



(1) Best reconstruction error environment impulse responses.



(2) Worse reconstruction error environment impulse responses.

Figure 3.19: Environment impulse response for the best and the worst reconstruction errors.

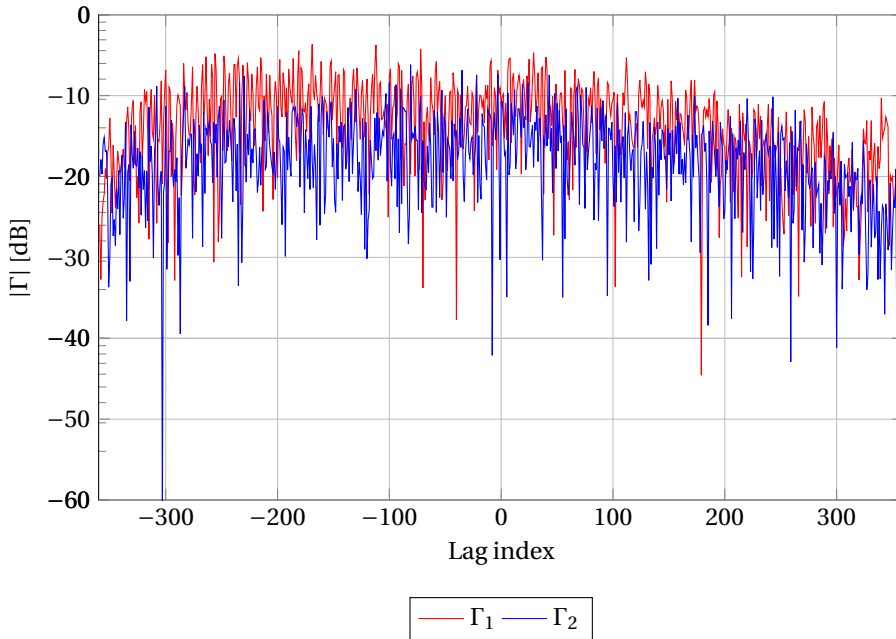


Figure 3.20: Cross-correlation between the environment impulse responses obtained with *REF* antenna and *TEST* antenna for two different configurations yielding the best ( $\Gamma_1$ ) and the worse ( $\Gamma_2$ ) reconstruction errors.

of this phenomena the estimated environment response could be compared to noise and would probably require to apply some stochastic signal processing to have a better understanding of the phenomena. The method could also be slightly improved by applying a high-pass filter on the obtain corrected pattern because in some rare cases, for a reason to be determined, a high frequency component signal is introduced by the correction algorithm. Interestingly, contrary to classical methods the ADM does not deteriorate the given initial echoic pattern, which is always an asset for a correction method. As we have seen, a physical meaning of the environment angular transfer function lacks to allow the method to be extended for passive Device Under Tests (DUTs). For such DUTs, as it should also be for generic radiated immunity tests, there is no other option than using more complex active shaping techniques to compensate the echoic behaviors of the environment.

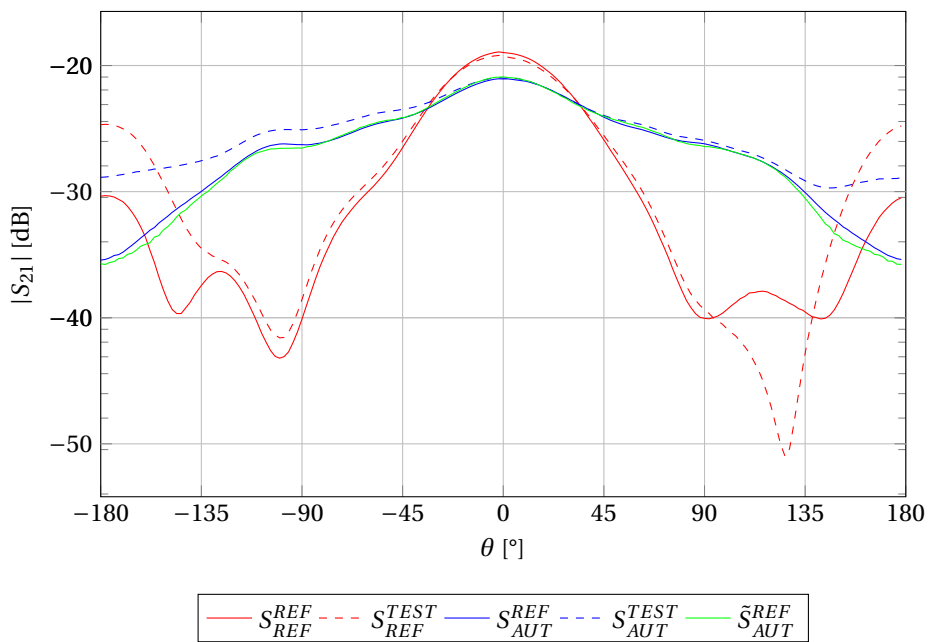
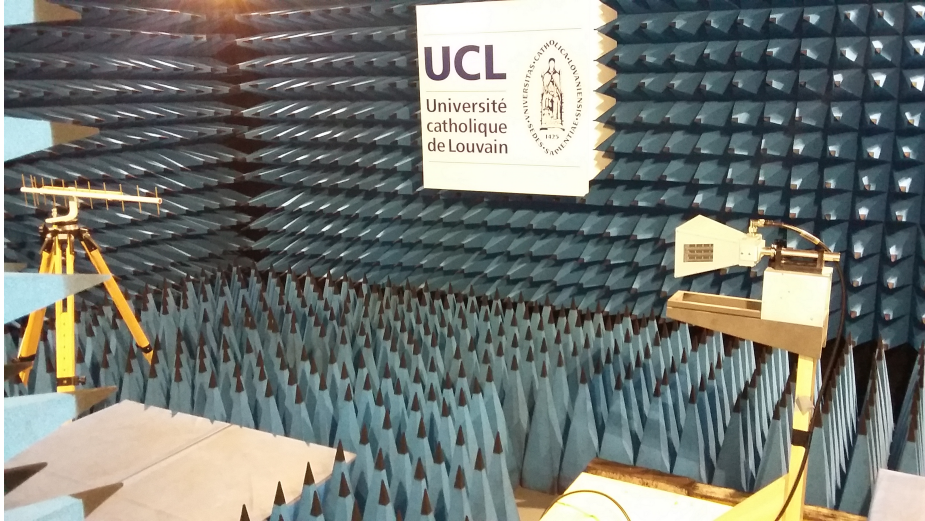


Figure 3.21: Experimental deconvolution results for test case 5.



(1) Reference environment



(2) Test environment

Figure 3.22: Experimental deconvolution setup for test case 6.

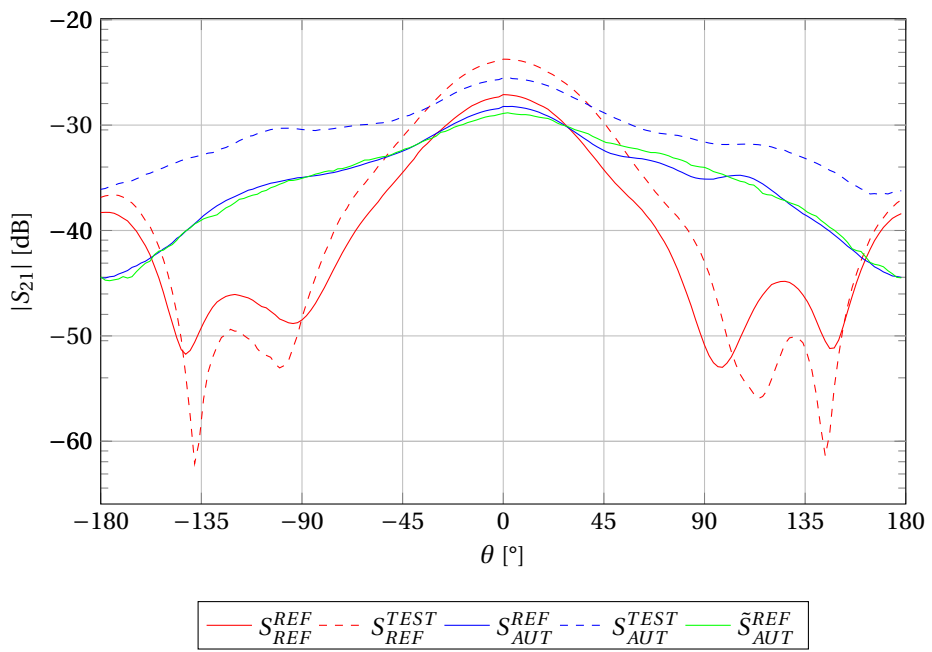


Figure 3.23: Experimental deconvolution results for test case 6.



PART

II

---

# ACTIVE SHAPING OF ELECTROMAGNETIC FIELDS



# Introduction: active shaping of electromagnetic fields

## 4.1 Introduction

THE optimal control of Partial Differential Equations (PDEs) is a very general concept, which consists in finding ways to drive the solution of the considered PDEs along or to a given trajectory or state. In particular, optimal control theory is applicable to PDEs describing wave propagation, such as the Maxwell's equations that describe the electromagnetic phenomena we are interested in. In the time domain, Maxwell's equations read

$$\vec{\nabla} \times \vec{E} = -\frac{\partial \vec{B}}{\partial t}, \quad (4.1)$$

$$\vec{\nabla} \times \vec{H} = \vec{J} + \frac{\partial \vec{D}}{\partial t}, \quad (4.2)$$

$$\vec{\nabla} \cdot \vec{D} = \rho, \quad (4.3)$$

$$\vec{\nabla} \cdot \vec{B} = 0, \quad (4.4)$$

where  $\vec{E}$  is the electric field [ $V/m$ ],  $\vec{B}$  is the magnetic induction [ $T$ ],  $\vec{H}$  is the magnetic field [ $A/m$ ],  $\vec{D}$  is the electric displacement [ $C/m^2$ ],  $\vec{J}$  is the current density [ $A/m^2$ ] and  $\rho$  is the charge density [ $C/m^3$ ]. Equations (4.1) to (4.4) are respectively Maxwell-Faraday's law, Maxwell-Ampere's law, Gauss' law and Gauss' magnetic law.

In what follows, we only consider linear, homogenous and isotropic media potentially including an imposed current density  $\vec{J}^0$  [ $A/m^2$ ], where the following constitutive laws hold

$$\vec{D} = \epsilon \vec{E}, \quad (4.5)$$

$$\vec{B} = \mu \vec{H}, \quad (4.6)$$

$$\vec{J} = \sigma \vec{E} + \vec{J}^0, \quad (4.7)$$

where  $\epsilon$  is the electric permittivity [ $F/m$ ],  $\mu$  the magnetic permeability [ $H/m$ ] and  $\sigma$  the

conductivity  $[S/m]$ . Combining these equations yields

$$\vec{\nabla} \times \vec{\nabla} \times \vec{E} + \epsilon\mu \frac{\partial^2 \vec{E}}{\partial t^2} + \mu\sigma \frac{\partial \vec{E}}{\partial t} = -\mu \frac{\partial \vec{j}^0}{\partial t}, \quad (4.8)$$

which in the time-harmonic regime can be restated in terms of the phasor fields  $\hat{E}, \hat{j}^0$

$$\vec{\nabla} \times \vec{\nabla} \times \hat{E} - k^2 \hat{E} - j\omega\mu\sigma \hat{E} = -j\omega\mu \hat{j}^0, \quad (4.9)$$

with  $k^2 = \omega^2 \epsilon\mu = \frac{\omega}{c}$ , where  $k$  is the wave number and  $c$  is the speed of light.

## 4.2 Hilbert Uniqueness Method

The control of electromagnetic waves in the time domain is rather complicated since a set of states must be found to drive a given system from an initial state  $A$  toward a final given state  $B$  in a given time  $T$ , each travelled state being directly controlled by the control element(s) over the time. A mathematical framework to build an appropriate control to drive such a system to a rest state has been proposed proposed by Lions, J. [107] and named Hilbert Uniqueness Method (HUM). Existence and unicity results for this method on the searched control and time  $T$  to reach the rest state have been demonstrated.

### 4.2.1 General principle

In order to get a qualitative understanding of HUM, let us consider the boundary control of the scalar wave equation. Given  $T$ , the scalar wave equation

$$\nabla^2 u - \frac{1}{c^2} \frac{\partial^2 u}{\partial t^2} = 0 \quad (4.10)$$

is considered in  $\Omega \times ]0, T[$ , with the initial conditions

$$y(\cdot, 0) = u^0, \quad \frac{\partial u}{\partial t}(\cdot, 0) = u^1. \quad (4.11)$$

The typical geometry of the problem is described in Fig. 4.1. We assume that the system can be modified using a Dirichlet boundary condition on  $\Gamma_c$ , a portion of  $\Gamma$  the boundary of  $\Omega$ , such that

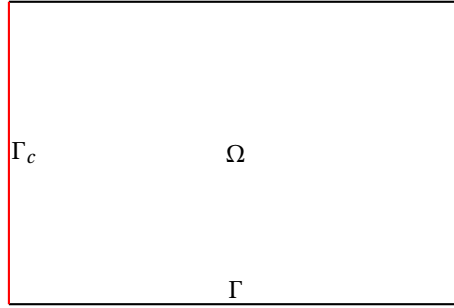
$$u = v \quad \text{on} \quad \Gamma_c \times ]0, T[, \quad (4.12)$$

with  $v$  the control function, whereas

$$u = 0 \quad \text{on} \quad \Gamma \setminus \Gamma_c \times ]0, T[. \quad (4.13)$$

---

[107] Lions, J. "Exact Controllability, Stabilization and Perturbations for Distributed Systems".

Figure 4.1: Exact control on  $\Omega$  by the boundary  $\Gamma_c$  using HUM.

Given  $T$ , we wish to find, if possible,  $v$  such that

$$u(\cdot, T) = 0, \quad \frac{\partial u}{\partial t}(\cdot, T) = 0, \quad (4.14)$$

i.e. the rest state at the given time  $T$ . The following system is introduced

$$\begin{cases} \nabla^2 \phi - \frac{1}{c^2} \frac{\partial^2 \phi}{\partial t^2} = 0 & \text{on } \Omega \times ]0, T[, \\ \phi(\cdot, 0) = \phi^0 & \text{on } \Omega, \\ \frac{1}{c} \frac{\partial \phi}{\partial t}(\cdot, 0) = \phi^1 & \text{on } \Omega, \\ \phi = 0 & \text{on } \Gamma \times ]0, T[, \end{cases} \quad (4.15)$$

which given appropriate  $\phi^0$  and  $\phi^1$  [107], (4.15) admits a single solution. It can be shown [109], [108] that the following problem is then solved

$$\begin{cases} \nabla^2 \psi - \frac{1}{c^2} \frac{\partial^2 \psi}{\partial t^2} = 0 & \text{on } \Omega \times ]0, T[, \\ \psi(\cdot, T) = 0 & \text{on } \Omega, \\ \frac{\partial \psi}{\partial t}(\cdot, T) = 0 & \text{on } \Omega, \\ \psi = \begin{cases} \partial \phi / \partial \vec{n} & \text{on } \Gamma \times (0, T), \\ 0 & \text{on } \Gamma \setminus \Gamma_c \times (0, T) \end{cases} \end{cases} \quad (4.16)$$

always admits at least a weak solution. Given  $\phi^0$  and  $\phi^1$ , the relation

$$\Lambda \{\phi^0, \phi^1\} = \left\{ \frac{\partial \psi}{\partial t}(\cdot, 0), -\psi(\cdot, 0) \right\} \quad (4.17)$$

is uniquely defined, and for  $T$  large enough, can be solved for  $\Psi$ . Indeed, given  $u^0$  and  $u^1$ , (4.15) is solved and the control function is chosen such that

$$v = \nabla \phi \cdot \vec{n} \quad \text{on } \Gamma \times (0, T). \quad (4.18)$$

[107] Lions, J. "Exact Controllability, Stabilization and Perturbations for Distributed Systems".

[109] Lions, J. et al. *Problèmes aux limites non homogènes et applications*.

[108] Lions, J. *Optimal control of systems governed by partial differential equations*.

Using (4.17), (4.18) and (4.16), we have

$$u(v) = \psi, \quad (4.19)$$

verifying (4.14). A control  $v$  has thus been constructed, driving the initial system to rest at time  $T$ .

Of course, since we have assumed  $T$  to be large enough, having a lower bound  $T_c$  on  $T$  would be interesting. Intuitively, the smaller  $\Gamma_c$  the larger  $T$  should be chosen. The Geometrical Control Condition (GCC) [10] has been introduced to allow an estimation of the minimum time  $T_c$  in which a system can be driven to rest. Assuming that  $\Omega$  is star-shaped with respect to  $\Gamma_c$ , it is shown that the GCC imposes a minimum time  $T_c$  such that

$$T_c > \frac{1}{c} \text{diameter } \Omega, \quad (4.20)$$

meaning that the minimal time  $T_c$  should allow a wave starting from the boundary control  $\Gamma_c$  to reach the farther point from  $\Omega$ .

**Electromagnetic waves** The control of Maxwell's equations follows the same principles [45]. The direct problem becomes

$$\left\{ \begin{array}{ll} \nabla \times \nabla \times \vec{\phi} - \frac{1}{c^2} \frac{\partial^2 \vec{\phi}}{\partial t^2} = 0 & \text{on } \Omega \times ]0, T[ , \\ \nabla \cdot \vec{\phi} = 0 & \text{on } \Omega \times ]0, T[ , \\ \vec{\phi}(\cdot, 0) = \vec{\phi}^0 & \text{on } \Omega , \\ \frac{1}{c} \frac{\partial \vec{\phi}}{\partial t}(\cdot, 0) = \vec{\phi}^1 & \text{on } \Omega , \\ \vec{\phi} \times \vec{n} = \begin{cases} \vec{g} & \text{on } \Gamma \times (0, T), \\ 0 & \text{on } \Gamma \setminus \Gamma_c \times (0, T). \end{cases} \end{array} \right. \quad (4.21)$$

The control  $\vec{g}$  is chosen such that

$$\vec{g} = -\nabla \times \vec{\psi}|_{\Gamma_c} \quad \text{on } \Gamma \times (0, T) \quad (4.22)$$

in which  $\vec{\psi}$  is the solution to the homogenous adjoint problem

$$\left\{ \begin{array}{ll} \nabla \times \nabla \times \vec{\psi} - \frac{1}{c^2} \frac{\partial^2 \vec{\psi}}{\partial t^2} = 0 & \text{on } \Omega \times ]0, T[ , \\ \nabla \cdot \vec{\psi} = 0 & \text{on } \Omega \times ]0, T[ , \\ \vec{\psi} \times \vec{n} = 0 & \text{on } \Gamma \times ]0, T[ , \\ \vec{\psi}(\cdot, 0) = \vec{\psi}^0 & \text{on } \Omega , \\ \frac{1}{c} \frac{\partial \vec{\psi}}{\partial t}(\cdot, 0) = \vec{\psi}^1 & \text{on } \Omega . \end{array} \right. \quad (4.23)$$

The initial values  $\vec{\psi}^0$  and  $\vec{\psi}^1$  yielding  $\vec{G}$  (4.22) thus verify

$$\Lambda \{ \vec{\psi}^0, \vec{\psi}^1 \} = \{ \vec{\phi}_1, -\vec{\phi}_0 \}. \quad (4.24)$$

[10] Bardos, C. et al. "Sharp Sufficient Conditions for the Observation, Control, and Stabilization of Waves from the Boundary".

[45] Darbas, M. et al. "Exact boundary controllability of the second-order Maxwell system: Theory and numerical simulation".

If  $T$  is large enough,  $\Lambda$  is invertible and the direct problem is once again solved. From a practical point of view, the most interesting thing to note comes from the control  $\vec{g}$  (4.22). Compared to the scalar control  $\nu$  (4.18), the gradient has been replaced by the curl operator, which seems rather natural when going from the scalar wave equation to the electromagnetic wave equation.

**Evolution towards an arbitrary state** By linearity, it is possible to reach any arbitrary state (assuming that it verifies the wave equation) at time  $T$ . The control value is then built by superimposing the control  $\nu$  bringing the system to the rest state and another control  $w$  bringing the system to the desired target state. This control  $w$  is built by solving the same adjoint problem (4.16) with different initial conditions. More precisely, finding  $\nu$  implies to solve (4.16) backward, but here on the contrary, the time reversed value of  $w$  is found by solving backward a time reversed version of (4.16), which leads to a forward solving. In practice, it means that the operator  $\Lambda$  remains the same to find  $\nu$  and  $w$ .

#### 4.2.2 Numerical examples

HUM has been implemented numerically, following [72], [129], [32], through the FEM on the scalar wave equation using MATLAB.

The following steps are used to find a control  $\nu$  driving the considered system to rest at time  $T$ :

1. Assembly of  $\Lambda$ : For each node of a finite element mesh  $\vec{x}_0$  of  $\Omega$ , the following couple is formed  $\{\phi^0, \phi^1\} = \{\delta(\vec{x} - \vec{x}_0), \delta(\vec{x} - \vec{x}_0)\}$ , and the following is applied
  - “Forward” resolution ( $0 \rightarrow T$ ) of (4.15) ( $\phi$ ),
  - Computation of the normal derivative of  $\phi$  ( $\frac{\partial \phi}{\partial \vec{n}}$ ),
  - “Backward” resolution ( $T \rightarrow 0$ ) of (4.16) with the boundary condition  $\psi = \frac{\partial \phi}{\partial \vec{n}}$  on  $\Gamma_c$ .

Each column of  $\Lambda$  is finally composed of  $\left\{ \frac{\partial \psi}{\partial t}(\cdot, 0), -\psi(\cdot, 0) \right\}$ .

2. Computation of  $\phi^0$  and  $\phi^1$  by solving the system (4.17),
3. Computation of  $\nu$  on  $\Gamma_c$  by using  $\phi^0$  and  $\phi^1$  in (4.18):
  - “Forward” resolution ( $0 \rightarrow T$ ) of (4.15) for the couple  $\{\phi^0, \phi^1\}$  obtained from the previous step,

---

[72] Glowinski, R. et al. “A numerical approach to the exact boundary controllability of the wave equation (I) Dirichlet controls: Description of the numerical methods”.

[129] Rasmussen, J. M. “Boundary Control of Linear Evolution PDEs - Continuous and Discrete”.

[32] Castro, C. et al. “Numerical approximation of the boundary control for the wave equation with mixed finite elements in a square”.

- Computation of the normal derivative of  $\phi$  on  $\Gamma_c$  ( $\nu = \frac{\partial\phi}{\partial\bar{n}}$ ).

As a first example, in Fig. 4.2, the evolution towards a rest state of a wave enclosed in a square domain has been reported at different instants. The right pictures show the behavior with the boundary control  $\nu$  enabled, whereas the left pictures illustrate the evolution without applying any control, for comparison. In both cases, a centered Gaussian pulse with a null time derivative is used as initial situation. Clearly, the applied control  $\nu$  drives the system toward the desired state i.e. rest state. The final time  $T$  has been set to 66 ns. The controlling boundary  $\Gamma_c$  is restricted to one side of the bounding square, while the other edges are set to 0.

In the second example, illustrated in Fig. 4.3, the same system, with the same initial situation is used, but is driven toward two different states (only the initial and the final states are illustrated for conciseness). The first state (“A”) is another Gaussian pulse and the second state (“B”) is a plane wave, both reached at time  $T = 66$  ns. Of course, the obtained fields are only obtained at time  $T = 66$  ns, and are not maintained for  $t > T = 66$  ns, contrary to the rest state that lasts “forever”.

**Distributed control** To conclude this chapter dedicated to HUM, we propose a last example in which the boundary control has been replaced by a distributed control inside  $\Omega$ . In the example, illustrated in Fig. 4.4, two control points are used to drive the system from a Gaussian pulse modulated by a sinusoid toward an annular Gaussian pulse, with standard deviation  $s$  and radius  $R$

$$S_n(r) = \frac{I_0\left(\frac{Rr}{s^2}\right)}{I_0\left(\frac{R^2}{s^2}\right)} e^{-\frac{R^2-r^2}{2s^2}}, \quad (4.25)$$

where  $r = \sqrt{x^2 + y^2}$ , and  $I_\alpha$  is the Bessel function of the second kind [1].

Once again, HUM has been able to find the right control time sequence to drive the system from the initial state to the target state in the given time  $T = 500$  ns. It should be emphasized, once again, that when a non rest state is reached at time  $T$ , the wave propagation inevitably continues such that the reached state is only transient.

While the above results, obtained on a square domain discretized with a few thousand of finite elements, nicely illustrate the applicability of HUM in a simple setting, the numerics of applying HUM to more realistic and larger configurations are actually quite subtle. It is known that numerical algorithms for the boundary control of wave equations may indeed diverge when the mesh size tends to zero, due to high-frequency spurious oscillations [72]. While various regularization techniques have been proposed

---

[1] Abramowitz, M. et al. *Handbook of Mathematical Functions: With Formulas, Graphs, and Mathematical Tables*.

[72] Glowinski, R. et al. “A numerical approach to the exact boundary controllability of the wave equation (I) Dirichlet controls: Description of the numerical methods”.

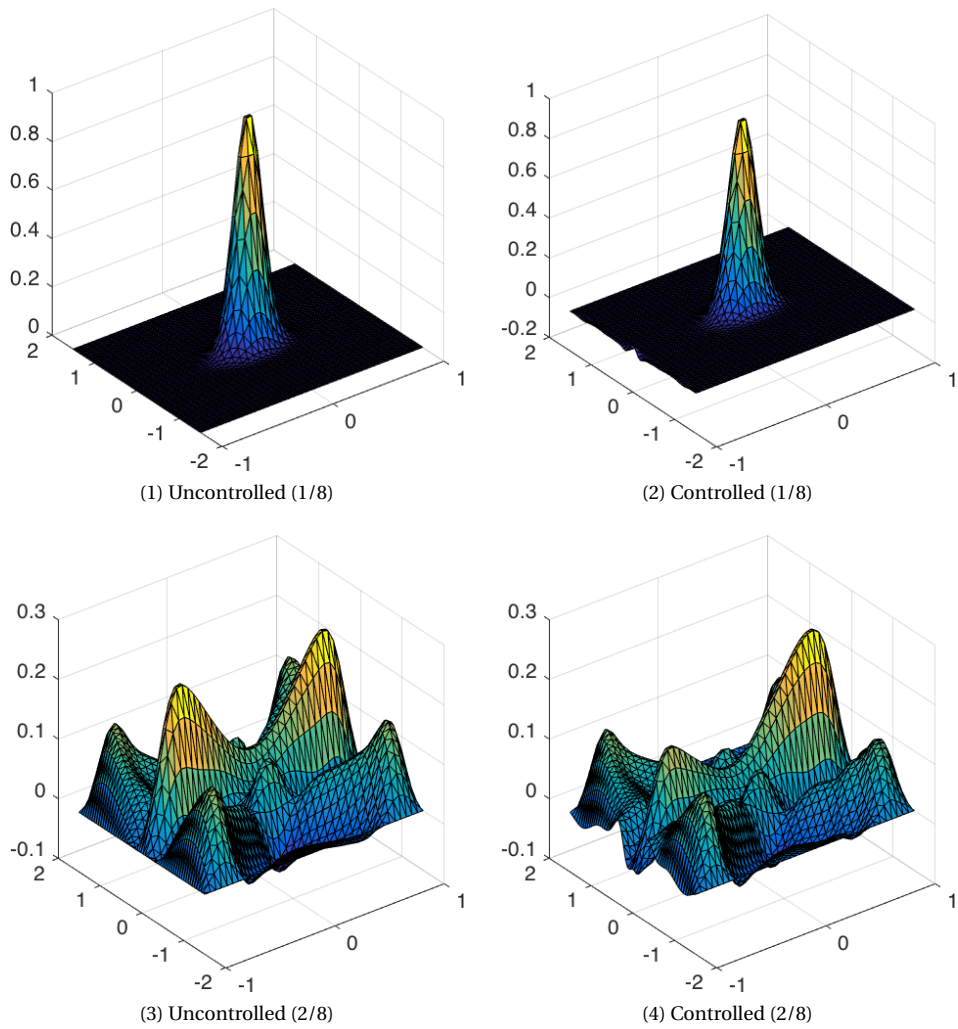


Figure 4.2: Boundary control of the scalar wave equation in a 2D cavity to reach a null field at time  $T$  ( $1/4$ ).

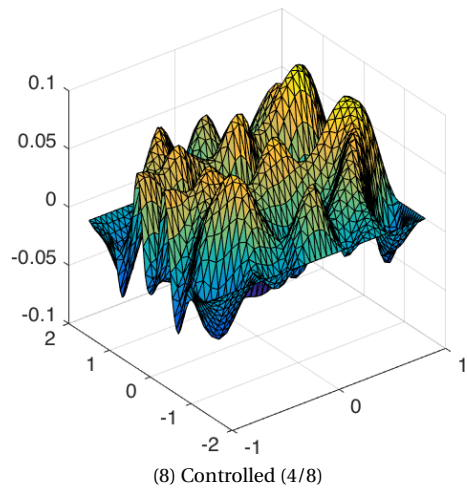
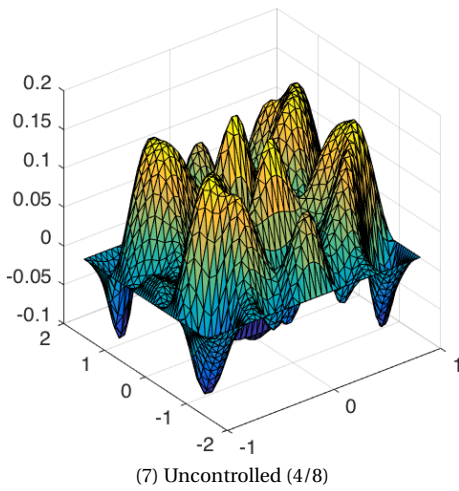
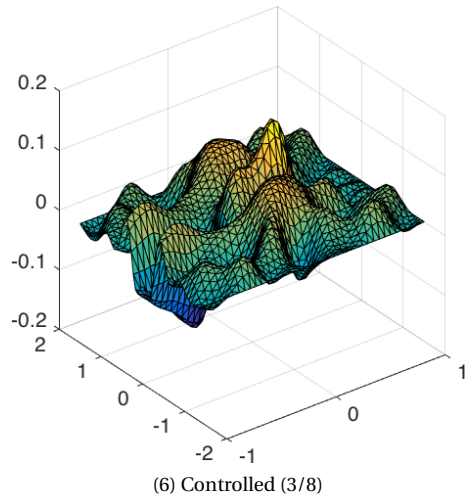
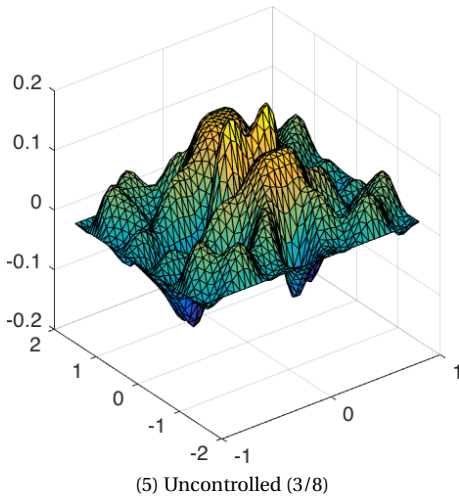


Figure 4.2: Boundary control of the scalar wave equation in a 2D cavity to reach a null field at time  $T$  (2/4).

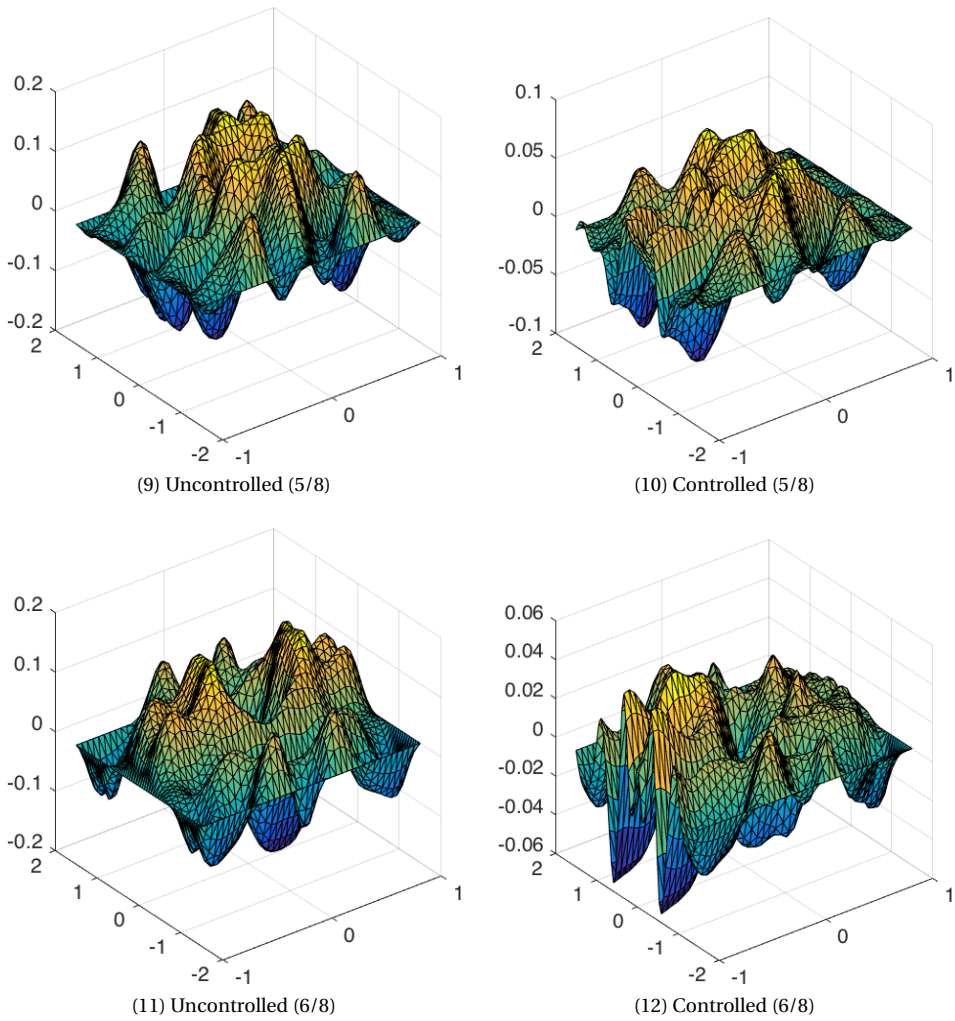
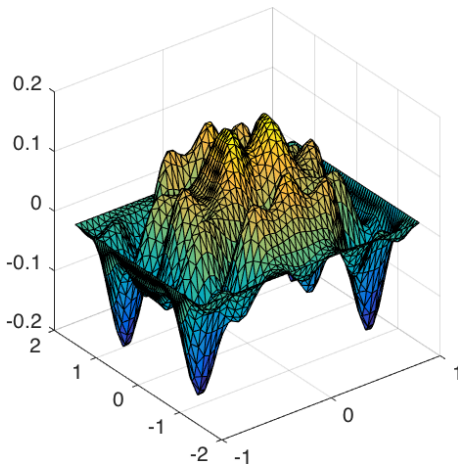
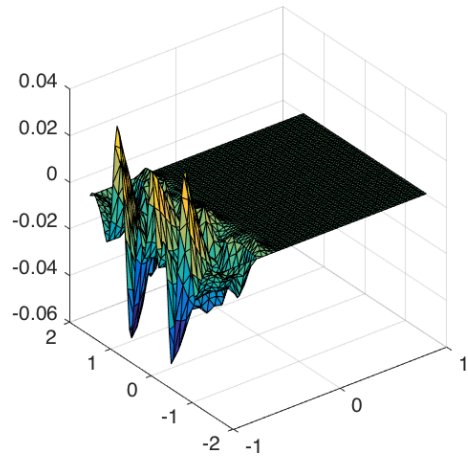


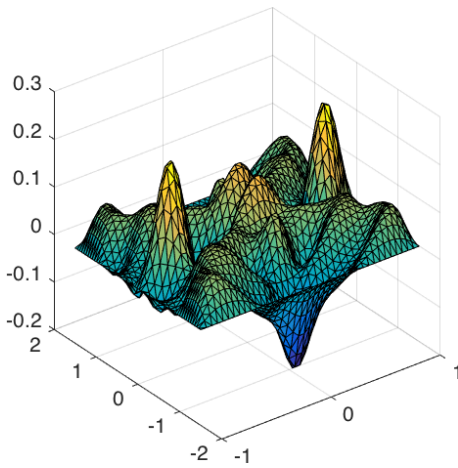
Figure 4.2: Boundary control of the scalar wave equation in a 2D cavity to reach a null field at time  $T$  ( $3/4$ ).



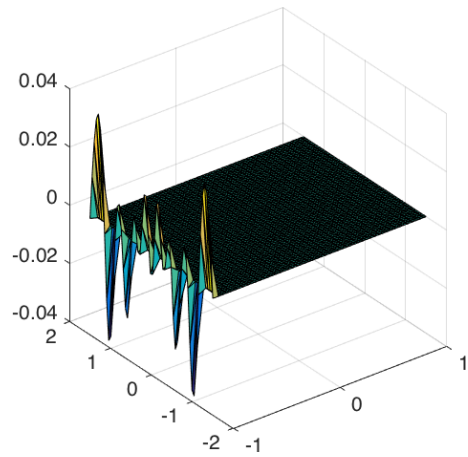
(13) Uncontrolled (7/8)



(14) Controlled (7/8)



(15) Uncontrolled (8/8)



(16) Controlled (8/8)

Figure 4.2: Boundary control of the scalar wave equation in a 2D cavity to reach a null field at time  $T$  (4/4).

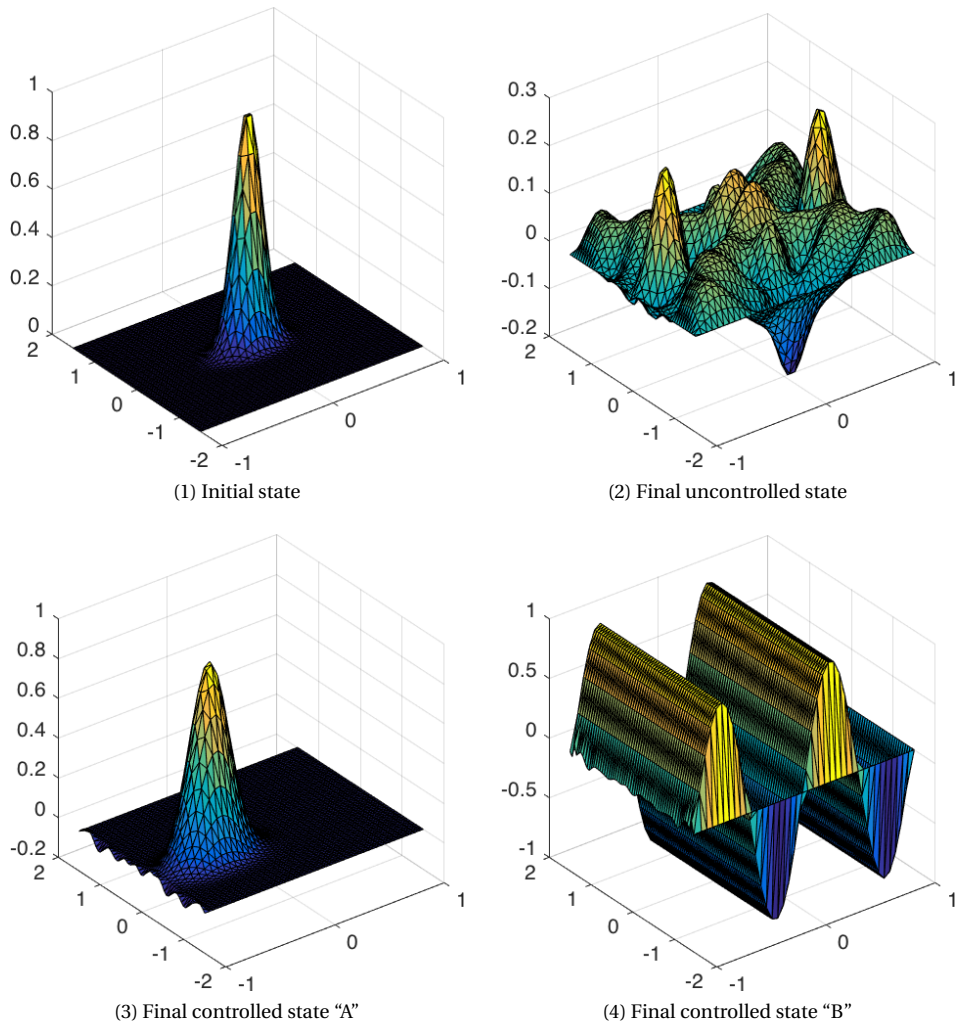


Figure 4.3: Boundary control of the scalar wave equation in a 2D cavity to reach a Gaussian pulse ("A") or a sine ("B") field at time  $T$ .

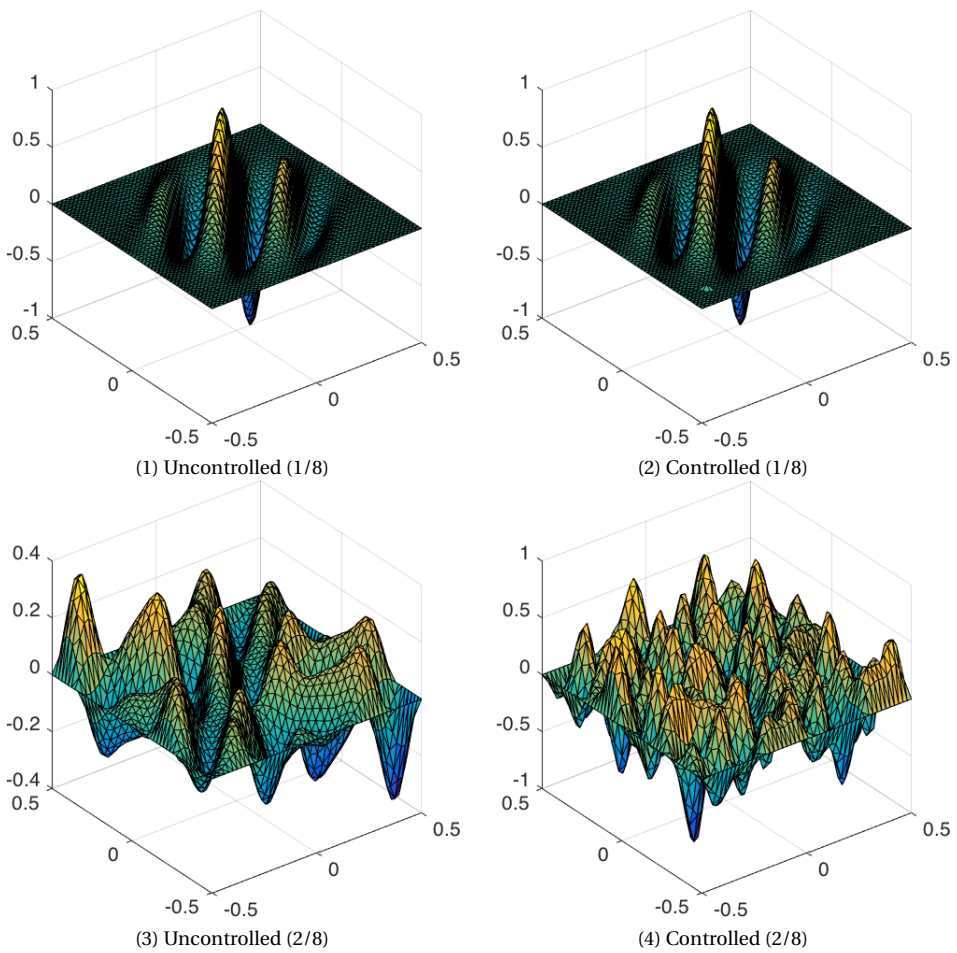


Figure 4.4: Inner control of the scalar wave equation in a 2D cavity to reach an annular Gaussian field at time  $T$  ( $1/4$ ).

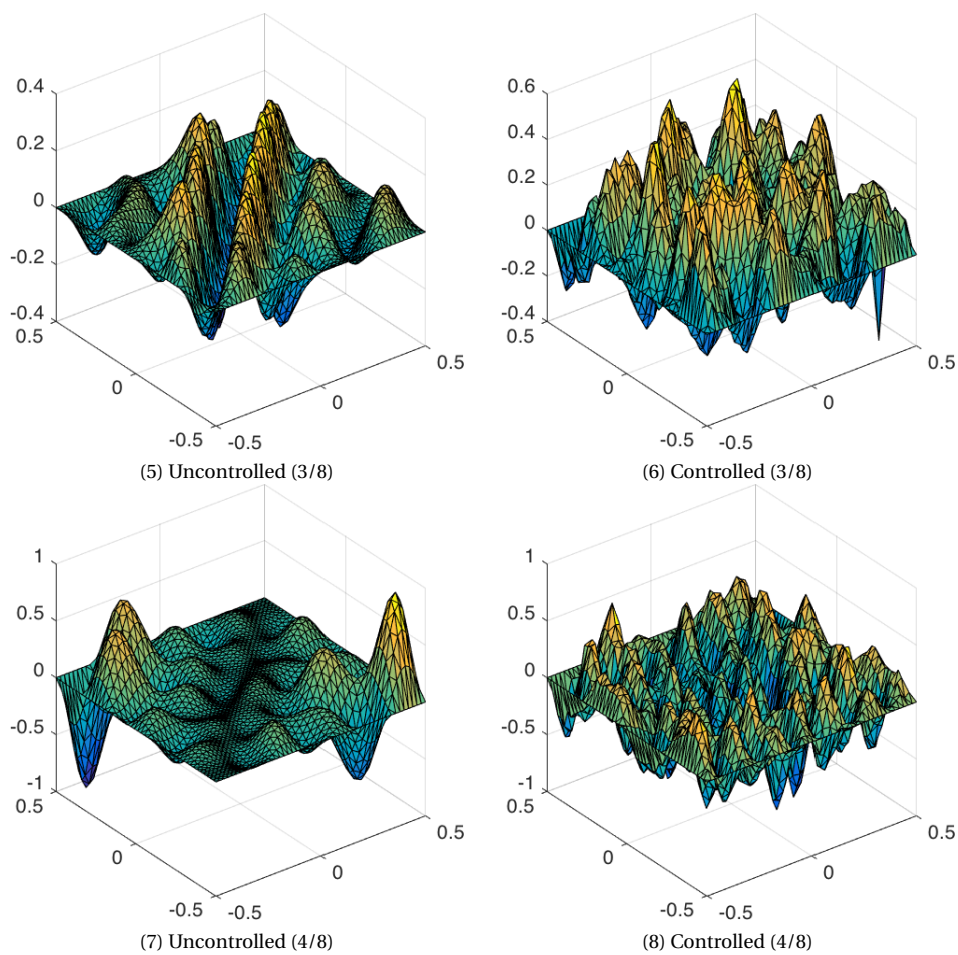


Figure 4.4: Inner control of the scalar wave equation in a 2D cavity to reach an annular Gaussian field at time  $T$  (2/4).

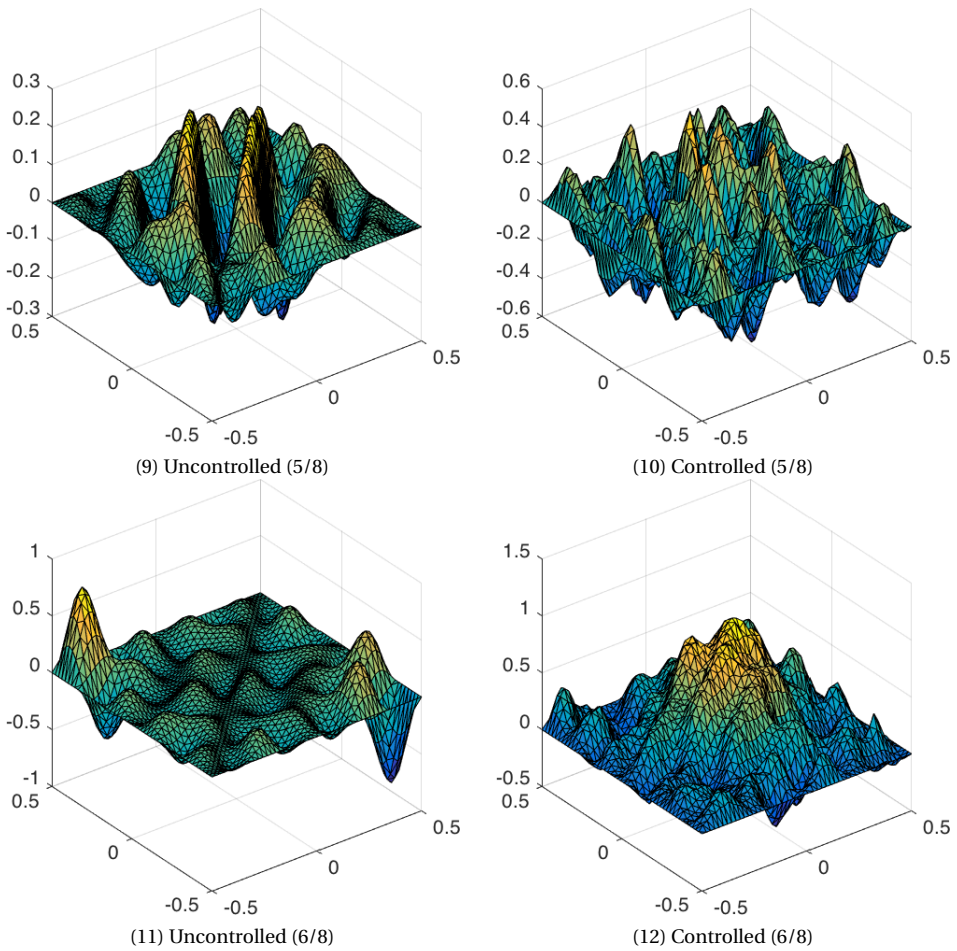


Figure 4.4: Inner control of the scalar wave equation in a 2D cavity to reach an annular Gaussian field at time  $T$  ( $3/4$ ).

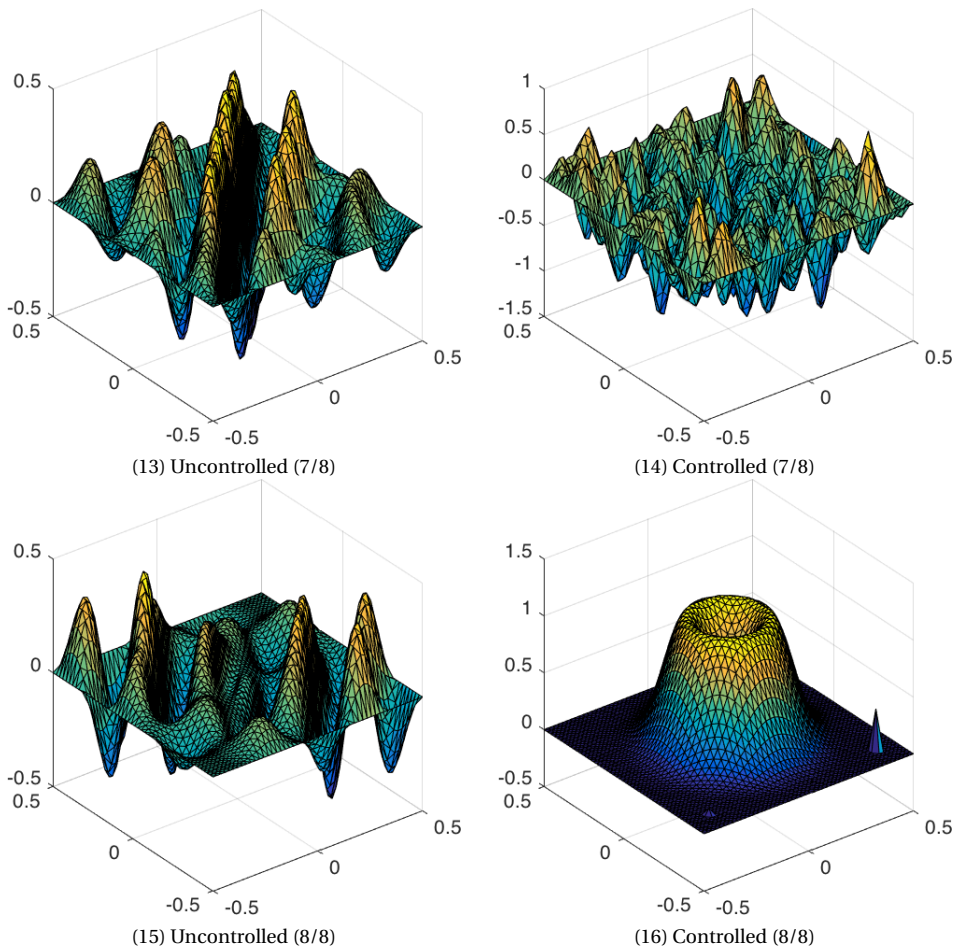


Figure 4.4: Inner control of the scalar wave equation in a 2D cavity to reach an annular Gaussian field at time  $T$  (4/4).

[98], [72], [75], [24], [2], the robustness of the procedure with respect to time  $T$  and the discretized geometry is still under investigation. More fundamentally, the applicability of HUM for the active shaping of Ultra High Frequency (UHF) electromagnetic fields is hampered by two practical aspects. First, to achieve a reasonable control time  $T$ , the bandwidth of generators required to produce the control signals, either on the boundary or distributed in the target domain, is very large and out of reach of most common EMC generators and amplifiers. Second, the successful application of HUM requires the knowledge of the (transient) noise in the system, which in practice is seldom achievable.

This motivates the study of a less general control technique based on Time Reversal (TR) which is inherently robust with respect to noise in lossless media.

### 4.3 Time Reversal

---

Originally proposed for acoustic waves by M. Fink in [59],[60] and transposed by G. Lerosey [104], [105] for electromagnetic waves, the TR method relies on the wave equation time-reversal symmetry. Precisely, this property is obtained when the phenomenon described by a time dependant PDE remains unchanged when replacing the time variable  $t$  by its opposite  $-t$ . In lossless media, i.e. for  $\sigma = 0$ , the wave equation (4.8) has the time-reversal symmetry which leads to that a time reversed wave follows exactly the same path as the direct wave did, propagating back toward the source of the direct wave itself.

The principles of TR are summarized hereafter. We consider a source of emission located at a point  $o$  in free-space, surrounded by a virtual closed surface  $S$  bounding a volume  $V$  (Fig. 4.5). The theoretical TR operation is performed in four steps:

1. The source located in  $o$  radiates after being excited by a current density  $\vec{j}^0$ ,
2. The electromagnetic wave that reaches the surface  $S$  is recorded in order to be time reversed,
3. The surface  $S$  emits the reversed electromagnetic wave (the source is inactive:  $\vec{j}^0 = 0$ ),
4. The emitted electromagnetic wave refocuses on the point  $o$ , like an image of the reversed current density  $\vec{j}^0$ .

---

[98] Lebeau, G. et al. "Experimental Study of the HUM Control Operator for Linear Waves".

[72] Glowinski, R. et al. "A numerical approach to the exact boundary controllability of the wave equation (I) Dirichlet controls: Description of the numerical methods".

[75] Hansen, P. *Rank-Deficient and Discrete Ill-Posed Problems*.

[24] Briggs, W. et al. *A Multigrid Tutorial, Second Edition*.

[2] Alabau-Boussouira, F. et al. *Control of Partial Differential Equations*.

[59] Fink, M. "Time reversal of ultrasonic fields. I. Basic principles".

[60] Fink, M. "Time-reversed Acoustics".

[104] Lerosey, G. et al. "Time reversal of electromagnetic waves."

[105] Lerosey, G. "Retournement temporel d'ondes électromagnétiques et application à la télécommunication en milieux complexes".

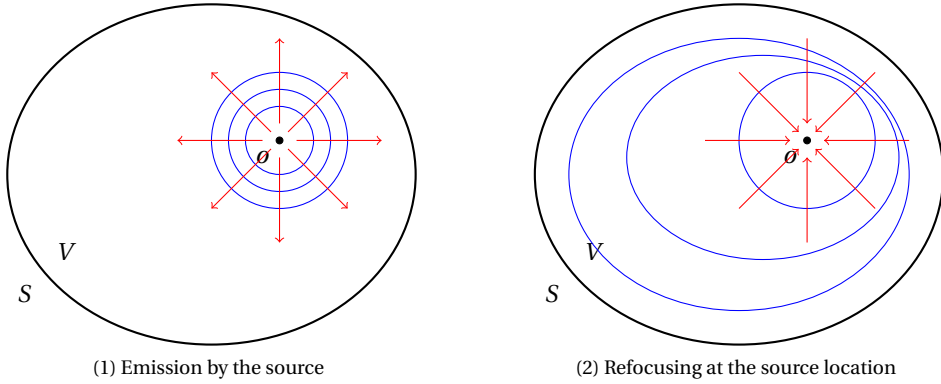


Figure 4.5: Theoretical TR.

As demonstrated in [61], TR allows energy space-time focusing at the source. TR actually uses the environment as a self-matched filter, as physically, there is never any back-propagation of waves [55],[54].

We propose to apply hereafter the TR method theoretically for an electromagnetic source located in free-space [137], [26]. The original development for acoustic waves can be found in [31].

### 4.3.1 Time Reversal in free-space for harmonic sources

**Step 1: Source radiation** The solution of (4.9) in free-space ( $\sigma = 0$ ) can be found by introducing the dyadic Green function  $\vec{\vec{G}}$  solution of the problem

$$\vec{\nabla} \times \vec{\nabla} \times \vec{\vec{G}} - k^2 \vec{\vec{G}} = -\delta \vec{I} \quad (4.26)$$

where  $\delta$  is the Dirac distribution and  $\vec{I}$  the identity tensor. Multiplying (4.26) on the left by  $\hat{\vec{E}}$  and on the right by  $\vec{C}$  and subtracting (4.9) premultiplied by  $\vec{\vec{G}} \cdot \vec{C}$ , brings

$$\vec{\nabla} \times \vec{\nabla} \times \hat{\vec{E}} \cdot \vec{\vec{G}} \cdot \vec{C} - \hat{\vec{E}} \cdot \vec{\nabla} \times \vec{\nabla} \times \vec{\vec{G}} \cdot \vec{C} = -j\omega\mu\hat{\vec{J}}^0 \cdot \vec{\vec{G}} \cdot \vec{C} + \delta \hat{\vec{E}} \cdot \vec{I} \cdot \vec{C}, \quad (4.27)$$

where  $\vec{C}$  is an arbitrary real non-zero vector. The left hand side of (4.27) is then reexpressed, using

$$\vec{\nabla} \cdot (\vec{A} \times \vec{B}) = \vec{B} \cdot \vec{\nabla} \times \vec{A} - \vec{A} \cdot \vec{\nabla} \times \vec{B} \quad (4.28)$$

[61] Fink, M. et al. "Acoustic time-reversal mirrors".

[55] Dyab, W. et al. "Antenna reciprocity and the theory of electromagnetic time reversal".

[54] Dyab, W. M. G. et al. "A Critical Look at the Principles of Electromagnetic Time Reversal and its Consequences".

[137] Scott, I. "Developments in time-reversal of electromagnetic fields using the transmission-line modelling method".

[26] Carminati, R. et al. "Theory of the time reversal cavity for electromagnetic fields".

[31] Cassereau, D. et al. "Time-reversal of ultrasonic fields. III. Theory of the closed time-reversal cavity".

such that

$$\vec{\nabla} \times \vec{\nabla} \times \hat{\vec{E}} \cdot \vec{\vec{G}} \cdot \vec{C} - \hat{\vec{E}} \cdot \vec{\nabla} \times \vec{\nabla} \times \vec{\vec{G}} \cdot \vec{C} = \vec{\nabla} \cdot \vec{\nabla} \times \hat{\vec{E}} \times \vec{\vec{G}} \cdot \vec{C} - \vec{\nabla} \cdot \vec{\nabla} \times \vec{\vec{G}} \cdot \vec{C} \times \hat{\vec{E}}. \quad (4.29)$$

Integrating (4.27) on a volume  $V$  and using (4.29) leads to

$$\int_V \vec{\nabla} \times \vec{\nabla} \times \hat{\vec{E}} \cdot \vec{\vec{G}} \cdot \vec{C} - \hat{\vec{E}} \cdot \vec{\nabla} \times \vec{\nabla} \times \vec{\vec{G}} \cdot \vec{C} dV = \int_V -j\omega\mu \hat{\vec{J}}^0 \cdot \vec{\vec{G}} \cdot \vec{C} + \delta \hat{\vec{E}} \cdot \vec{\vec{I}} \cdot \vec{C} dV. \quad (4.30)$$

The divergence theorem is applied on the left hand side of (4.30), for  $S$  a closed surface bounding  $V$

$$\int_V \vec{\nabla} \times \vec{\nabla} \times \hat{\vec{E}} \cdot \vec{\vec{G}} \cdot \vec{C} - \hat{\vec{E}} \cdot \vec{\nabla} \times \vec{\nabla} \times \vec{\vec{G}} \cdot \vec{C} dV = \int_S \vec{\nabla} \times \hat{\vec{E}} \times \vec{\vec{G}} \cdot \vec{C} - \vec{\nabla} \times \vec{\vec{G}} \cdot \vec{C} \times \hat{\vec{E}} d\vec{S}, \quad (4.31)$$

with  $d\vec{S} = \vec{n} dS$ ,  $\vec{n}$  being the outgoing unit normal to  $S$ . The right hand side of (4.30) is simplified using the Dirac distribution properties

$$\int_V -j\omega\mu \hat{\vec{J}}^0 \cdot \vec{\vec{G}} \cdot \vec{C} + \delta \hat{\vec{E}} \cdot \vec{\vec{I}} \cdot \vec{C} dV = \int_V -j\omega\mu \hat{\vec{J}}^0 \cdot \vec{\vec{G}} \cdot \vec{C} dV + \hat{\vec{E}} \cdot \vec{C}. \quad (4.32)$$

Finally, an expression of  $\hat{\vec{E}}$  in the direction of  $\vec{C}$  is found by using (4.31) and (4.32) in (4.30)

$$\hat{\vec{E}} \cdot \vec{C} = j\omega\mu \int_V \hat{\vec{J}}^0 \cdot \vec{\vec{G}} \cdot \vec{C} dV + \int_S \vec{\nabla} \times \hat{\vec{E}} \times \vec{\vec{G}} \cdot \vec{C} - \vec{\nabla} \times \vec{\vec{G}} \cdot \vec{C} \times \hat{\vec{E}} d\vec{S}, \quad (4.33)$$

which expresses the electric field within the volume  $V$  in function of the current source (the first term) and in function of the flux crossing the boundary surface  $S$  (the second term). Furthermore, assuming that both  $\vec{\vec{G}}$  and  $\vec{E}$  behaves like outgoing waves on  $S$  [26] (i.e. having dependance of the form  $e^{-jk(\|\vec{r}-\vec{r}'\|)} / (\|\vec{r}-\vec{r}'\|)$ ,  $r'$  being the distance to the source), the integrand in (4.33) vanishes, such that we obtain

$$\hat{\vec{E}} \cdot \vec{C} = j\omega\mu \int_V \hat{\vec{J}}^0 \cdot \vec{\vec{G}} \cdot \vec{C} dV. \quad (4.34)$$

**Step 2: Time reversal of the electric field** The field (4.34) is now time reversed, or equivalently complex conjugated in the frequency domain (denoted by  $\cdot^*$ )

$$\hat{\vec{E}}^* \cdot \vec{C} = -j\omega\mu \int_V \hat{\vec{J}}^{0*} \cdot \vec{\vec{G}}^* \cdot \vec{C} dV. \quad (4.35)$$

**Step 3: Surface radiation** A time reversed electric field distribution is now propagating from the boundary surface  $S$  into the inner volume  $V$ , without source. An incoming wave condition is observed on  $S$  for  $\vec{\vec{G}}$  and  $\hat{\vec{E}}$  preventing this time any vanishing of the integrand in (4.33). Actually, the step is the same as step 1, but with  $\vec{J} = 0$  and using the complex conjugate  $\vec{E}^*$  since the field has been time-reversed

$$\vec{\nabla} \times \vec{\nabla} \times \hat{\vec{E}}^* - k^2 \hat{\vec{E}}^* = 0. \quad (4.36)$$

Finally, an expression of  $\hat{\vec{E}}^*$  in the direction of  $\vec{C}$ , similar to (4.33) without the source term, is obtained

$$\hat{\vec{E}}^* \cdot \vec{C} = \int_S \vec{\nabla} \times \hat{\vec{E}}^* \times \vec{\vec{G}} \cdot \vec{C} - \vec{\nabla} \times \vec{\vec{G}} \cdot \vec{C} \times \hat{\vec{E}}^* d\vec{S}. \quad (4.37)$$

**Step 4: Refocusing at the source location** The refocused electric field  $\vec{E}_R$  at the source location is exactly the same as in (4.37)

$$\hat{\vec{E}}_R \cdot \vec{C} = \int_S \vec{\nabla} \times \hat{\vec{E}}^* \times \vec{G} \cdot \vec{C} - \vec{\nabla} \times \vec{G} \cdot \vec{C} \times \hat{\vec{E}}^* d\vec{S}. \quad (4.38)$$

Now, to relate the complex conjugate field  $\vec{E}^*$  of the direct field to  $\vec{E}_R$ , we simply use the same procedure as in step 1, leading to (4.33), but considering the complex conjugate of the equation (4.9), to obtain

$$\hat{\vec{E}}^* \cdot \vec{C} = -j\omega\mu \int_V \hat{\vec{J}}^{0*} \cdot \vec{G} \cdot \vec{C} dV + \int_S \vec{\nabla} \times \hat{\vec{E}}^* \times \vec{G} \cdot \vec{C} - \vec{\nabla} \times \vec{G} \cdot \vec{C} \times \hat{\vec{E}}^* d\vec{S}. \quad (4.39)$$

Subtracting (4.39) from (4.38) yields

$$\hat{\vec{E}}_R \cdot \vec{C} - \hat{\vec{E}}^* \cdot \vec{C} = j\omega\mu \int_V \hat{\vec{J}}^{0*} \cdot \vec{G} \cdot \vec{C} dV, \quad (4.40)$$

which can be finally reworked, using the complex conjugate of (4.34), to derive

$$\begin{aligned} \hat{\vec{E}}_R \cdot \vec{C} &= j\omega\mu \int_V \hat{\vec{J}}^* \cdot (\vec{G} - \vec{G}^*) \cdot \vec{C} dV \\ &= -2\omega\mu \int_V \hat{\vec{J}}^{0*} \cdot \Im(\vec{G}) \cdot \vec{C} dV. \end{aligned} \quad (4.41)$$

The final expression of the refocused electric field is then, since (4.41) is valid for any non-null  $\vec{C}$

$$\hat{\vec{E}}_R = -2\omega\mu \int_V \hat{\vec{J}}^{0*} \cdot \Im(\vec{G}) dV. \quad (4.42)$$

**Refocused electric field for monochromatic space impulse source** Using Dirac source of the form

$$\hat{\vec{J}}_I^* = \delta(\|\vec{r} - \vec{r}'\|) \hat{\vec{J}}^*, \quad (4.43)$$

with the free-space Green function

$$\vec{G}_I = \frac{e^{-jk(\|\vec{r} - \vec{r}'\|)}}{\|\vec{r} - \vec{r}'\|} \vec{I}, \quad (4.44)$$

the expression (4.42) becomes

$$\begin{aligned} \hat{\vec{E}}_R(r') &= -2\omega\mu \int_V \hat{\vec{J}}_I^* \cdot \Im(\vec{G}_I) dV \\ &= -2\omega\mu \hat{\vec{J}}^{0*} \Im\left(\frac{e^{-jk\|\vec{r} - \vec{r}'\|}}{\|\vec{r} - \vec{r}'\|}\right) \vec{I} \end{aligned} \quad (4.45)$$

$$= 2\omega\mu k \hat{\vec{J}}^{0*} \frac{\sin k\|\vec{r} - \vec{r}'\|}{k\|\vec{r} - \vec{r}'\|} \vec{I}. \quad (4.46)$$

The refocused field is thus proportional to the original conjugated source, modulated by a cardinal sine, centered at the source, and whose spreading depends on the wave number of the source, and thus of the frequency.

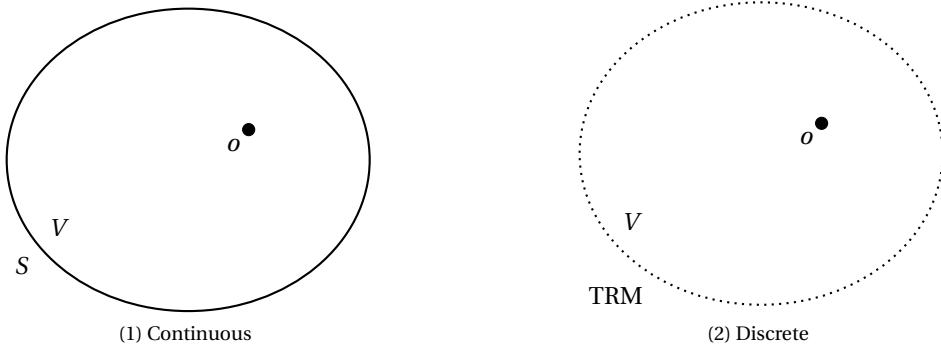


Figure 4.6: Discretization of the TRM.

### 4.3.2 Time Reversal Mirror

In practice, the surface  $S$  should be able to record, reverse and re-emit any crossing electromagnetic wave is replaced by a finite number of antennas. These antennas, assimilated to a collection of point-wise emitters and receivers forms the so called Time Reversal Mirror (TRM) [132] (Fig. 4.6).

The number of elements making up the TRM have of course an impact on the quality of the refocused field. Generally, using a large number of elements will produce a more accurate refocused field compared to the original conjugated source ( $\hat{J}^0$ ). A comparison of a generated field using the continuous (integral) model against the discrete (sum) model is given in Fig. 4.7. In this example, a TRM composed of 128 elements is numerically equivalent to the integral continuous form.

Knowing the Green function for free-space, it is straightforward to apply a TR operation using the analytical formula. For illustration purposes, we have applied the TR steps in a two-dimensional setting where the electric field has a single non zero component perpendicular to the plane:

$$\hat{E}_z(\vec{r}) = K_0(Jk \|\vec{r}\|) \hat{J}_z, \quad (4.47)$$

where  $K_0$  is the modified Bessel function of the second kind (the Green function),  $k$  is the wave number and  $\vec{J}_z^0$  is the current source density at the origin  $\vec{r} = (0, 0)$ . The refocused field, generated by the  $N$  elements of the TRM arranged in circle of radius  $R$  and center  $(0, 0)$  is

$$\hat{E}_R(\vec{r}) = \sum_{i=1}^N K_0(Jk \|\vec{r} - \vec{r}_i\|) \hat{E}_{z,i}^* \Delta\phi, \quad (4.48)$$

where  $r_i$  is the distance from the  $i$ -th source of the TRM to the origin and  $\Delta\phi = \frac{2\pi R}{N}$ .

In Fig. 4.8, the refocused field using (4.48) is shown for two different frequencies. The expected behavior from (4.46) is observed, with a smaller focal spot for the highest frequency.

[132] Rosny, J. de et al. "Theory of Electromagnetic Time-Reversal Mirrors".

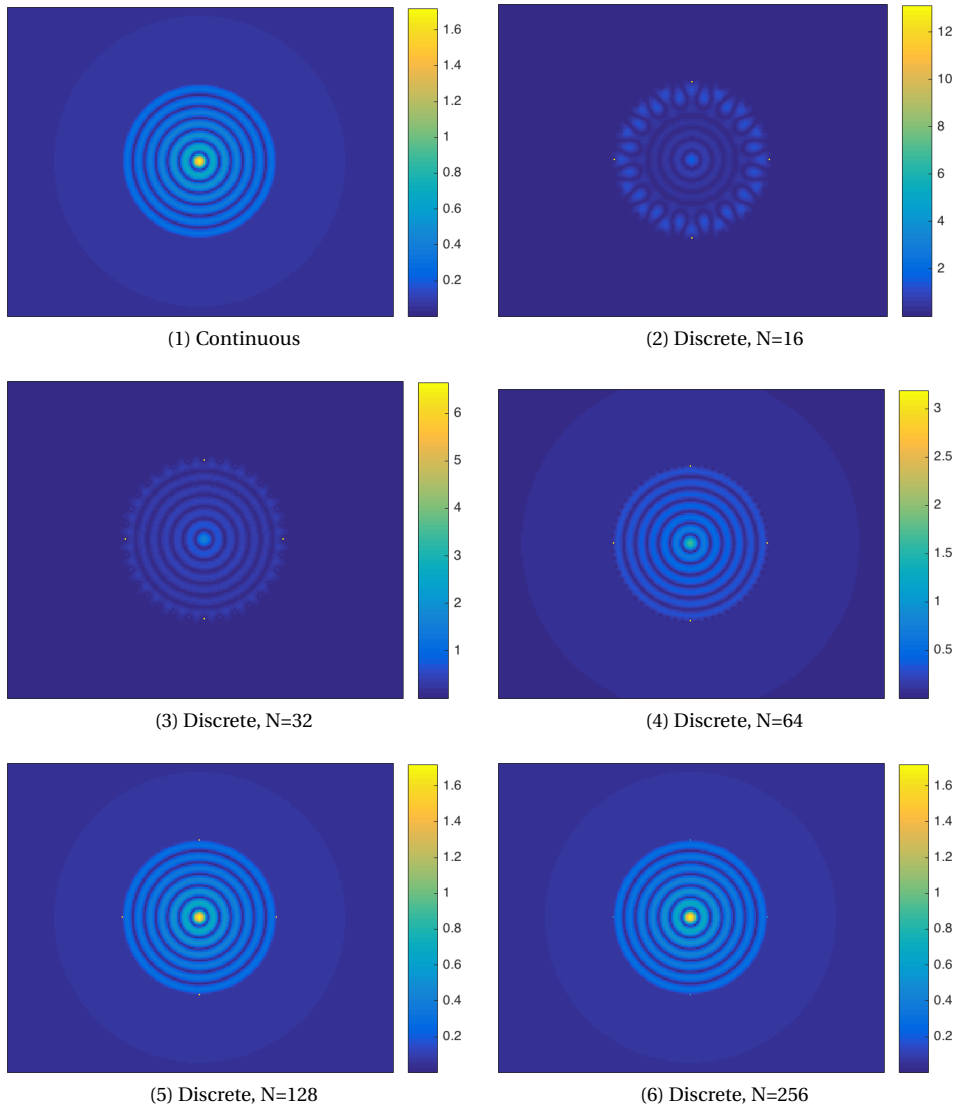
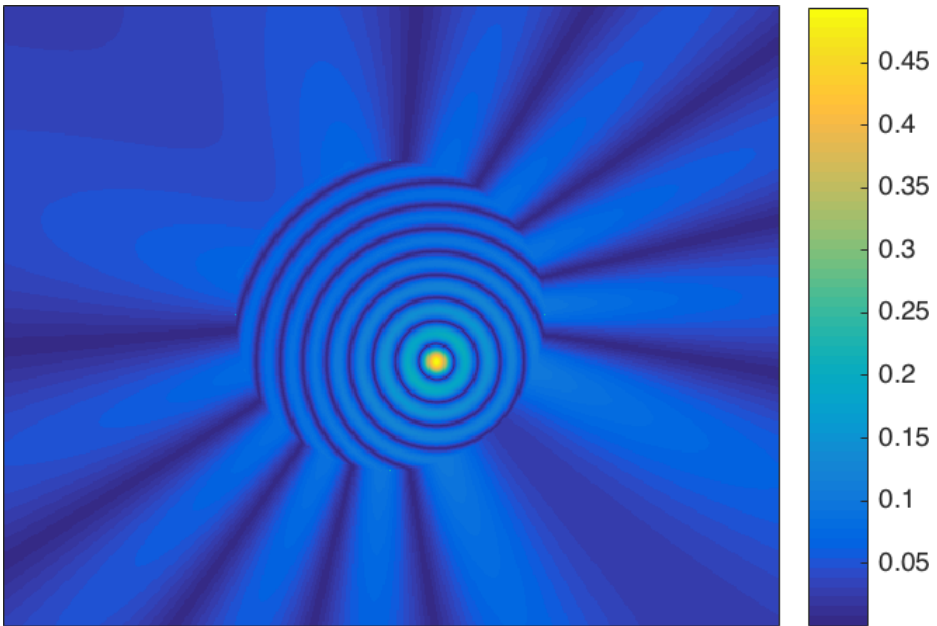
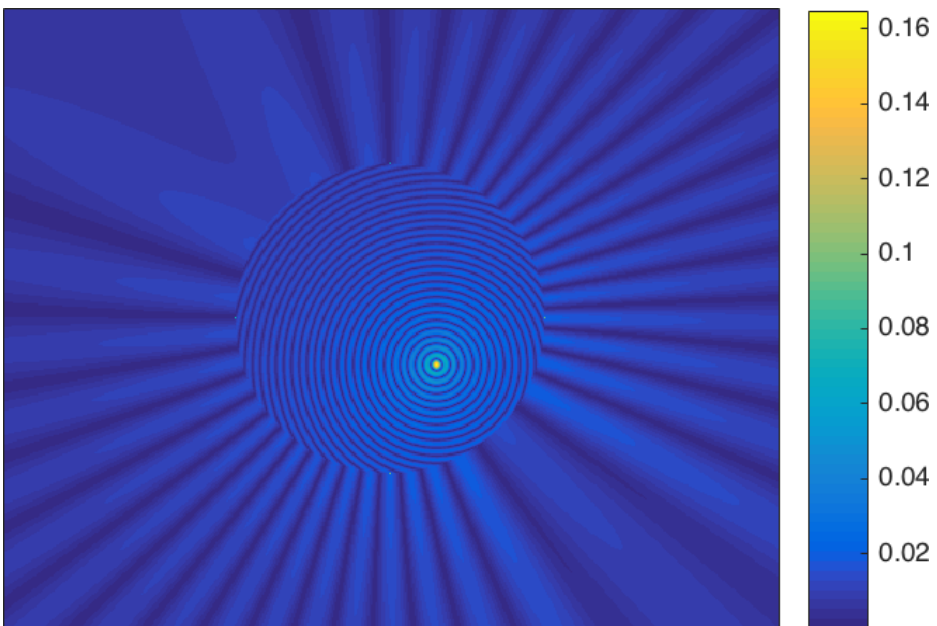


Figure 4.7: Comparison of TR refocusing between a continuous ideal TRM and a discrete TRM for different TRM elements at 1 GHz in free-space.



(1) 1 GHz



(2) 3 GHz

Figure 4.8: Comparison of the TR refocusing with a fixed TRM of 360 elements at 2 different frequencies in free-space.

An important issue from a practical point of view is the number of elements composing the TRM. As stated in [61], a spacing between the TRM elements of at most  $\frac{\lambda}{2}$  is suitable but not mandatory (a sampling greater than  $\frac{\lambda}{2}$  may introduce grating lobes). This is in adequation with the classical sampling criterion for electromagnetic fields [91], [157]. As seen in Fig. 4.9, the number of TRM elements, keeping the TRM radius constant ( $R = 1$  m), does not impact the focal spot width, but rather the background noise level.

**Virtual increase of the Time Reversal Mirror number of elements** The number of TRM elements has a rather large impact on the space-time refocusing. However, using a large number of transducers in the time domain is a limiting factor due to the experimental complexity of such a system. Indeed, for each transducer, dedicated electronics should record, reverse and emit the needed signals. Furthermore, all the signals should also be synchronously emitted, which is a rather complex task with several signals. For practical purposes, the TRM should thus contain as few transducers as possible without altering the quality of the refocused signal and maintaining a low background noise level. In the previous example (Fig. 4.9), we have seen that using a TRM made of 64 elements for a radius of 1 m was satisfactory. Although using 64 transducers in acoustics is possible [156], it is much more complicated for electromagnetic waves in the UHF range and it requires specific instruments to sample, process and emit all the signals synchronously.

Interestingly, it has been shown in [49], for elastic waves, that using a single element TRM in a reflective cavity could lead to excellent space-time refocusing. Similarly, for electromagnetic waves, using a reverberating cavity, i.e. a reverberating room, provides an adequate multipath environment to reduce the number of TRM elements [47]. This behavior can be explained using the image current theory [77], in which any dipole moment placed in a PEC or Perfect Magnetic Conductor (PMC) ground plane neighborhood can be replaced by the same dipole moment plus an additional dipole moment of the appropriate amplitude and orientation, as detailed in Fig. 4.10 (the ground plane is thus removed). This behavior is an extension of the well-known *method of image charges*, by considering two distant charges forming a dipole moment. Similarly, the image theory is thus also applicable for moving charges, and thus for currents [5].

The same theory is applicable with several ground planes, and thus directly applicable with a rectangular (or parallelepipedic) cavity. Due to the multiple ground planes, each image current of order  $n$  generates multiple image currents of different order, forming

---

[61] Fink, M. et al. "Acoustic time-reversal mirrors".

[91] Joy, E. et al. "Spatial sampling and filtering in near-field measurements".

[157] Yaghjian, A. "An overview of near-field antenna measurements".

[156] Wu, F. et al. "Time reversal of ultrasonic fields. II. Experimental results".

[49] Draeger, C. et al. "One-Channel Time Reversal of Elastic Waves in a Chaotic 2D-Silicon Cavity".

[47] Davy, M. et al. "Focusing and amplification of electromagnetic waves by time-reversal in an leaky reverberation chamber".

[77] Harrington, R. *Time-Harmonic Electromagnetic Fields*.

[5] Amador, E. "Modèles de compréhension par la théorie des images des phénomènes transitoires et du régime permanent en chambre réverbérante électromagnétique".

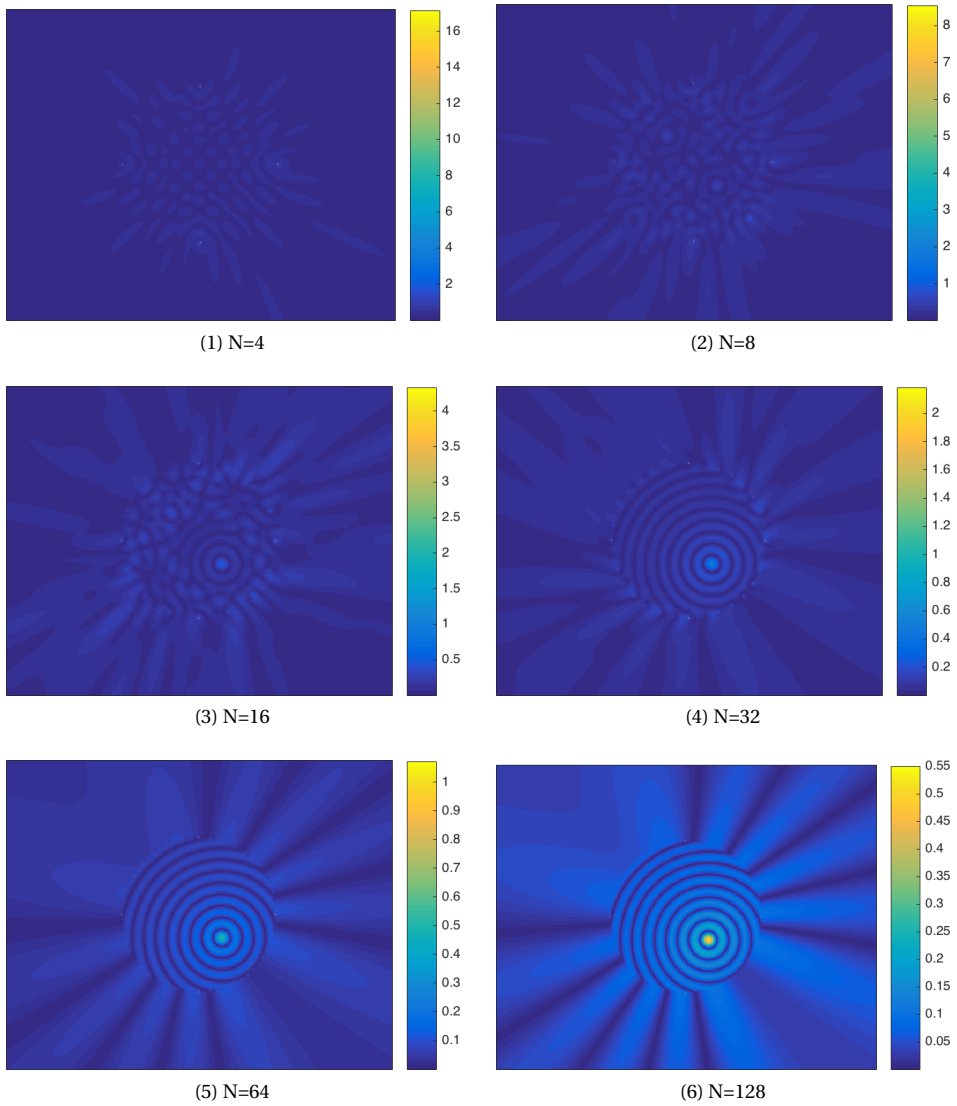


Figure 4.9: Comparison of TR refocusing with different numbers of TRM elements at 1 GHz in free-space.

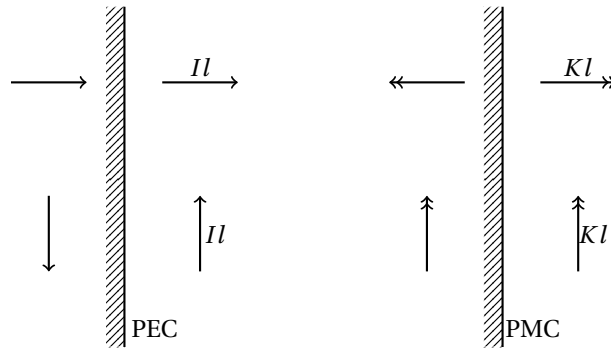


Figure 4.10: Image current theory principles for a PEC (left) or a PMC (right) ground plane.  $Il$  is the electric dipole moment and  $Kl$  is the magnetic dipole moment.

for example, the illustrated pattern in Fig. 4.11 for a 2D cavity up to the 5<sup>th</sup> order (PEC). Furthermore, the method is still applicable in a lossy reverberation chamber by introducing a damping factor  $R$  [4], [3] multiplying the amplitude of each current such that the image currents of orders  $n$  are defined by

$$I_n = I_0 R^n \quad \text{with} \quad 0 < R < 1, \quad (4.49)$$

where  $I_0$  is the source current. Higher order images have thus lower and lower amplitudes.

The value of  $R$  can be determined experimentally from the time constant  $\tau$  of the cavity and then using the formula

$$R \approx e^{-\frac{L}{2c\tau}}, \quad (4.50)$$

where  $c$  is the speed of light and  $L$  is the mean distance between two successive reflections. Typically, an experimental value of  $R \approx 0.99$  is found. The introduction of wall losses should be carefully taken into account since the environment is not, in this case, completely reversible [48]. Walls made of good conductors generally have very good quality factors  $Q$  and thus long time constant  $\tau$  with minimal losses such that the environment is still reversible [138]. The impact is different if the propagation media itself has significant losses, as opposed to vacuum or air.

Fig. 4.11 clearly illustrates the virtual increase of the number of TRM elements in a reverberating cavity. Any element of the TRM in the cavity actually induces several images, improving thus the space-time refocusing quality. A numerical method based on image theory was proposed in [141] for TR in reverberating cavities.

[4] Amador, E. et al. "Studying the pulse regime in a reverberation chamber with a model based on image theory".

[3] Amador, E. et al. "Reverberation Chamber Modeling Based on Image Theory: Investigation in the Pulse Regime".

[48] De La Gorgue de Rosny, J. "Milieux réverbérants et réversibilité".

[138] Scott, I. et al. "Time Reversal in Lossy Material: An Assessment."

[141] Spirlet, M. et al. "Modelling time reversal applications in a reverberation chamber using the current image method".

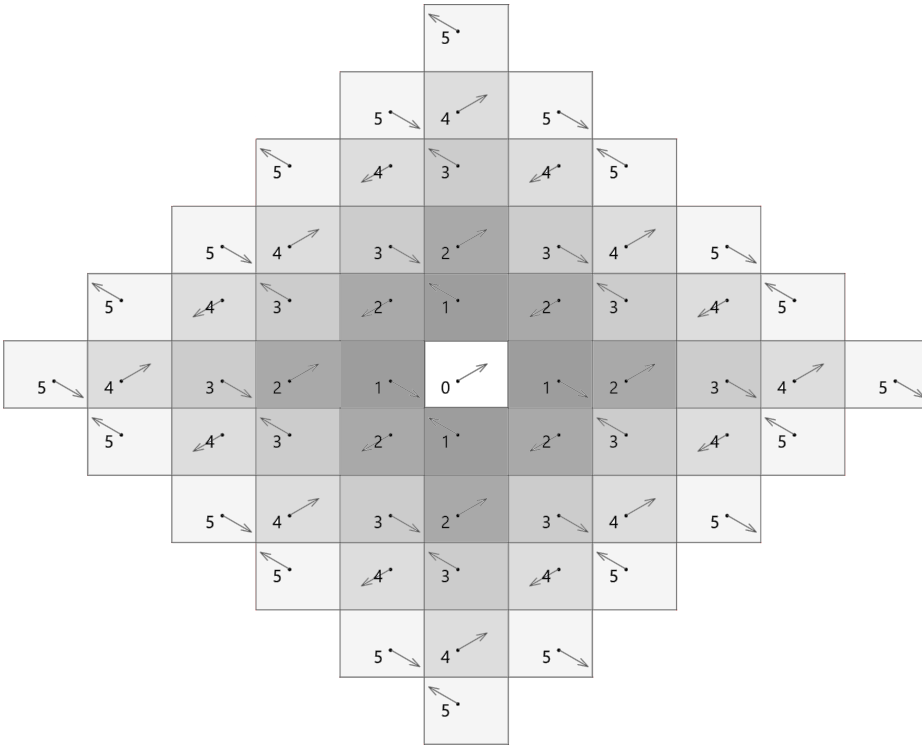


Figure 4.11: Illustration of the image currents distribution in a 2D cavity up to the 5<sup>th</sup> order.

### 4.3.3 Time Reversal in reverberating cavities for pulsed sources

Let us now consider TR in the time domain by considering pulses fitted to appropriate frequency bandwidths. Although the shape of the generated pulses used for the sources is arbitrary, the fitting parameters are mostly dictated by the needed frequency spectrum. A Gaussian pulse is particularly suited for this purpose, since the Fourier transform of a Gaussian pulse is also a Gaussian pulse. The time domain signal of a Gaussian pulse, of amplitude  $A$ , centered on the time value  $t_c$ , with a frequency bandwidth of  $\Delta f$  and centered on the frequency  $f_c$  is given by

$$p_G(t) = A \cos(2\pi f_c(t - t_c)) e^{-\frac{5 \log_{10} e}{|\Delta f|} ((t - t_c)\pi \Delta f)^2}, \quad (4.51)$$

while its corresponding spectrum magnitude is

$$|P_G(f)| = A' e^{-\frac{|\Delta f|}{5 \log_{10} e} \left(\frac{f - f_c}{\Delta f}\right)^2}. \quad (4.52)$$

In Fig. 4.12, a Gaussian pulse of 500 MHz bandwidth and 1 GHz centered is plotted, with its frequency spectrum. The bandwidth is generally chosen at  $-3$  dB, corresponding

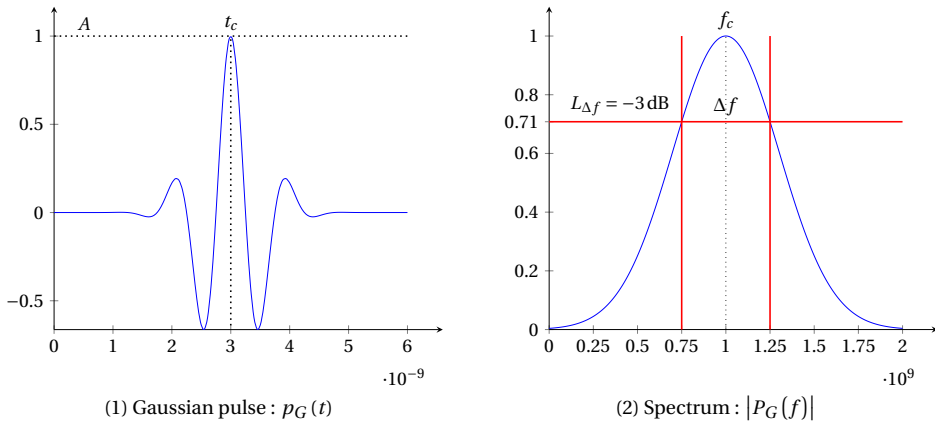


Figure 4.12: Gaussian pulse in the time domain and its corresponding spectrum.

thus to a factor of 0.708 of linear attenuation compared to the maximum value. Due to the phase shift to the desired center frequency  $f_c$ , the time domain Gaussian pulse is thus modulated by a cosine of the same frequency.

We have used the FEM solver GetDP [52] to solve the full-wave problem of electromagnetic wave propagation inside a reverberation cavity as the complexity of the Green's functions in a cavity makes it less amenable to analytic calculations. A Newmark scheme [122] is used for the time iterations. In Fig. 4.13-1, a 2 element TRM is used (bottom left and top right) to refocus energy on a spot near the center of the cavity, which is bounded by PEC walls. Since the emitted front wave is a Gaussian pulse centered at 1 GHz with a 500 MHz bandwidth, the refocused wave front is thus the same reversed Gaussian pulse. The same operation was performed in Fig. 4.13-2 but with a TRM composed of 8 elements. The behavior of the refocusing, in function of the number of TRM elements, is the same as in Fig. 4.9 for free-space, except that the number of elements is lower. Actually, more than one element is needed in the TRM to provide high quality refocusing [38],[41], [42], [39], since a rectangular cavity is "straight" and does not provide a fully chaotic environment [73]. It also worth noting that, in the cavity, the elements of the TRM does not need to physically bound the source for the method to work. The TRM efficiency can be optimized by acting on its element locations and

[52] Dular, P. et al. "A general environment for the treatment of discrete problems and its application to the finite element method".

[122] Newmark, N. "A Method of Computation for Structural Dynamics".

[38] Cozza, A. "Statistics of the performance of time reversal in a lossy reverberating medium".

[41] Cozza, A. et al. "Enforcing a deterministic polarization in a reverberating environment".

[42] Cozza, A. et al. "Polarization selectivity for pulsed fields in a reverberation chamber".

[39] Cozza, A. "The Role of Losses in the Definition of the Overmoded Condition for Reverberation Chambers and Their Statistics".

[73] Gros, J.-B. "Spatial statistics of open chaotic cavities : Applications to electromagnetic cavities".

on the recording duration of the incoming signals [57].

**Time Reversal Electromagnetic Chamber** A disadvantage of the TR method is its need of a source: without an emitting source, there is no energy refocusing. This is problematic for applications where a source cannot be positioned at the location of the wished refocusing. Typically, in an EMC radiated immunity test, since the EUT is not supposed to radiate intentionally, a classical TR method will not work. To solve this problem, a second antenna network is built around the passive EUT as a source for the TR operation, in addition to the antenna network forming the TRM. This antenna network is called the Equivalent Surface Network (ESN), and allows to generate a radiation instead of an EUT placed in the center of this circular network [119], [120], [121], by applying the equivalence principle [77] illustrated in Fig. 4.14. Indeed, the equivalence principle states that the electromagnetic field outside a volume  $V$  bounded by a surface  $S$ , produced by some inner sources  $\vec{J}$  and  $\vec{M}$  remain identical if the inner sources are replaced by surface currents  $\vec{J}_s$ ,  $\vec{M}_s$  on  $S$  with a null electromagnetic field inside  $V$ . Actually, the equivalence principle is more general, since, it basically states that several source distributions outside a given region  $\bar{V}$  can produce an equivalent electromagnetic field inside the region  $\bar{V}$ . The equivalent surface  $S$  is then discretized to form the ESN.

The combination of a metallic enclosure cavity, a TRM and an ESN define a so-called Time Reversal Electromagnetic Chamber (TREC). Such a TREC making use of multipath propagation, allows to some extent to generate controlled wavefronts in complex environments. Another method called Linear Combination of Configuration Fields (LCCF) method has been proposed in [14], [12] and [13], also inspired by the TR method, provides similar assets for active shaping of electromagnetics fields.

**Using the Time Reversal Electromagnetic Chamber** A TR operation in the TREC is achieved exactly the same way as “normal” TR, by performing the 4 following steps [121] illustrated in Fig. 4.16:

1. A signal  $x(t)$  is emitted by the ESN such that each element is fed by the signal  $\alpha_j^k x(t)$  with  $\alpha_j^k$  the weight of the element  $j$  of the ESN in the polarization  $k$  (i.e. a vertical or horizontal polarization selection).

---

[57] Feng, J. et al. “Amplification of electromagnetic waves by time reversal mirror in a leaky reverberation chamber”.

[119] Moussa, H. et al. “Directive Wavefronts Inside a Time Reversal Electromagnetic Chamber”.

[120] Moussa, H. et al. “Experimental demonstration of directive pulsed wavefront generation in reverberation chambers”.

[121] Moussa, M. “Etude théorique et expérimentale des techniques de retournement temporel application à la caractérisation de composants et dispositifs dans une chambre réverbérante”.

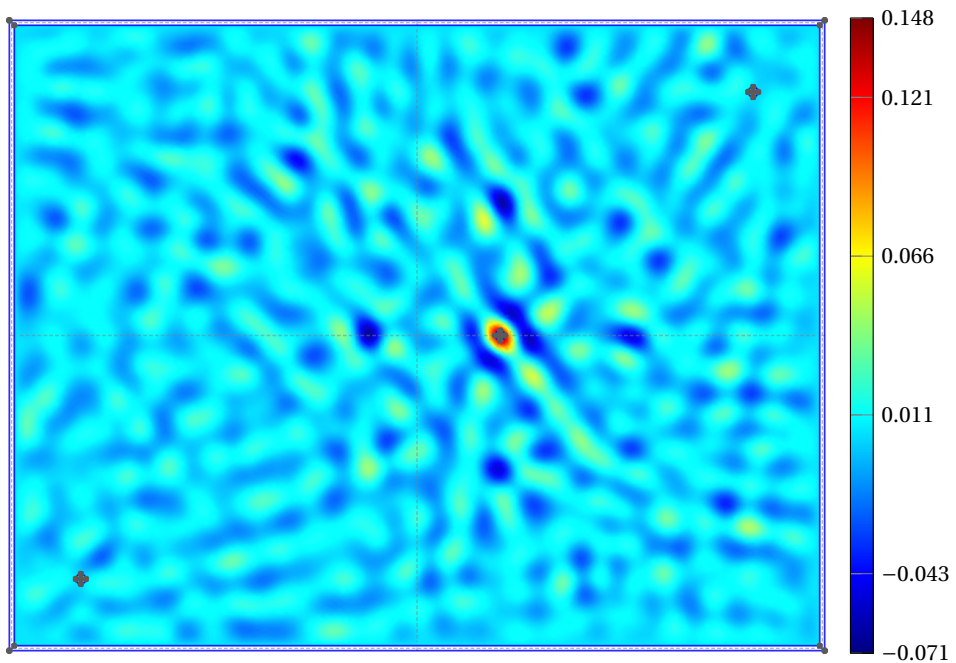
[77] Harrington, R. *Time-Harmonic Electromagnetic Fields*.

[14] Benoit, J. et al. “Source identification in time domain electromagnetics”.

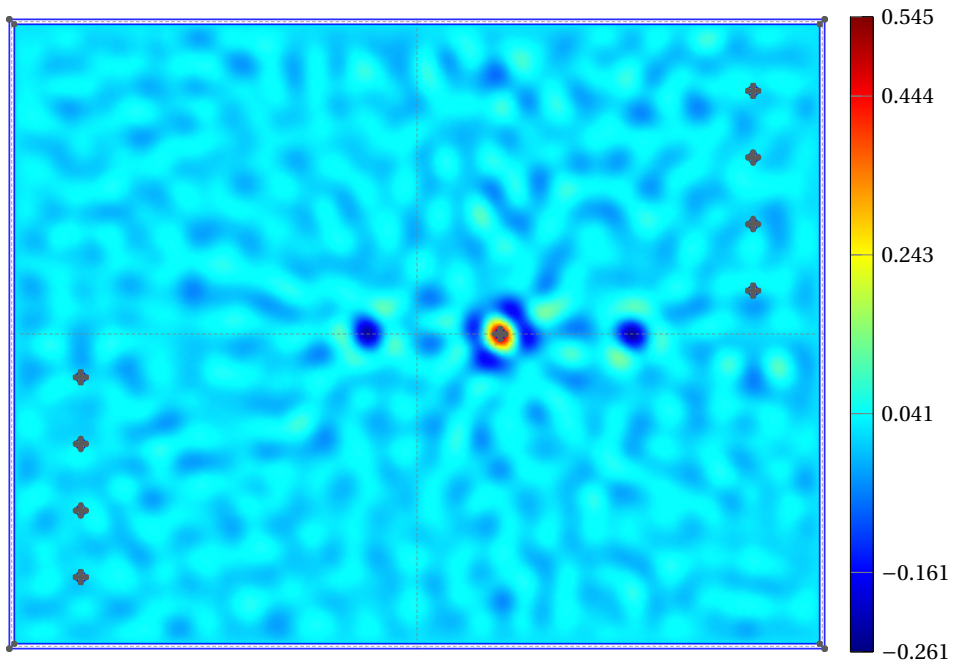
[12] Benoit, J. et al. “A new technique to obtain a specific electromagnetic field at a given time”.

[13] Benoit, J. et al. “Identification de sources temporelles pour des problèmes de lignes de transmission”.

[121] Moussa, M. “Etude théorique et expérimentale des techniques de retournement temporel application à la caractérisation de composants et dispositifs dans une chambre réverbérante”.



(1) N=2



(2) N=8

Figure 4.13: Comparison of the TR refocusing ( $E_z(t = t_R)$ ) with different numbers of TRM elements for a Gaussian pulse centered at 1 GHz with a 500 MHz bandwidth in a reverberating cavity.

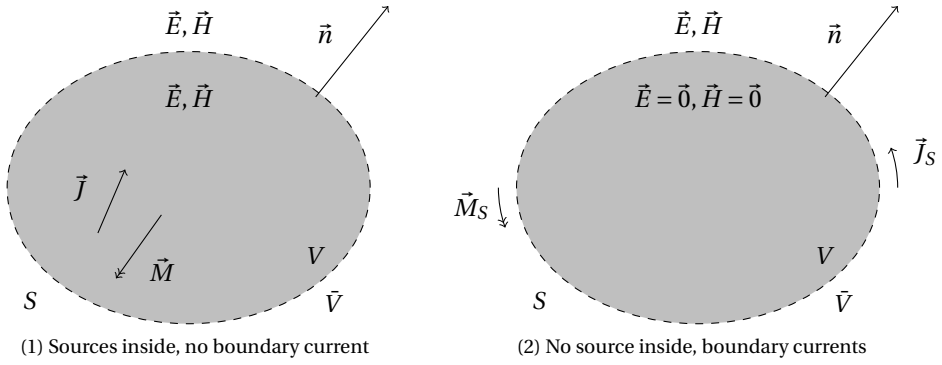


Figure 4.14: Illustration of the equivalence principle by two equivalent configurations.

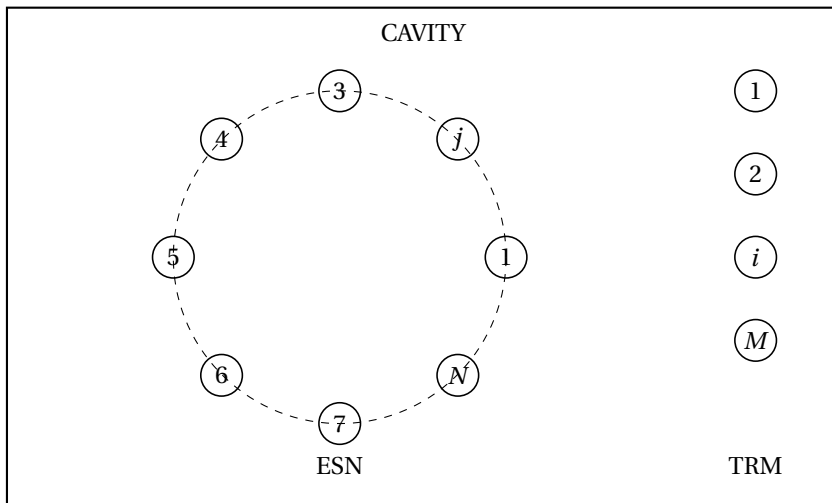


Figure 4.15: Composition of the TREC

2. The signals  $y_i^k(t)$  are received by each antenna of the TRM. Each element collects the contributions emitted by each element of the ESN. Let  $h_{ij}^k(t)$  the transmission channel between the element  $i$  of the TRM and the element  $j$  of the ESN following the polarization  $k$ . The signals on the TRM elements are defined by

$$y_i^k(t) = \sum_{j=1}^M h_{ij}^k(t) \star \alpha_j^k x(t), \quad \hat{y}_i^k(f) = \hat{x}(f) \sum_{j=1}^M \alpha_j^k \hat{h}_{ij}^k(f). \quad (4.53)$$

3. The TRM antennas emit the collected reverse signal  $u_i^k(t)$

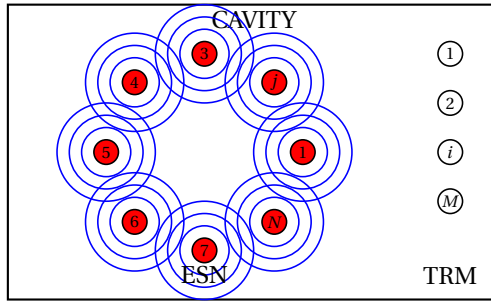
$$u_i^k(t) = y_i^k(-t), \quad \hat{u}_i^k(f) = \left( \hat{y}_i^k(f) \right)^*. \quad (4.54)$$

4. A signal  $r_j^k(t)$ , image of the reversed initial signal  $x(t)$ , is refocused on the ESN such that

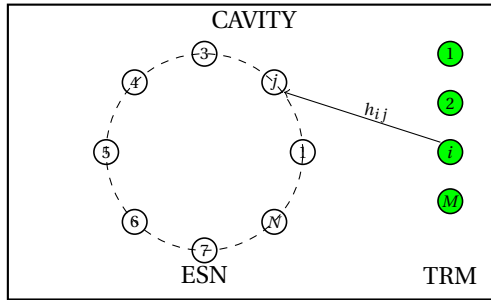
$$r_j^k(t) = \sum_i^M \sum_j^N h_{ij}^k(t) \star h_{ij}^k(-t) \star \alpha_j^k x(-t), \quad \hat{r}_j^k(f) = \hat{x}^*(f) \sum_i^M \sum_j^N \alpha_j^k \left| \hat{h}_{ij}^k(f) \right|^2. \quad (4.55)$$

The obtained refocused signal (4.55) on the ESN is, as for classical TR, the reversed signal emitted by the source, which is in this case the ESN. It means that any wavefront impinging the ESN also impinges the center of the inner volume delimited by the latter. Moreover, by acting on the weights  $\alpha_j^k$  of the ESN elements, it is possible to control the direction of arrival of the wavefront [37], which was not possible with classical TR. Even more interestingly, the method is able to generate coherent wavefronts in a reverberation chamber which is a rather counter intuitive result due to the inherent nature of electromagnetic fields arising in cavities.

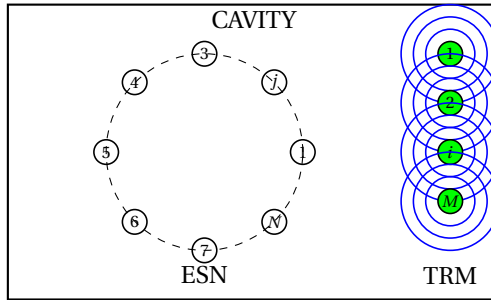
**Numerical examples** A rectangular cavity of 5 m by 4 m is used to illustrate the TR method in a TREC. The refocusing instants are presented in Fig. 4.17, for several configurations of TRM and ESN. As expected, a signal is refocused on each ESN element. If the number of ESN elements is sufficient, respecting a sampling criterion of  $\lambda/2$ , the localized wavefront tends to become a single circular wavefront moving towards the center of the ESN. Unfortunately, using isotropic ESN elements, the generated wavefront also propagates from the center of the ESN to the exterior. To prevent that behavior, the emitted wavefront by the ESN at the first step, should be directed to the exterior of the ESN only. A possible solution, depicted in Fig. 4.18, is to use directive antennas in place of isotropic elements for the ESN. The behavior of the refocusing remains the same: with a too low number of ESN elements, the refocusing is still localized on the element, but when the number is sufficient, a full circular wavefront propagates toward the center of the ESN, without this time, a wavefront moving in the other direction (this is not very clear with static pictures, but it becomes obvious with an animated version).



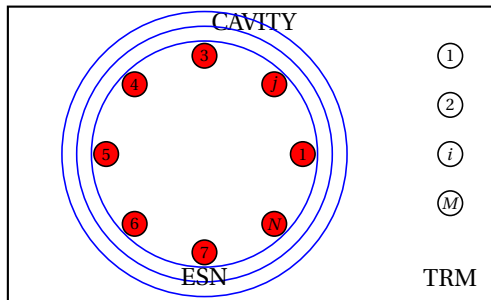
(1) Emission by the ESN



(2) Recording by the TRM



(3) Emission by the TRM



(4) Refocusing on the ESN

Figure 4.16: The TR steps for the TREC.

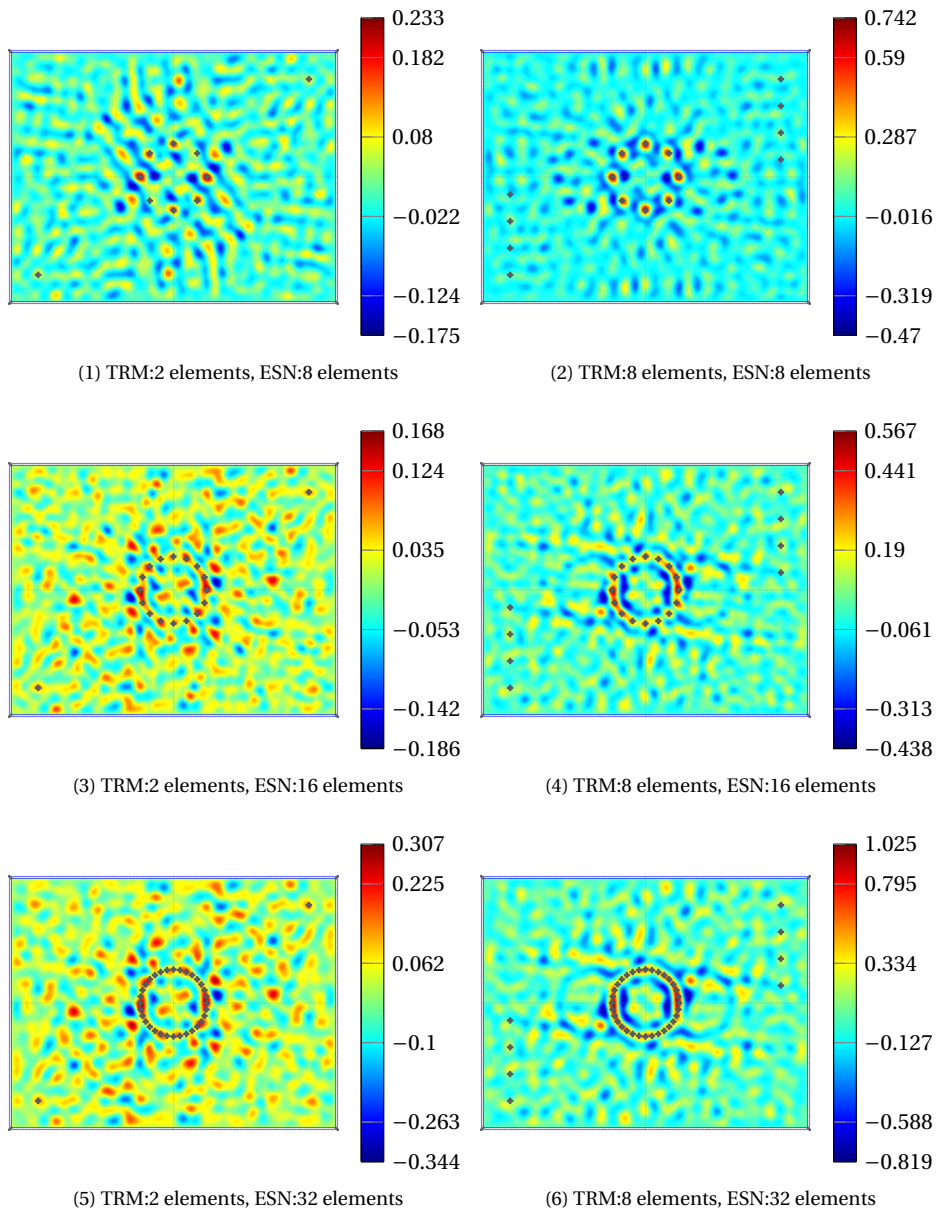


Figure 4.17: Comparison of the TR refocusing ( $E_z(t = t_R)$ ) using a TREC with different numbers of TRM and ESN elements for a Gaussian pulse centered at 1 GHz with a 500 MHz bandwidth. The ESN elements are isotropic.

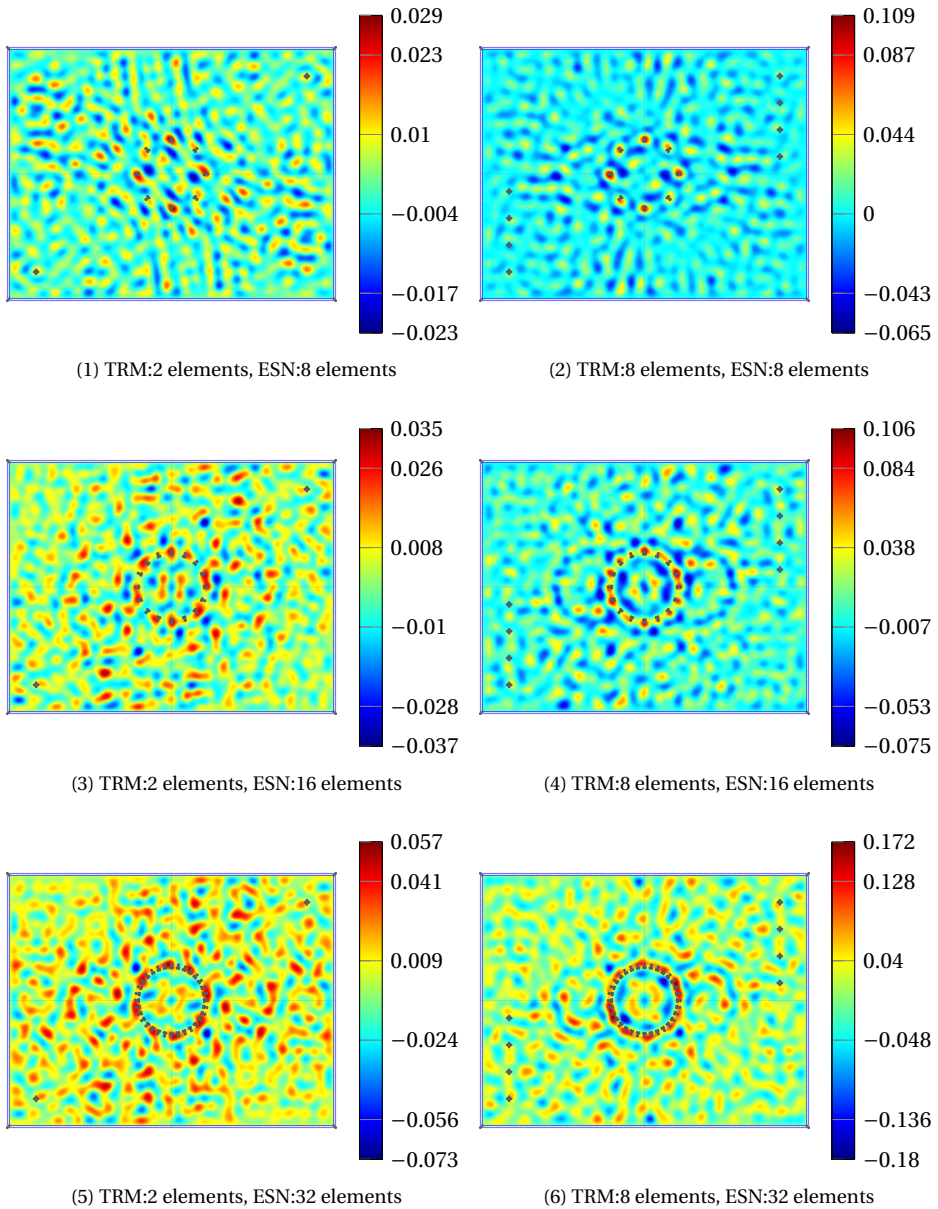


Figure 4.18: Comparison of the TR refocusing ( $E_z(t = t_R)$ ) using a TREC with different numbers of TRM and ESN elements for a Gaussian pulse centered at 1 GHz with a 500 MHz bandwidth. The ESN elements are directive.

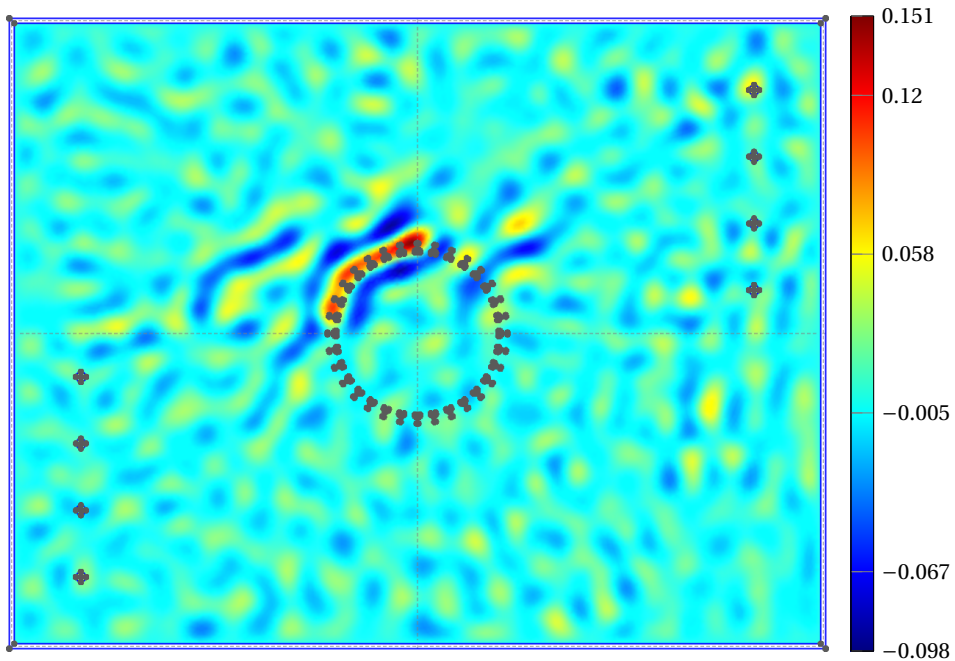


Figure 4.19: TR refocusing ( $E_z(t = t_R)$ ) using a TREC with 8 TRM and 32 ESN elements for a Gaussian pulse centered at 1 GHz with a 500 MHz bandwidth. Only a quarter of the ESN is active, with directive radiating elements.

A last example is given in Fig. 4.19, where only a quarter of the ESN has been activated (through the weights  $\alpha_j^k$ ) with directive elements. The generated wavefront impinges thus only the selected elements, which allows the produce wavefronts propagating in any arbitrary direction, with any arbitrary shape and polarization, just by selecting the appropriate signal  $x(t)$  and ESN weights  $\alpha_j^k$ .

One of the interesting features of using a TREC is that the transfer functions between the ESN elements and the TRM elements have to be determined just once. Practically, it means that the two first steps of the procedure are unnecessary. This allows to save time by directly starting at the third step, the TRM radiation, directly followed by the last refocusing step. However, several important issues remain for using a TREC to shape electromagnetic wavefronts. First of all, the transverse shape of the refocused wavefront, due to the way it is built, is always either cylindrical or spherical, despite the fact that its longitudinal shape can be freely chosen (by adjusting  $x(t)$ ). It is therefore not possible, for example, to generate a plane wave of any arbitrary direction whereas it is very common in EMC testing. Secondly, since only the location of the refocusing

[37] Cozza, A. “Emulating an Anechoic Environment in a Wave-Diffusive Medium Through an Extended Time-Reversal Approach”.

is controlled on each ESN element, there is no guarantee that the resulting refocused wavefront has still the right shape and amplitude when arriving at the centre of the ESN. Then, there might be also some issues when dealing with pulse signals for some purposes such as EMC testing. Indeed, the radiated immunity tests are performed in the frequency domain, with a rather significant dwell time allowing to test an EUT in worst case conditions. Using time domain pulses containing the appropriate frequency spectrum leads to use very short pulses, far away from the usual required dwell times. This issue is obviously beyond the scope of this work, but should really be taken into account. And finally, generating such wavefronts is certainly elegant using the TREC [40], [115] but not mandatory: this could be equivalently achieved using a phased array of antennas without any TR.

## 4.4 Conclusions

---

In this chapter, we have introduced several techniques to actively shape electromagnetic fields in complex environments and detailed 2 of them: the Hilbert Uniqueness Method and the Time Reversal Electromagnetic Chamber. While both have many appealing features and are being used in specific applicative contexts [46], [43], they also present intrinsic limitations for their experimental use in the UHF range. This motivates the investigations of our third simpler approach: the direct optimal control of electromagnetic fields in the frequency domain.

---

[40] Cozza, A. et al. "Accurate Radiation-Pattern Measurements in a Time-Reversal Electromagnetic Chamber".

[115] Meton, P. et al. "Analysis of wavefront generation in a reverberation chamber for antenna measurements".

[46] Darbas, M. et al. "Numerical reconstruction of small perturbations in the electromagnetic coefficients of a dielectric material".

[43] Cozza, A. et al. "Procédé de contrôle de la directivité et la polarisation de distributions cohérentes de champ dans un milieu réverbérant".

# Optimal control of time-harmonic electromagnetic fields

## 5.1 Introduction

AFTER having considered optimal control theory in the time domain, and analyzed the shortcomings of HUM and TR to shape wavefronts generated in reverberating environments in chapter 4, this chapter addresses optimal control theory in the time-harmonic domain. The general idea pursued in this chapter is to use an antenna array to generate an appropriate counter-field to compensate any undesired noise, and to superpose any field map. Achieving such an active shaping in free-space is well-known. The use of an array of transducers approximating an equivalent surface bounding a domain where to control noise has been developed for acoustic waves, such as in [25], [70], [155], [110],[111], for active shielding and acoustic noise control techniques. Similar methods have been proposed for active electromagnetic cloaking, especially in optical frequencies [116], [158], [50] by using the equivalent Love's (Schelkunoff's) surface (already introduced in chapter 4, Fig. 4.14) [139], or by using polynomial approximation for Laplace and Helmholtz equations [152]. Using the UHF range is rather uncommon in active cloaking [140], as higher frequencies are generally encountered in the literature [136]. The originality in this chapter is to achieve active shaping of electromagnetic waves in any reverberating environment.

To this aim, the method developed in this chapter relies on optimal control theory [95],

- [25] Burgess, J. C. "Active adaptive sound control in a duct: A computer simulation".
- [70] Fuller, C. R. et al. "Active control of sound and vibration".
- [155] Wright, S. et al. "Active control of environmental noise".
- [110] Lončarić, J. et al. "Active Shielding and Control of Noise".
- [111] Lončarić, J. et al. "Optimization in the Context of Active Control of Sound".
- [116] Miller, D. A. B. "On perfect cloaking".
- [158] Zheng, H. H. et al. "Exterior optical cloaking and illusions by using active sources: A boundary element perspective".
- [50] Du, J. et al. "Broadband optical cloak and illusion created by the low order active sources".
- [139] Selvanayagam, M. et al. "An Active Electromagnetic Cloak Using the Equivalence Principle".
- [152] Vasquez, F. G. et al. "Active Exterior Cloaking for the 2D Laplace and Helmholtz Equations".
- [140] Selvanayagam, M. et al. "Experimental Demonstration of Active Electromagnetic Cloaking".
- [136] Schurig, D. et al. "Metamaterial Electromagnetic Cloak at Microwave Frequencies".
- [95] Lagnese, J. E. "Exact Boundary Controllability of Maxwell's Equations in a General Region".

[36], [35] rather than on the equivalence principle.

The generic problem setting is depicted in Fig. 5.1, where one aims to control a part  $\Omega_o$  of the global environment  $\Omega$  in which distributed control sources  $\vec{u}$  on  $\Omega_c$  have been included. A field  $\vec{E}_f$  generated by one or more noise sources  $\vec{f}$  has to be replaced by an arbitrary field  $\vec{E}_o$  in  $\Omega_o$ , which is generated by the control sources  $\vec{u}$ . By superposition, finding the control source  $\vec{u}$  allowing to replace the field  $\vec{E}_f$  by  $\vec{E}_o$  is equivalent to sum the contribution of the control sources  $\vec{u}_z$ , compensating  $\vec{E}_f$  and causing a null field in  $\Omega_o$ , and the contribution of the control sources  $\vec{u}_a$  leading to the field  $\vec{E}_o$  on  $\Omega$ . This is equivalent to minimizing the energy functional

$$J(\vec{E}, \vec{u}) = \frac{1}{2} \int_{\Omega_o} \|\vec{E}(x) - \vec{E}_o(x) + \vec{E}_f(x)\|^2 d\Omega + \frac{\lambda}{2} \int_{\Omega_c} \|\vec{u}(x)\|^2 d\Omega, \quad (5.1)$$

where  $\vec{E}$  is the state function (i.e. the electric field, depending on the location  $\vec{x}$ ). The solution  $(\vec{E}, \vec{u})$  needs to be restricted using the appropriate constraints pertaining to the physics of the problem

$$\begin{cases} \nabla \times \nabla \times \vec{E} - k^2 \vec{E} = \vec{u} \mathbb{1}_{\Omega_c} & \text{on } \Omega \\ \vec{n} \times \vec{E} = 0 & \text{on } \partial\Omega, \end{cases} \quad (5.2)$$

where  $\mathbb{1}_{\Omega_c}$  is the indicator function, and  $\vec{n}$  is the outgoing unit normal to  $\partial\Omega$ , the boundary of  $\Omega$ .

The objective functional  $J$  in (5.1) consists in two terms: the first one ensures that the resulting field after control will get as close to the target function as possible (in  $L_2$  norm) while the second one has a regularizing effect by measuring the cost of the applied control. The parameter  $\lambda$  has to be chosen such that  $|\lambda| \geq 0$ , but preferably  $|\lambda| > 0$  to avoid singular or *bang-bang* controls [29]. The target function  $\vec{E}_o$  should also be solution of the wave equation and interestingly encompasses either a null field or any other pattern such as spherical or plane waves. The target field map is limited to  $\Omega_o$  which is surrounded by the distributed control  $\Omega_c$ . Using a distributed control located around the region to control ( $\Omega_o$ ) is preferred rather than placing the control on the boundary of  $\Omega$  since in practice, we are more likely to encounter that kind of configuration. The constraint (5.2) is the classical time-harmonic electromagnetic wave equation assorted with a homogeneous Dirichlet boundary condition. For the sake of clarity, we have used a homogeneous Dirichlet condition, but any valid boundary condition could be chosen.

To solve the optimization problem  $\min J(\vec{E}, \vec{u})$ , the optimality conditions are written [17],

[36] Courilleau, P. et al. "On the controllability of time-harmonic electromagnetic fields in chiral media".

[35] Courilleau, P. et al. "On the controllability of Maxwell's equations in a class of complex media".

[29] Casas, E. "Second Order Analysis for Bang-Bang Control Problems of PDEs".

[17] Bergounioux, M. et al. "Primal-Dual Strategy for Constrained Optimal Control Problems".

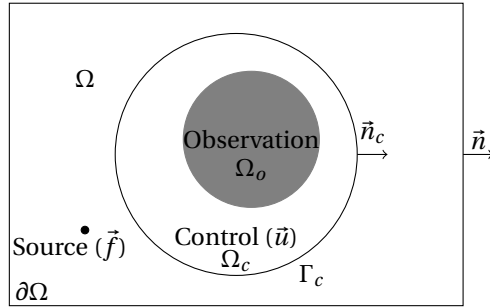


Figure 5.1: Generic configuration for the optimal control of the electric field in the  $\Omega_o$  region.

[113], [114] (see also [28],[21],[27], [30] for existence and uniqueness of the solution)

$$\begin{cases} \vec{\nabla} \times \vec{\nabla} \times \vec{E} - k^2 \vec{E} = \vec{u} \mathbb{1}_{\Omega_c} & \text{on } \Omega \\ \vec{\nabla} \times \vec{\nabla} \times \vec{p} - k^2 \vec{p} = (\vec{E}_f - \vec{E}_o + \vec{E}) \mathbb{1}_{\Omega_o} & \text{on } \Omega \\ \vec{u} = \vec{p} / \lambda & \text{on } \Omega_c \end{cases} \quad (5.3)$$

with  $\vec{p}$  a Lagrange multiplier [86], [106], [17].

By applying the weighted residuals method on each equation of (5.3), a variational form is found, allowing to solve the optimization problem numerically using the FEM.

Find  $\vec{p}$ ,  $\vec{u}$  and  $\vec{E}$  such that

$$\begin{cases} - \int_{\Omega} (\nabla \times \vec{p}) \cdot (\nabla \times \vec{p}') d\Omega + k^2 \int_{\Omega} \vec{p} \cdot \vec{p}' d\Omega \\ \quad + \int_{\Omega_o} (\vec{E} - \vec{E}_o + \vec{E}_f) \cdot \vec{p}' d\Omega_o = 0 \\ \lambda \int_{\Omega_c} \vec{u} \cdot \vec{u}' d\Omega_c + \int_{\Omega_c} \vec{p} \cdot \vec{u}' d\Omega_c = 0 \\ - \int_{\Omega} (\nabla \times \vec{E}) \cdot (\nabla \times \vec{E}') d\Omega + k^2 \int_{\Omega} \vec{E} \cdot \vec{E}' d\Omega \\ \quad + \int_{\Omega_c} \vec{u} \cdot \vec{E}' d\Omega_c = 0 \end{cases} \quad (5.4)$$

hold for all appropriate test functions  $\vec{p}'$ ,  $\vec{u}'$  and  $\vec{E}'$  [117].

[113] Maurer, H. et al. "Optimization Techniques for Solving Elliptic Control Problems with Control and State Constraints: Part 1. Boundary Control".

[114] Maurer, H. et al. "Optimization Techniques for Solving Elliptic Control Problems with Control and State Constraints. Part 2: Distributed Control".

[28] Casas, E. "Control of an Elliptic Problem with Pointwise State Constraints".

[21] Bonnans, J. F. et al. "Optimal Control of Semilinear Multistate Systems with State Constraints".

[27] Casas, E. "Boundary Control of Semilinear Elliptic Equations with Pointwise State Constraints".

[30] Casas, E. et al. "Second Order Sufficient Optimality Conditions for Some State-constrained Control Problems of Semilinear Elliptic Equations".

[86] Ito, K. et al. *Lagrange Multiplier Approach to Variational Problems and Applications*.

[106] Leugering *Constrained optimization and optimal control for partial differential equations*.

[17] Bergounioux, M. et al. "Primal-Dual Strategy for Constrained Optimal Control Problems".

## 5.2 Numerical examples

To illustrate the previously described method, several test cases are proposed in the following. Different 2D environments have been tested, from free-space to fully reverberating cavities. The weak form (5.4) has been implemented into the finite element solver GetDP [52] by using Whitney elements [154], [22] for discretizing all the quantities. All the meshes were generated with Gmsh [71]. Extending this rather straightforward implementation of the optimality conditions, more advanced augmented Lagrangian techniques could also be considered [18].

**Electric field control in free-space** In this first test case, illustrated in Fig. 5.2, the method is used to find the control sources  $\vec{u}$  allowing to compensate the field  $\vec{E}_f$  generated by the source  $\vec{f}$ . The field  $\vec{E}_f$  on  $\Omega_o$  is first computed by solving the problem

$$\left\{ \begin{array}{ll} \vec{\nabla} \times \vec{\nabla} \times \vec{E}_f - k^2 \vec{E}_f = 0 & \text{on } \Omega \setminus \{x_f\} \\ \vec{n} \times \vec{E}_f = 0 & \text{on } \partial\Omega \\ \vec{E}_f(x_f) = \vec{f}. \end{array} \right. \quad (5.5)$$

A PML, surrounding  $\Omega$ , is introduced to model infinity [15], [16]. The results of the control in free-space are displayed in Fig. 5.3. For illustration, three different representative fields have been chosen to be imposed as  $\vec{E}_o$  in the controlled region  $\Omega_o$ : a null field, a plane wave and a cylindrical wave. Fig. 5.3 exhibits a very good compensation of the undesired field  $\vec{E}_f$  caused by the source  $\vec{f}$ , and moreover, the superimposed fields are also accurately generated in the controlled region (beyond  $1 \times 10^{-6}$  in relative error).

**Electric field control in a reverberating room** The numerical problem of controlling electromagnetic waves inside a cavity is numerically simpler to address compared to free-space since infinity does not need to be modelled. Test case 2, depicted in Fig. 5.4 using the same domain  $\Omega$  as test case 1 with the exception that a PEC boundary condition is applied on  $\partial\Omega$ , the boundary of  $\Omega$

$$\vec{n} \times \vec{E} = 0 \quad \text{on } \partial\Omega. \quad (5.6)$$

[52] Dular, P. et al. "A general environment for the treatment of discrete problems and its application to the finite element method".

[154] Whitney, H. *Geometric integration theory*.

[22] Bossavit, A. "Whitney forms: a class of finite elements for three-dimensional computations in electromagnetism".

[71] Geuzaine, C. et al. "Gmsh: A 3-D finite element mesh generator with built-in pre- and post-processing facilities".

[18] Bergounioux, M. et al. "Augmented Lagrangian Techniques for Elliptic State Constrained Optimal Control Problems".

[15] Berenger, J.-P. "A perfectly matched layer for the absorption of electromagnetic waves".

[16] Berenger, J.-P. *Perfectly Matched Layer (PML) for Computational Electromagnetics*.

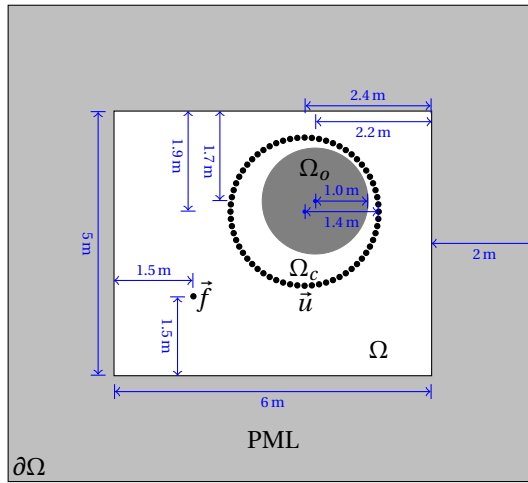
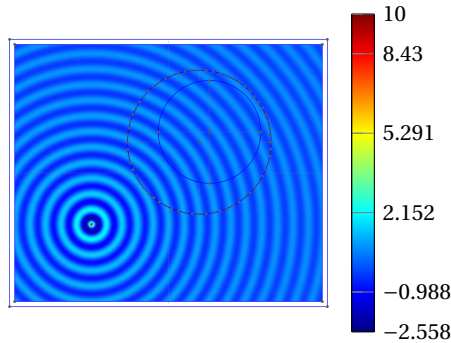


Figure 5.2: Configuration of test case 1.



(1) Without control

Figure 5.3: 2D control in free-space of the electric field in a target zone (1/2).

The results of the control in this 2D cavity, shown in Fig. 5.5, exhibit a very good capability to generate the different target fields in a rather complex environment. Compared to the test case 1, in free-space, where the values of the control elements  $\vec{u}$  could simply be deduced from the free-space Green's function, the Green's function for test case 2 is much more complicated, causing the explicit calculation of the control non trivial, which makes the optimal control approach very appealing.

**Electric field control in a realistic room** Finally, in a third test case (Fig. 5.4), the control method is applied on the same 2D cavity, but with concrete walls with a conductivity

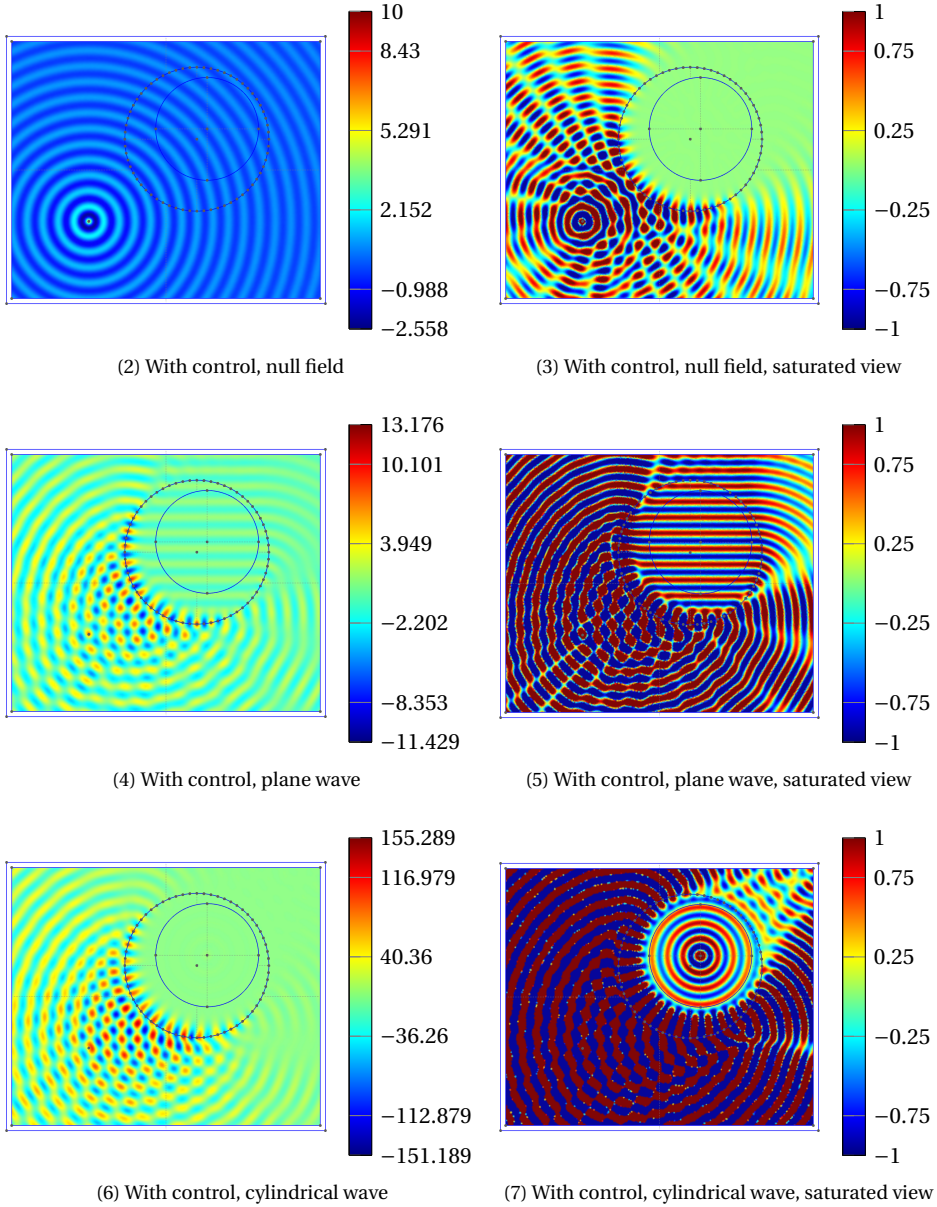


Figure 5.3: 2D control in free-space of the electric field in a target zone (2/2).

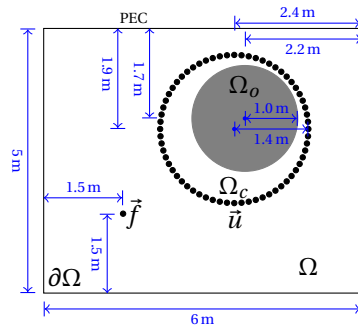
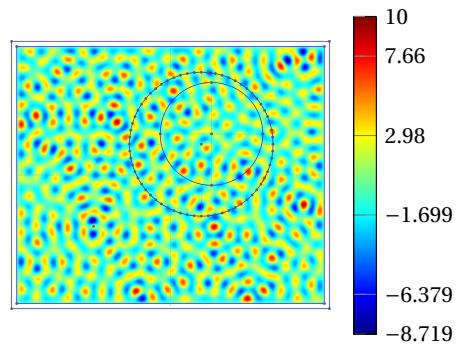


Figure 5.4: Configuration of test case 2.



(1) Without control

Figure 5.5: 2D control in a reverberation chamber of the electric field in a target zone (1/2).

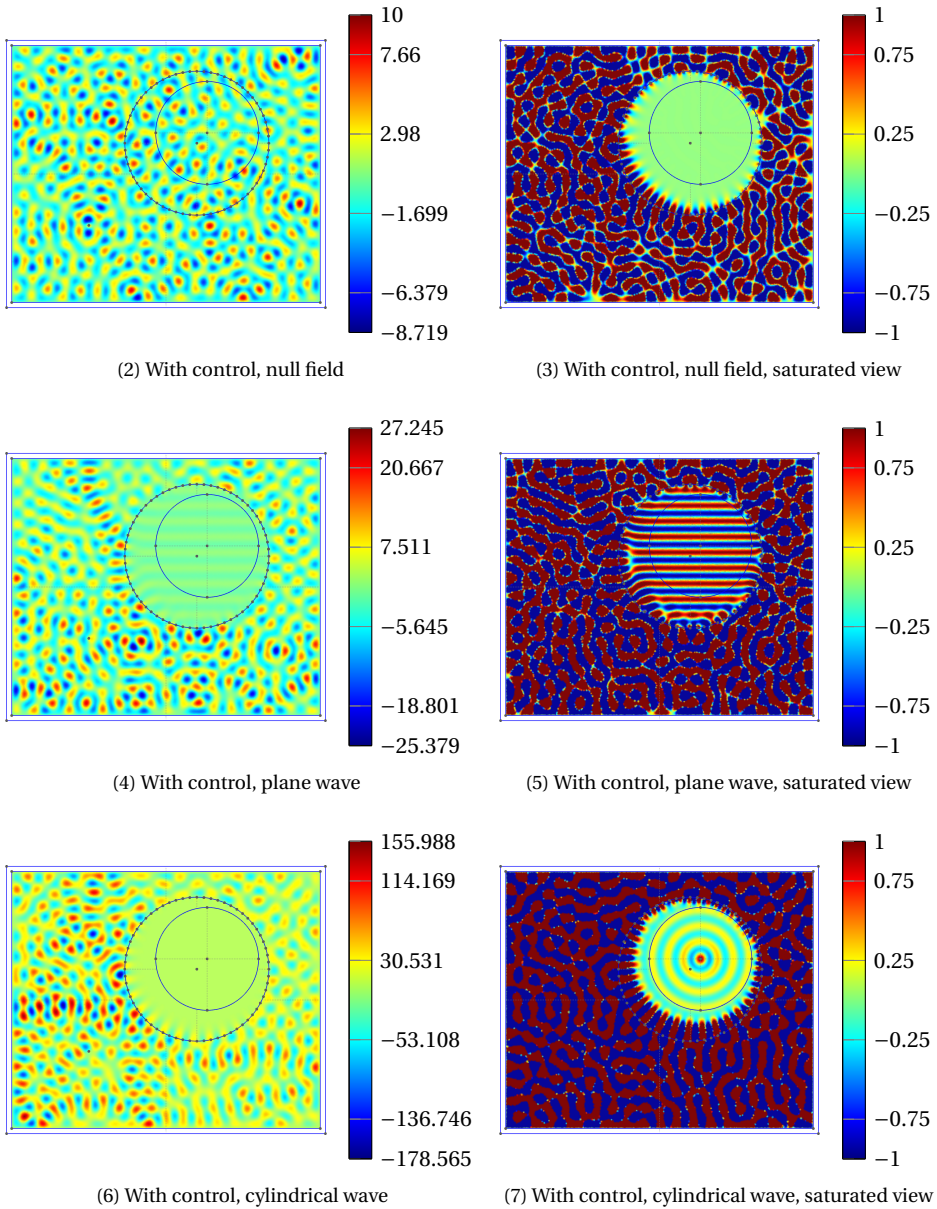


Figure 5.5: 2D control in a reverberation chamber of the electric field in a target zone (2/2).

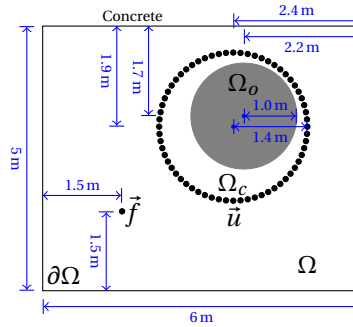


Figure 5.6: Configuration of test case 3.

$\sigma_w = 1 \times 10^{-4}$  S and with a relative permittivity  $\epsilon'_{rw} = 8$  [123], [124], [149]. In that case, the boundary condition to use is an Impedance Boundary Condition (IBC) [88], [90]

$$\vec{n} \times \vec{E} = Z \vec{n} \times (\vec{n} \times \vec{H}) \quad \text{on } \partial\Omega. \quad (5.7)$$

where

$$Z = \frac{1}{j\omega\epsilon_0(\epsilon_{rw} - 1)d_w} \quad (5.8)$$

with  $d_w$  the width of the wall and the complex permittivity  $\epsilon_{rw} = \epsilon'_{rw} - j\frac{\sigma_w}{\omega\epsilon_0}$ .

As shown in Fig. 5.7, the control method accurately compensate the field generated by the source  $\vec{f}$ , but also exactly brings the three expected target fields  $\vec{E}_o$  in the controlled region  $\Omega_o$ .

Compared to the TREC method studied in chapter 4, these three test cases highlight the better accuracy and higher flexibility of the optimal control approach. It is however important to note that the electric field outside the controlled region is totally uncontrolled, meaning that potentially high field levels are produced in the global domain  $\Omega$ . While it is therefore possible to add supplementary constraints in (5.2) to limit the field values, this will adversely affect the accuracy of the generated target field  $\vec{E}_o$ . Furthermore, a serious assumption has been made to obtain the control i.e. that the field  $\vec{E}_f$  generated by the source  $\vec{f}$  is exactly known at any point of the controlled domain  $\Omega_o$ . In

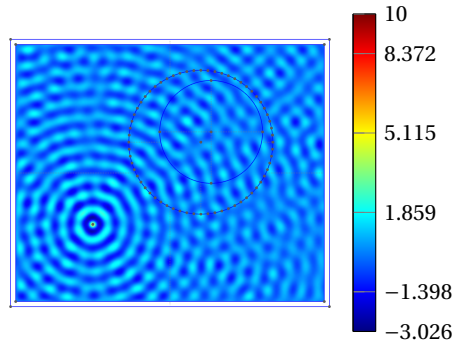
[123] Ogunsola, A. et al. "Modelling shielding properties of concrete".

[124] Ogunsola, A. et al. "Shielding properties of conductive concrete against transient electromagnetic disturbances".

[149] Thajudeen, C. et al. "Measured complex permittivity of walls with different hydration levels and the effect on power estimation of twri target returns".

[88] Jin, J. M. et al. "Finite Element Analysis of Complex Antennas and Arrays".

[90] Jin, J. et al. *Finite Element Analysis of Antennas and Arrays*.



(1) Without control

Figure 5.7: 2D control in a realistic room of the electric field in a target zone (1/2).

the following, an alternative reconstruction method without the need of sampling  $\vec{E}_f$  in the whole controlled domain  $\Omega_o$  is presented.

### 5.3 Noise reconstruction

While *numerically*, it is possible to sample the field to compensate  $\vec{E}_f$  in the whole domain to control, applying such technique in practice is not realistic. As a result, an alternative method, is proposed to reconstruct  $\vec{E}_f$  in  $\Omega_o$  from boundary (surface) quantities. As seen in Fig. 5.1 the boundary is chosen to be  $\Gamma_c$  such that the Stratton-Chu integral formulation [147] can be used to reconstruct the inner field inside  $\Gamma_c$  from

$$\vec{E}(\vec{x}) = \int_{\Gamma_c} j\omega\mu(\vec{n}_c \times \vec{H})\mathcal{G} + (\vec{n}_c \times \vec{E}) \times \nabla\mathcal{G} + (\vec{n}_c \cdot \vec{E})\nabla\mathcal{G} dS \quad (5.9)$$

with  $\mathcal{G}$  the Green function. Interestingly, the controlled region being a free-space area, the Green function is known

$$\mathcal{G}_{2D} = \frac{j}{4}\mathcal{H}_0^1(kr), \text{ and } \mathcal{G}_{3D} = \frac{e^{jkr}}{4\pi r}, \quad (5.10)$$

for two-dimensional (2D) and three-dimensional (3D) domains respectively.

For numerical purposes, the integral in (5.9) is computed using a numerical quadrature on  $N_c$  points, the number of control elements. In our setups we choose  $\Gamma_c$  as a circle of radius  $R_c$  and use the trapezoidal integration rule, which leads to spectral convergence:

$$\vec{E}_f = \sum_{i=1}^{N_c} \left( j\omega\mu(\vec{n}_c \times \vec{H})_i \mathcal{G}_i + (\vec{n}_c \times \vec{E})_i \times \nabla\mathcal{G}_i + (\vec{n}_c \cdot \vec{E})_i \nabla\mathcal{G}_i \right) \Delta S_i. \quad (5.11)$$

[147] Stratton, J. A. et al. "Diffraction Theory of Electromagnetic Waves".

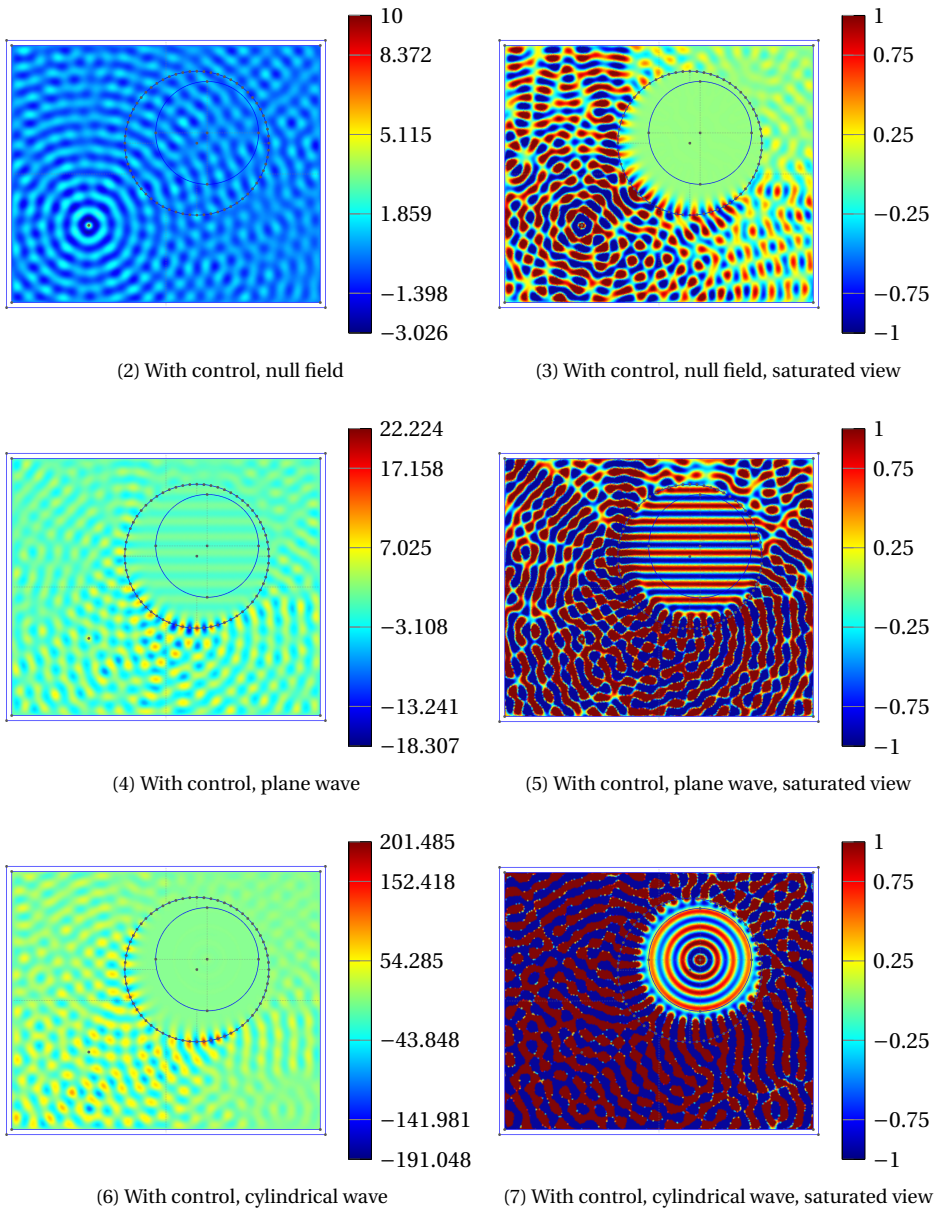
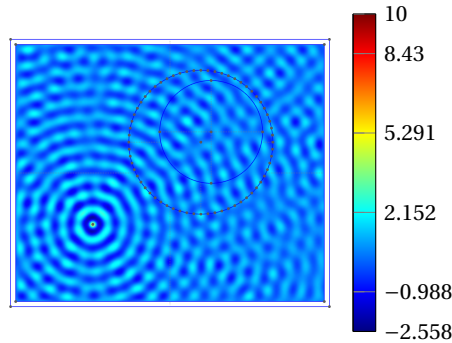


Figure 5.7: 2D control in a realistic room of the electric field in a target zone (2/2).



(1) Without control

Figure 5.8: 2D control in free-space of the electric field in a target zone (1/2).

As a result,  $\Delta S_i$  simply becomes the constant value  $\frac{2\pi R_c}{N_c}$ . A sampling criterion of at most  $\lambda/2$  [91] should be applied to ensure a correct reconstruction. The weak formulation (5.4) remains the same except that  $\vec{E}_f$  is replaced by  $\tilde{\vec{E}}_f$ , implying that the quality of the generated field  $\vec{E}_o$  is thus directly conditioned by the accuracy of the reconstructed field  $\tilde{\vec{E}}_f$  compared to the true field  $\vec{E}_f$ .

## 5.4 Numerical examples with noise reconstruction

The control method using field reconstruction for  $\vec{E}_f$  has been tested in the same situations as those presented above in Figs. 5.3, 5.5 and 5.7. The results are given in Figs. 5.8 to 5.10 for test cases 1, 2 and 3 respectively. The method works as expected. The degradation in the generated target field stems from the fact that the reconstruction formula is not tainted by the (large) dispersion error of the low order FEM. This discrepancy will not be encountered in experimental setups and could be reduced by resorting to high order FEM. It should be noted that this formula also implies to sample the magnetic field to obtain an image of  $\nabla \times \vec{E}$  needed in the Stratton-Chu formula (5.9). Obtaining accurate measurements of the magnetic field is however difficult in the UHF range due to the lack of efficient magnetic field probes at high frequencies. Indeed, small magnetic probes having a high spatial resolution and high frequency bandwidth generally have a poor sensitivity due to the reduced size of the embedded magnetic loop.

In this section, we have presented a promising method to control waves in any arbitrary environment. It is possible to generate any desired field in a target region by solving an optimization problem directly embedded in a weak formulation. Nevertheless, the field to be compensated  $\vec{E}_f$  needs to be quantified accurately to guarantee good target

[91] Joy, E. et al. "Spatial sampling and filtering in near-field measurements".

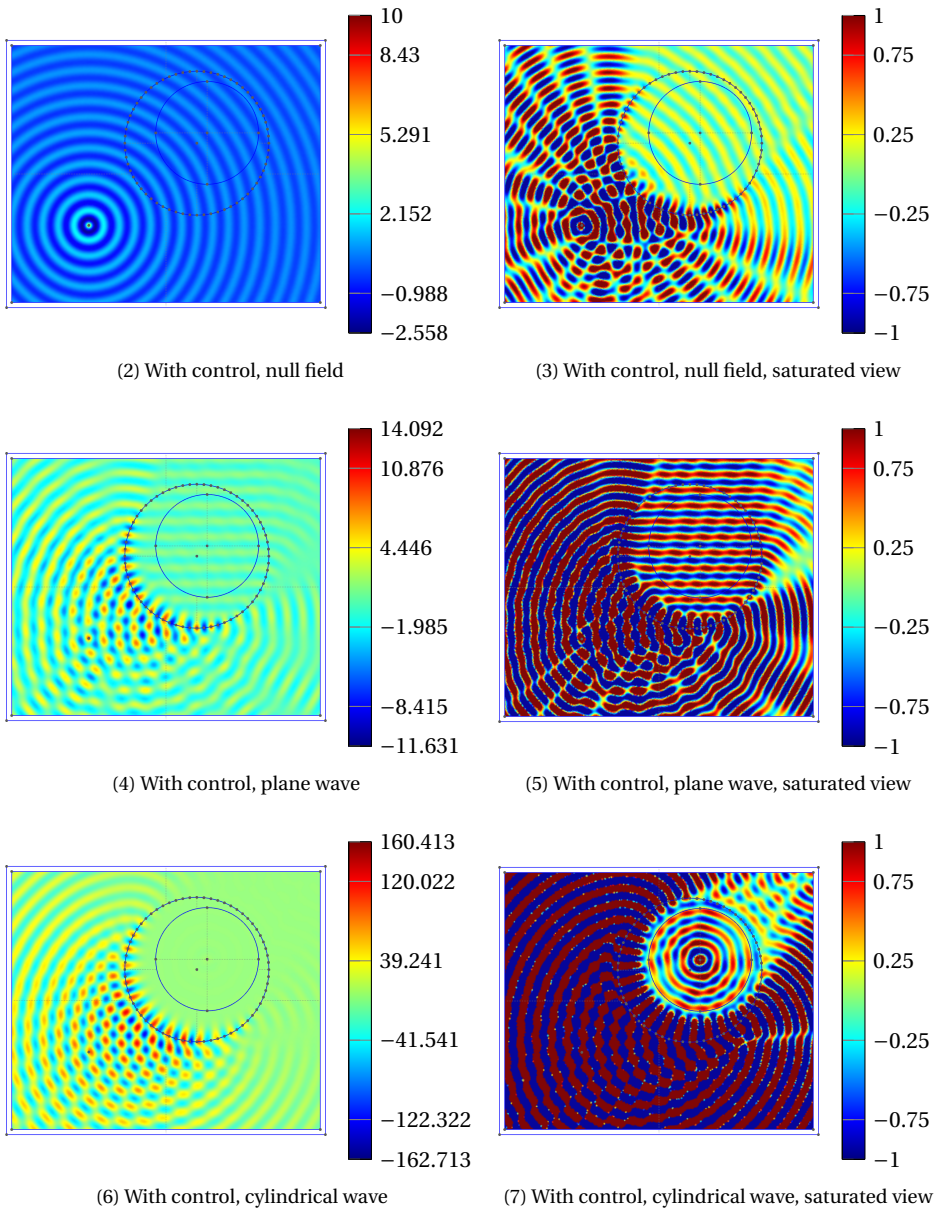
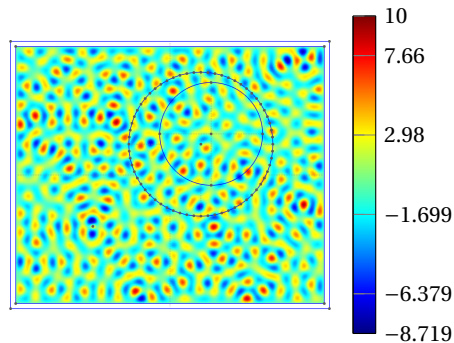


Figure 5.8: 2D control in free-space of the electric field in a target zone (2/2).



(1) Without control

Figure 5.9: 2D control in a reverberation chamber of the electric field in a target zone (1/2).

field accuracy. This frequency control method provide more capabilities and accuracy compared to TR methods.

## 5.5 Conclusions

---

In this chapter, the control of time-harmonic waves by using optimization methods has demonstrated a very good capability to control accurately a part of an environment in the frequency domain. Contrary to other methods, this optimal control based method is not limited to free-space and provides a systematic framework to perform active shaping of electromagnetic waves in complex and/or reverberating environments. The main issue remains in the needed reconstruction of the noise to be compensated, which is a rather difficult and error-prone task that should be avoided if possible, due to the poor quality of reconstruction and the requirement to sample also the magnetic field at high frequencies. After having validated the method numerically in this chapter, an experimental validation is proposed in the last chapter (chapter 6).

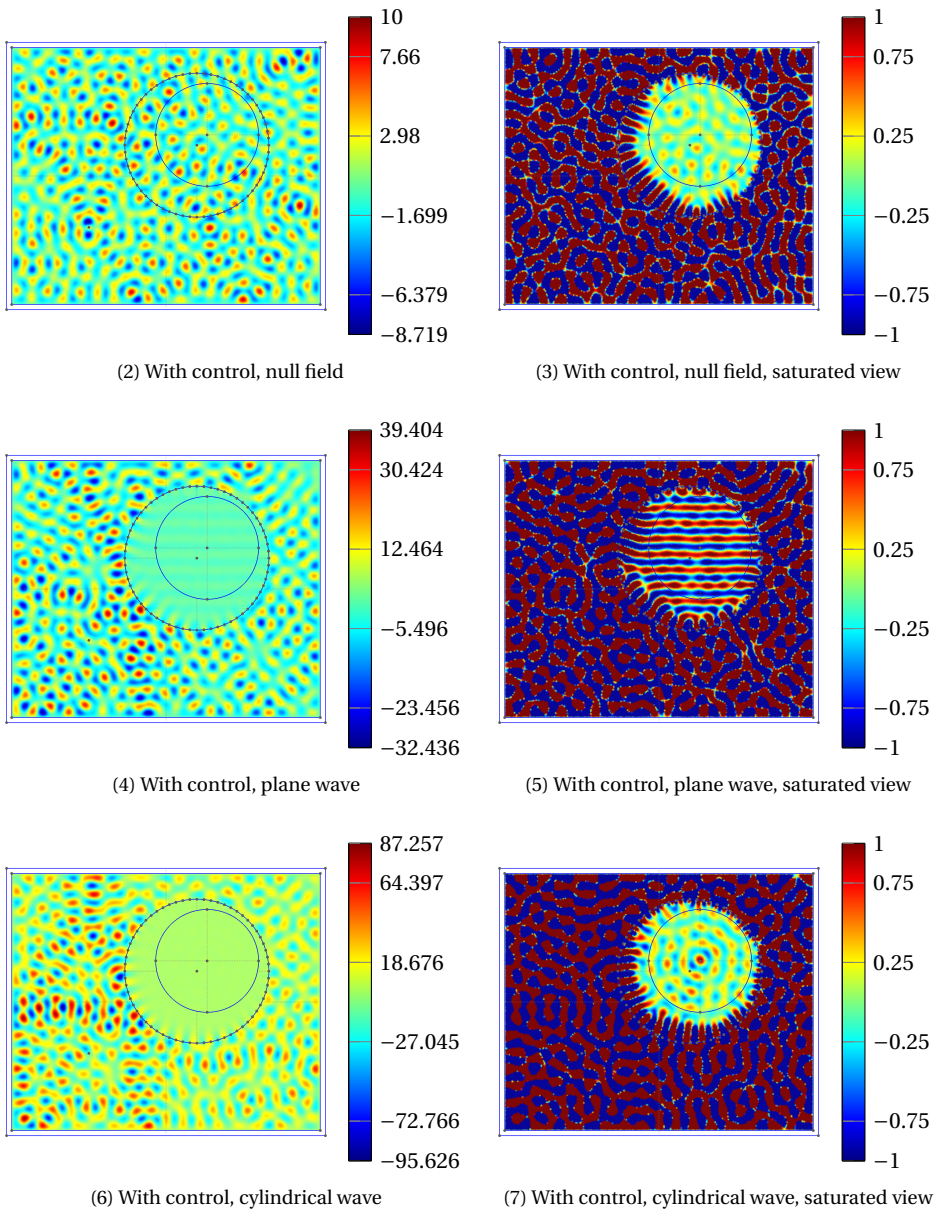
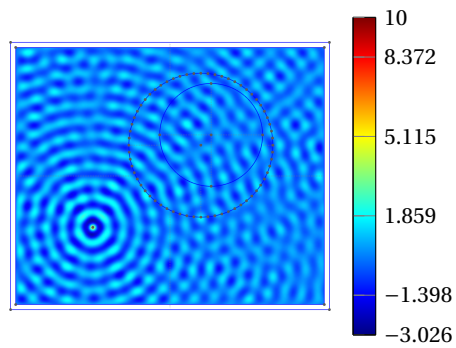


Figure 5.9: 2D control in a reverberation chamber of the electric field in a target zone (2/2).



(1) Without control

Figure 5.10: 2D control in a realistic room of the electric field in a target zone (1/2).

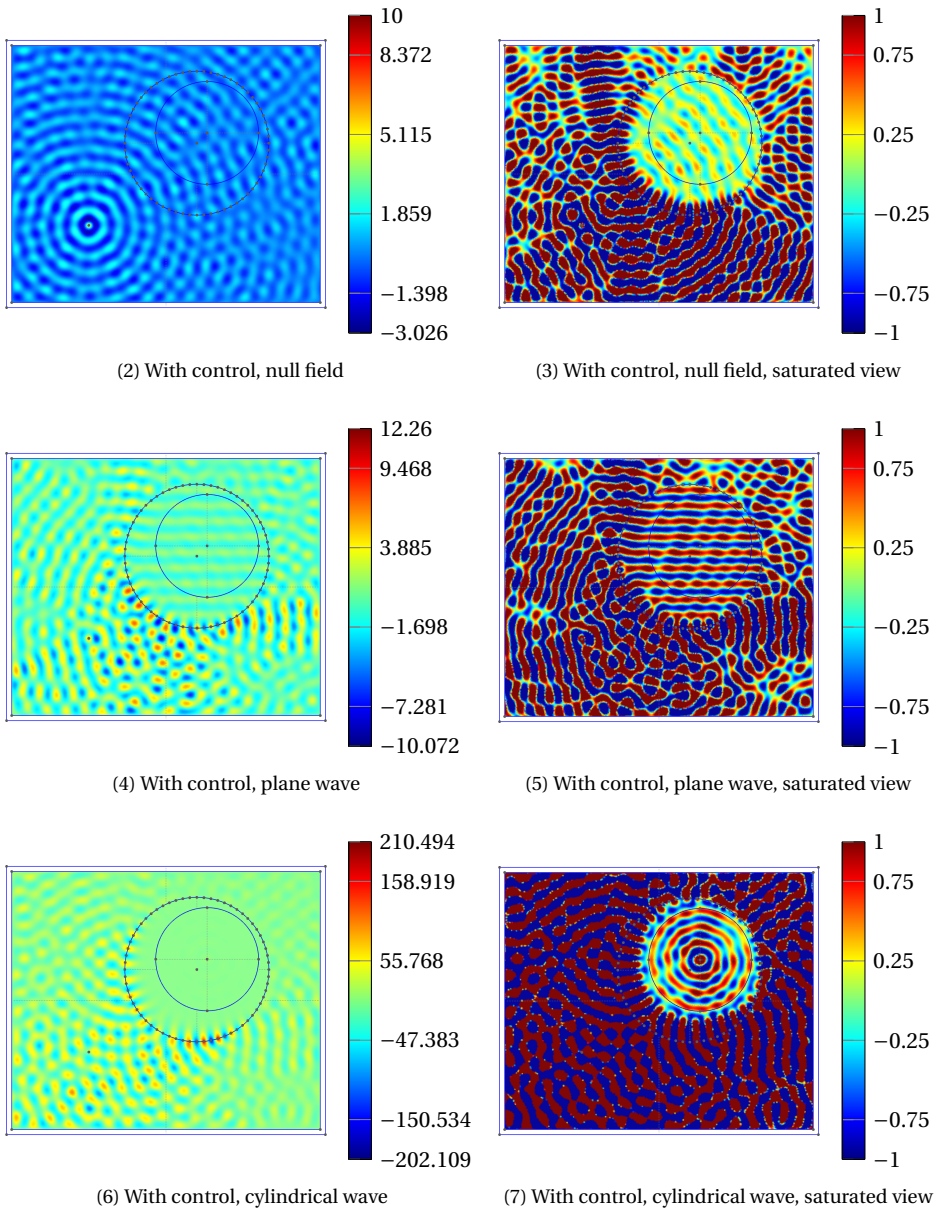


Figure 5.10: 2D control in a realistic room of the electric field in a target zone (2/2).



---

# Experimental control of time-harmonic electromagnetic fields

---

## 6.1 Introduction

---

IN chapter 5, time-harmonic waves have been controlled in complex environments, such as a reverberating room. However, to match the target field with a sufficient accuracy, many antennas were needed. This is principally due to the fact that the sampling criterion of  $\lambda/2$  must be enforced for the Stratton-Chu formula to produce an accurate reconstructed field. The level of accuracy for experimental applications is however generally of a few decibels, which provides more freedom compared to the high level of accuracy claimed in numerical applications. Reducing the number of sampling elements is thus difficult, but reducing the number of control elements could be considered. Even with a reduced number of control elements, such as 8 or 16, the controlling system remains difficult to develop. The main issues occur in the phase and amplitude control, as well as in the phase coherence. The system should indeed allow phase shift and amplitude fine tuning, but should also guarantee to provide exactly the same frequency at each channel to prevent any phase drift. Although such systems are already available “off the shelf”, they are very expensive.

In a one-dimensional environment, as highlighted in chapter 4, the boundary control can be drastically reduced since it requires at most two control sources. Moreover, a single control element is sufficient if the region to control is connected to a boundary of the domain.

Developing a control system allowing to control precisely the phase and the amplitude of only two channels is much easier to tackle (the first channel is used to generate the source to be cancelled while the second channel produces the control source). Such a phase coherent dual source generator, detailed in Appendix C.4, has thus been developed to allow the experimental control of one-dimensional environment. Phase coherence is guaranteed, since a single generator feeds both channels (using a power splitter) with sinusoidal signals having exactly the same frequency. An 8-bit digital phase shifter is used to produce a phase shifted signal on one channel while a 6-bit digital step attenuator is employed to get an attenuated signal, as shown in Fig. 6.1. Both channel signal amplitudes are thus tuned by the output amplitude of the generator, plus

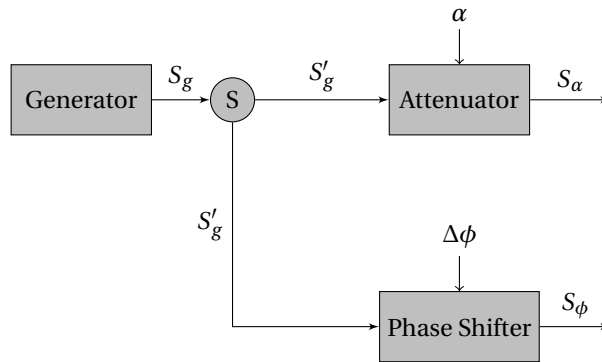


Figure 6.1: Block diagram of the source/control generator:  $S_\alpha$  is applied to the source while  $S_\phi$  is applied to the control.  $S$  denotes a power splitter.

a programmable attenuation  $\alpha$  (0.5 dB to 31.5 dB with 0.5 dB step) for the attenuation channel. The phase shifted channel allows a phase shift  $\Delta\phi$  adjustable from  $0^\circ$  to  $360^\circ$  with a  $1.4^\circ$  step.

Using this control system it is now possible to control several one-dimensional environments. Two different test cases have been chosen to experimentally illustrate the capabilities of the frequency control method exposed in chapter 5. The first test case aims to control the voltage within a transmission line, and the second test case applies a control on the electric field inside a rectangular waveguide network. As a result, both conducted and radiated waves are addressed.

## 6.2 Voltage control within a transmission line

In test case 1, a lossy transmission line network is used as environment, as illustrated in Fig. 6.2. This test case precisely consists in a “H” shaped transmission line network fed by a voltage generated by the harmonic source located at the tip of the upper left leg of the network. The working frequency is fixed at 1 GHz. The control voltage is applied through the tip of the upper right leg of the network while the controlled region  $\Omega_o$  is chosen in the lower left leg. However, using coaxial transmission lines, it is not possible to measure the voltage within the cable, due to the efficient shielding of such a cable. The controlled section of the transmission line has thus been replaced by a microstrip line of the same impedance ( $50\ \Omega$ ) to avoid unintended reflections. By doing so, an image of the voltage across the line is measured through the generated electric field around the microstrip line using a near-field E-probe. The parameters of the designed microstrip line are presented in Fig. 6.3. A total length of 2.0 m has been chosen to increase losses and to complexify the control task. The full experimental setup is shown in Fig. 6.4. Since near-field probe measurements are not accurate, a null target voltage is chosen to ease the discrimination between the measurements in the controlled/uncontrolled microstrip line.



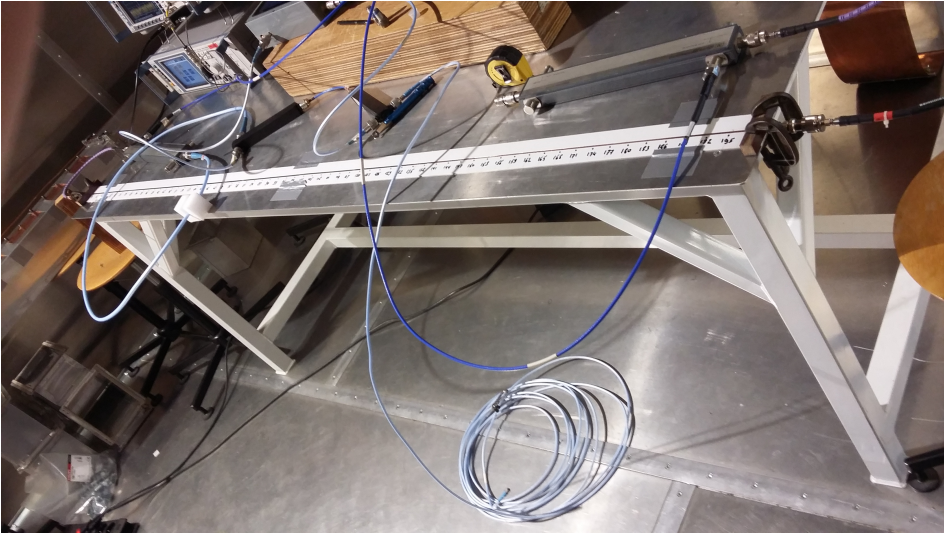


Figure 6.4: Experimental setup of the test case 1.

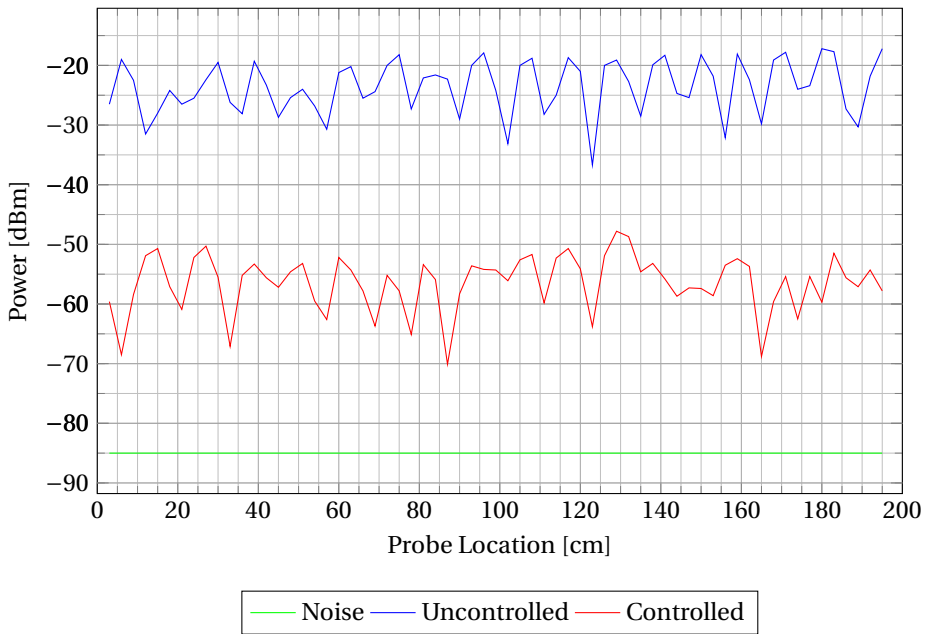


Figure 6.5: Experimental results of the voltage control within the microstrip line.

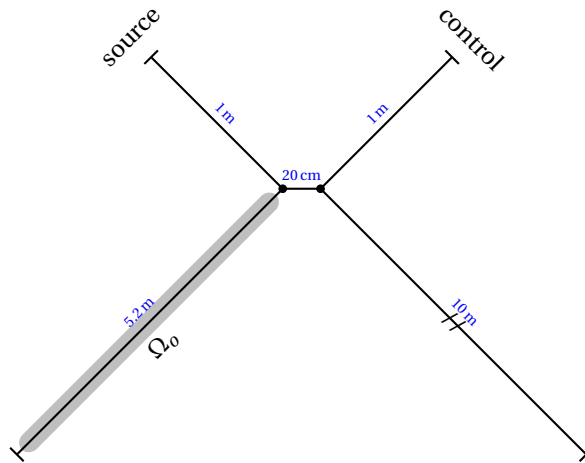


Figure 6.6: Configuration of the test case 4.

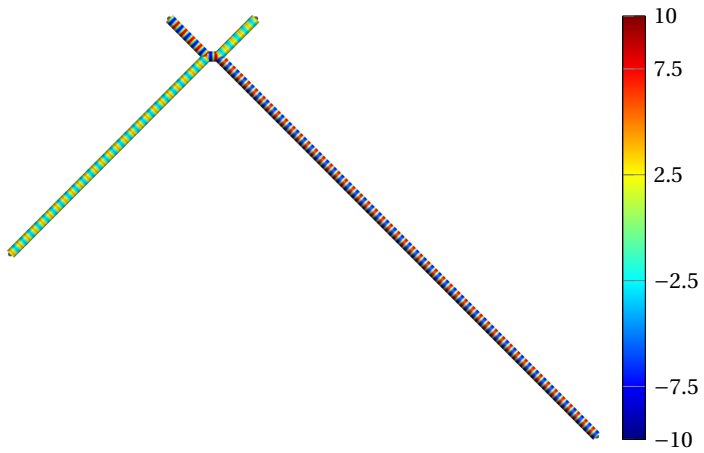
control pair found manually.

### 6.3 Electric field control within a waveguide

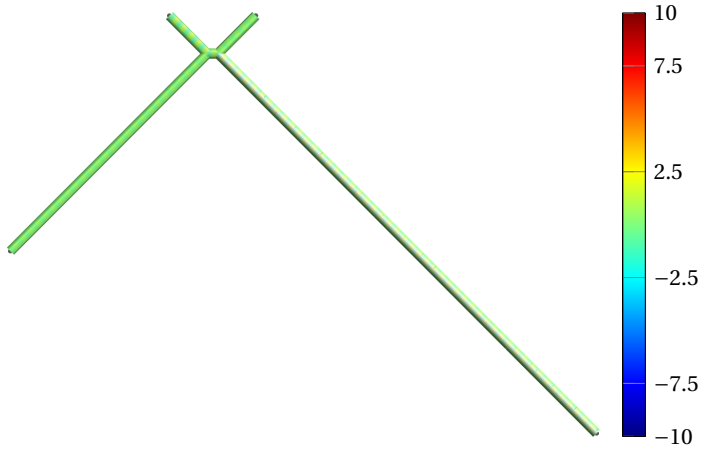
The problem of experimentally controlling radiated waves is now addressed through a second test case. A rectangular waveguide network, detailed in Fig. 6.8 has been chosen as the environment to be controlled. To obtain a one-dimensional behavior of the electric field inside the waveguide, some geometrical adjustments are needed to constraint the electric field vertically. Wave-front shaping in a waveguide could be obtained in the same manner in [20]. A section of  $18\text{ cm} \times 15\text{ cm}$  for a frequency of  $1\text{ GHz}$  is chosen, allowing to propagate the  $\text{TE}_{01}$  mode only. Consequently, a single vertical electric field component is propagated. Moreover, large dimensional values of the waveguide network have been chosen to ease the measurement of the electric field in the controlled section of the waveguide. The waveguide network is composed of different aluminium stretches mechanically fastened together with several clamps. A slit in the middle of  $\Omega_o$  allows to insert a moving antenna probe to measure the received power along the controlled part of the waveguide while a soft lip electromagnetic seal guarantees shielding continuity while displacing the probe. The probe consists of a monopole connected to a dedicated power sensor circuit, as detailed in Appendix C.3.

Two vertical monopoles ( $\lambda/4$ ) are used to feed the network by the source field and by the control field, fed themselves by a sinusoidal signal having a frequency of  $1.0\text{ GHz}$ . The target field  $\vec{E}_o$  is once again chosen to be null in the controlled region  $\Omega_o$  located in the bottom arm of the network.

[20] Böm, J. et al. “Wave Front Shaping in Quasi-One-Dimensional Waveguides”.



(1) Without control



(2) With control

Figure 6.7: Numerical 1D control of the electric field in a transmission line.

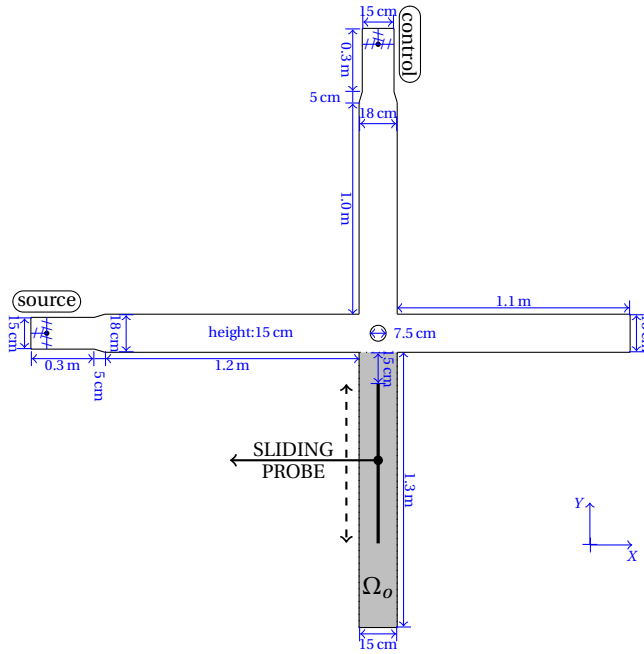


Figure 6.8: Configuration of the experimental test case 2.

The aim of this experimental test case is to manually find the best control pair, leading to the smallest resulting field amplitude in the controlled region  $\Omega_o$ . Using a pair of  $\alpha = 17.5$  dB and  $\Delta\phi = 188^\circ$  brings the lowest resulting field amplitude, as plotted in Fig. 6.10. Compared to the measured power before applying any control value, the measured power is reduced by 25 dB on average in the controlled region, which is a bit worse than in test case 1. The small performance degradation is probably related to the unbalance of the field strength caused by the source and the control. An attenuation of  $\alpha = 17.5$  dB actually means that the level of the generated field (source and control) is low, reducing thus the sensitivity of the probe. Furthermore, the presence of non vertical components in the waveguide cannot completely be excluded, which would effectively be measured by the probe, but need more control source to be cancelled, since the one-dimensional behavior is not guaranteed anymore.

The numerical equivalent test case has also been achieved, where the conducting walls of the waveguide are modelled by an IBC (5.7), using

$$Z = \frac{1+J}{\sigma_w \delta_w}, \quad (6.1)$$

with the skin depth  $\delta_w = \sqrt{\frac{2}{\omega \sigma_w \mu_w}}$  and  $\sigma_w = 1.9 \times 10^7$  S/m. The configuration remains the same as the experimental test case, as detailed in Fig. 6.11. As shown in Fig. 6.12, the applied control allows to reach accurately the null target field in the controlled



Figure 6.9: Experimental setup of the test case 2.

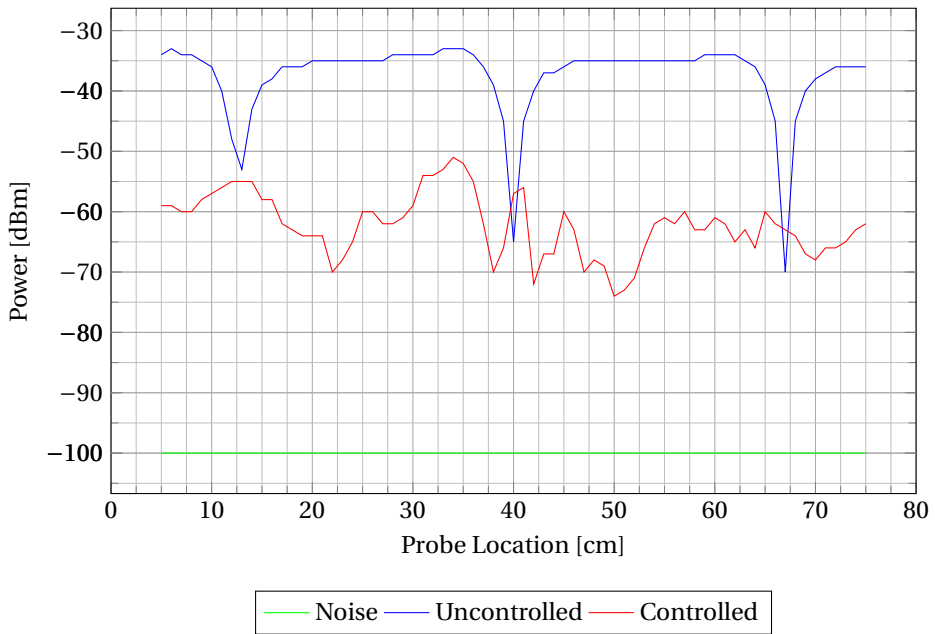


Figure 6.10: Experimental results of the field control within the waveguide.

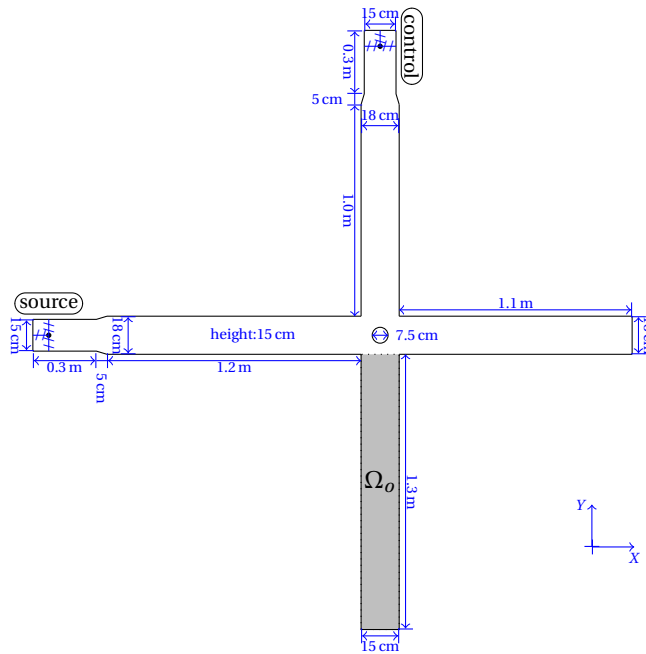


Figure 6.11: Configuration of the test case 2.

region  $\Omega_o$ . As for test case 1, the control pair found experimentally closely matches the numerical one ( $\alpha = 17.1$  dB and  $\Delta\phi = 195^\circ$ ).

The comparison between the experimental test cases with their numerical equivalent shows that experimentally estimating and reconstructing the field or the voltage to compensate is not necessary and can advantageously be replaced by an accurate numerical simulation of the test case. Once the numerical model is built, it can even be used to compute the optimal control values allowing to reach accurately the target field  $\vec{E}_o$ . The experimental part requires thus only to generate appropriate sources with the right amplitude and phase shift given by the numerical model. This is becoming interesting for more complex controlled environments needing many control sources, as it is not conceivable to perform an optimization by hand.

## 6.4 Conclusions

This chapter has provided an experimental validation for the frequency control method for two simple albeit non trivial one-dimensional test cases. A good agreement has been found between the control values given by a manual search of the null target field in the controlled region  $\Omega_o$  and the values given by the optimization algorithm directly embedded in the numerical model solver. This implies that an accurate modelling of the experimental configurations could easily provide the necessary experimental

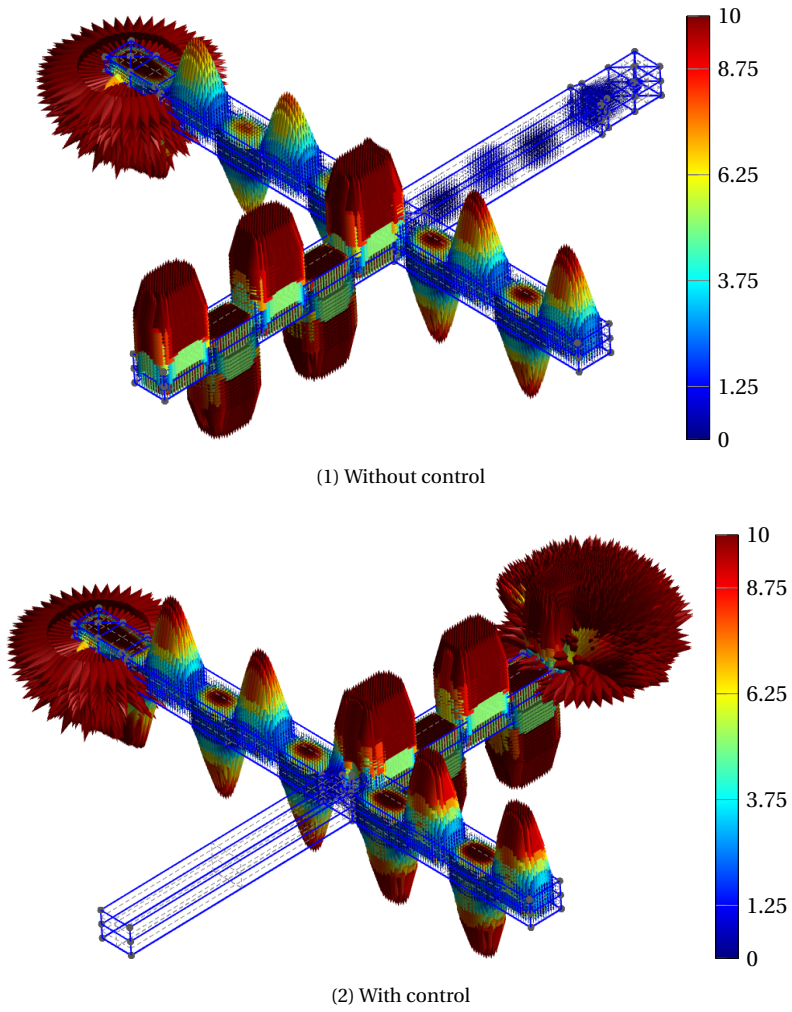


Figure 6.12: Numerical 3D control of the electric field in a waveguide.

control values, even for complex situations presented in chapter 6, where a manual search becomes unaffordable.

Those promising results open interesting perspectives for handling more complex cases involving more control elements in three-dimensional reverberating environments. With the continuously increasing of the performance of phase coherent multi output high-frequency generators, we believe that the initial goal of this thesis, i.e. to control electromagnetic fields in complex and reverberating environments with a “portable” anechoic chamber, will become achievable.





---

## Conclusions

**I**N this thesis we have explored several measurement correction and active shaping methods for electromagnetic fields from complementary points of view, from theory to numerical experiments, to experimental validations. A summary of the main achievements reached during this thesis, as well as general conclusions are presented hereafter, followed by insights and potential improvements for future work.

### 6.5 Main achievements and conclusions

---

Electromagnetic field correction and/or control has been addressed repeatedly over the years. However, only very few articles in the abundant literature have actually crossed the experimental barrier, being usually confined to the often quite optimistic world of numerical simulations. One of our main contribution has consisted in showing that numerical methods could be transposed in practical experimental configurations (relatively) close to industrial needs. For both correction and shaping methods our strategy has been to first analyze the most relevant methods to be later considered experimentally with regards to their implementation complexity and potential applicability.

The first numerical method transposed experimentally is the Angular Deconvolution Method, a correction method that we have modified to cope with potential singularities and to handle complex non-anechoic configurations. The second numerical method transposed experimentally is an optimal control method of the time-harmonic electromagnetic waves. Experimental motivations have led us to validate the method in one-dimensional environments. It has been shown that an accurate model of the experimental configuration could actually provide accurate control values for the experimental test, preventing thereby the need of a tedious and challenging experimental sampling. To the best of our knowledge, these two experimental transpositions had never been attempted before, and the promising results obtained for both methods allow us to envision far more complex applications in the near future.

Working at the interface between theory, numerical methods and experiments, and finding harmony between these quite compartmentalized areas, was also a personal achievement. Indeed, while juggling both computer modeling and laboratory work can

sometimes be frustrating and time consuming, it is quite magical when everything falls into place and when theory and measurements complement each other.

## 6.6 Prospects for future work

---

Numerous prospects for future work exist.

With respect to the correction of electromagnetic measurements in reverberating environments, the Angular Deconvolution Method requires only few improvements to be used for concrete antenna characterization, such as increasing the method robustness during the numerical data processing. Three-dimensional corrections could also be considered, but however would require more sophisticated equipment to perform reliable measurements which somehow go against the goal pursued in this thesis of developing fast, easily implementable and affordable correction methods for laboratories and companies.

With respect to active shaping techniques, several steps remain to be achieved to obtain our sought-after “portable” anechoic chamber. We have indeed obtained promising results for the control of the electric field in one-dimensional geometries but there is a huge gap to bridge to deal with real applications, for which numerous challenging tasks will need to be tackled.

**Electromagnetic field control in three-dimensional environments** To control a region of a three-dimensional environment, several control elements are needed, whose number will determine the quality of the generated electromagnetic field and the size of the controlled region. A system allowing phase coherent generation of multiple signals (32 or 64 for example) having their own phase and amplitude needs to be built. This task is rather complex since it involves to route high-frequency signals ensuring constant phase delay, but also equitable power distribution.

**Non-ideal instrumentation constraints** To cope with real equipment, instruments and situations, the optimization algorithm needs to be adapted to take their imperfections into account by adding constraints to limit the maximum input power for example. In the same way, the resulting field in the uncontrolled part of the environment should also be bounded due to legal constraints.

**Automatic adjustment of the number and location of control sources** To control a region, so far the location and the number of control elements have always been fixed, but could possibly be chosen through the optimization algorithm by requiring an arbitrary level of accuracy of the resulting controlled field.

**Advanced noise reconstruction** To allow the compensation of unknown noise sources that cannot be directly embedded in the numerical model, in addition to the Stratton-Chu integral formula, a faster, more robust and efficient noise reconstruction method should be investigated.

**Active control** To achieve true active electromagnetic noise control, a closed loop control could be implemented to take the variation of the compensated noise into account. This task is complementary to the previous one, since a quasi-real time reconstruction of noise has to be considered.

The three first prospects could be tackled using today's techniques and technology, allowing to deal with more complex three-dimensional environments. The last two prospects are much more complex to solve and represent longer term perspectives. In particular, providing efficient noise reconstruction techniques is a very difficult task whose solution will prove paramount to the eventual conception of a portable anechoic chamber.



---

## Measurement chain from chapter 3

THE complete setup used through the different test cases of chapter 3 has already been presented in the considered chapter. A detailed analysis on the inherent uncertainty introduced by the experimental ADM is also proposed (section 3.2). The quantification of the error on the collected raw values, given by the VNA, due to the whole measurement chain, illustrated in Fig. A.1, has however not been addressed. The measurement chain used in chapter 3 is detailed in Table A.1, with an estimation of the committed error on each collected measurement of  $S_{21}$ . There are of course many factors to take into account, with also significant error discrepancies considering the whole considered parameter ranges. For each parameter, the worst case is chosen to ensure to obtain the worse global error made on the measured samples. For example, the VNA accuracy on the transmission coefficient varies from 0.05 dB to 0.5 dB in function of the measured level. The error is finally estimated to  $\pm 0.9$  dB.

The measurement uncertainty, compared to the method uncertainty bounds given in Fig. 3.2, is completely acceptable. The measurement error might nevertheless increase in less controlled measurement conditions, particularly in the case where the full setup has to be moved from a site to another, which is not taken into account in the error estimation given in Table A.1.

Table A.1: Measurement chain for the Angular Deconvolution Method and error on raw data.

Id	Instrument	Role	Model	Parameter	Error [dB]	Max. [dB]
1	Vector network analyzer	S-parameters measurements	Rohde & Schwarz ZVA24	S21	0.5	0.5
2a	Horn antenna	AUT or TEST antenna	Rohde & Schwarz HL907	Alignment	0.2	0
2b	Horn antenna	AUT or TEST antenna	Schwartzbeck BBHA-9120-AS	Alignment	0.2	0.2
3a	Log-periodic antenna	Emission antenna	Rohde & Schwarz HL223	Alignment	0.2	0
3b	Yagi-Uda antenna	Emission antenna	Handmade	Alignment	0.2	0.2
4a	Fixed turntable	AUT or TEST rotation	Siepel	Azimuth	0.4	0
4b	Mobile turntable	AUT or TEST rotation	Handmade	Azimuth	0.4	0.4
5	Cables	Signal/power transmission	HUBER+SUHNER	Tightening	0.5	0.5
6	Tripod	Emission antenna support	Berlebach	Position	0.3	0.3
Total						0.9



(1) Instruments and control



(2) Using the built-in turntable



(3) Using the mobile turntable

Figure A.1: Experimental setup for the ADM method.



---

## Measurement chain from chapter 6

THE experimental measurements given in chapter 6, from Figs. 6.5 and 6.10, have to be compared to the error introduced by the measurement of the voltage along the microstrip line or the electric field in the waveguide. The aim of the two experimental test cases were to demonstrate the significant decrease of the measured power levels when the right control value is applied. The uncertainty on the collected power should thus be lower enough to discriminate the effect of the applied control. Once again, several parameters in the measurement chain have to be taken into account to obtain relevant error bounds. The most critical ones have been quantified and are reported in Table B.1. The global error is estimated to  $\pm 2.9$  dB, which is rather low for such a setup. This is somehow expected, since very few parameters are changed from one measurement set to another. Assembling and disassembling the setup between measurements would cause a significant increase of the measurement error and has thus been avoided. As seen in Figs. B.1 and B.2, a simple modification on the cable positions or fastening would impact to measured power. The given results in Table B.1, should thus be taken with the greatest caution.

Considering the levels from Figs. 6.5 and 6.10, the measurement error has thus no significant impact on the outcome of the experimental control method.

Table B.1: Measurement chain for the frequency control and error on raw data.

Id	Instrument	Role	Model	Parameter	Error [dB]	Max. [dB]
1	RF generator	1GHz sine generation	Rohde & Schwarz SMF-100A	Output power	0.3	0.3
2	RF splitter	Power splitter between phase shifter and step attenuator	Pulse electronics corp. DASSPLIT2WNF	Power ratio	0.2	0.2
3	Phase shifter/Amplitude attenuator	Digital phase shifter and step attenuator	Handmade	Att./Shift error	0.8	0.8
4a	RF probe	Field to voltage converter	Handmade	Position	1	1
4b	Near field probe	Field to voltage converter	Rohde & Schwarz HZ-14	Position	1.5	0
5a	RF power meter	Power measurement	Handmade	Input power	2.5	2.5
5b	Spectrum	Power measurement	Rohde & Schwarz	Input power	0.5	0
6	Cables	Signal/power transmission	HUBER+SUHNER	Tightening	0.5	0.5
Total						2.9

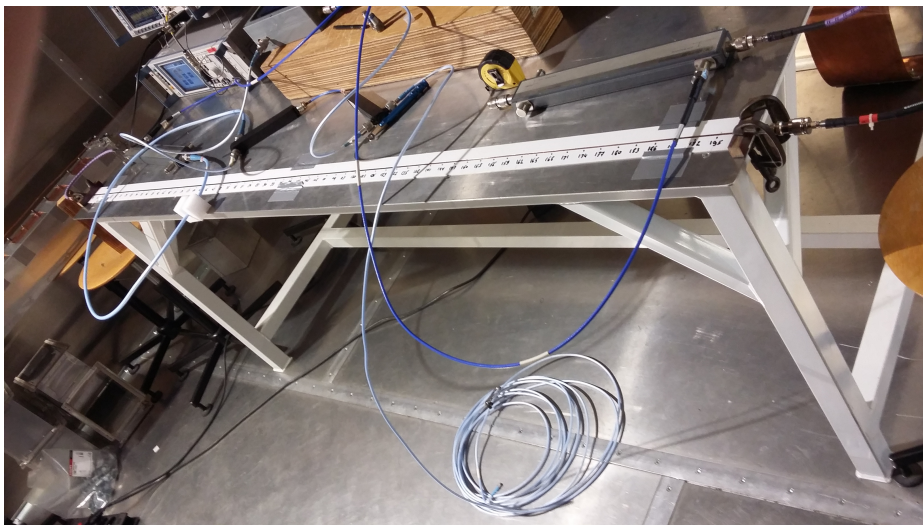


Figure B.1: Experimental setup for the transmission line control.



Figure B.2: Experimental setup for the waveguide network control.



---

## Hardware and software development

WITHOUT instruments and equipments, it is not possible to achieve any practical experiment. Thanks to the EMC laboratory of the University of Liège, a very large amount of the necessary elements of the experimental setups were already available. However, some specific needs have required to develop some hardware or software by ourselves. Some of those projects are presented below.

### C.1 EMCLab

---

The EMC laboratory of the University of Liège is fully automated using commercial softwares to achieve the usual EMC test and procedures. Nevertheless, these commercial softwares are not flexible enough to allow custom control of the driven instruments. For this reason, a fully flexible automation software, namely EMCLab, has been developed. This software relies on the “NI VISA .NET class library” developed by National Instruments. This library provides the necessary interfaces to control and manage any Virtual Instrument Software Architecture (VISA) compatible instrumentation system comprising GPIB, VXI, PXI, Serial, Ethernet, and USB interfaces. To be controllable, the instrument should be compatible with the Standard Commands for Programmable Instruments (SCPI) commands, classically known under the “GPIB” commands, naming both the protocol and the communication bus. With EMCLab, it is therefore possible to control one or several instruments, using a user interface, without the need of physically interacting with each of them. Repetitive measurement tasks are thus easily automated, saving time and allowing to achieve measurements without any human intervention. EMCLab consists in 4 different modules, addressing different purposes described in the following. EMCLab is written in C# and is intended to be run on “Windows” operating systems, and is readily downloadable on <http://www.spirlet.net>.

#### C.1.1 Instrument Library

All the available instruments are referenced in the library to be further used in any automation project. An instrument is added by providing some identification and

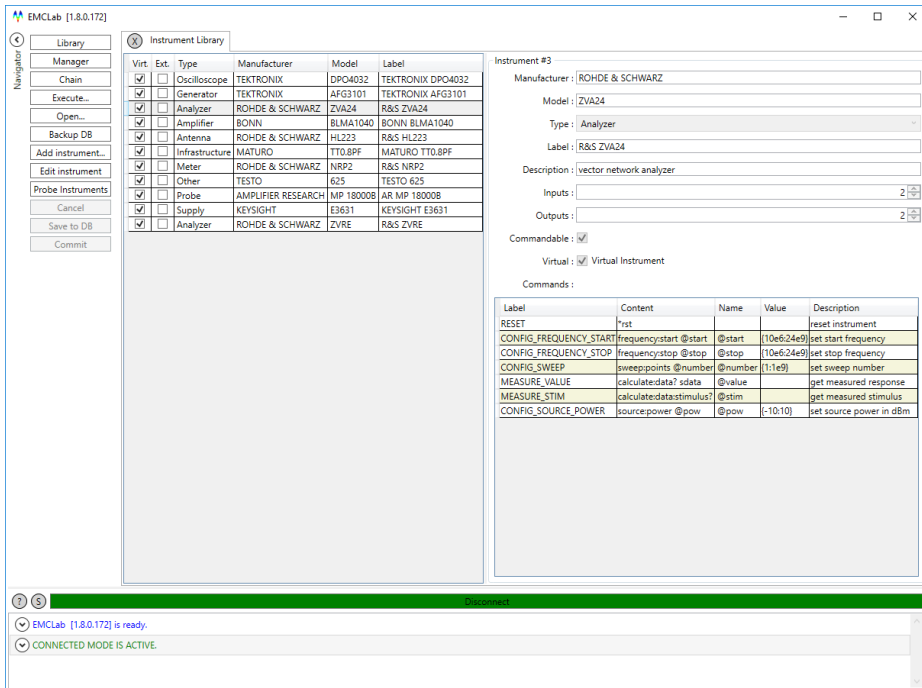


Figure C.1: Instruments library module of EMCLab.

information fields and most importantly the necessary SCPI commands that will be used to interact with the instrument in an automation project. The library module is shown in Fig. C.1 with on the left, the list of available instruments and on the right, information relative to the current selected instrument. The right bottom list on the picture summarizes the encoded SCPI commands, with the needed parameters to be provided during the execution. A parameter can be either an input or an output depending on the desired effect. For example, an output parameter is generally used to set a frequency, whereas an input parameter is used to obtain the result of a voltage measurement command.

### C.1.2 Instrument Manager

The instrument manager is used to command an instrument using SCPI commands manually, i.e. by entering manually the output commands and querying the values in a terminal. This module is very handy to test and validate the commands encoded in the library, or to check the presence of an instrument on a particular bus. This module can also be used for very simple automation. As seen in Fig. C.2, the available detected instruments are listed on the right of the screen, and the individual session of each instrument are displayed on the right of the screen, with the terminal window showing the send/received commands and the responses.

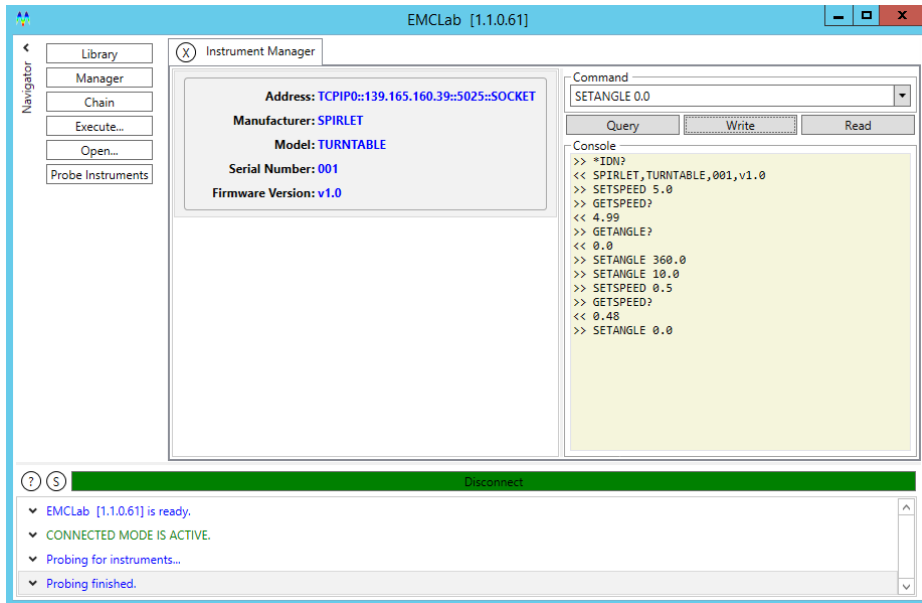


Figure C.2: Instruments manager module of EMCLab.

### C.1.3 Measurement Chain Editor

The measurement chain editor allows to effectively build the measurement chain to be automated. The available instruments from the library are picked up from a list on the top of the window, as depicted in Fig. C.3 and placed in the bottom window, meaning that this instrument will be required during the execution of the automated session. Each selected block instrument has a list of available SCPI commands. Checking a command on the block will automatically add it to the visual automated sequence programming on the right of the window. Several commands from several instruments can be mixed in a fully flexible automated sequence. In addition to the selected commands, control structures can be added to the automated sequence allowing to perform loops, conditional actions, macros, data plotting and recording during the execution,... The parameters needed by the SCPI commands are filled in the bottom part of the window to set the right configuration parameters on each instrument. The parameters related to any control structure are also configured at this time, and it is also possible to use complex parameter expressions containing mathematical function and depending on other parameters, as it would be done using any programming language.

### C.1.4 Execution Engine

The execution engine, shown in Fig. C.4, controls and monitors the execution of the automated sequence previously built in the measurement chain editor. It is also respon-

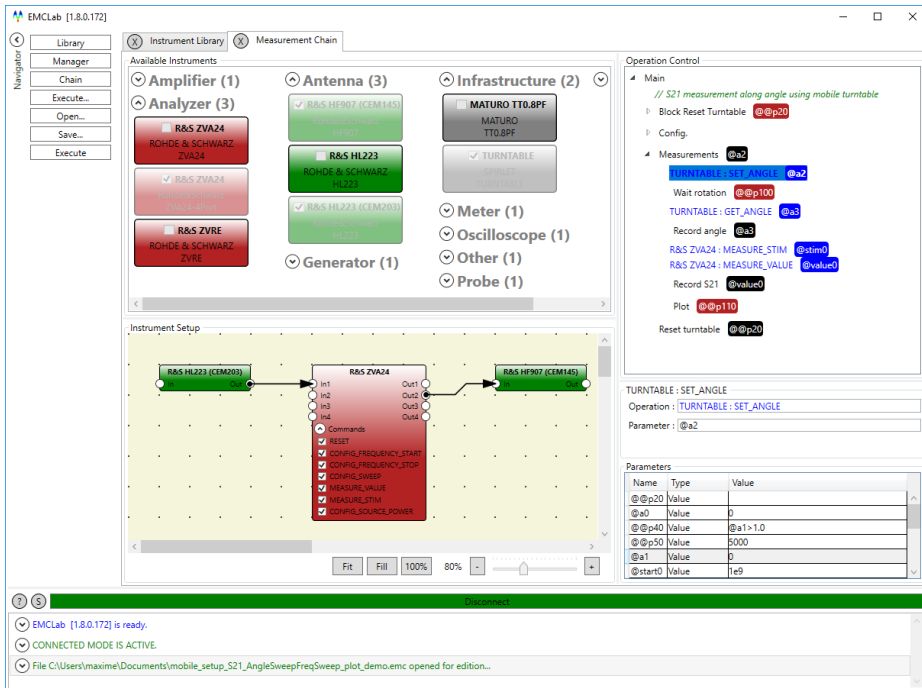


Figure C.3: Measurement Chain Editor module of EMCLab.

sible of recording and displaying the collected data. An “offline” mode is available to test the measurement chain automated sequence without requiring the whole needed set of instruments to be connected. This is very useful, since as in every programming language, some debugging is sooner or later needed. The recorded data are stored in a file on the computer and can also be sent by email at the end of the execution, if the associated option is checked.

## C.2 Mobile turntable

Using the Angular Deconvolution Method, the need of a mobile turntable has led us to build ours. The available turntable in the SAC is integrated and cannot be disassembled from the room. Moreover, the cost of such a commercial mobile turntable is completely unaffordable compared to the planned use ( $\pm 8000$  €). The turntable frame, shown in Fig. C.5, is entirely made of wood to reduce wave reflections. A stepper motor, with a reduction of 256, allows a fine rotation step angle of about  $0.1^\circ$  while providing enough torque to rotate the tray loaded with a tripod (the mechanical tolerance limits practically the minimum step angle to  $1^\circ$ ). The stepper motor is controlled using an “Arduino” card with the “Motor Shield” card. A computer power supply provides the necessary power, and a casing to host the control cards. The “Ethernet Shield” card was also embedded to

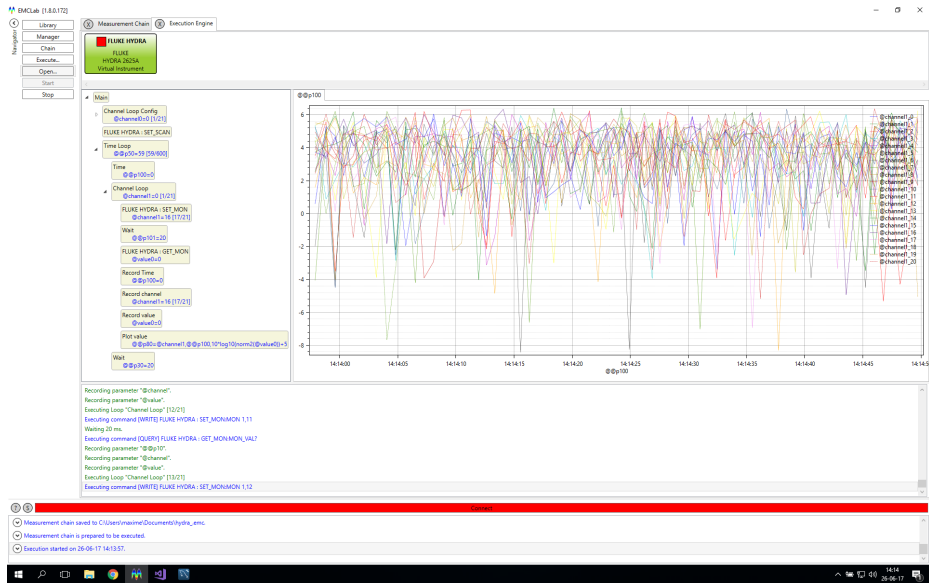


Figure C.4: Execution engine of EMCLab.

allow Ethernet communications, such that the turntable is fully remotely controllable. The control is achieved by sending SCPI commands and is compatible with VISA. The cost of the handmade solution is under 400 €.

### C.3 RF probe meter

Using a small antenna probe connected to a spectrum would have been sufficient to measure the power in the waveguide, using the appropriate probe. But, in the beginning of the experimental test case involving the waveguide network, some issues were encountered due to external electromagnetic disturbances. To overcome this issue, the full setup was moved in a Faraday's cage. Unfortunately, the power cable of the spectrum was still perturbing the measurements. The solution found was to build a simple RF power meter, based on a logarithmic detector chip from Analog Devices (ADL5513), converting the RF measured power to a DC voltage easily measurable by an "Arduino" card and its 8 bits analog to digital converter. The resulting system and the antenna probe inserted in the waveguide are shown in Fig. C.6.

### C.4 Phase coherent dual source generator

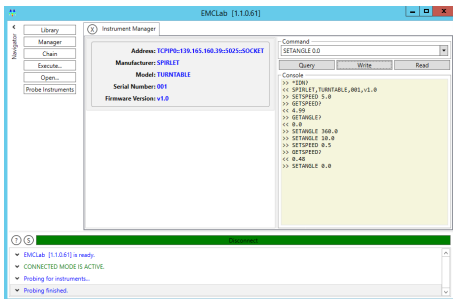
To achieve the frequency control experimental test cases, coherent sources are needed to guarantee the phase shift between the control and the source signals. Such a system



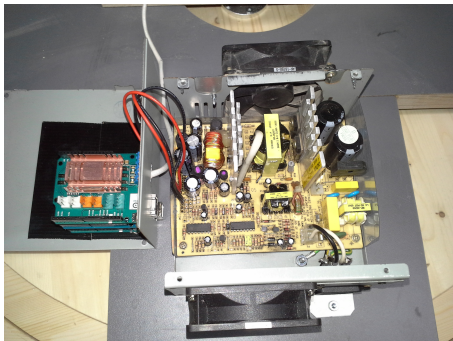
(1) Mobile turntable with remote control



(3) Mobile turntable tripod



(2) Mobile turntable remote control



(4) Mobile turntable controller: inside



(5) Mobile turntable controller: outside

Figure C.5: Mobile turntable.



(1) RF power meter



(2) RF power probe



(3) RF power probe fitting the waveguide slit

Figure C.6: RF power meter and probe.

is once again very expensive and has thus be developed by our means. The aim was to develop a system fed by a single generator providing a 1 GHz sinusoidal signal, allowing on one channel to modify the output amplitude compared to the input signal, and on the second channel to modify the phase shift with respect to the input signal. An 8-bit digital phase shifter (Peregrine Semiconductor DPO PE44820) was used to produce a phase shifted signal on one channel, and a 6-bit digital step attenuator (Peregrine Semiconductor DSA PE4312) was used to get an attenuated signal. Both channel signal amplitudes are determined by the output amplitude of the generator, but the attenuation channel has an extra programmable attenuation from 0.5 dB to 31.5 dB with 0.5 dB step). The phase shift is adjustable from  $0^\circ$  to  $360^\circ$  with  $1.4^\circ$  step on the phase shift channel.

The control of the programmable attenuation and phase shift is achieved using an embedded application run on a “Raspberry Pi” card. The chosen operating system is “Windows 10 IoT Core”, using a convenient touchscreen to modify the attenuation or

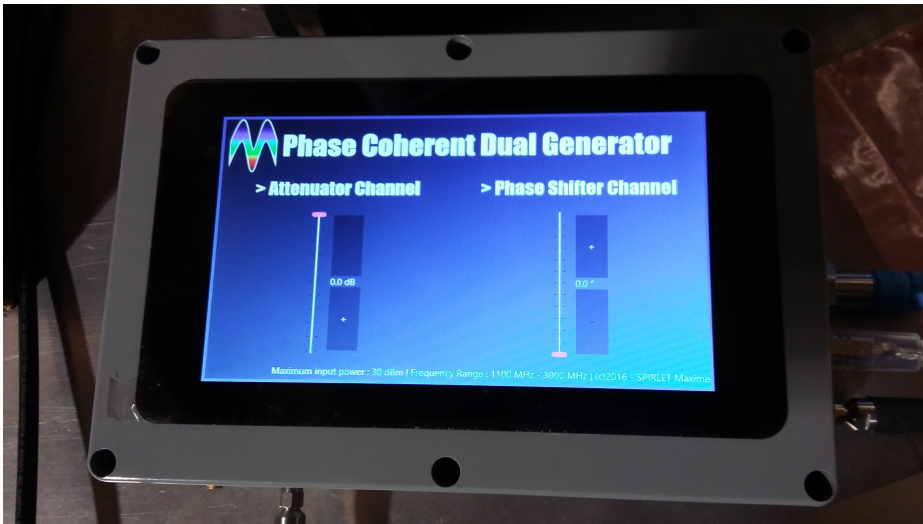


Figure C.7: Dual source phase coherent generator interface.

the phase shift on the respective channels as shown in Fig. C.7. A serial communication allows to send the necessary commands from the “Raspberry Pi” to the Peregrine chips. The phase shift chip DSA PE4312 is normally intended to be used from 1.7 GHz to 2.2 GHz, but using the appropriate settings it is possible to work at 1 GHz. To achieve this, a very helpful support was provided by Mr. David Kirkbride, EU Field Applications Manager/Engineer, from Peregrine Semiconductors UK (many thanks to him).




---

## List of Figures

1.1	Experimental data sweep used for benchmarking the different correction methods. . . . .	15
1.2	Correction methods without noise ( $\sigma_w = 0, \sigma_r = 0$ ). . . . .	16
1.3	Correction methods with noise ( $\sigma_w = 0.01, \sigma_r = 0$ ). . . . .	17
1.4	Correction methods with noise ( $\sigma_w = 0, \sigma_r = 0.03$ ). . . . .	18
1.5	Correction methods with noise ( $\sigma_w = 0.01, \sigma_r = 0.01$ ). . . . .	19
2.1	Illustration example setup: the deconvolution method requires 2 measurement steps in the test ( <i>TEST</i> ) environment plus one step in the reference ( <i>REF</i> ) environment. . . . .	25
2.2	Correction using the angular deconvolution method of the echoic pattern $E_{AUT}^{TEST}$ . The corrected pattern is $\tilde{E}_{AUT}^{REF}$ and should match the true pattern $E_{AUT}^{REF}$ whereas the environment transfer function has been estimated using $E_{REF}^{REF}$ and $E_{REF}^{TEST}$ . . . . .	26
2.3	Environment response estimation and its Fourier Transform. . . . .	27
2.4	Illustration of the reflection caused by a ground plane. . . . .	28
2.5	Radiating patterns of two different antennas ( <i>TEST</i> and <i>AUT</i> ) in free-space ( <i>REF</i> ) or in the presence of a PEC ground plane ( <i>TEST</i> ), with the effect of introducing grating lobes in the antenna patterns $P_{REF}^{TEST}$ and $P_{AUT}^{TEST}$ . . . . .	29
3.1	Setup of the uncertainty tests. . . . .	32
3.2	Experimental deconvolution with uncertainty bounds (1/3). . . . .	33
3.2	Experimental deconvolution with uncertainty bounds (2/3). . . . .	34
3.2	Experimental deconvolution with uncertainty bounds (3/3). . . . .	35
3.3	Setup of the test case 1. . . . .	39
3.4	Setup of the test case 2. . . . .	39
3.5	Experimental deconvolution setup for test case 1. . . . .	40
3.6	Experimental deconvolution results for test case 1. . . . .	40
3.7	Experimental deconvolution results for test case 2. . . . .	41
3.8	Parametric results depending on $d$ for the experimental deconvolution at 1000 MHz, using a log-periodic fixed antenna. . . . .	42

3.9	Parametric results depending on $d$ for the experimental deconvolution at 1000 MHz, using a yagi-uda fixed antenna. . . . .	43
3.10	Parametric results depending on $s$ for the experimental deconvolution at 1000 MHz, using a log-periodic fixed antenna. . . . .	44
3.11	Parametric results depending on $s$ for the experimental deconvolution at 1000 MHz, using a yagi-uda fixed antenna. . . . .	45
3.12	Visualization of the worse reconstruction result from Fig. 3.8 obtained using Antenna "A" with $d = 390$ cm. . . . .	46
3.13	Visualization of the worse reconstruction result from Fig. 3.9 obtained using Antenna "A" with $d = 450$ cm. . . . .	47
3.14	Visualization of the worse reconstruction result from Fig. 3.10 obtained using Antenna "A" with $s = 120$ cm. . . . .	48
3.15	Visualization of the worse reconstruction result from Fig. 3.11 obtained using Antenna "A" with $s = 180$ cm. . . . .	49
3.16	Experimental deconvolution setup for test case 4. . . . .	49
3.17	Experimental deconvolution results for test case 3. . . . .	50
3.18	Experimental deconvolution results for test case 4. . . . .	50
3.19	Environment impulse reponse for the best and the worse reconstruction errors. . . . .	51
3.20	Cross-correlation between the environment impulse reponses obtained with <i>REF</i> antenna and <i>TEST</i> antenna for two different configurations yielding the best ( $\Gamma_1$ ) and the worse ( $\Gamma_2$ ) reconstruction errors. . . . .	52
3.21	Experimental deconvolution results for test case 5. . . . .	53
3.22	Experimental deconvolution setup for test case 6. . . . .	54
3.23	Experimental deconvolution results for test case 6. . . . .	55
4.1	Exact control on $\Omega$ by the boundary $\Gamma_c$ using HUM. . . . .	61
4.2	Boundary control of the scalar wave equation in a 2D cavity to reach a null field at time $T$ (1/4). . . . .	65
4.2	Boundary control of the scalar wave equation in a 2D cavity to reach a null field at time $T$ (2/4). . . . .	66
4.2	Boundary control of the scalar wave equation in a 2D cavity to reach a null field at time $T$ (3/4). . . . .	67
4.2	Boundary control of the scalar wave equation in a 2D cavity to reach a null field at time $T$ (4/4). . . . .	68
4.3	Boundary control of the scalar wave equation in a 2D cavity to reach a Gaussian pulse ("A") or a sine ("B") field at time $T$ . . . . .	69
4.4	Inner control of the scalar wave equation in a 2D cavity to reach an annular Gaussian field at time $T$ (1/4). . . . .	70
4.4	Inner control of the scalar wave equation in a 2D cavity to reach an annular Gaussian field at time $T$ (2/4). . . . .	71
4.4	Inner control of the scalar wave equation in a 2D cavity to reach an annular Gaussian field at time $T$ (3/4). . . . .	72
4.4	Inner control of the scalar wave equation in a 2D cavity to reach an annular Gaussian field at time $T$ (4/4). . . . .	73
4.5	Theoretical TR. . . . .	75

4.6	Discretization of the TRM. . . . .	78
4.7	Comparison of TR refocusing between a continuous ideal TRM and a discrete TRM for different TRM elements at 1 GHz in free-space. . . . .	79
4.8	Comparison of the TR refocusing with a fixed TRM of 360 elements at 2 different frequencies in free-space. . . . .	80
4.9	Comparison of TR refocusing with different numbers of TRM elements at 1 GHz in free-space. . . . .	82
4.10	Image current theory principles for a PEC (left) or a PMC (right) ground plane. $Il$ is the electric dipole moment and $Kl$ is the magnetic dipole moment. . . . .	83
4.11	Illustration of the image currents distribution in a 2D cavity up to the 5 <sup>th</sup> order. . . . .	84
4.12	Gaussian pulse in the time domain and its corresponding spectrum. . . . .	85
4.13	Comparison of the TR refocusing ( $E_z(t = t_R)$ ) with different numbers of TRM elements for a Gaussian pulse centered at 1 GHz with a 500 MHz bandwidth in a reverberating cavity. . . . .	87
4.14	Illustration of the equivalence principle by two equivalent configurations. . . . .	88
4.15	Composition of the TREC . . . . .	88
4.16	The TR steps for the TREC. . . . .	90
4.17	Comparison of the TR refocusing ( $E_z(t = t_R)$ ) using a TREC with different numbers of TRM and ESN elements for a Gaussian pulse centered at 1 GHz with a 500 MHz bandwidth. The ESN elements are isotropic. . . . .	91
4.18	Comparison of the TR refocusing ( $E_z(t = t_R)$ ) using a TREC with different numbers of TRM and ESN elements for a Gaussian pulse centered at 1 GHz with a 500 MHz bandwidth. The ESN elements are directive. . . . .	92
4.19	TR refocusing ( $E_z(t = t_R)$ ) using a TREC with 8 TRM and 32 ESN elements for a Gaussian pulse centered at 1 GHz with a 500 MHz bandwidth. Only a quarter of the ESN is active, with directive radiating elements. . . . .	93
5.1	Generic configuration for the optimal control of the electric field in the $\Omega_o$ region. . . . .	97
5.2	Configuration of test case 1. . . . .	99
5.3	2D control in free-space of the electric field in a target zone (1/2). . . . .	99
5.3	2D control in free-space of the electric field in a target zone (2/2). . . . .	100
5.4	Configuration of test case 2. . . . .	101
5.5	2D control in a reverberation chamber of the electric field in a target zone (1/2). . . . .	101
5.5	2D control in a reverberation chamber of the electric field in a target zone (2/2). . . . .	102
5.6	Configuration of test case 3. . . . .	103
5.7	2D control in a realistic room of the electric field in a target zone (1/2). . . . .	104
5.7	2D control in a realistic room of the electric field in a target zone (2/2). . . . .	105
5.8	2D control in free-space of the electric field in a target zone (1/2). . . . .	106
5.8	2D control in free-space of the electric field in a target zone (2/2). . . . .	107
5.9	2D control in a reverberation chamber of the electric field in a target zone (1/2). . . . .	108

5.9	2D control in a reverberation chamber of the electric field in a target zone (2/2). . . . .	109
5.10	2D control in a realistic room of the electric field in a target zone (1/2). . . .	110
5.10	2D control in a realistic room of the electric field in a target zone (2/2). . . .	111
6.1	Block diagram of the source/control generator: $S_\alpha$ is applied to the source while $S_\phi$ is applied to the control. $S$ denotes a power splitter. . . . .	114
6.2	Configuration of the experimental test case 1. . . . .	115
6.3	Crosscut of the microstrip line. . . . .	115
6.4	Experimental setup of the test case 1. . . . .	116
6.5	Experimental results of the voltage control within the microstrip line. . . .	116
6.6	Configuration of the test case 4. . . . .	117
6.7	Numerical 1D control of the electric field in a transmission line. . . . .	118
6.8	Configuration of the experimental test case 2. . . . .	119
6.9	Experimental setup of the test case 2. . . . .	120
6.10	Experimental results of the field control within the waveguide. . . . .	120
6.11	Configuration of the test case 2. . . . .	121
6.12	Numerical 3D control of the electric field in a waveguide. . . . .	122
A.1	Experimental setup for the ADM method. . . . .	131
B.1	Experimental setup for the transmission line control. . . . .	135
B.2	Experimental setup for the waveguide network control. . . . .	135
C.1	Instruments library module of EMCLab. . . . .	138
C.2	Instruments manager module of EMCLab. . . . .	139
C.3	Measurement Chain Editor module of EMCLab. . . . .	140
C.4	Execution engine of EMCLab. . . . .	141
C.5	Mobile turntable. . . . .	142
C.6	RF power meter and probe. . . . .	143
C.7	Dual source phase coherent generator interface. . . . .	144




---

## List of Tables

3.1	Experimental deconvolution uncertainty results ( $Q_x$ where $x$ is the frequency in MHz) . . . . .	37
-----	---	----

3.2	Summary of the considered test cases. . . . .	38
A.1	Measurement chain for the Angular Deconvolution Method and error on raw data. . . . .	130
B.1	Measurement chain for the frequency control and error on raw data. . . . .	134





---

## Bibliography

- [1] M. Abramowitz and I. Stegun. *Handbook of Mathematical Functions: With Formulas, Graphs, and Mathematical Tables*. 9th. Applied mathematics series. Dover Publications, 1970.
- [2] F. Alabau-Boussouira, R. Brockett, O. Glass, J. L. Rousseau, and E. Zuazua. *Control of Partial Differential Equations*. 2012.
- [3] E. Amador, C. Lemoine, P. Besnier, and A. Laisné. “Reverberation Chamber Modeling Based on Image Theory: Investigation in the Pulse Regime”. In: *Electromagnetic Compatibility, IEEE Transactions on* 52.4 (Nov. 2010), pp. 778–789.
- [4] E. Amador, C. Lemoine, P. Besnier, and A. Laisné. “Studying the pulse regime in a reverberation chamber with a model based on image theory”. In: *Electromagnetic Compatibility (EMC), 2010 IEEE International Symposium on*. July 2010, pp. 520–525.
- [5] E. Amador. “Modèles de compréhension par la théorie des images des phénomènes transitoires et du régime permanent en chambre réverbérante électromagnétique”. PhD thesis. INSA de Rennes, Oct. 2011.
- [6] M. I. Andries. “Recherche de méthodes expérimentales de simulation de canaux de propagation en chambre réverbérante à brassage de modes”. PhD thesis. INSA de Rennes, Apr. 2013.
- [7] R. Ayestaran, G. Leon, S. Loredó, J. Lopez-Fernandez, and F. Las-Heras. “Sparse deconvolution based on regularisation for echo correction in antenna measurement”. In: *Microwaves, Antennas Propagation, IET* 6.12 (Sept. 2012), pp. 1299–1305.
- [8] L. Babour. “Etude et Conception d’Antennes Ultra Large Bande Miniaturisées en Impulsionnel”. PhD thesis. Institut National Polytechnique de Grenoble - INPG, May 2009.
- [9] C. A. Balanis. *Antenna Theory: Analysis and Design*. 2nd Ed. Wiley, 1997.
- [10] C. Bardos, G. Lebeau, and J. Rauch. “Sharp Sufficient Conditions for the Observation, Control, and Stabilization of Waves from the Boundary”. In: *SIAM Journal on Control and Optimization* 30.5 (Sept. 1992), pp. 1024–42.

- [11] X. Bégaud. *Les antennes Ultra Large Bande*. Collection Télécom. Hermes Science Publications, 2010.
- [12] J. Benoit, C. Chauviere, and P. Bonnet. “A new technique to obtain a specific electromagnetic field at a given time”. In: *Electromagnetic Compatibility (APEMC), 2012 Asia-Pacific Symposium on*. May 2012, pp. 521–524.
- [13] J. Benoit, C. Chauvière, and P. Bonnet. “Identification de sources temporelles pour des problèmes de lignes de transmission”. In: *17e Colloque International et Exposition sur la Compatibilité Electromagnetique (CEM2014 Clermont-Ferrand)*. 2014.
- [14] J. Benoit, C. Chauvière, and P. Bonnet. “Source identification in time domain electromagnetics”. In: *Journal of Computational Physics* 231.8 (2012), pp. 3446–3456.
- [15] J.-P. Berenger. “A perfectly matched layer for the absorption of electromagnetic waves”. In: *Journal of Computational Physics* 114.2 (1994), pp. 185–200.
- [16] J.-P. Berenger. *Perfectly Matched Layer (PML) for Computational Electromagnetics*. Ed. by C. A. Balanis. Synthesis Lectures on Computational Electromagnetics. Morgan & Claypool, 2007, p. 117.
- [17] M. Bergounioux, K. Ito, and K. Kunisch. “Primal-Dual Strategy for Constrained Optimal Control Problems”. In: *SIAM Journal on Control and Optimization* 37.4 (1999), pp. 1176–19.
- [18] M. Bergounioux and K. Kunisch. “Augmented Lagrangian Techniques for Elliptic State Constrained Optimal Control Problems”. In: *SIAM Journal on Control and Optimization* 35.5 (1997), pp. 1524–1543.
- [19] J. Black D.N. and E. Joy. “Test zone field compensation”. In: *Antennas and Propagation, IEEE Transactions on* 43.4 (Apr. 1995), pp. 362–368.
- [20] J. Böm and U. Kuhl. “Wave Front Shaping in Quasi-One-Dimensional Waveguides”. In: *2016 IEEE International Workshop on Metrology for AeroSpace (MetroAeroSpace) Proceedings* (June 23, 2016).
- [21] J. F. Bonnans and E. Casas. “Optimal Control of Semilinear Multistate Systems with State Constraints”. In: *SIAM Journal on Control and Optimization* 27.2 (Mar. 1989), pp. 446–10.
- [22] A. Bossavit. “Whitney forms: a class of finite elements for three-dimensional computations in electromagnetism”. In: *IEE Proceedings A - Physical Science, Measurement and Instrumentation, Management and Education - Reviews* 135.8 (Nov. 1988), pp. 493–500.
- [23] J. P. Boyd. “A fast algorithm for Chebyshev, Fourier, and sinc interpolation onto an irregular grid”. In: *Journal of Computational Physics* 103.2 (1992), pp. 243–257.
- [24] W. Briggs, V. Henson, and S. McCormick. *A Multigrid Tutorial, Second Edition*. Second. Society for Industrial and Applied Mathematics, 2000.
- [25] J. C. Burgess. “Active adaptive sound control in a duct: A computer simulation”. In: *The Journal of the Acoustical Society of America* 70.3 (1981), pp. 715–726.

- [26] R. Carminati, R. Pierrat, J. de Rosny, and M. Fink. “Theory of the time reversal cavity for electromagnetic fields”. In: *Opt. Lett.* 32.21 (Nov. 2007), pp. 3107–3109.
- [27] E. Casas. “Boundary Control of Semilinear Elliptic Equations with Pointwise State Constraints”. In: *SIAM Journal on Control and Optimization* 31.4 (July 1993), pp. 993–14.
- [28] E. Casas. “Control of an Elliptic Problem with Pointwise State Constraints”. In: *SIAM Journal on Control and Optimization* 24.6 (Nov. 1986), pp. 1309–10.
- [29] E. Casas. “Second Order Analysis for Bang-Bang Control Problems of PDEs”. In: *SIAM Journal on Control and Optimization* 50.4 (2012), pp. 2355–2372.
- [30] E. Casas, F. Troltsch, and A. Unger. “Second Order Sufficient Optimality Conditions for Some State-constrained Control Problems of Semilinear Elliptic Equations”. In: *SIAM Journal on Control and Optimization* 38.5 (2000), pp. 1369–23.
- [31] D. Cassereau and M. Fink. “Time-reversal of ultrasonic fields. III. Theory of the closed time-reversal cavity”. In: *Ultrasonics, Ferroelectrics and Frequency Control, IEEE Transactions on* 39.5 (Sept. 1992), pp. 579–592.
- [32] C. Castro, S. Micu, and A. Münch. “Numerical approximation of the boundary control for the wave equation with mixed finite elements in a square”. In: *IMA Journal of Numerical Analysis* 28.1 (2008), pp. 186–214.
- [33] H. Chen, S. Van Huffel, and J. Vandewalle. “Frequency-selective techniques based on singular value decomposition (SVD), total least squares (TLS), and bandpass filtering”. In: *Proc. SPIE* 2296 (1994), pp. 601–611.
- [34] Council of European Union. *Directive 2014/30/EU of the european parliament and of the council.* 2014.
- [35] P. Courilleau, T. H. Molinaro, and I. G. Stratis. “On the controllability of Maxwell’s equations in a class of complex media”. In: *Bull. Greek Math. Soc* 54 (2007), pp. 97–113.
- [36] P. Courilleau, T. H. Molinaro, and I. G. Stratis. “On the controllability of time-harmonic electromagnetic fields in chiral media”. In: *Advances in Mathematical Sciences and Applications* 16.2 (2006), p. 491.
- [37] A. Cozza. “Emulating an Anechoic Environment in a Wave-Diffusive Medium Through an Extended Time-Reversal Approach”. In: *Antennas and Propagation, IEEE Transactions on* 60.8 (2012), pp. 3838–3852.
- [38] A. Cozza. “Statistics of the performance of time reversal in a lossy reverberating medium”. In: *Physical Review E: Statistical, Nonlinear, and Soft Matter Physics* 80.5 (Nov. 2009), pp. 056604–056614.
- [39] A. Cozza. “The Role of Losses in the Definition of the Overmoded Condition for Reverberation Chambers and Their Statistics”. In: *IEEE Transactions on Electromagnetic Compatibility* 53.2 (2011), pp. 296–307.
- [40] A. Cozza and A. Abou-El-Aileh. “Accurate Radiation-Pattern Measurements in a Time-Reversal Electromagnetic Chamber”. In: *IEEE Antennas and Propagation Magazine* 52.2 (2010), pp. 186–193.

- [41] A. Cozza and H. Moussa. “Enforcing a deterministic polarization in a reverberating environment”. In: *Electronics Letters / IEE Electronics Letters* 45.25 (Dec. 2009), pp. 1299–1301.
- [42] A. Cozza and H. Moussa. “Polarization selectivity for pulsed fields in a reverberation chamber”. In: *2010 Asia-Pacific Symposium on Electromagnetic Compatibility (APEMC)*. Chine, Apr. 2010, pp. 574–577.
- [43] A. Cozza and H. Moussa. “Procédé de contrôle de la directivité et la polarisation de distributions cohérentes de champ dans un milieu réverbérant”. Brevet WO 2010/112763. Oct. 2010.
- [44] M. Dadić and R. Zentner. “A technique for elimination of reflected rays from antenna measurements performed in echoic environment”. In: *{AEU} - International Journal of Electronics and Communications* 61.2 (2007), pp. 90–94.
- [45] M. Darbas, O. Goubet, and S. Lohrengel. “Exact boundary controllability of the second-order Maxwell system: Theory and numerical simulation”. In: *Computers & Mathematics with Applications* 63.7 (2012), pp. 1212–1237.
- [46] M. Darbas and S. Lohrengel. “Numerical reconstruction of small perturbations in the electromagnetic coefficients of a dielectric material”. In: *Journal of Computational Mathematics* 32.1 (2014), pp. 21–38.
- [47] M. Davy, J. de Rosny, and M. Fink. “Focusing and amplification of electromagnetic waves by time-reversal in an leaky reverberation chamber”. In: *Antennas and Propagation Society International Symposium, 2009. APSURSI '09. IEEE*. 2009, pp. 1–4.
- [48] J. De La Gorgue de Rosny. “Milieux réverbérants et réversibilité”. PhD thesis. 2000, 1 vol., 159 p.
- [49] C. Draeger and M. Fink. “One-Channel Time Reversal of Elastic Waves in a Chaotic 2D-Silicon Cavity”. In: *Physical Review Letters* 79 (1997), pp. 407–410.
- [50] J. Du, S. Liu, and Z. Lin. “Broadband optical cloak and illusion created by the low order active sources”. In: *Opt. Express* 20.8 (Apr. 2012), pp. 8608–8617.
- [51] Z. Du, J. I. Moon, S.-s. Oh, J. Koh, and T. K. Sarkar. “Generation of Free Space Radiation Patterns From Non-Anechoic Measurements Using Chebyshev Polynomials”. In: *Antennas and Propagation, IEEE Transactions on* 58.8 (Aug. 2010), pp. 2785–2790.
- [52] P. Dular, C. Geuzaine, F. Henrotte, and W. Legros. “A general environment for the treatment of discrete problems and its application to the finite element method”. In: *IEEE Transactions on Magnetics* 34.5 (Sept. 1998), pp. 3395–3398.
- [53] A. Dutt and V. Rokhlin. “Fast Fourier Transforms for Nonequispaced Data”. In: *SIAM Journal on Scientific Computing* 14.6 (1993), pp. 1368–1393.
- [54] W. M. G. Dyab, T. K. Sarkar, A. Garcia-Lamperez, M. Salazar-Palma, and M. A. Lagunas. “A Critical Look at the Principles of Electromagnetic Time Reversal and its Consequences”. In: *Antennas and Propagation Magazine, IEEE* 55.5 (Oct. 2013), pp. 28–62.

- [55] W. Dyab, T. Sarkar, and M. Salazar-Palma. "Antenna reciprocity and the theory of electromagnetic time reversal". In: *Antennas and Propagation Society International Symposium (APSURSI), 2012 IEEE*. July 2012, pp. 1–2.
- [56] A. Farahbakhsh and M. Khalaj-AmirHosseini. "Analytic Method to Retrieve Antenna Free-Space Radiation Pattern Above Ground Plane". In: *Antennas and Wireless Propagation Letters, IEEE* 14 (2015), pp. 731–734.
- [57] J. Feng, C. Liao, L. L. Chen, and H. J. Zhou. "Amplification of electromagnetic waves by time reversal mirror in a leaky reverberation chamber". In: *Microwave and Millimeter Wave Technology (ICMMT), 2012 International Conference on*. Vol. 5. May 2012, pp. 1–4.
- [58] J. A. Fessler and B. P. Sutton. "Nonuniform fast Fourier transforms using min-max interpolation". In: *IEEE Transactions on Signal Processing* 51.2 (2003), pp. 560–574.
- [59] M. Fink. "Time reversal of ultrasonic fields. I. Basic principles". In: *Ultrasonics, Ferroelectrics and Frequency Control, IEEE Transactions on* 39.5 (Sept. 1992), pp. 555–566.
- [60] M. Fink. "Time-reversed Acoustics". In: *Scientific American Magazine* (Nov. 1999), pp. 91–97.
- [61] M. Fink and C. Prada. "Acoustic time-reversal mirrors". In: *Inverse Problems* 17.1 (2001), R1.
- [62] V. Fiumara, A. Fusco, V. Matta, and I. M. Pinto. "Free-Space Antenna Field / Pattern Retrieval in Reverberation Environments". In: *Antennas and Wireless Propagation Letters, IEEE* vol. 4 (2005).
- [63] N. Fortino. "Conception et caractérisation d'antennes imprimées pour systèmes Ultra-Large-Bande impulsions". PhD thesis. Université de Nice Sophia-Antipolis, Feb. 2006.
- [64] B. Fourestie and Z. Altman. "Gabor schemes for analyzing antenna measurements". In: *Antennas and Propagation, IEEE Transactions on* 49.9 (Sept. 2001), pp. 1245–1253.
- [65] B. Fourestie, Z. Altman, and M. Kanda. "Anechoic chamber evaluation using the matrix pencil method". In: *Electromagnetic Compatibility, IEEE Transactions on* 41.3 (Aug. 1999), pp. 169–174.
- [66] B. Fourestie, Z. Altman, and M. Kanda. "Efficient detection of resonances in anechoic chambers using the matrix pencil method". In: *Electromagnetic Compatibility, IEEE Transactions on* 42.1 (Feb. 2000), pp. 1–5.
- [67] B. Fourestie, Z. Altman, J. Wiart, and A. Azoulay. "Correlate measurements at different test sites". In: *Antennas and Propagation, IEEE Transactions on* 47.10 (Oct. 1999), pp. 1569–1573.
- [68] A. E. Fridman. *The Quality of Measurements: A Metrological Reference*. New York, NY: Springer New York, 2012.

- [69] M. Frigo and S. Johnson. "FFTW: an adaptive software architecture for the FFT". In: *Acoustics, Speech and Signal Processing, 1998. Proceedings of the 1998 IEEE International Conference on*. Vol. 3. May 1998, 1381–1384 vol.3.
- [70] C. R. Fuller and A. H. von Flotow. "Active control of sound and vibration". In: *IEEE Control Systems* 15.6 (Dec. 1995), pp. 9–19.
- [71] C. Geuzaine and J.-F. Remacle. "Gmsh: A 3-D finite element mesh generator with built-in pre- and post-processing facilities". In: *International Journal for Numerical Methods in Engineering* 79.11 (2009), pp. 1309–1331.
- [72] R. Glowinski, C.-H. Li, and J.-L. Lions. "A numerical approach to the exact boundary controllability of the wave equation (I) Dirichlet controls: Description of the numerical methods". In: *Japan Journal of Applied Mathematics* 7.1 (1990), pp. 1–76.
- [73] J.-B. Gros. "Spatial statistics of open chaotic cavities : Applications to electromagnetic cavities". Theses. Université Nice Sophia Antipolis, Dec. 2014.
- [74] P. Hallbjörner. "Reflective antenna efficiency measurements in reverberation chambers". In: *Microwave and Optical Technology Letters* 30.5 (2001), pp. 332–335.
- [75] P. Hansen. *Rank-Deficient and Discrete Ill-Posed Problems*. Society for Industrial and Applied Mathematics, 1998.
- [76] T. B. Hansen. "Spherical Near-Field Scanning With Higher-Order Probes". In: *IEEE Transactions on Antennas and Propagation* 59.11 (Nov. 2011), pp. 4049–4059.
- [77] R. Harrington. *Time-Harmonic Electromagnetic Fields*. IEEE Press Series on Electromagnetic Wave Theory. Wiley, 1961.
- [78] M. Hiebel. *Fundamentals of Vector Network Analysis*. Rohde & Schwarz, 2007.
- [79] D. A. Hill. *Electromagnetic theory of reverberation chambers*. Tech. rep. 1506. Boulder, CO, ETATS-UNIS: National Institute of Standards and Technology, Dec. 1998, 60 pp.
- [80] D. A. Hill. "Plane wave integral representation for fields in reverberation chambers". In: *IEEE Transactions on Electromagnetic Compatibility* 40 (3 1998), pp. 209–217.
- [81] C. Holloway, H. Shah, R. Pirkl, W. Young, D. Hill, and J. Ladbury. "Reverberation Chamber Techniques for Determining the Radiation and Total Efficiency of Antennas". In: *Antennas and Propagation, IEEE Transactions on* 60.4 (Apr. 2012), pp. 1758–1770.
- [82] Y. Hua and T. Sarkar. "Matrix pencil method for estimating parameters of exponentially damped/undamped sinusoids in noise". In: *Acoustics, Speech and Signal Processing, IEEE Transactions on* 38.5 (May 1990), pp. 814–824.
- [83] Y. Hua and T. Sarkar. "On SVD for estimating generalized eigenvalues of singular matrix pencil in noise". In: *Circuits and Systems, 1991., IEEE International Symposium on*. June 1991, 2780–2783 vol.5.

- [84] Y. Huang, R. Narayanan, and G. Kadambi. "Electromagnetic coupling effects on the cavity measurement of antenna efficiency". In: *Antennas and Propagation, IEEE Transactions on* 51.11 (Nov. 2003), pp. 3064–3071.
- [85] M. Huynh. *Wideband Compact Antennas for Wireless Communication Applications*. Virginia Polytechnic Institute and State University, 2004.
- [86] K. Ito and K. Kunisch. *Lagrange Multiplier Approach to Variational Problems and Applications*. Society for Industrial and Applied Mathematics, 2008.
- [87] J. W. T. James W. Cooley. "An Algorithm for the Machine Calculation of Complex Fourier Series". In: *Mathematics of Computation* 19.90 (1965), pp. 297–301.
- [88] J. M. Jin, Z. Lou, Y. J. Li, N. W. Riley, and D. J. Riley. "Finite Element Analysis of Complex Antennas and Arrays". In: *IEEE Transactions on Antennas and Propagation* 56.8 (Aug. 2008), pp. 2222–2240.
- [89] J. Jin. *The Finite Element Method in Electromagnetics*. A Wiley-Interscience publication. Wiley, 2002.
- [90] J. Jin and D. Riley. *Finite Element Analysis of Antennas and Arrays*. Wiley, 2009.
- [91] E. Joy and D. Paris. "Spatial sampling and filtering in near-field measurements". In: *Antennas and Propagation, IEEE Transactions on* 20.3 (May 1972), pp. 253–261.
- [92] P.-S. Kildal, C. Carlsson, and J. Yang. "Measurement of free-space impedances of small antennas in reverberation chambers". In: *Microwave and Optical Technology Letters* 32.2 (2002), pp. 112–115.
- [93] J. Koh, A. De, T. Sarkar, H. Moon, W. Zhao, and M. Salazar-Palma. "Free Space Radiation Pattern Reconstruction from Non-Anechoic Measurements Using an Impulse Response of the Environment". In: *Antennas and Propagation, IEEE Transactions on* 60.2 (Feb. 2012), pp. 821–831.
- [94] J. Kunisch and J. Pamp. "UWB radio channel modeling considerations". In: *ICEAA*. Turin, Sept. 2003.
- [95] J. E. Lagnese. "Exact Boundary Controllability of Maxwell's Equations in a General Region". In: *SIAM Journal on Control and Optimization* 27.2 (Mar. 1989), pp. 374–15.
- [96] G. Le Fur. "Contribution aux méthodes de mesure de rendement d'antenne. Caractérisation par "ULB Wheeler Cap" et via le retournement temporel en chambre réverbérante". PhD thesis. Université Rennes 1, Nov. 2009.
- [97] D. A. Leatherwood and E. B. Joy. "Plane wave, pattern subtraction, range compensation". In: *IEEE Transactions on Antennas and Propagation* 49.12 (Dec. 2001), pp. 1843–1851.
- [98] G. Lebeau and M. Nodet. "Experimental Study of the HUM Control Operator for Linear Waves". In: *Experimental Mathematics* 19.1 (2010), pp. 93–120.
- [99] C. Lee, A. Duffy, and C. Lee. "Antenna Efficiency Measurements in a Reverberation Chamber Without the Need for a Reference Antenna". In: *Antennas and Wireless Propagation Letters, IEEE* 7 (2008), pp. 448–450.

- [100] C. Lemoine. “Contribution à l’analyse statistique des mesures en chambre réverbérante à brassage de modes. Applications à la détermination de l’efficacité de brassage et de l’incertitude de mesure dans un contexte CEM et radiofréquences”. PhD thesis. INSA de Rennes, July 2008.
- [101] C. Lemoine, E. Amador, and P. Besnier. “On the K-factor estimation for rician channel simulated in reverberation chamber”. In: *IEEE Transactions on Antennas and Propagation* 59.3 (Mar. 2011), pp. 1003–1012.
- [102] C. Lemoine, E. Amador, P. Besnier, J. Sol, J.-M. Floc’H, and A. Laisné. “Statistical estimation of antenna gain from measurements carried out in a mode-stirred reverberation chamber”. In: *XXXth URSI General Assembly and Scientific Symposium*. Istanbul, Turquie, Oct. 2011, pp. 1–4.
- [103] G. Leon Fernandez, S. Loredo, S. Zapatero, and F. Las Heras Andres. “Radiation pattern retrieval in non-anechoic chambers using the matrix pencil algorithm”. In: *Progress In Electromagnetics Research Letters* 9 (2009), pp. 119–127.
- [104] G. Lerosey, J. De Rosny, A. Tourin, A. Derode, G. Montaldo, and M. Fink. “Time reversal of electromagnetic waves.” In: *Phys Rev Lett* 92.19 (2004), p. 193904.
- [105] G. Lerosey. “Retournement temporel d’ondes électromagnétiques et application à la télécommunication en milieux complexes”. PhD thesis. ESPCI ParisTECH, Dec. 2006.
- [106] Leugering. *Constrained optimization and optimal control for partial differential equations*. Ed. by G. Leugering, S. Engell, A. Griewank, M. Hinze, R. Rannacher, V. Schulz, M. Ulbrich, and S. Ulbrich. Basel: Birkhäuser, 2012, pp. xi + 622.
- [107] J. Lions. “Exact Controllability, Stabilization and Perturbations for Distributed Systems”. In: *SIAM Review* 30.1 (1988), pp. 1–68.
- [108] J. Lions. *Optimal control of systems governed by partial differential equations*. Grundlehren der mathematischen Wissenschaften. Springer-Verlag, 1971.
- [109] J. Lions and E. Magenes. *Problèmes aux limites non homogènes et applications*. Problèmes aux limites non homogènes et applications vol. 1. Dunod, 1968.
- [110] J. Lončarić, V. Ryaben’kii, and S. Tsynkov. “Active Shielding and Control of Noise”. In: *SIAM Journal on Applied Mathematics* 62.2 (2001), pp. 563–596.
- [111] J. Lončarić and S. Tsynkov. “Optimization in the Context of Active Control of Sound”. In: *Computational Science and Its Applications — ICCSA 2003*. Ed. by V. Kumar, M. Gavrilova, C. Tan, and P. L’Ecuyer. Vol. 2668. Lecture Notes in Computer Science. Springer Berlin Heidelberg, 2003, pp. 801–810.
- [112] S. Loredo, M. Pino, F. Las-Heras, and T. Sarkar. “Echo identification and cancellation techniques for antenna measurement in non-anechoic test sites”. In: *Antennas and Propagation Magazine, IEEE* 46.1 (Feb. 2004), pp. 100–107.
- [113] H. Maurer and H. D. Mittelmann. “Optimization Techniques for Solving Elliptic Control Problems with Control and State Constraints: Part 1. Boundary Control”. In: *Computational Optimization and Applications* 16.1 (2000), pp. 29–55.

- [114] H. Maurer and H. D. Mittelmann. "Optimization Techniques for Solving Elliptic Control Problems with Control and State Constraints. Part 2: Distributed Control". In: *Computational Optimization and Applications* 18.2 (2001), pp. 141–160.
- [115] P. Meton, F. Monsef, A. Cozza, M. Lambert, and J. Joly. "Analysis of wavefront generation in a reverberation chamber for antenna measurements". In: *Antennas and Propagation (EuCAP), 2013 7th European Conference on*. Apr. 2013, pp. 867–871.
- [116] D. A. B. Miller. "On perfect cloaking". In: *Opt. Express* 14.25 (Dec. 2006), pp. 12457–12466.
- [117] P. Monk. *Finite Element Methods for Maxwell's Equations*. Numerical mathematics and scientific computation. Clarendon Press, 2003.
- [118] D. C. Montgomery and G. C. Runger. *Applied Statistics and Probability for Engineers*. 5th edition. Wiley, 2011.
- [119] H. Moussa, A. Cozza, and M. Cauteman. "Directive Wavefronts Inside a Time Reversal Electromagnetic Chamber". In: *Proceedings of the IEEE EMC Society Symposium on Electromagnetic Compatibility*. AUSTIN, États-Unis, 2009, pp. 159–164.
- [120] H. Moussa, A. Cozza, and M. Cauterman. "Experimental demonstration of directive pulsed wavefront generation in reverberation chambers". In: *ELECTRONICS LETTERS / IEE Electronics Letters* 46.9 (Jan. 2010), pp. 623–624.
- [121] M. Moussa. "Etude théorique et expérimentale des techniques de retournement temporel application à la caractérisation de composants et dispositifs dans une chambre réverbérante". PhD thesis. Université Paris Sud - Paris XI, July 2011.
- [122] N. Newmark. "A Method of Computation for Structural Dynamics". In: (1959).
- [123] A. Ogunsola, U. Reggiani, and L. Sandrolini. "Modelling shielding properties of concrete". In: *Electromagnetic Compatibility, 2006. EMC-Zurich 2006. 17th International Zurich Symposium on*. 2006, pp. 34–37.
- [124] A. Ogunsola, U. Reggiani, and L. Sandrolini. "Shielding properties of conductive concrete against transient electromagnetic disturbances". In: *Microwaves, Communications, Antennas and Electronics Systems, 2009. COMCAS 2009. IEEE International Conference on*. 2009, pp. 1–5.
- [125] S. J. Orfanidis. *Electromagnetic Waves and Antennas*.
- [126] M. Piette. "Antenna radiation efficiency measurements in a reverberation chamber". In: *Radio Science Conference, 2004. Proceedings. 2004 Asia-Pacific*. Aug. 2004, pp. 19–22.
- [127] S. G. Rabinovich. *Measurement Errors and Uncertainties: Theory and Practice*. New York, NY: Springer New York, 2005.
- [128] S. Ramo, J. R. Whinnery, and T. V. Duzer. *Fields and Waves in communication electronics*. 3rd edition. Wiley, 1994.

- [129] J. M. Rasmussen. “Boundary Control of Linear Evolution PDEs - Continuous and Discrete”. PhD thesis. Technical University of Denmark, Aug. 2, 2004.
- [130] K. Rosengren and P.-S. Kildal. “Radiation efficiency, correlation, diversity gain and capacity of a six-monopole antenna array for a MIMO system: theory, simulation and measurement in reverberation chamber”. In: *Microwaves, Antennas and Propagation, IEE Proceedings* - 152.1 (Feb. 2005), pp. 7–16.
- [131] K. Rosengren, P.-S. Kildal, C. Carlsson, and J. Carlsson. “Characterization of antennas for mobile and wireless terminals in reverberation chambers: Improved accuracy by platform stirring”. In: *Microwave and Optical Technology Letters* 30.6 (2001), pp. 391–397.
- [132] J. de Rosny, G. Lerosey, and M. Fink. “Theory of Electromagnetic Time-Reversal Mirrors”. In: *Antennas and Propagation, IEEE Transactions on* 58.10 (Oct. 2010), pp. 3139–3149.
- [133] M. Sacchi, T. Ulrych, and C. Walker. “Interpolation and extrapolation using a high-resolution discrete Fourier transform”. In: *Signal Processing, IEEE Transactions on* 46.1 (Jan. 1998), pp. 31–38.
- [134] I. Santamaría-Caballero, C. J. Pantaleón-Prieto, and A. Artés-Rodríguez. “Sparse deconvolution using adaptive mixed-Gaussian models”. In: *Signal Processing* 54.2 (1996), pp. 161–172.
- [135] H. Schantz. *The Art And Science Of Ultrawideband Antennas*. Artech House Antennas and Propagation Library. Artech House, 2005.
- [136] D. Schurig, J. J. Mock, B. J. Justice, S. A. Cummer, J. B. Pendry, A. F. Starr, and D. R. Smith. “Metamaterial Electromagnetic Cloak at Microwave Frequencies”. In: *Science* 314.5801 (2006), pp. 977–980.
- [137] I. Scott. “Developments in time-reversal of electromagnetic fields using the transmission-line modelling method”. PhD thesis. University of Nottingham, July 2010.
- [138] I. Scott, A. Vukovic, and P. Sewell. “Time Reversal in Lossy Material: An Assessment.” In: *PIERS Online* (2007), pp. 1259–1263.
- [139] M. Selvanayagam and G. V. Eleftheriades. “An Active Electromagnetic Cloak Using the Equivalence Principle”. In: *IEEE Antennas and Wireless Propagation Letters* 11 (2012), pp. 1226–1229.
- [140] M. Selvanayagam and G. V. Eleftheriades. “Experimental Demonstration of Active Electromagnetic Cloaking”. In: *Phys. Rev. X* 3 (4 2013), p. 041011.
- [141] M. Spirlet, V. Broun, P. Camus, C. Geuzaine, V. Beauvois, and I. Molenberg. “Modelling time reversal applications in a reverberation chamber using the current image method”. In: *Electromagnetic Compatibility (EMC EUROPE), 2013 International Symposium on*. 2013, pp. 359–364.
- [142] M. Spirlet, C. Geuzaine, and V. Beauvois. “Estimation of semi-anechoic chamber radiation patterns from in-situ measurements using the angular responses of the environment”. In: *18th International Symposium on ElectroMagnetic Compatibility (CEM 2016 Rennes)*. July 11, 2016.

- [143] M. Spirlet, C. Geuzaine, and V. Beauvois. “Experimental Correction of Radiation Patterns Between Electromagnetic Environments”. In: *IEEE Transactions on Antennas and Propagation* 65.3 (Mar. 2017), pp. 1330–1338.
- [144] M. Spirlet, C. Geuzaine, and V. Beauvois. “Optimal Control of Time Harmonic Electromagnetic Waves in the UHF Range”. In: *IEEE Transactions on Microwave Theory and Techniques* (2018).
- [145] M. Spirlet. “Experimental Control of One-Dimensional Electromagnetic Environments in the UHF Range”. In: *PIERS 2017*. St-Petersburg, May 24, 2017.
- [146] I. O. for Standardization. *ISO 5725 : Accuracy (trueness and precision) of measurement methods and results*. Standard. 1994.
- [147] J. A. Stratton and L. J. Chu. “Diffraction Theory of Electromagnetic Waves”. In: *Phys. Rev.* 56 (1 July 1939), pp. 99–107.
- [148] J. A. Stratton. *Electromagnetic Theory*. 1st ed. McGraw-Hill, 1941.
- [149] C. Thajudeen, A. Hoorfar, F. Ahmad, and T. Dogaru. “Measured complex permittivity of walls with different hydration levels and the effect on power estimation of twri target returns”. In: *Progress In Electromagnetics Research* Vol. 30.B (2011), pp. 177–199.
- [150] J. T. Toivanen, T. A. Laitinen, and P. Vainikainen. “Modified Test Zone Field Compensation for Small-Antenna Measurements”. In: *IEEE Transactions on Antennas and Propagation* 58.11 (Nov. 2010), pp. 3471–3479.
- [151] C. Tounou. “Contribution à l’étude de systèmes à diversité d’antennes sur terminaux compacts”. PhD thesis. Université de Limoges, 2008.
- [152] F. G. Vasquez, G. W. Milton, and D. Onofrei. “Active Exterior Cloaking for the 2D Laplace and Helmholtz Equations”. In: *Phys. Rev. Lett.* 103 (7 Aug. 2009), p. 073901.
- [153] H. Wheeler. “The Radiansphere around a Small Antenna”. In: *Proceedings of the IRE* 47.8 (Aug. 1959), pp. 1325–1331.
- [154] H. Whitney. *Geometric integration theory*. 1960, p. 534.
- [155] S. Wright and B. Vuksanovic. “Active control of environmental noise”. In: *Journal of Sound and Vibration* 190.3 (1996), pp. 565–585.
- [156] F. Wu, J.-L. Thomas, and M. Fink. “Time reversal of ultrasonic fields. II. Experimental results”. In: *Ultrasonics, Ferroelectrics and Frequency Control, IEEE Transactions on* 39.5 (Sept. 1992), pp. 567–578.
- [157] A. Yaghjian. “An overview of near-field antenna measurements”. In: *Antennas and Propagation, IEEE Transactions on* 34.1 (Jan. 1986), pp. 30–45.
- [158] H. H. Zheng, J. J. Xiao, Y. Lai, and C. T. Chan. “Exterior optical cloaking and illusions by using active sources: A boundary element perspective”. In: *Phys. Rev. B* 81 (19 2010), p. 195116.

